Fabrication and Properties of Nanocapacitors and Nanostructures prepared by Nanosphere Lithography

by

Michael Coutts

Submitted for the Degree of

Doctor of Philosophy

2016

University of Technology Sydney

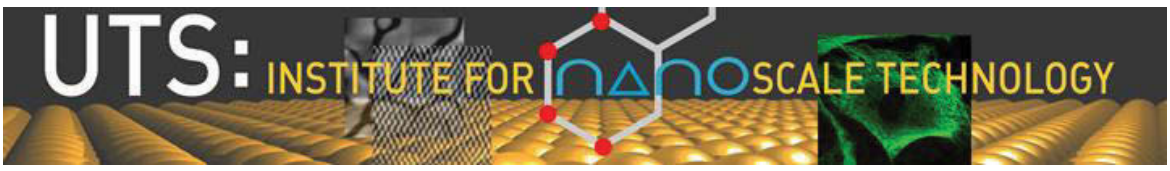

Certificate of Original Authorship

I certify that the work in this thesis has not previously been submitted for a degree, nor has it been submitted as a part of requirements for a degree except as fully acknowledged within the text.

I also certify that the dissertation has been written by me. Any help that I have received in my research work and the preparation of the dissertation has been acknowledged. In addition, I certify that all information sources and literature used are indicated in the dissertation.

Michael Coutts

_____

Date:

Acknowledgements

First and foremost, I would like to thank my primary supervisor Assoc Prof Andrew McDonagh, the most patient person I know. I cannot thank you enough for your knowledge and guidance throughout the years.

Also special thanks to my co-supervisors Prof Mike Cortie and Dr Hadi Zareie. The depth of Mike's knowledge and enthusiasm of Hadi have helped me greatly.

For experimental assistance I would like to thank Dr Ric Wuhrer (UWS), Mr Jean-Pierre Guerbois, Dr Ronald Shimmon, Dr Mark Berkahn, Dr Dylan Riessen, Dr Cuong Ton-That, Mr Geoff McCredie, Prof Matthew Phillips, Dr Tristan Rawling, Ms Katie McBean, Dr Angus Gentle, Dr Brian Reedy, Dr Matthew Arnold, Dr Annette Dowd, A/Prof Vicki Keast and A/Prof Mike Ford.

For support and encouragement thanks go to fellow postgraduate students Dr Nadine Harris, Dr Johnathan Edgar, Dr Marty Blaber, Dr Dakrong Pissuwan, Dr Nick Stokes, Mr Sylvan Rudduck, Dr Burak Cankurtaran, Dr Christine Austin, and Dr Amir Moezzi.

Thanks also goes to the assessors of this thesis, your feedback is greatly appreciated.

Finally, for financial support the Australian Research Council (DP0877539, DP0984354) and the University of Technology Sydney is acknowledged.

Table of Contents

List of Figures

List of Tables

Abbreviations

γ- PGA = Poly-γ-Glutamic Acid

AC = Activated Carbon

AES = Auger Electron Spectroscopy

AFM = Atomic Force Microscopy

AMU = Atomic Mass Units

AR NSL = Angle-Resolved NanoSphere Lithography

CAFM = Conducting Atomic Force Microscopy

CL = Cathodoluminescence

DSC = Differential Scanning Calorimetry

CV curve = Cathodic potential or Cyclic Voltammetry curve

CVD = Chemical Vapour Deposition

CVP = Capacitance Voltage Profile

DC = Direct Current

DCM = Dichloromethane

DNA = Deoxyribonucleic Acid

DPV = Differential Pulse Voltammetry

DRAM = Dynamic Random Access Memory

DWCNT = Double-Walled Carbon Nanotubes

EDS = Energy-Dispersive X-ray Spectroscopy

E_F = Fermi level

ESEM = Environmental Scanning Electron Microscopy

fcc = Face-centred cubic

GO = Graphene Oxide

hcp = Hexagonal close-packing

HOMO = Highest Occupied Molecular Orbital

HOPG = Highly Ordered/Orientated Pyrolytic Graphite

HV = High Vacuum

IC = Integrated Circuit

IR = Inner Region

IUPAC = International Union of Pure and Applied Chemistry

IV = Current Voltage

LUMO = Lowest Unoccupied Molecular Orbital

LSV = Linear Sweep Voltammetry

MCC = Metal Carbonyl Cluster

MPC = Monolayer Protected Cluster

MS = Mass Spectrometry

MWCNT = Multi-Walled Carbon NanoTube

n-type = Negative-type

NMR = Nuclear Magnetic Resonance

NSL = NanoSphere Lithography

p-type = Positive-type

PANi = Polyaniline

PEDOT = Poly (3,4-ethylenedioxythiophene)

pFPT = Poly(3-(4-fluorophenyl)thiophene)

pMeT = Poly(3-methylphenylthiophene)

PS = Polystyrene

pTh = Poly(thiophene)

PVD = Physical Vapour Deposition

QCM = Quartz Crystal Microbalance

RF = Radio Frequency

RPM = Revolutions Per Minute

SAM = Self-Assembled Monolayer

SE = Secondary Electron

SDS = Sodium Dodecyl Sulphate

SEM = Scanning Electron Microscopy

SERS = Surface Enhanced Raman Spectroscopy

STM = Scanning Tunnelling Microscopy

STS = Scanning Tunnelling Spectroscopy

Surfactant = Surface active agent

SWCNT = Single-Walled Carbon NanoTube

T_A = Annealing Temperature

TEM = Transmission Electron Microscopy

TFT = Thin Film Transistor

TGA = Thermogravimetric Analysis

TLC = Thin Layer Chromatography

T_M = Melting Temperature

T_S = Substrate Temperature

UHV = Ultra High Vacuum

UTS = University of Technology, Sydney

UV = Ultraviolet

XPS = X-ray Photoelectron Spectroscopy

ZSR = Zero State Response

Publications and Conference Proceedings Arising From This Work

1. Coutts. M. J.; Zareie. H. M.; Cortie. M. B.; Phillips. M. R.; Wuhrer. R.; McDonagh. A. M., *Exploiting Zinc Oxide Re-emission to Fabricate Periodic Arrays.* ACS Applied Materials & Interfaces. 2010 **2**(6): p. 1774-1779.
2. Cortie. M. B.; Coutts. M.J.; Ton-That. C.; Dowd. A.; Keast. V. J.; McDonagh. A. M., *On the Coalescence of Nanoparticulate Gold Sinter Ink.* J. Phys. Chem. C. 2013 **117**(21): p. 11377–11384.
3. Coutts. M. J.; Zareie. H. M.; Cortie. M. B.; McDonagh. A. M., *Charging of gold/ metal oxide/ gold nanocapacitors in a scanning electron microscope.* Nanotechnology. 2014 **25**(15): p. 155703.
4. Coutts. M. J.; Zareie. H. M.; Cortie. M. B.; Phillips. M. R.; Wuhrer. R.; McDonagh. A. M., *Patterning nanostructures for ZnO nanorod growth. International Conference on Nanoscience and Nanotechnology (ICONN 2010)*. 2010. Sydney, Australia.
5. Riessen. D.; Coutts. M. J.; Zareie. H. M.; McDonagh. A.M., *Ruthenium phthalocyanine thin films on gold*. *International Conference on Nanoscience and Nanotechnology (ICONN 2010)*. 2010. Sydney, Australia.
6. Coutts. M. J.; Zareie. H. M.; Cortie. M. B.; Phillips. M. R.; Wuhrer. R.; McDonagh. A. M., *Solution Growth of Zinc Oxide on Templates Fabricated by Re-emission of Sputtered Materials*. *Inaugural One-day Student Symposium in Inorganic Chemistry*. 2011. School of Chemistry, The University of Sydney, Australia.

Abstract

Nanosphere lithography was used to synthesise nanoscale capacitors as well as arrays of zinc oxide nanostructures. Close-packed polystyrene nanospheres were used as masks and periodic arrays of metals / metal oxides were deposited through the inter-sphere voids onto substrates. The technique was optimised to produce hexagonally close-packed arrays of polystyrene spheres for a range of sphere sizes (200-1500 nm). Nanoscale capacitors were synthesised via evaporative and sputter deposition to produce structures consisting of gold / metal oxide / gold layers on a silicon substrate. A range of metal oxides were investigated including alumina, silica, zinc oxide, titania and hafnia. A significant development reported here involves the charging of these devices and their characterisation using scanning electron microscopy techniques. These methods enable the measurement of the charging time constants of materials in a non-destructive fashion without the requirement to connect wires or contacts. Nanostructures fabricated using zinc oxide as a dielectric material produced rings of zinc oxide nanostructures on the silicon substrate and a mechanism for the ring formation is proposed here. The resultant structures were used as templates to seed the hydrothermal growth of zinc oxide nanostructures. Arrays of zinc oxide nanostructures were also produced using techniques that enable control over the position and amount of growth.

Chapter 1:

Introduction

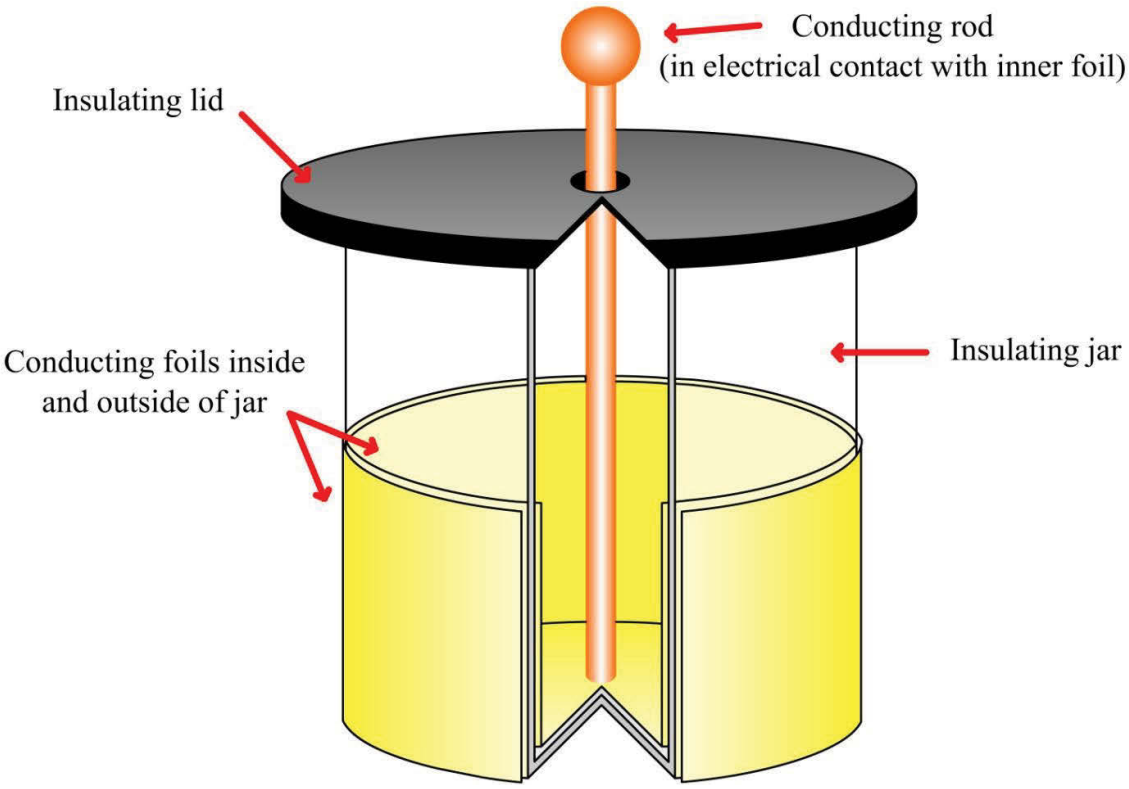

1 Introduction

1-1 Thesis overview

This thesis examines discrete nanoscale capacitors and nanoparticulate matter. The theme that unifies these aspects is that of capacitance in nanostructures.

Chapter 1 provides an introduction to capacitors and nanocapacitors. Early capacitors are described in conjunction with a description of the science behind their operation. The concept of capacitance is introduced along with current research aimed at maximising power and energy densities as well as the synthesis of capacitors with nanoscale dimensions.

Chapter 2 provides experimental details and parameters for the work described in this thesis together with some theoretical background to the techniques.

Chapter 3 examines the fabrication of large arrays of periodic nanostructures utilising nano / microsphere lithography. The effect of sphere mask size as well as solution volume and concentration on both domain sizes and surface coverage of hexagonally close packed regions are studied. The effect of gold's kinetic energy upon substrate interaction and subsequent structures obtained during nanosphere lithography (NSL) is presented.

The optimisation of the microsphere lithography process in Chapter 3 allowed the demonstration of nanoscale capacitors in Chapter 4. Triangular parallel-plate capacitors were fabricated by a combination of nanosphere lithography and physical vapour deposition. The devices were comprised of dielectric material sandwiched between two layers of gold, on a silicon substrate. A variety of dielectric fillings were investigated. Charging of the capacitors was investigated in a scanning electron microscope by monitoring the change in brightness of the images of the devices as a function of time to form an experimental estimate of charging time constant (RC).

During the synthesis of gold / zinc oxide /gold nanocapacitors (described in Chapter 4) an interesting phenomenon was observed where zinc oxide was deposited out of the 'line-of-sight' trajectory of the nanosphere lithography mask. This was further investigated in Chapter 5 with the synthesis of hexagonal ring-shaped structures of zinc oxide using microsphere lithography and metal / metal oxide sputtering. This synthesis

exploits the surface re-emission of zinc oxide to deposit materials in regions out of the line-of-sight of the sputtering target. These rings can nucleate the hydrothermal growth of zinc oxide crystals. Control over the growth could be exercised by varying growth solution concentration, temperature, or by applying an external potential.

General conclusions and areas for future work are described in chapter 6.

In early work, the sintering mechanism of electrically insulating thiol encapsulated gold nanoparticles to form conducting thin films of gold was studied. It was hoped that the understanding of this mechanism would aid the investigation of gold nanoparticles as capacitors and / or nanoscale wires. However, a full investigation into the uses of the gold sinter inks with nanocapacitors was not pursued and so this work has not been placed in the body of this thesis and can be found in the appendix.

1-2 Capacitors

The continued miniaturisation of electronic circuits requires that their components (e.g. resistors, transistors, diodes, and capacitors [1]) be correspondingly shrunk in size. This process has proceeded to the point where many components have now attained sub-100 nm, i.e. nanoscale, dimensions. Components such as resistors are readily scaled to these dimensions and their fabrication is now straightforward. Other components however pose more significant challenges. Single electron transistors have been investigated extensively although thermal noise can be problematic [2]. Rectification by molecular devices (nanoscale diodes) has received considerable attention [3] with some fundamental limits to their operation identified [4]. In contrast to these components, somewhat less attention has been paid to the equally important question of capacitance at the nanoscale (with the exception of parasitic capacitance [5]). Here, recent developments in this field are explored.

1-2.1 The evolution of Capacitors - A Brief History

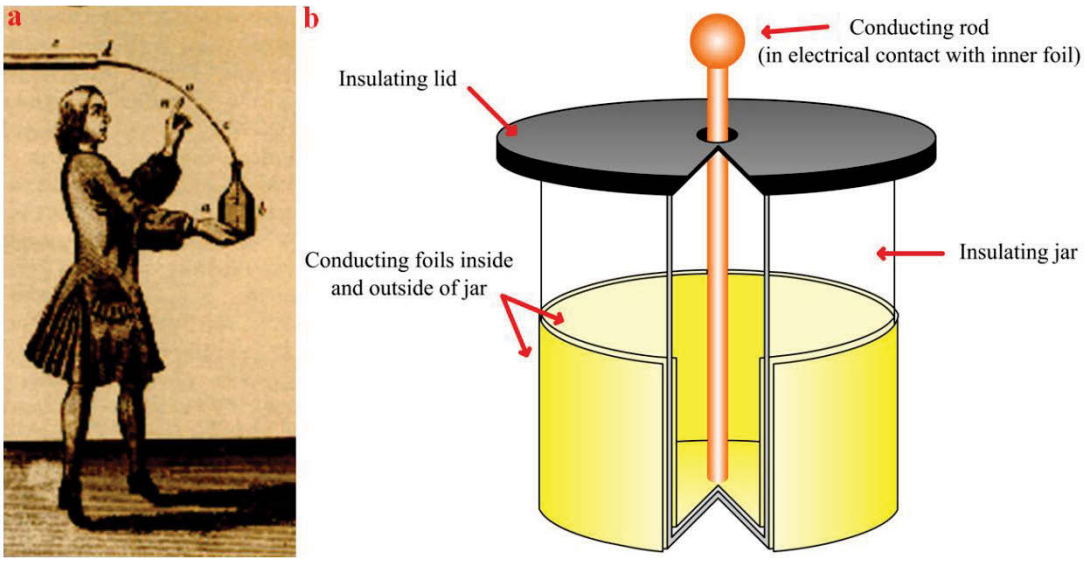

Figure 1-1. (a) Illustration representing electrical discharge of a Leyden jar through the body. Image adapted from [6]. (b) Schematic of a Leyden jar.

A capacitor is an electronic device that can store electrical charge. Capacitors are often used in portable devices that require high power densities, such as an electronic flash in a camera. At times of high demand, a capacitor can release its charge within a fraction of a second to power the device. Capacitors are also used to eliminate fluctuations in voltage by absorbing excess charge and releasing charge when the voltage is insufficient [7]. They can be used to block DC voltages [8], and are used as stand-alone power supplies, or in combination with batteries.

The Leyden jar was the first capacitor to utilise mutual capacitance (charge storage between two adjacent conductors). The device was invented independently in 1745 by Pieter van Musschenbroek [9] and Ewald Georg von Kleist [10]. Incipient devices consisted of two electrically isolated conducting foils (originally tinfoil in Musschenbroek's device) coating the inside and outside of a glass jar between a half and two thirds of the total height, see Figure 1-1(b). Applying charge to one of the plates (through some form of static generation) results in surface charge equal in magnitude and opposite in sign on the other plate. The glass acts as a dielectric material – a material that has insulating properties but can be polarised by an electric field. The Leyden jar was capable of storing significantly more charge than was previously possible (by induction on large metal sheets or metal spheres utilising self-capacitance).

Daniel Gralath was the first natural philosopher to connect several Leyden jars together [11] and these devices, along with ‘flat capacitors’ invented by Benjamin Franklin in 1752 [12] were the most popular charge storage devices until the invention of the galvanic cell in 1780 which was capable of producing a more constant but less powerful supply of charge (i.e. a lower power density but higher energy density).

Later, the terms ‘flat capacitor’ and ‘Leyden jar / bottle batteries’ were largely superseded with ‘condensor’ (coined by Volta [13]), in the late 1800s / early 1900s, when superior condensors were required for radio applications. A popular design used rolled up sheets of metal foil separated by a flexible dielectric material (known as coil condensors). This allowed greater surface area electrodes (defined by Faraday [14]) to be stored in a more compact space. Tesla pioneered the use of electrodes immersed in polarisable oils [13] and other electrolytes. This reduced heating by molecular bombardment for high frequency applications [6]. A proliferation of devices with anodised electrodes, patented by Charles Pollak [15], next appeared. The most common of these, the aluminium electrolytic capacitor consisted of two pieces of aluminium foil separated by a paper spacer soaked in electrolyte. One of the aluminium foil rolls was oxidised electrochemically to form the anode with a very thin, uniform dielectric, while the electrolyte and non-oxidised foil formed the cathode. This configuration resulted in a polarisable device, capable of accommodating charge flow in only one direction. The use of foils and an aluminium case gave a lightweight, compact, low cost, robust device which became popular in power supply smoothing and low frequency decoupling applications. Around the 1950s, tantalum electrolytic capacitors became popular and are generally favoured over aluminium based devices where higher capacitances and reliability are of paramount importance. Electrolytic capacitors are second only to ceramic capacitors in popularity. First appearing in the 1930s, ceramic capacitors are multilayered devices containing different ceramics depending on the required application, common examples include titanium dioxide, strontium titanate, and barium titanate. Other popular types of capacitors include polycarbonate based devices for high precision circuits, glass capacitors for high performance radio frequency (RF) applications and metallised polystyrene capacitors for compact size.

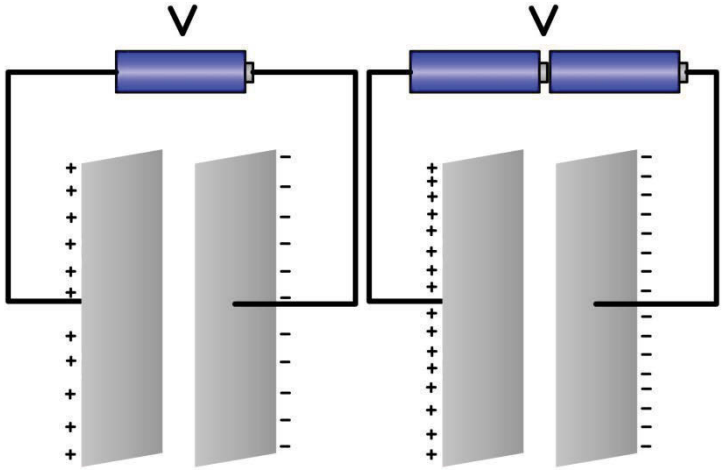

Figure 1-2. Schematics representing the charging of two parallel plates by different potentials.

Figure 1-2 shows a relatively simple example of a parallel plate capacitor connected to a power supply. Charge build-up results in parallel electric field lines between the plates and through the dielectric material. Electrons in the atoms of the dielectric material are confined to their atomic radii and are not free to move but the electric field can distort the electron density, polarising each atom. The dielectric remains electrically neutral overall but the surface layers closest to the plates will have charge opposite in sign to that of the conducting plates. This charge build-up at the edges of the dielectric will produce its own electric field in the opposite direction to the one produced by the electrodes. Increasing the potential (V) of the power supply increases the amount of charge on each plate linearly by an experimental constant, C, yielding the relationship:

$$q = CV$$

Where q is the charge (in Coulombs) and C is the proportionality constant between charge and applied potential, or the material's capacitance. Capacitance (measured in Farads) is therefore the amount of charge stored at a potential difference (Volts):

$$C = \frac{q}{V}$$

Although charge can be stored on naked metallic surfaces in vacuum or air, more effective storage becomes possible when conducting surfaces are immersed in electrolytes. Energy storage in electrolytic capacitors utilises double-layer capacitance or more complex pseudo-capacitance. Double-layer capacitance, first demonstrated experimentally with platinum electrodes [16] and then described theoretically by Helmholtz stores energy as charge separation at the interface between the solid electrode surface and the polarised liquid electrolyte (Figure 1-3.) [17].

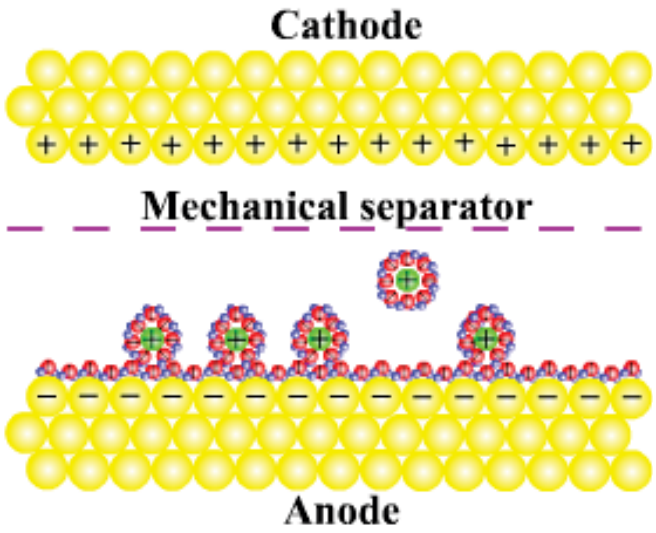

Figure 1-3. Schematic of double-layer capacitance.

Double-layer capacitance is responsible for fast charge transfer and consequently high power output. The high capacitance values achieved by devices utilising this phenomenon is a consequence of the large electric field values induced through the molecularly thin monolayer of solvent molecules polarised at the electrodes surface. In a capacitor that employs pseudo-capacitance, the majority of charge is transferred at, or near the solid electrode surface via relatively fast, reversible redox reactions. This may involve surface adsorption of ions from the electrolyte or redox reactions [17, 18]. Materials that employ pseudo-capacitance rely on redox reactions and consequently cannot deliver charge as fast as double-layer capacitors. However more charge can be stored per gram.

For the simple dry parallel plate capacitor (composed of two electrodes separated by a dielectric material, often paper, thin plastics, metal oxides or ceramics), the capacitance can be calculated using the formula [19]:

$$C = \varepsilon_o \varepsilon_r A/L$$

Where ε_0 is the vacuum permittivity, ε_r is the relative permittivity of the dielectric (formerly known as the dielectric constant), A is the plate area (m^2), and L is the distance separating the plates (m).

Capacitance is proportional to the surface area of the electrode and inversely proportional to the distance between the electrodes. Hence, using nanoscale materials

with high surface area can increase the capacitance significantly as will reducing the distance between electrodes to nanoscale dimensions.

1-2.2 Ideal Capacitance at the Nanoscale

The simplest example of a capacitor is a naked isolated conducting sphere. If the shape of a nanoparticle is approximated as spherical, the self-capacitance can be derived using Gauss's law:

$$C = 4\pi\varepsilon_0 r$$

For a bare isolated sphere where r is the particle radius (m), or:

$$C = 4\pi\varepsilon_0\varepsilon_r\left(\frac{r}{d}\right)(r+d)$$

when the sphere is insulated by some form of dielectric material such as stabilising ligands or oxide surface layer of a thickness, d (m) [20]. Spherical capacitors that rely on self-capacitance are relatively inefficient, for example the earth has a theoretical self-capacitance of ~710 μF [21]. This is a major limitation for designing spherical capacitors at the nanoscale.

Nanoscale capacitors can have high power densities, short charging times, an ability to release their entire charge very quickly, and long cycle life (>10,000 cycles) [8, 22, 23]. In principle, capacitors of such small size have potential advantages in the design of electronic devices, where devices with nanoscale dimensions can utilise the extremely high capacitance and power densities of nanoscale capacitors. The cost of electrode material can be an important consideration for commercial applications of nanoscale capacitors [17]. For example, ruthenium oxide pseudo-capacitors exhibit excellent performance but this material is expensive and relatively toxic, limiting its commercial use.

The electrochemical properties required of nanoscale capacitor materials in electrolytic capacitors include high conductivity of the electrode material and electrolyte (< 1 mΩ-cm), and fast, reversible charging / discharging capability. Nanoporous materials should have a uniform pore size distribution for stable charge transfer that is large enough to allow free diffusion of electrolyte ions through the material. Aqueous electrolytes have been found to have considerably lower resistance (1-2 Ω-cm) than organic electrolytes (20-60 Ω-cm), and are less toxic, cheaper and non-flammable [24].

Therefore aqueous electrolytes are often used [17, 25] even though their operating voltage is limited to about 1.2 V by the electrochemical breakdown of water [24].

As capacitors are required for high speed power supplies, the kinetics of charge storage must be fast enough to allow for short charging times and high speed discharge without excessive power losses. For a capacitor to have a long cycle life in applications that do not require power signal smoothing, the material must be capable of reversible charge storage [22]. Also, material purity is important as contamination in the electrode or electrolyte can lead to current leakage and self-discharge of the capacitor [17]. For practicality, electrode materials should have reasonable mechanical strength and be resistant to corrosion in their electrolytes. Both the electrode material and electrolyte should have good chemical and temperature stability (in both active and quiescent states) in order to remain functional in the conditions imposed by specific applications [26, 27]. Finally, the electrode material should have a large, accessible surface area (~1 to 2000 m^2g^{-1} range).

Current research into nanoscale capacitors generally involves one of two approaches; utilising materials with nanoscale properties to achieve large capacitance values in micro / macro scale devices, or the synthesis and characterisation of capacitors which are nanoscale themselves (often atto- to nanoFarad capacitances). In the first approach, electrochemical capacitors are being intensely studied for use in portable devices. Continued advances in mobile consumer electronics are driving a need for small, robust and lightweight power supplies capable of delivering large energy and power densities [28]. Conventionally batteries (single use and rechargeable) are utilised for high energy storage while capacitors handle power intense applications. When both of these properties are required the two components may be used together. Extensive research has been conducted in this field and there are several reviews available on the topic [29-33], however this field is moving at such a rapid pace that all reviews have a relatively short shelf life.

1-2.3 Methods to Measure Nanoscale Capacitance

The most common method for determining capacitance experimentally involves the measurement of a materials or devices current-voltage characteristic or I-V curve. This is a plot of the resultant electrical current flowing through a sample relative to an

applied potential. I-V curves can subsequently be used to measure capacitance by utilising the expression:

$$C = \frac{i}{s}$$

Where: *i* is the current response (generally reported as the zero state response (ZSR) between 0 and 1 V but can be measured for any voltage range) and *s* is the potential sweep rate (*dV/dt*).

Measuring capacitance at the nanoscale however, poses specific challenges compared to macroscale devices. The most obvious of which being size constraints making the connection of wires / leads for individual measurements of nanoscale devices exceptionally difficult [34]. Capacitance values are typically very small (sub attoFarads for example in devices such as gold nanoparticles with fewer than 150 'core' atoms are common [35]), such values mean that experimental and background noise becomes problematic and great care must be taken to account for / minimise this. The inherently small nature of the devices also means that to account for noise, and to be discernible from parasitic capacitance i.e. capacitance of wires and interconnects, very large current and electric field densities in devices are required [36]. These conditions have the potential to modify device components e.g. possibly introducing asymmetric capacitance [37] or even causing destructive testing (particularly in devices comprised of organic material [38]). Materials can also possess very different properties at the nanoscale, for example the orientation of a materials crystal structure can have a huge impact on the surface states interacting with any probe [39].

Techniques for measuring capacitance at the nanoscale take two broad approaches; 1) Measuring electrodes constructed of nanoscale materials or solution ensembles of devices / materials (such as monolayer protected clusters) with electroanalytical based techniques such as cyclic voltammetry (CV) [40] or differential pulse voltammetry (DPV) for materials that exhibit quantised charging [41]. 2) Measuring individual devices / interfaces directly by techniques such as scanning tunnelling microscopy (STM) [42], scanning capacitance microscopy (SCM) [43] which utilises conducting atomic force microscopy (CAFM), or a combination of techniques such as nanoprobing in conjunction with scanning electron microscopy [44] or atomic force microscopy [45].

Cyclic voltammetry is a voltammetry technique that is an extension of linear sweep voltammetry (LSV), which itself developed from polarography as invented by Heyrovský [46-48]. In linear sweep voltammetry the current between a working electrode and counter electrode is measured as a function of a constantly ramped voltage (relative to a reference electrode). The three electrode setup is generally preferred in voltammetry experiments due to the fact that redox reactions occurring at the working electrode make stable voltage measurements problematic in a two electrode system.

In cyclic voltammetry once the desired end voltage has been reached, the voltage is then returned to its original potential in the reverse linear manner of the initial sweep. Cyclic voltammetry is used in capacitor characterisation primarily to determine a materials capacitance behaviour. Redox reactions (pseudo-capacitance) in analytes result in peaks / troughs in a CV curve corresponding to an oxidation or reduction and later in the scan to a reversal of the process (materials that do not undergo a reversal are unsuitable for use as capacitors in the measured range). While CV curves of capacitive materials that employ double-layer capacitance have an absence of these peaks and tend to be more rectangular in nature. CV also enables robustness testing of samples to determine how many charge / discharge cycles devices can maintain ideal behaviour.

Differential pulse voltammetry involves probing the resultant current when the voltage sweep is performed as an increasing series of voltage steps rather than a continuous voltage sweep. The current measurement is performed just before the next voltage pulse is induced. The primary advantage of differential pulse voltammetry is the minimisation of background current (provided by the sweep) resulting in a higher proportion of Faradic current being probed and hence more information on the redox processes is provided. Reversible redox processes are characterised by symmetrical peaks, while irreversible processes demonstrate asymmetric characteristics. It has been demonstrated by Murray's group [35] that the change in voltage between DPV peaks can be used to estimate the capacitance of a device sufficiently small that the charge transfer is quantised, this is done using the expression:

$$\Delta V = \frac{e}{C_{CLU}}$$

Where ΔV is the change in potential between DPV peaks, e is the elementary charge of an electron (1.602 x 10^{-19} C) and C_{CLU} is the capacitance of an individual gold nanoparticle (F).

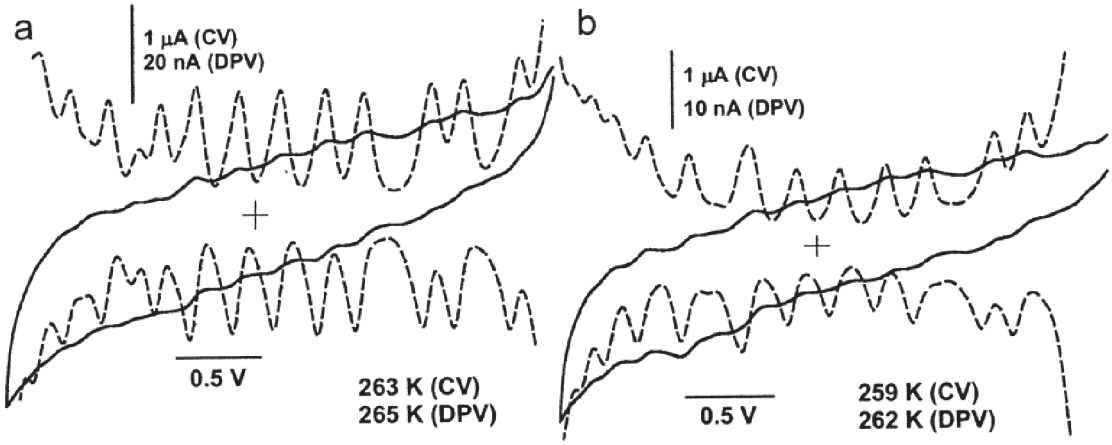

Figure 1-4. DPV (dashed lines) and CV (solid lines) curves for hexanethiolate ligand monolayer protected clusters (MPCs). DPV highlights the peaks in the CV curve attributed to quantised electron double-layer charging. Curves adapted from [35].

The extremely high spatial resolution and current sensitivity of scanning tunnelling microscopy makes it an indispensable tool for measuring the capacitance of nanoscale devices. I-V curves are the simplest and most prevalent technique used, however, Capacitance Voltage Profiling (CVP) (stemming from the semiconductor industry [49]) is also common. Here, a series of capacitance measurements are taken for a range of voltages [50]. In a similar manner to DPV capacitance measurements can also be made where the charging characteristics of devices are quantised [51].

Conducting atomic force microscopy allows the electrical characterisation of an area comparable to the sharpness of an atomic force microscopy (AFM) tip by utilising conductive tips to image an area of a sample and subsequently perform I-V curves on a desired region [52].

Scanning capacitance microscopy provides capacitance information in conjunction with surface topography by measuring the current produced by an AC bias induced between a conducting AFM tip and the sample [53, 54]. Also developed for the semiconductor industry SCM initially used conducting tips such as platinum / iridium

wires attached to conventional AFM tips [55], today silicon nitride tips coated in conducting material such as platinum or platinum / iridium alloys are more common.

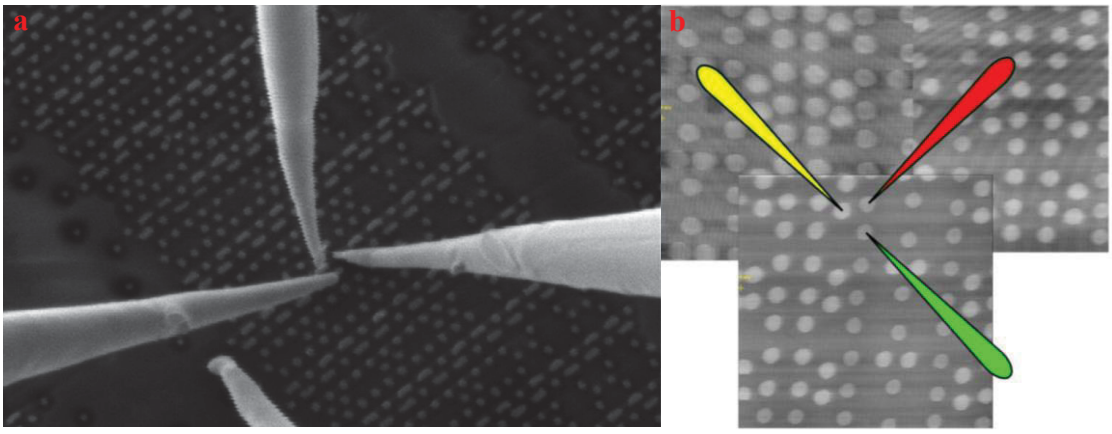

Figure 1-5. Nanoprobing to characterise the electrical properties of devices. (a) SEM micrograph of nanomanipulators making point contacts with a device. Image adapted from [44]. (b) AFM image of terminal contacts of a device which was electrically characterised by three CAFM tips making point contacts simultaneously (represented by schematic overlay). Image adapted from [45].

Figure 1-5 show examples of how nanoprobing can be used in conjunction with SEM or CAFM to electrically characterise a device. In conjunction with SEM, nanoprobing provides a flexible method for electrically characterising samples.

SEM had also been demonstrated to experimentally estimate the capacitance of nanoscale devices at UTS [19]. Discrete nanoscale capacitors were imaged under low accelerating voltage conditions and the change in secondary electron signal was measured as a function of time. The primary advantages of this approach is its non-destructive nature and relative ease of measurement. However, this demonstration was only a proof-of-concept and more work was required to understand the process better.

In the next section, the materials chemistry associated with nanoscale capacitors and the associated challenges are discussed.

1-2.4 Materials for Nanoscale Capacitors

Metal Oxides

A significant amount of research has been undertaken into nanoscale electrochemical capacitors incorporating ruthenium oxide. Ruthenium oxide in the amorphous, hydrated form has an extremely high capacitance of 720-768 Fg^{-1} [56-58] and is currently the best performing material in this class. The cyclic voltammogram for amorphous, hydrated ruthenium oxide, Figure 1-6, is almost rectangular in shape, indicating near-ideal capacitance behaviour.

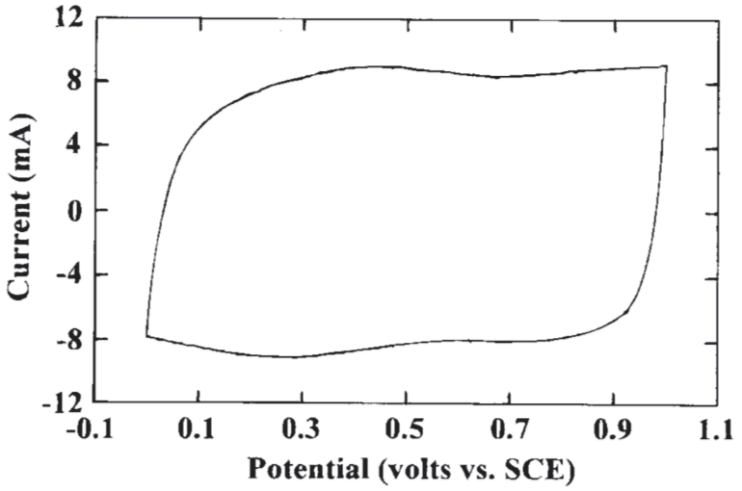

Figure 1-6. Cyclic Voltametric curve of $RuO_2.xH_2O$ [57]

Although these properties shine favourably on ruthenium oxide for use in nanoscale capacitors, the high cost of the material (due to the relative scarcity of ruthenium) is a limiting factor.

Unsurprisingly, current research revolves around attempts to alloy ruthenium oxide with other metals, disperse ruthenium oxide in less expensive materials, or find an alternative transition metal oxide with similar electrochemical properties.

Jeong and Manthiram [59] synthesised an amorphous ruthenium-chromium oxide alloy for electrochemical capacitor applications. They achieved a maximum specific capacitance of 840 Fg^{-1}, but samples with high chromium content were found to have a short cycle life. However, a 15% Cr content provided specific capacitance of 740 Fg^{-1} and robustness over many cycles.

Long *et al.* [60] proposed a mixture of ruthenium and titanium oxides in an aero gel matrix, however the specific capacitance of the material was very low (1.2 Fg^{-1}). Alloying does not appear to be a promising strategy for enabling the commercial use of ruthenium oxides in nanoscale capacitor materials since a large proportion of ruthenium oxide is still required.

Perhaps a more promising strategy is the dispersion of ruthenium oxide in carbon nanotubes, nanofibers and graphene sheets. Kim *et al.* [61, 62] achieved an exceptional specific capacitance of 1170 Fg^{-1} by electrodepositing ruthenium oxide onto a carbon nanotube substrate. Lee *et al.* [63] also reported high specific capacitance of 824 Fg^{-1} for a nanocomposite made up of amorphous ruthenium oxide and vapour grown carbon fibres. Stability tests over 10,000 cycles indicated that this electrode material is very robust with capacitors retaining 90-97% of their capacity. The addition of ruthenium oxide to the carbon materials also increased the rate of charging / discharging processes due to the fast faradic reactions of a pseudo-capacitive nature. Dispersions of ruthenium oxide in cheaper materials is a feasible solution to the cost and toxicity issues surrounding pristine ruthenium oxide and could contribute to a commercial nanoscale capacitor material.

Nano-manganese dioxide [64] has a reported specific capacitance of 250 Fg^{-1} but this is much lower than that of ruthenium oxide. Robustness testing also revealed that repeated charging / discharging cycles results in a rapid decrease in capacitance.

Other transition metal oxides which have been investigated include aluminium oxide and silicon dioxide. A summary of the electrode materials and their specific capacitance values is given in Table 1-1.

Table 1-1. Metal Oxide materials for nanoscale capacitor applications.

Electrode Material	Specific Capacitance (Fg^{-1})	Citation
Nanometre Au layers on Si with alternating TiO_2 layers	273 (nF)	[65]
Cr incorporated in amorphous, hydrated RuO_2	840	[59]
poly-Si and SiO_2 layers on a quartz wafer	28 (pF)	[66]
Carbon nanotube film with deposited RuO_2	1170	[62]
Carbon nanotube film with electrodeposited RuO_2	1170	[61]
Vapour Grown carbon fibre with a dispersion of $RuO_2.xH_2O$	824	[63]
Ultra-thin SiO_2 layer incorporated with redox active molecules	Not tested	[67]

Ultra-thin SiO_2 layer with surface monolayer of porphyrin molecules	15.74 (μFcm^{-2})	[68]
(Ru-Ti)O*x* aero gel	1.2	[60]
Nano-MnO_2	250	[64]
Nanoporous Al_2O_3 layers on carbon nanotube electrodes	177 ($nFcm^{-2}$)	[69]
Ultra-thin SiO_2 layer with Co nanocrystal floating gates	Not tested	[70]
Hydrous RuO_2	720	[57]
Hydrous RuO_2	768	[56]
Hydrous RuO_2 and carbon black electrodes (90:10)	716	[58]

As well as electrochemical capacitors, capacitors of nanoscale dimensions utilising metal oxides for dynamic random access memory (DRAM) devices have also been investigated. Tantalum pentoxide in pristine [71] and doped [72] forms is a popular choice. Tantalum pentoxides have a high relative permittivity (or dielectric constant κ) [73] and together with a high resistivity translates to an ability to store large amounts of charge. However, in its pristine form both the unreacted metal and the metal oxide interface poorly with silicon and silicon oxides / nitrides [74]. Some success has been made with doping with materials such as titanium during the deposition process to improve material contacts [75]. Deposited top contacts have also been shown to influence degradation of the oxide layer [76].

Metal Nitrides

Transition metal nitrides receive little attention as materials for nanoscale capacitors. This is mostly due to their relatively poor resistivities. Choi and Kumta [77] synthesised high purity vanadium nitride nanocrystals and evaluated its electrochemical properties. They achieved very high specific capacitance of 850 Fg^{-1}, which is comparable to ruthenium oxide. The long term stability of the crystals was highly dependent on the size of the crystallites and the capacitors began to lose capacity after 350 cycles. The crystals were also found to be unstable at high pH values of electrolyte, which are common conditions in capacitors. Although the initial capacitance appeared promising, the stability of this material does not appear to be suitable for capacitors.

Shelimov *et al.* [78] attempted to utilise a metal nitride with poor results. Nanoscale capacitors composed of alternating conducting (carbon) and insulating (boron nitride) layers within anodic aluminium templates had a specific capacitance of 13 μFcm^{-2} but the boron nitride films were inadequate at resisting capacitance leakage. The

electrochemical characteristics of the capacitor degraded over time, with resistance increasing by an order of magnitude after only a few days.

Carbon Nanotubes

Carbon nanotubes possess several desirable characteristics including high chemical stability, low mass density, low resistivity, considerable mechanical strength and large surface area that have sparked interest into their use [22, 79]. The accessibility, relatively low cost and ease of processing also makes carbon nanotubes attractive [80].

Current research into carbon nanotube capacitors involves two broad approaches. Firstly; maximising surface-electrolyte interactions to increases double-layer capacitance and produce higher power densities. Secondly; incorporating composites of metal oxides (or similar materials), utilising pseudo-capacitance to increase energy densities.

Surface-electrolyte interaction can be improved by chemical treatment (also called activation) by acids [81-87], bases [84-86, 88-97], carbon dioxide [98] or steam [99]. Oxidation, thermally [100-104] as well as with strong acids [98, 105, 106] or by electrochemical methods [107] can introduce defects into the nanotubes structure and open the end-caps of carbon nanotubes [102] thereby increasing the surface area and 'wettability' by the formation of COOH groups [82, 99]. Doping [93, 108-110] or functionalisation [102, 111, 112] also affects electrolyte interaction.

Carbon nanotubes have also been used in composite with materials such as conducting polymers and metal oxides to increase the specific capacitance and energy density of devices. Conducting polymers such as polyaniline [113-116], polypyrrole [83, 84, 86, 97, 112, 117-123], and other polymers [121, 124] are used, giving higher specific capacitance values. Metal oxide carbon nanotube composites have also been shown to have a synergistic effect with materials such as ruthenium [104, 125-129], manganese [123, 130-135], iron [136], cobalt [137], nickel [137, 138], indium [139], as well as zinc oxide and cobalt hydroxide [140]. Repeated heating / cooling cycles have been shown to increase specific capacitance values for electrodes composed of carbon nanotubes [141].

Table 1-2. gives an overview of specific capacitance values obtained for single walled (SW) and multi walled carbon nanotubes (MWCNTs) under different conditions. Energy density values are also given where reported.

Table 1-2. Carbon nanotubes for nanoscale capacitor applications

Electrode Material	Energy density ($Wh\ kg^{-1}$)	Specific Capacitance (Fg^{-1})	Citation
Multi-walled Carbon Nanotubes H_2SO_4 electrolyte		102	[142]
Single-Walled Carbon Nanotubes	15.8	73-180	[22, 143]
SWCNT, high purity	94	160	[144]
SWCNT, paper		35.9	[145]
SWCNT, stretchable		54	[146]
SWCNT, arc discharge, pellet pressed	7	180	[147]
SWCNT, arc discharge, air oxidized (350^{o}C)	2	140	[100]
SWCNT, arc discharge, HNO_3 activated		105	[81]
SWCNT, arc discharge, KOH activated, pellet pressed	6.5	178	[88]
SWCNT, arc discharge, fluorinated		55	[111]
SWCNT, arc discharge, KOH activated		55	[89]
SWCNT, electrochemically oxidized (KOH)		113	[107]
SWCNT, dicyanamide electrolyte		24.3	[148]
SWCNT, $LiClO_4$/propylene carbonate electrolyte		45	[149]
SWCNT / carbon nanohorn composite		46	[150]
SWCNT, printed	6	36	[151]
SWCNT, compressive stress (LiCl electrolyte)		41.4	[152]
SWCNT, CVD, liquid-induced densification (micron length)	69.4	80	[153]
SWCNT, p-doped		69	[108]
SWCNT, unzipped	24.7	114	[143]
SWCNT, carboxylic functionalised, spray deposition		155	[99]
Carbon nanotubes grown on graphite foil electrode		115.7	[27]
Carbon nanotubes with $LiN(SO_2CF_3)_2$/acetamide electrolyte		30	[154]
Carbon nanotubes, arc discharge, current collector free	0.02	39	[155]
Carbon nanotubes, triton-X 100 composite		39	[156]
Double-Walled Carbon nanotubes, HNO_3 oxidised		54	[105]
DWCNT, p-doped		45	[108]
Multi-Walled Carbon nanotubes		135	[85]
MWCNT, bamboo shaped (many defects), KOH activated		116	[90]
MWCNT, KOH activated		28.3-53.6	[91, 92]
MWCNT, nitrogen doped, KOH activated		44.3	[93]
MWCNT, modified electrolyte (indigo carmine)	1.7	50	[157]
MWCNT, activated with KOH	35	40-90	[95, 158]
MWCNT, CO_2 activated, acid oxidised		60.4	[98]

MWCNT, air oxidised		50	[101]
MWCNT, partially air oxidized, H_2SO_4 + HNO_3 modified		33.5	[102]
MWCNT, H_2SO_4 + HNO_3 activated (COOH functionalised)		51.3	[82]
MWCNT, film, electrostatic spray deposition		108	[159]
MWCNT, carbon nanofiber composite (randomly orientated)		37.8	[160]
MWCNT, CVD, KOH activated		50-90	[94, 96, 97]
MWCNT, CVD, HF treated, KOH activated		130	[84]
MWCNT, CVD, HNO_3 treated, KOH activated		137	[85]
MWCNT, CVD, HF treated, polypyrrole coated, KOH activated		163-170	[84, 86]
MWCNT, CVD, mixed with carboxymethylcellulose (paste)		79	[161]
MWCNT, CVD, H_2SO_4 electrolyte		12	[162]
MWCNT, CVD, high density		20	[163]
MWCNT, CVD, air oxidised powder		48	[103]
MWCNT, CVD, oxidised by H_2SO_4/HNO_3 mixture		51.3	[106]
MWCNT, CVD electrophoretic deposition onto nickel foils		21	[164]
MWCNT, CVD transferred to Ni electrodes (vertically aligned)		14.1-24	[165, 166]
MWCNT, CVD on stainless steel electrodes (organic electrolyte)		58	[167]
MWCNT, CVD $LiClO_4$/ethylene/propylenecarbonate electrolyte	20	16.8	[168]
MWCNT, CVD transferred to Ni organic electrolyte		24.5	[169]
MWCNT, CVD transferred to Al electrode (vertically aligned)		17	[170]
MWCNT, CVD transferred to paper (horizontally aligned)		87.5	[171]
MWCNT, CVD on anodised aluminium oxide template		49	[172]
MWCNT, CVD, anodised aluminium oxide template		365	[173]
MWCNT, CVD on graphite foil, acid treated		115.7	[87]
MWCNT, CVD cellulose/ionic liquid cast as substrate/electrolyte	13	36	[174]
MWCNT, CVD boron doped		12.1	[109]
MWCNT, low aspect ratio		24.7	[175]
MWCNT, high aspect ratio		22.5	[175]
MWCNT, vertically aligned, ionic-liquid electrolyte	19.6	440	[176]
MWCNT, polyoxometallate monolayer	1.3	40	[177]
MWCNT, grown in anodised aluminium oxide template		315	[178]
MWCNT, Mg based gel polymer electrolyte	17	41	[179]
MWCNT, carboxylic functionalised, spray deposition		77	[99]
Vertically aligned carbon nanotubes, nitrogen doped.		5.24	[110]

Table 1-3 describes results achieved for both SW and MWCNT composites.

Table 1-3. Carbon nanotube composites for nanoscale capacitor applications.

Electrode Material	Energy density (Wh kg^{-1})	Specific Capacitance (Fg^{-1})	Citation
SWCNT / RuO_2 nanocomposite (inkjet printed)	18.8	138	[125]
SWCNT / In_2O_3 nanowire composite (transparent)	1.29	64	[139]
SWCNT, polypyrrole nanocomposite		131-265	[117, 118]
SWCNT, arylsulfonic acid functionalised, pyrrole treated		350	[112]
SWCNT, DNA nanocomposite		27	[180]
SWCNT, C_{60}-Pd, 1-pyrenebutiric acid composite		90	[181]
SWCNT, C_{60}-Pd, polybithiophene composite		200	[124]
SWCNT, arc-discharge, polypyrrole nanocomposite		265	[118]
SWCNT, arc-discharge, polyaniline nanocomposite	228	485	[113]
SWCNT, polyaniline nanocomposite		225-706	[114-116]
SWCNT, CVD, MnO_2 composite (ball milled)		385.4	[130]
CNT, $Co(OH)_2$ composite, anodised aluminium oxide template		12.74	[140]
MWCNT, carbon nanofiber composite CVD		37.8	[160]
MWCNT, CVD, HF treated, polypyrrole coated, KOH activated		163-170	[84, 86]
MWCNT, CVD polypyrrole composite		165-180	[97, 119, 120]
MWCNT, polypyrrole / poly(3-methyl-thiophene) composite	1.8	87	[121]
MWCNT, CVD, NiO nanocomposite		160	[138]
MWCNT, MnO_2 mixture	32.91	59	[131]
MWCNT, MnO_2 nanocomposite on graphite electrode		160	[132]
MWCNT, MnO_2 nanocomposite		579	[133]
MWCNT, MnO_2 coated		250	[134]
MWCNT, Mn-Mo oxide nanocomposite		408	[135]
MWCNT, CVD, RuO_2 nanoparticle functionalisation		304.29	[104]
MWCNT, RuO_2 nanocomposite (low ruthenium concentration)		120	[126]
MWCNT, RuO_2 nanocomposite (microwave oxidation)		493.9	[127]
MWCNT, CVD, RuO_2 composite		80	[128]
MWCNT, CVD, RuO_2 nanocomposite (calcination)	10.5	628	[129]
MWCNT, Pt nanocomposite		300	[182]
MWCNT, $Ni(OH)_2$ nanocomposite		221	[183]
MWCNT, polymer, Ru/In nanocomposite	18.1	319	[184]
MWCNT, acid activated, polypyrrole composite		192	[83]
MWCNT, polypyrrole composite		192-790	[122, 185]
MWCNT, surfactant, polypyrrole/MnO_2 composite		268	[123]
MWCNT, coated with polypyrrole		163	[186]
MWCNT, asymmetric, Fe_2O_3/CNT composite anode	50	100	[136]

Graphene

Capacitors incorporating graphene have gained a huge amount of interest in recent years due to their very high surface areas (2630 m^2g^{-1} maximum theoretical value for both sides of a graphene sheet being completely exposed [187]) giving rise to high double-layer capacitance. Like carbon nanotubes, graphene capacitor research generally takes the approach of enhancing electrode-electrolyte interactions for increased power densities and incorporation of composites for higher energy densities.

Graphene oxide (GO) is generally synthesised by a modified Hummers method [188]. This involves oxidising and exfoliating graphene sheets to give isolated sheets of graphene oxide. Graphene oxide can then be reduced to graphene via chemical reductions such as hydrazine [189-197] or sodium borohydride [198], as well as hydrothermally [199-204], with microwaves [205] or by electrochemical methods [206].

Acid [207, 208] and base [209, 210] activations as well as surface functionalisation's [193, 202, 211-213] have been used to increase wettability. Good results were achieved when steps are taken to prevent the graphene sheets from agglomerating by incorporating other carbon nanomaterials [197, 208, 214-217] or preventative steps being taken in the electrode assembly [218, 219] and synthesis [220, 221].

The formation of nanocomposites of graphene with conducting polymers, metal oxides and activated carbon (AC) has been used to increase the effect of pseudo-capacitance and hence energy densities of the device. Analogous to carbon nanotubes, polyaniline [194, 196, 213, 222-225] and polypyrrole [226-228] are the polymers of choice, however, others have been used [225, 229]. Metal oxides reported to be incorporated into graphene based devices are very similar to those used in CNTs, they include ruthenium [222, 230], manganese [231-234], tin [195, 235], iron [203, 222], zinc [195, 236, 237], titanium [222], cobalt [238], bismuth [204] and cerium oxides [239].

Table 1-4 and 1-5 give an overview of specific capacitance values obtained for graphene based electrodes under different conditions. Energy density values are also given where reported.

Table 1-4. Capacitive data for graphene based materials.

Electrode Material	Energy density (Wh kg^{-1})	Specific Capacitance (Fg^{-1})	Citation
Graphene, chemical vapour deposition		255	[220]
Graphene, reduced from GO (hydrazine)	17.8	39-366	[191-197]
Graphene, reduced from GO (sodium borohydride)	15.4	135	[198]
Graphene, reduced from GO (microwave treatment)		191	[205]
Graphene, reduced from GO (heat treatment)	28.5	205	[199]
Graphene, thermally reduced, inkjet printed	6.74	132	[201]
Graphene, electrochemically reduced from GO		165	[206]
Graphene, reduced from GO (p-phenylene diamine)		164	[240]
Graphene, reduced from GO, surfactant intercalation		159-194	[221]
Graphene, reduced from GO not dried	150.9	273.1	[218]
Graphene, reduced from GO, in propylene carbonate		147.2	[241]
Graphene, KOH modified	18.9	136	[209]
Graphene, hydrothermally reduced from GO		175	[200]
Graphene, reduced from GO, KOH modified	70	166	[210]
Graphene, reduced from GO, layer-by-layer assembly		247	[219]
Graphene, reduced from GO in ethylene glycol	11.5	52.7-83.0	[215, 235]
Graphene, reduced from thermally treated GO	20.0	276	[192]
Partially reduced graphene from GO in H_2SO_4		348	[207]
Partially reduced graphene, GO in organic		158	[207]
Graphene, nitrogen doped from reduced GO (hydrazine)	80.5	138.1	[193]
Graphene, nitrogen doped	48	280	[211]
Graphene, hydrothermally reduced, amine substituted		217.8	[202]
Graphene, reduced from GO, organic substituted		258	[212]
Graphene/azo polyelectrolyte		49	[242]
Graphene, poly(ionic-liquid) modified	6.5	187	[243]
Hollow graphene shells		157	[244]
Graphene from GO (hydrothermal reduction)		71-139	[203, 204]
Sulfonated graphene		316	[213]
Graphene from GO, Li_2SO_4 electrolyte		238.0	[218]
Graphene from GO, Na_2SO_4 electrolyte		98.8	[218]
Curved graphene sheets	85.6	154.1	[214]
Graphene, reduced / multiwalled carbon nanotubes	45.3	120-326	[215-217]
Graphene, reduced from GO / carbon nanotubes		266	[197]
Reduced GO, nanodiamond composite (acid activated)		143	[208]

Table 1-5. Graphene composites.

Electrode Material	Energy density ($Wh\ kg^{-1}$)	Specific Capacitance (Fg^{-1})	Citation
Graphene SnO_2 composite from GO in ethylene glycol		99.7	[235]
Graphene / MnO_2 nanocomposite	11.4	328	[231]
Graphene / MnO_2 nanocomposite / AC nanofibers	51.1	113.5	[232]
Graphene / polypyrrole nanocomposite	10.5-94.9	267-482	[226-228]
Graphene, RuO_2 nanoparticle coating	20.1	570	[230]
Graphene, Ni^{2+}/Al^{3+} layered double hydroxide composite		781.5	[245]
Graphene / Fe_3O_4 composite (GO hydrothermal reduction)	67	480	[203]
Graphene / RuO_2 nanocomposite		265	[222]
Graphene / MnO_2 nanocomposite, asymmetric electrode	30.4	31.0	[233]
GO / MnO_2 nanocomposite		197.2	[234]
Graphene / CeO_2 nanocomposite		191	[239]
Graphene / ZnO nanocomposite		62-146	[195, 236, 237]
Graphene / SnO_2 nanocomposite		42.7	[195]
Graphene / TiO_2 nanocomposite		60	[222]
Graphene / Fe_3O_4 nanocomposite		180	[222]
Graphene / Co_3O_4 nanocomposite		243.2	[238]
Graphene / Bi_2O_3 nanocomposite		255	[204]
Graphene / polyaniline nanocomposite		210-375	[196, 222]
GO / polyaniline nanocomposite		555-746	[223, 224]
GO / polyaniline paper		42	[194]
GO / polymer nanocomposite		130	[229]
Graphene / polyaniline paper		489	[194]
Graphene / polyaniline/(sodium 4-styrenesulfonate)		301	[225]
Graphene / poly(sodium 4-styrenesulfonate)		172	[225]
Sulfonated graphene / polyaniline nanocomposite	68	763	[213]

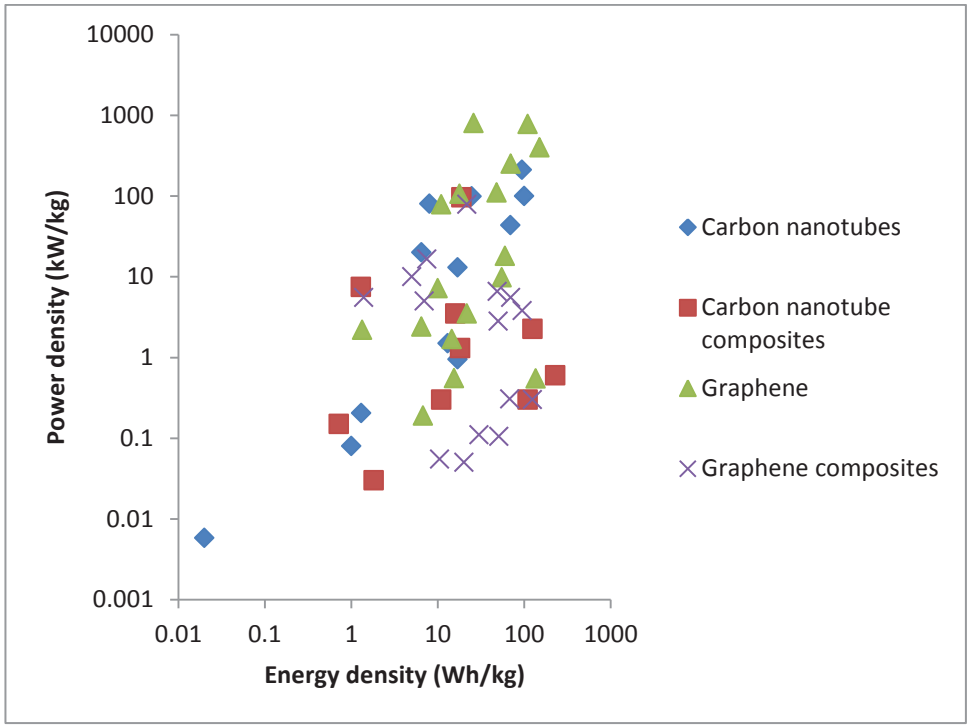

Figure 1-7. Power density *vs.* Energy density for carbon nanotube and graphene based capacitors. Data has been extracted from reported values.

A graphical representation of reported energy and power densities for graphene and carbon nanotube based capacitors is presented in Figure 1-7. The performance of graphene and CNT based electrochemical capacitors varies across many orders of magnitude depending on the materials incorporated and the experimental methods of the researchers. Composites of both carbon nanotube and graphene based capacitors appear to perform poorly compared to non-composite devices, this is unsurprising though given the mass dependence of both the power and energy densities being measured.

Biological Nanocapacitors

Barrientos *et al*. [246] presented a "biological" nanocapacitor, consisting of alternating layers of electrically conductive polyaniline and insulating poly-γ-glutamic acid synthesised by enzymatic catalysis and natural bacterial reactions respectively. (See Figure 1-8). A maximum capacitance of 19.63 pF and a capacitance density of 0.55 $pFmm^{-2}$ was achieved. Barrientos *et al.* believe that their biological nanocapacitor has the potential for use in low power devices. There are however, more reliable materials already available to deliver low power levels (as mentioned above), hence the commercial use of biological nanocapacitors of this nature is probably unviable.

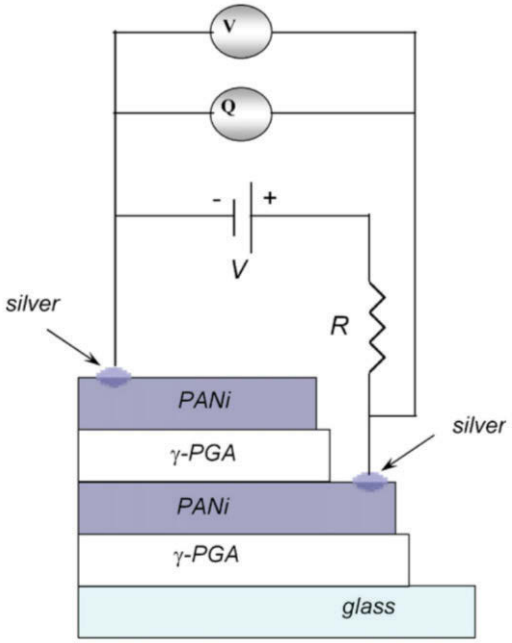

Figure 1-8. Schematic representation of the nanocapacitors studied by Barrientos *et al.* [246].

Conducting Polymers

The use of conducting polymers as an alternative to, or in combination with carbon materials has received considerable attention owing to useful properties such as high corrosion resistance and low cost. However, the use of conducting polymers in a stand-alone fashion is usually not viable in commercial products because of insufficient mechanical strength [247].

Mastragostino *et al.* [248] reported on the properties of potential conducting polymers for supercapacitor applications; poly(thiophene) (pTh), poly(3-(4-fluorophenyl)thiophene) (pFPT) and poly(3-methylphenylthiophene) (pMeT). The maximum specific capacitance of the three polymers respectively was determined as 95, 35, and 135 Fg^{-1} [248]. In another report by Mastragostino *et al.* [249], four supercapacitors were constructed from different combinations of the 3 polymers. The electrode configuration and associated composition of the four superconductors constructed by Mastragostino *et al.* are shown in Table 1-6.

Table 1-6. Electrode composition of the different composite polymer supercapacitors. Adapted from [249]

Supercapacitor Code	Electrode Configuration	Composition
A	(-) pFPT / pTh (+)	30% / 30%
B	(-) pMeT / pMeT (+)	30% / 30%
C	(-) pMeT / pMeT (+)	30% / 55%
D	(-) pMeT / pTh (+)	30% / 30%

Supercapacitor D displayed the best performance with close to 100% columbic efficiency and high stability over 6000 cycles. The capacitor was stored for 5 days in the discharged state and when recharged, delivered the same charge as in previous tests. Supercapacitor C also displayed promising columbic efficiency and good cyclability.

Fusalba *et al.* [250] reported the use of a poly (cyclopenta(2,1-b;3,4-b')dithiophen-4-one) electrode with a specific capacitance of ~70 Fg^{-1}. The discharge capacity of the capacitor was observed to decrease over the first 20 cycles before reaching a constant value for the next 80 cycles. Hence, the stability of this material needs to be improved before it can be used for commercial nanoscale capacitor applications.

Later [251], a polymer composite produced by electropolymerisation of polypyrrole and polyaniline was deposited onto a carbon paper electrode and exhibited a specific capacitance of 60 Fg^{-1}. This material does not appear to exhibit ideal capacitor properties as indicated by the shape of the cyclic voltammogram (Figure 1-9).

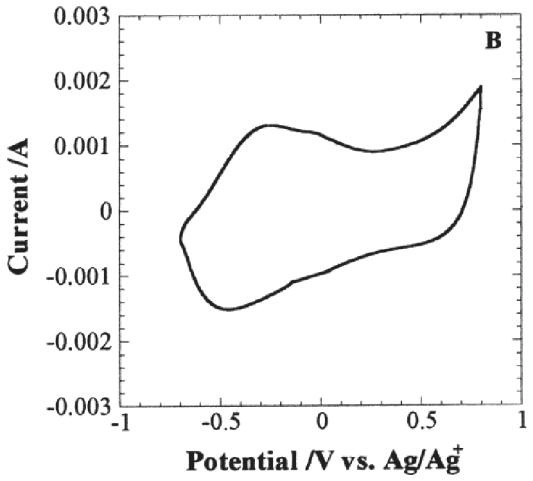

Figure 1-9. Cyclic Voltammetric curve for the polypyrrole/polyaniline copolymer Adapted from [251].

A nanocomposite consisting of poly (3,4-ethylenedioxythiophene) (PEDOT) and MoO_3 has been reported as having very high specific capacitance in the range of 300 Fg^{-1} [26]. PEDOT has been found to have superior thermal stability over other available conducting polymers although its disadvantages include poor cycle life and the tendency to become an insulator upon full oxidation. Thus, more research is required to determine the cycle life and conditions that favour the conductive form.

In order to enhance the capacitance properties of polyaniline and provide an electrode material which has significant mechanical strength, Downs *et al.* [252] constructed electrodes composed of multi-walled carbon nanotubes coated with polyaniline film. The carbon nanotube substrate enabled more efficient polymerisation and higher current densities were observed. The average specific capacitance achieved was 241 x 10^{-3} Fcm^{-2}.

Table 1-7. Summary of the literature utilising conductive polymers for nanoscale capacitor applications.

Electrode Material	Specific Capacitance (Fg^{-1})	Citation
Single-walled carbon nanotube, polypyrrole nanocomposite	265	[118]
Alternate layers of polyaniline and poly(γ-glutamic acid) nanofilms	19.63 pF	[246]
Polyaniline films on a platinum substrate	600-780	[253]
Poly(3,4-ehtylenedioxythiophene) film electrodes	100 Fcm^{-3}	[23]
Polyaniline films formed on multiwalled carbon nanotubes	241 $mFcm^{-2}$	[252]
Poly3-(3,4-difluorophenylthiophene)/3-(4-fluorophenylthiophene)	-	[254]
Polyaniline-polypyrrole copolymer	60	[251]
Poly (cyclopenta(2,1-b;3,4-b')dithiophen-4-one)	70	[250]
Poly(3,4-ethylene-dioxythiophene)-poly(styrenesulfonate)-polypyrrole film	70	[255]
Multi-walled carbon nanotube, polypyrrole composite	192	[185]
Multi-walled carbon nanotubes coated with polypyrrole	163	[186]
Carbon nanotube composite with phenolic resin powder	25 Fcm^{-3}	[256]
Poly(thiophene)/(3-(4-fluorophenyl)thiophene)/(3-methylphenylthiophene)	95, 35, 135	[248]
Poly(3-methylthiophene)	220	[249]
Poly (3,4-ethylene dioxythiophene)-MoO_3 nanocomposite	300	[26]
Multi-walled carbon nanotubes with polyoxometallate monolayers	40	[18]

Other Materials

Nanostructured carbon films grown by cluster-beam deposition were investigated by Diederich *et al.* [257]. The maximum specific capacitance was 75 Fg^{-1} and the power density was found to be as high as 506 $kWkg^{-1}$. The main advantage of these materials is that once deposited, they do not need any further treatment.

Honda *et al.* [258] investigated nanoporous honeycomb diamond electrodes for double-layer capacitor applications. Diamond is superior to other allotropes of carbon in that it has extremely high electrochemical stability and is functional over a wide potential window in both aqueous and non-aqueous media [258]. A specific capacitance value of 1.97 x 10^{-3} Fcm^{-2} was reported in 2000 which was improved to 3.91 x 10^{-3} Fcm^{-2} in 2001 [259]. Although the capacitance properties are promising, further development is required in the manufacturing process, since the current method causes damage to the electrodes and reduces the potential window.

Monolayer-Protected Clusters

Monolayer-protected clusters (MPCs) consist of a metallic electrically conducting core, surrounded by a protective monolayer of an insulating material [260]. Cluster cores can be as few as 14 atoms (one 'bulk' atom surrounded by 13 'shell' atoms [261]) or as large as several million atoms. MPCs are synthesised by wet techniques which usually involve the reduction of a metal salt in the presence of a stabilising ligand. The most common MPCs are gold, capped by alkanethiols with a chain length of four to fourteen carbon atoms [262]. The stabilising ligands prevent metallic cores from coming into contact and introduce an activation barrier.

MPCs display double-layer capacitance behaviour due to the large difference in the Fermi level of the core and the conduction band energy of the conducting / semi-conducting shell. Electrons that diffuse inside the shell can be contained for sustained periods of time resulting in stored charge [263].

Early research into these particles electrical properties was hampered by the polydispersity of the particles, which were generally synthesised by the Brust-Schiffrin method [264]. Fractioning of the synthesised particles and synthetic adjustments to achieve lower size distribution ensembles [265] aided in removing the "smearing" of results where particles of several different sizes were measured simultaneously [266-268].

An electrode of sufficiently small size may undergo "quantised" charge transfer (sometimes referred to as a coulombic stair-case) in which differences in charge can be attributed to the transfer of individual electrons across the double-layer capacitive barrier [269].

Ingram *et al.* [270] reported MPCs composed of a Au_{146} core (1.64 nm in diameter) with a truncated-decahedral structure surrounded by a shell of around 56 hexanethiolate groups. These relatively monodisperse MPCs exhibited a coloumbic staircase with six charging steps which is attributed to additional electrons trapped in the cluster. The average capacitance of the cluster was determined to be 0.56 aF (9.5 Fg^{-1}).

Murrays' group has pioneered the monolayer protected clusters capacitance research area since shortly after the Brust method was popularised. Similar to Ingram, Templeton *et al.* [260, 271] described the use of highly monodisperse alkanethiolate MPCs consisting of a cluster of 146 gold atoms utilising cyclic voltammetry and scanning tunnelling microscopy to probe the capacitance of organic suspensions and individual clusters respectively. This work has also been furthered by Hicks [265] and Quinn [272] showing with differential pulse voltammetry (DPV) curve peaks assignable to electron transitions between MPC^{6-} to MPC^{7+} charged species. Similar work has been done on $Au_{38}(CH_3(CH_2)_5SH)_{24}$ clusters [273].

A significant advancement was achieved with the first report of the crystallographic structure of a thiol stabilised gold nanoparticle. Jadzinsky and Calero *et al.* [274] were successful because they were the first to produce single crystals of gold nanoparticles stabilised by thiols, previously only the phenylphospine cluster $[(Ph_3P)_{14}Au_{39}Cl_6]^{2+}$ had been characterised [275] Jadzinsky and Caleros success was achieved by utilising phenylalkylthiol stabilisers and by crystallising in a mixed solvent solution. Significantly, the authors discovered that the thiols do not bind solely to one gold atom as was assumed with the early "thiolate bond model" [276]. Instead, a "staple" configuration was observed. In this configuration the sulfur headgroup binds to two surface gold atoms. This is significant work, not just for synthesising monodisperse MPCs. This information enhances researchers' knowledge of these particles and will be useful for example in more accurate molecular dynamic simulations of metal clusters.

Recent synthesis and crystallographic characterisation by Murrays' group followed up this work with the investigation of the $[N(C_8H_{17})_4][Au_{25}(SCH_2CH_2Ph)_{18}]$ cluster. These findings support the "staple" configuration and have also been supported

theoretically in a paper published concurrently to Murrays' [277] for Au_{25} clusters, an extension to previous work on Au_{38} [278]. Further work by Zhu has focused on the optical properties of these clusters synthesised with the Jadzinsky and Calero modification [279].

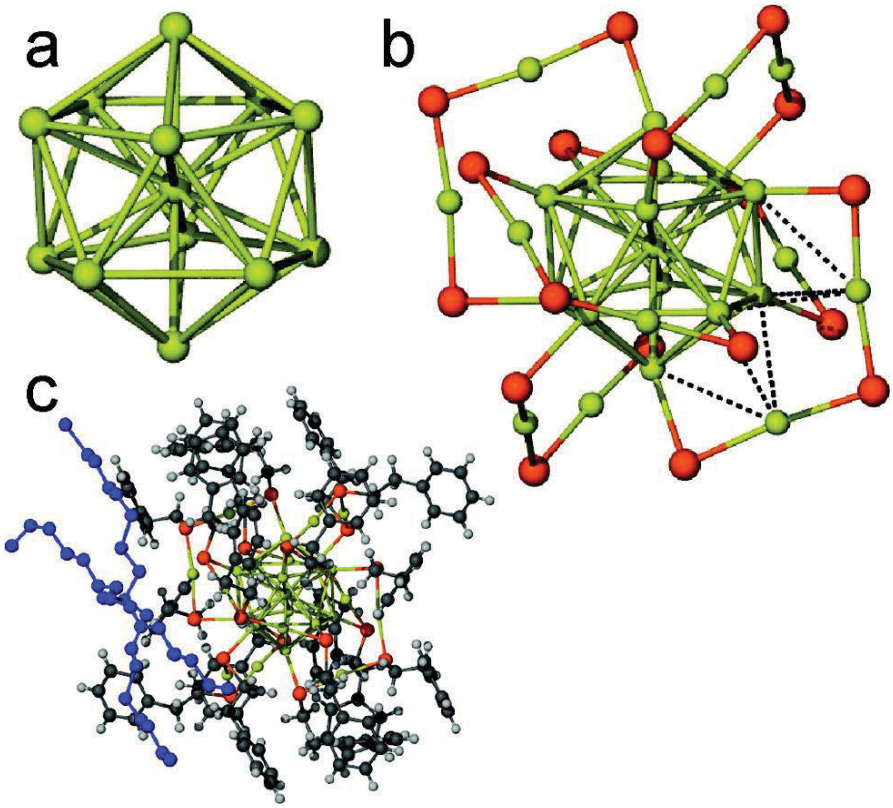

Figure 1-10. Schematic diagrams depicting the structure of (a) the Au_{13} core of the cluster. (b) the Au_{13} core with 6 –(Au_2S_3)- "staples" orientated around the 12 verticies. and (c) The [TOA^+][$Au_{25}(SCH_2CH_2Ph)_{18}$ complex (note, the real complex contains 2[TOA^+] ligands but has been omitted by the authors for clarity. Adapted from [280]

Heaven *et al.* [280] report in their supporting information that the Jadzinsky and Calero modification was not successful at producing single crystals every time. Therefore further research into synthesising more monodisperse clusters will need to be undertaken, these methods vary [281, 282], and can include etching in excess thiol solutions post Brust synthesis [283], and selective centrifugation [284]. Further advancements will continue to enhance knowledge in this field.

Murrays' group's research shows that the kinetics of charging is fast and that stored charge can be used for chemical reactions [260]. Research is currently being conducted

into the potential for these materials to be used in the solid state, such as deposited thin films [285].

There are however, alternatives to gold-alkanethiolate monolayer protected clusters under investigation. Oldfield *et al.* [263] produced clusters consisting of a gold core encapsulated by ~10 nm of tin dioxide. (See Figure 1-11). While Tunc *et al.* [286] synthesised 15 nm gold cores capped by 6 nm silica shells. The larger dielectric values of the insulating layers of these particles relative to alkanethiolates mean that electrons could be stored in the core for measurement times approaching 10 hr during which there was negligible evidence of charge dissipation [263]. However, this thickness also means that the rate of electron transfer out of the shell is consequently relatively slow [263] and may be unsuitable for IC applications.

Monodispersity is just as crucial for non-thiol stabilised particle solutions, hence research into size selectivity via DNA aggregation has been undertaken by Mirken *et al.* [287], crude size selection has been demonstrated for largely polydisperse particles, however the effectiveness for smaller size distributions has yet to be demonstrated.

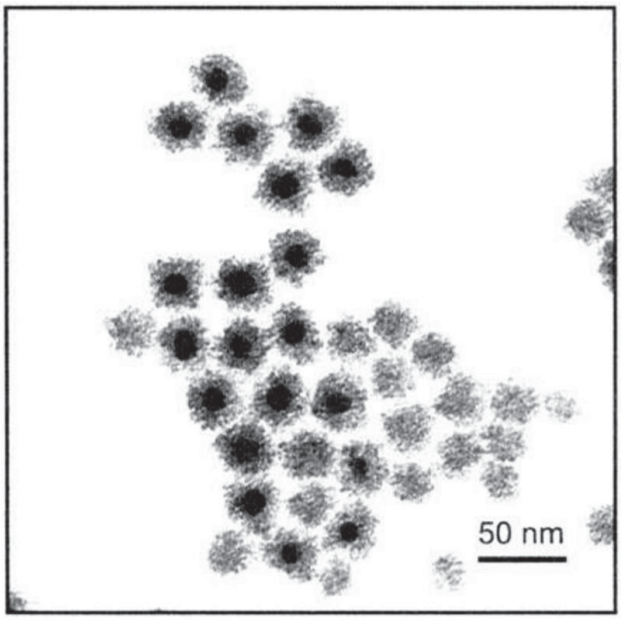

Figure 1-11. Transmission electron micrograph of gold particles encapsulated with a 10 nm tin dioxide layer. Adapted from [263].

Metal Carbonyl Clusters

A metal carbonyl cluster (MCC) is basically a kernel of metal atoms surrounded by a shell of carbonyl ligands. (Figure 1-12).

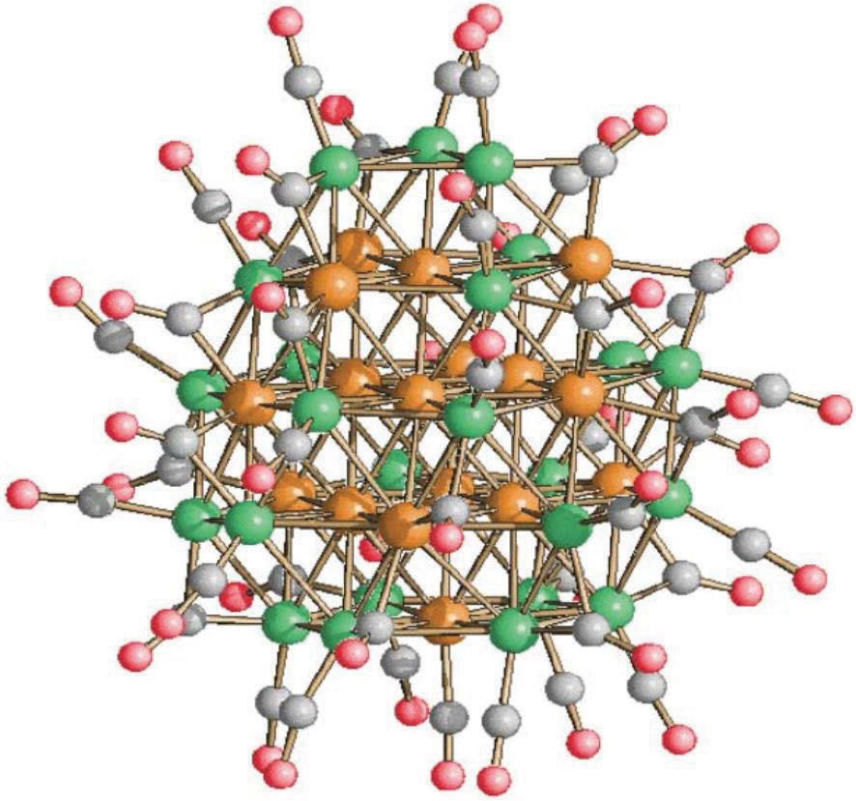

Figure 1-12. The structure of the $[HNi_{24}Pt_{17}(CO)_{25}(\mu\text{-}CO)_{21}]^{5-}$ pentaanion. Pt atoms shown as orange spheres, Ni green, C grey and O red. Adapted from [288].

MCCs like MPCs are synthesised by solution based techniques. The first report of a metal carbonyl compound was published by Ludwig Mond in 1890 [289]. Mond was interested in purifying nickel from its ores, the $Ni(CO)_4$ complex is formed under relatively mild conditions compared to other metals in the ore. MCCs have the advantage of increased monodispersity compared to MPCs. Their "electron sink" behaviour i.e. their ability to accept and donate charge is consequently easily visible in CV curves. The ligand shell insulates the metallic core to hinder intermolecular exchange of electrons to a certain degree, however due to the fact that carbonyl chains are usually shorter than the ligands used to stabilise MPCs quantum tunnelling plays a significantly greater role and practically storing charge for sustained periods of time is problematic. Depending on the composition of the metallic core, electrical properties

ranging from insulator to conductor can be achieved. It is known that most cobalt, nickel, platinum and silver centred MCCs have 2 to 6 redox changes with features of electrochemical reversibility [290, 291]. Table 1-8 displays several MCCs which are thought to behave like nanocapacitors.

Table 1-8. Capacitance of cylindrical and spherical MCCs and calculated relative permittivitys' of co-ordinated carbon monoxide. ($\varepsilon_{CO\ monolayer}$). Adapted from [290]. Farad per gram values have been inserted for ease of comparison to other materials.

MCC	*C* (aF)	*C* (F/g)	*r* (nm)	*d* (nm)	*l* (nm)	$\varepsilon_{CO\ monolayer}$
Cylindrical capacitor						
$[Pt_{19}(CO)_{22}]^{4-}$	0.37	52	0.40	0.13	1.08	1.7
Spherical capacitor						
$[Ni_{11}Sb_2(CO)_{18}]^{3-}$	0.21	91	0.38	0.19		1.7
$[HRh_{14}(CO)_{25}]^{3-}$	0.25	70	0.47	0.23		1.6
$[HNi_{24}Pt_{14}(CO)_{44}]^{5-}$	0.40	45	0.57	0.19		1.6
$[Ni_{38}Pt_6(CO)_{48}]^{6-}$	0.57	72	0.67	0.19		1.7

Fabrizi de Biani *et al.* [292] investigated the properties of the $[H_{6-n}Ni_{38}Pt_6(CO)_{48}]^{n-}$ clusters (n= 4-6). The $[Ni_{38}Pt_6(CO)_{48}]^{6-}$ and $[HNi_{38}Pt_6(CO)_{48}]^{5-}$ MCCs were found to display a very high redox aptitude with five reversible redox processes. The difference in the electrode potentials of consecutive redox couples mirror the differences between their ionization energies, suggesting that these nickel centered MCCs have electron sink behaviour [292].

Femoni *et al.* [288] have also demonstrated that $[HNi_{24}Pt_{17}(CO)_{46}]^{5-}$, $[Ni_{32}Pt_{24}(CO)_{56}]^{6-}$ and $[H_{6-n}Ni_{24}Pt_{14}(CO)_{44}]^{n-}$ (n = 4,5) readily undergo redox changes and protonation-deprotonation reactions in solution. The authors plan to devote further studies to discover the nanocapacitor potential of MCCs [288].

Research conducted by Collini *et al.* [291] led to the discovery that interstitial nickel atoms can alter the cluster valence electrons and can trigger reversible redox and multi-valence behaviour in otherwise electron-defined clusters. The group also discovered that progressive rhodium / nickel exchange can modify the electronic, chemical and architectural properties and induce multi-valence in MCCs [291].

While nickel, platinum and silver are the most commonly investigated central atoms in MCCs, there are other alternatives. In 2007, Collini *et al.* [293] investigated the

nanocapacitor behaviour of MCCs concentrating on rhodium-centred clusters, $[H_3Rh_{13}(CO)_{24}]^{2-}$, $[HRh_{14}(CO)_{25}]^{3-}$, and $[Rh_{15}(CO)_{27}]^{3-}$. While the group was unable to determine the number of electrons involved in redox processes and hence capacitance behaviour it shows that further research could lead to alternative clusters [293].

The use of MCCs as materials for nanoscale capacitors is an interesting field and offers more facile mechanical study relative to MPCs. Future research in this area specifically concerning different dielectrics (stabilising ligands) [294] could lead to further control over the redox procedures which govern charge transfer and ultimately their utilisation in capacitive circuits.

1-2.5 Applications of Nanoscale Capacitors

Potential applications for nanoscale capacitors include load-levelling of batteries during the start-up, acceleration and braking of hybrid electric vehicles [77], pulse power sources for electronic devices including camera flash equipment, pulse light generators, mobile phones, pagers, portable cameras, photodiode array detectors and other telecommunication systems [27, 63, 77], uninterruptible power supplies for computers and navigational systems [77], memory backup systems, and backup power storage devices in solar cells and fuel cells [18]. Nanoscale capacitors can be used as standalone power supplies, or when coupled to a battery in an electronic circuit, nanoscale capacitors can significantly increase the life of the primary battery by providing high-speed power during peak usage [17]. Pushparaj *et al.* fabricated carbon nanotube based capacitors where the electrolyte is cast in the cellulose substrate resulting in flexible, robust devices [174]. Carbon nanotube films have also been made flexible at the macro scale with polymer substrates [146]. Graphene [201] and carbon nanotube [125] based nanocapacitors have been fabricated by inkjet printing. Spray deposition of carbon nanotubes have also been demonstrated [99, 159].

1-2.6 Summary and Outlook

As described in section 1-2.2, the use of nanoscale materials with high surface areas will improve the capacitance of capacitors enormously. The use of nanoscale capacitors will significantly reduce the size of electrical components which currently restricts the

miniaturisation of electrical devices. Nanocapacitors used in the storage of information offer the potential for much higher storage densities.

The most promising materials for nanocapacitors appear to be carbon nanotubes and graphene as a consequence of their availability, reasonable cost, excellent electrical properties and high mechanical strength. Graphene electrochemical capacitors have achieved the highest capacitance of any of the materials studied in this chapter. Composites of polymers with carbon nanotubes have also resulted in promising capacitance properties whilst utilising cheaper, commercially viable materials.

Research into the nanocapacitance of metal carbonyl clusters and monolayer protected clusters has revealed capacitor-like properties which include reversible redox reactions and electron sink behaviour. However, the capacitance density of these materials must be enhanced greatly if they are to compete with the capacitance achieved by carbon nanotubes and metal oxide nanocapacitors.

Whilst current technology in manufacturing processes has allowed the construction of model nanocapacitors for research, methods need to be improved and modified for large scale production before the nanocapacitors discussed in this chapter become commercially available.

While the majority of research has been into fabricating macroscale electrodes of nanoscale materials, relatively little attention has been paid to synthesising and characterising discrete nanoscale capacitors. Current methods for measuring capacitance at the nanoscale remain challenging. Size constraints of the small components involved and the potential to damage materials with high electric field and current densities required for some measurements remain an issue.

1-3 Project Aims

The literature reveals an intense interest in fabricating capacitors that incorporate nanoscale components to achieve increasing power and energy densities for macro and micro scale electronic applications, however there is comparatively little research into synthesising entirely nanoscale capacitors that may be of use in future nanoscale devices. An obvious problem that arises in nanoscale devices is the difficulty in their characterisation due to their small size.

Therefore, the following project aims were developed:

- To investigate techniques that enable the fabrication of novel nanoscale capacitor devices.
- To fabricate arrays of such devices that enable their characterisation.
- To characterise the charge storage capabilities of these devices in a facile manner.

In each of the subsequent chapters, specific aims are stated together with hypotheses relevant to each phase of the work. In the next Chapter, experimental details are presented as well as theoretical concepts important to the work described in subsequent chapters.

Chapter 2:

Experimental Section

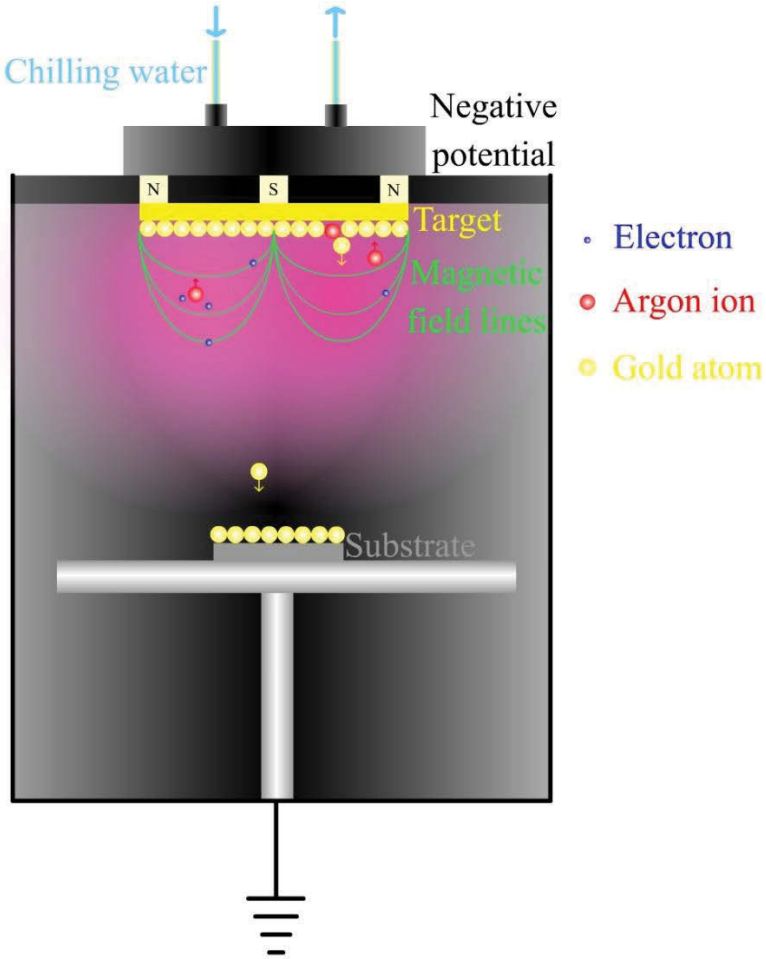

2 Experimental Section

2-1 Techniques Used In This Project

This section provides an overview of the instrumental techniques utilised in the current research project. Included are the physical vapour deposition techniques of evaporative and sputter depositions, scanning electron microscopy (including imaging and energy-dispersive X-ray spectroscopy), and atomic force microscopy.

2-1.1 Physical Vapour Deposition (PVD)

Physical vapour deposition is a term for vacuum deposition techniques that rely on the condensation of deposited material generated by physical processes (such as evaporation or sputter bombardment). The techniques differ from chemical vapour deposition (CVD) which utilise chemical reactions to generate volatilised species. This project utilises evaporative and sputter depositions which are discussed below, in conjunction with a brief background on the mechanism of thin film growth.

Thin Film Growth

Generally speaking, thin film growth involves three main stages [295]:

- Generation of volatilised species.
- Transport of species from the source to the substrate.
- Condensation onto the substrate.

Some of the main factors affecting thin film growth are:

- Substrate temperature T_S

T_S relative to the melting point (T_M) of the volatilised material can influence the grain size of deposited materials. Qualitatively speaking where $T_S << T_M$, very small grains are formed, as T_S increases the grain size of the deposited material increases, reaching a maximum just before T_S is sufficient to melt / evaporate the deposited material (this temperature varies depending on the material being deposited and the

films thickness due to the higher proportion of surface atoms relative to those in the bulk [296]).

- Annealing temperature T_A

When employed, post deposition annealing will increase the grain sizes of deposited material provided sufficient thermal energy to overcome the polycrystalline temperature of the film is present [297].

- Kinetic energy

Deposited materials with very low kinetic energy will have a very low surface mobility upon contact with the substrate and small grain sizes will result. Increasing the kinetic energy of deposited materials will increase the surface mobility and corresponding grain sizes only to a point. When superfluous kinetic energy is possessed by deposited materials, substrate impregnation will occur and grain sizes will again decrease.

Evaporative Deposition

Evaporative deposition is a PVD technique used to deposit thin films of metals (generally, metal oxides decompose before melting). Materials are heated to their melting point under reduced pressure (10^{-4} -10^{-8} Torr) at which point they evaporate and move away from the high thermal energy filament. Evaporation at the melting point is a consequence of the liquid being below the saturation temperature at reduced pressures. Evaporative deposition occurs in a molecular flow regime, where the mean free path of gas molecules is larger than the dimensions of the vacuum system, meaning deposited materials interact almost exclusively with the chamber walls independent of other molecules.

The mean free path of a gas molecule in a vacuum chamber can be given by the equation:

$$l = \frac{k_B T}{\pi d^2 P}$$

Where:

k_B = Boltzmann constant = 1.38 x 10^{-23} (m^2 kg s^{-2} K^{-1})

T = Temperature (K)

d = diameter of the gas molecules (m)

P = chamber pressure (T)

In this thesis, evaporative deposition is used for the formation of the top and bottom electrodes in the nanocapacitor setup.

Sputter Deposition

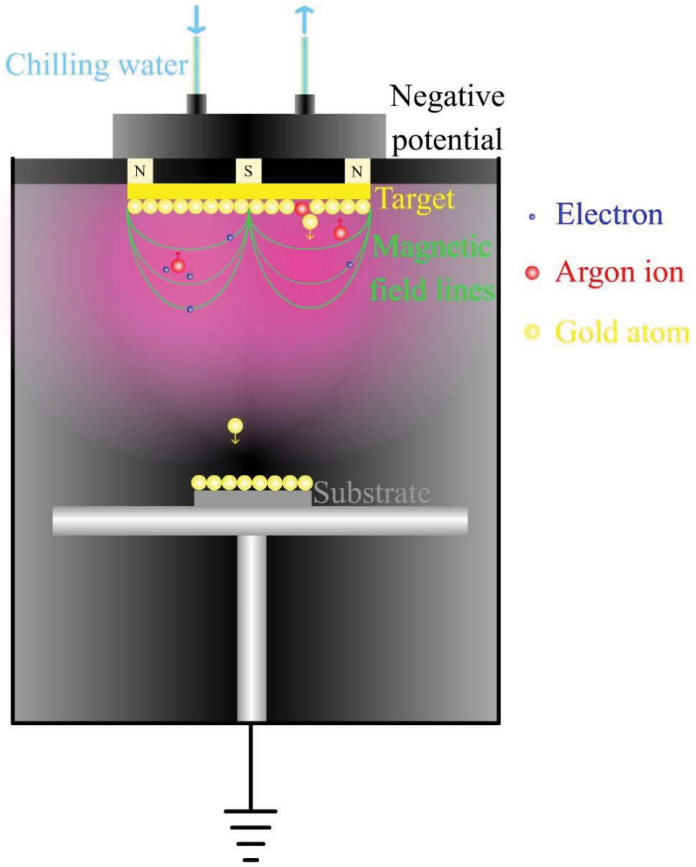

Figure 2-1. Schematic of a DC magnetron sputtering chamber.

Sputter deposition (also known as cathodic sputtering) is the result of a target (material to be deposited) being bombarded by energetic ions to dislodge material required for deposition in atomic or compound form.

The target is placed in a vacuum chamber in front of a large negative potential (Figure 2-1). A low partial pressure inert gas is leaked into the chamber and each gas atom / molecule has a small probability of colliding with a free electron, which are ever-present in reduced pressure systems. Collision between a leaked gas molecule / atom and a free electron can remove a valance electron creating both an ionised gas atom or molecule and another free electron. The positively charged ionised gas will be

strongly attracted to the large negative potential (the force of electric charge is approximately 39 orders of magnitude stronger than the force of gravity) and will accelerate towards it, colliding with the target beforehand. At the inelastic collision point a momentum transfer occurs and the material to be deposited can be ejected and moves away from the target to be deposited on the substrate. Substrate collisions produce SE emission which along with the electrons ejected from gas ionisation continues the process. To increase the efficiency of sputtering, strong magnets are used near the potential so that magnetic field lines align in a way that trap free electrons very close to the target (magnets were first introduced in the 60's [298, 299] and instruments that utilise them are referred to as magnetron sputtering systems). Magnetron sputtering is used for conducting targets, however when insulating and semiconducting targets are used extended bombardment with gas plasmas results in positive charge build-up which decreases the efficiency of the process. To counteract this RF-magnetron sputtering is used where the sign of the potential above the target is oscillated at radio frequencies.

There are several variables with this technique including; magnitude of potential, type / partial pressure of sputtering gas, substrate temperature, orientation, and separation from target. All these variables however give the user a large degree of control over film properties.

In this thesis, magnetron sputtering is employed to fabricate the top and bottom electrodes of the nanocapacitors, while RF magnetron sputtering is utilised to deposit dielectrics in the nanocapacitor synthesis.

2-1.2 Scanning Electron Microscopy (SEM)

Scanning electron microscopy (SEM) is a microscopy technique involving a focused beam of electrons. The technique is based on the principle that energetic electrons from the primary beam will produce SEs by inelastic collisions, which are subsequently ejected from a sample. Ejected electrons are attracted to a grid via a relatively low potential (+400V) and then accelerated by a higher potential to a Everhart-Thornley detector[300] where electrons are focused onto a scintillator and photons are directed to a photomultiplier which is responsible for the recorded signal. To form an image, the beam is focused by a magnetic lens (analogous to the lenticular lens of optical microscopes but utilising the Lorentz force to deflect the beam) and

then raster-scanned (controlled by electromagnets) over a surface. The emitted electron signal is plotted in a matrix of x-y positioning. Electron microscopy has several advantages over conventional light microscopy. Chiefly, light microscopy is limited by the Abbe diffraction limit where light with a wavelength λ focused through a lens with refractive index n to an angle θ will give a spot of diameter [301]:

$$d = \frac{\lambda}{2(nsin\theta)}$$

This means that features smaller than about 200 nm cannot be resolved in conventional light microscopes. Electrons, however, accelerated by potentials common in SEM are capable of resolving sub-nanometre structures.

Traditionally, samples to be imaged using SEM should be relatively conductive to prevent charge build-up, although innovations such as the environmental scanning electron microscope (ESEM) enable imaging of insulating samples for a small sacrifice in resolution by introducing water vapour into the microscope chamber to prevent excessive charge build-up. Alternatively, coating the specimens with a thin layer of conducting material (e.g., gold or carbon) enables imaging of samples with a small sacrifice in topographical information. However, in the work presented here, the charging phenomenon is exploited to characterise the capacitance of nanoscale structures under low accelerating voltages in a non-destructive manner. This technique has only been trialled in a proof-of-concept fashion [19] but this work examines the method in detail.

2-1.3 Energy-Dispersive X-ray Spectroscopy (EDS)

Energy-dispersive X-ray spectroscopy is a technique closely related to Auger electron spectroscopy (AES) [302] and XPS [303] used to determine the elemental composition of a sample.

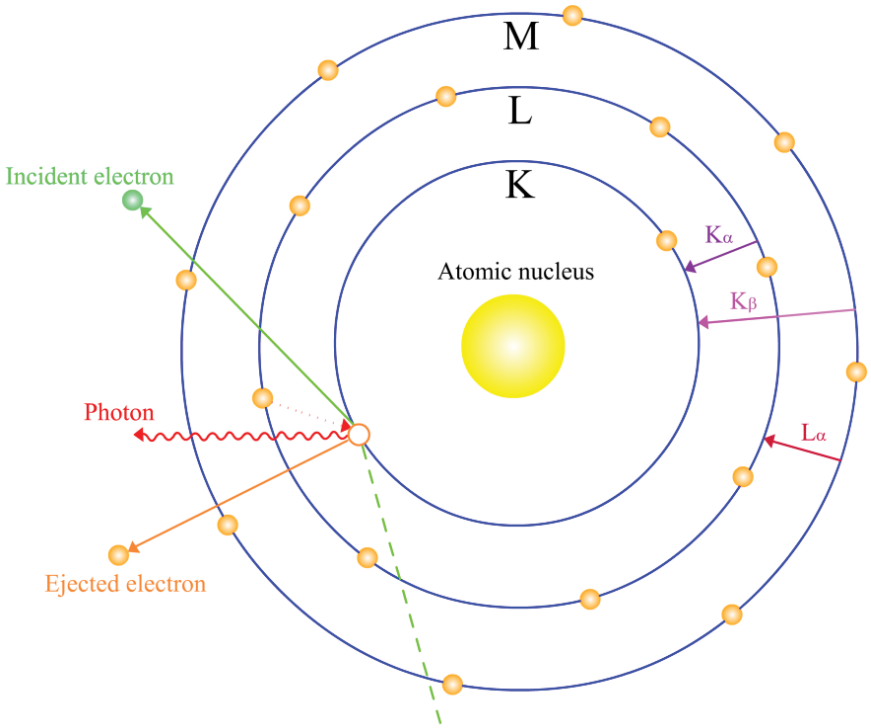

Figure 2-2. Schematic of the core shell electron ejection process and X-ray generation by outer shell filling.

Figure 2-2 shows a schematic representation of the X-ray generation process fundamental to this technique. An atomic nucleus is depicted, surrounded by electrons grouped into shells. Each shell represents a different energy level and is notated K, L, M with increasing distance from the nucleus. Electrons have higher ground state energies with increasing separation distance from the nucleus.

A high energy electron from an electron microscopes' focused electron beam (represented by the dashed and solid green lines) ejects a SE from an inner shell upon collision (orange line). Ejection leaves a hole which is filled by the migration of an outer shell electron (dashed orange line). The outer shell electron subsequently releases energy in the form of a photon during this migration (red line usually of X-ray energy). Photons are detected by an energy-dispersive spectrometer.

Photon energy is dependent on the difference in energies between the original state and the new state of the migrating electron, consequently different elements possess characteristic energy X-rays depending on the processes occurring. The probability of X-ray generation increases with increasing atomic number.

The notation used to describe the migration process takes into account a number of factors: 1) The element the electron is being ejected from. 2) The shell the electron

fills, which is labelled K for the inner shell and L and M for subsequent shells. 3) How far electrons migrate (how many shells), α is used for one shell, β for two etc. For example X-rays emitted from an M shell electron filling a K shell hole (purple line) would be described as SiK_{α}, however if the electron came from the L shell to fill the K shell (pink line) the notation would be SiK_{β}.

In this thesis, EDS is used to characterise the composition of deposited nanostructures.

2-1.4 Atomic Force Microscopy (AFM)

Atomic force microscopy is a scanning probe technique used to characterise sample topography. Chemically sharpened tips (commonly silicon nitrides) attached to a cantilever are scanned across a surface (in x and y dimensions) to map changes in height (z-dimension). The first AFM reported by Binnig, Quate, and Gerber in 1986 [304] consisted of a diamond tip glued to a cantilever (gold foil for a low spring constant that did not dislodge atoms in the sample being analysed). The tip was placed in contact with a surface and the cantilevers deflection was monitored by the tunnelling current of a scanning tunnelling microscope. High resolution results were achieved with tunnelling current feedback systems, however operating the microscope in ambient conditions resulted in contamination influencing conductivities [305]. Optical feedback systems removed this contamination sensitivity, first with optical interferometry [306] and later (and now more prevalent) laser deflection off the back of cantilevers onto photodiodes [307].

The primary advantage of AFM over STM is its ability to image non-conductive samples. Techniques such as phase imaging and conductive-AFM (CAFM) increase the flexibility of the technique.

AFM was used in the current work to characterise nanocapacitor samples and measure film thicknesses for deposition monitor calibration.

2-2 Experimental Details

This section provides details on the experimental parameters used in the experiments conducted in the current research.

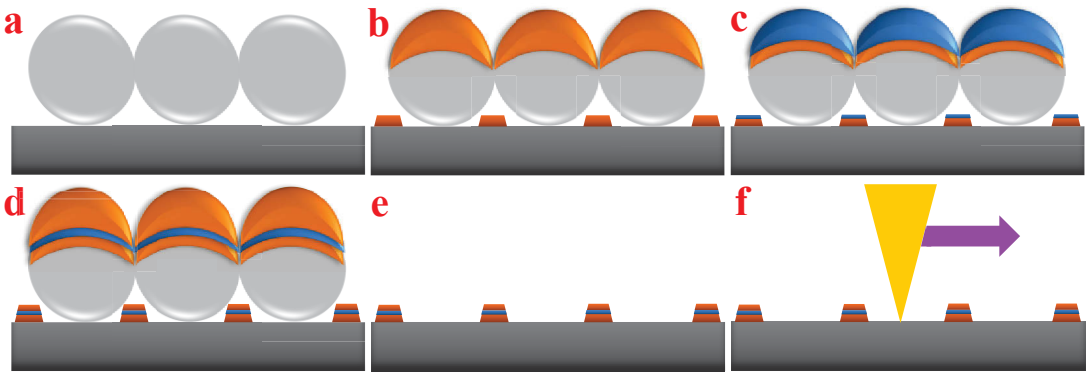

Figure 2-3. Schematic representation of the fabrication of discrete nanoscale capacitors and the charging process. (a) Close-packed latex spheres on silicon are prepared by spin-coating. (b) Close-packed spheres act as a mask so that gold deposited by evaporative deposition forms discrete, patterned structures on the silicon substrate. Gold also deposits on the latex spheres. (c) A metal oxide layer is deposited by RF magnetron sputtering. (d) A second layer of gold is deposited by evaporative deposition. (e) Removal of the latex spheres results in periodic nanostructured arrays of capacitive triangles. (f) Charging of the nanostructures is achieved by repeatedly scanning an electron beam (represented by yellow triangle and purple arrow) across the sample. Dark grey = Si substrate, Light grey = latex spheres, Orange = gold, Blue = metal oxide.

Figure 2-3 depicts the fabrication and charging processes for the nanocapacitors prepared in the current work. Nanosphere lithography uses mono- or bi-layers of close-packed monodisperse polystyrene (PS) spheres as templates for the production of relatively large area arrays of nanostructures [294-300]. Monodisperse PS latex spheres were deposited on piranha-etched silicon substrates by spin-coating, (a). The spheres formed a hcp structure that acts as a mask [19, 308-313] for the subsequent multilayer deposition of gold / metal oxide / gold films, (b-d). In this work, a number of different metal oxide dielectric materials were investigated namely; alumina (Al_2O_3), zinc oxide (ZnO), silica (SiO_2), hafnia (HfO_2) and titania (TiO_2). Removal of the spheres (e), results in periodic arrays of gold / metal oxide / gold nanocapacitors. The nanocapacitors were examined using a scanning electron microscope, (f).

2-2.1 Materials Fabrication

General

The following materials were sourced commercially and used as received; silicon (*p*-type; 100 or *n*-type; 111, ProSciTech), sulfuric acid (Lab scan), hydrogen peroxide (33 wt. %) (Sigma-Aldrich), MilliQ water (18.2 MΩ cm^{-1}), Triton X100 (Aldrich), zinc nitrate (Ajax), hexamine (BDH), ethanol (Chem Supply), methanol (Chem Supply), dichloromethane (Lab Scan), gold (AGR Matthey, fineness 99.99), zinc oxide (99.9% Williams Advanced Materials), alumina (99.9% Semiconductor Wafer Inc.), silica (Semiconductor Wafer Inc.), hafnia (99.9% Semiconductor Wafer Inc.), and titania (99.9% Williams Advanced Materials).

Spin-coating was performed using a Headway Research spin-coater. Gold was deposited in a Denton Vacuum DV502 turbo evaporative deposition chamber. Gold and metal oxides were also deposited in an Edwards E306 deposition chamber equipped with magnetron and RF magnetron sputter systems.

Substrate Preparation

Silicon substrates (*p*- and *n*-type, approx 1 cm^2 squares cut with glass cutter) were made hydrophilic by immersion in piranha solution (3:1 H_2SO_4:33 % H_2O_2 in water *CAUTION: this solution is a powerful oxidant that can become extremely exothermic and will destroy many organic materials!*) for 20 min followed by thorough rinsing with MilliQ water and drying in a stream of nitrogen gas.

Spin-Coating

Latex spheres ranging in size from 200–1500 nm were investigated. Spheres were in 10 or 2.5 % w/v aqueous solutions depending on the source (Sigma-Aldrich 2.5% or Bangs Laboratories 10%). Solutions were freshly prepared and sonicated for 1 min prior to dilution. Spheres were mixed with a 1:400 TritonX:methanol mixture between 10:1 and 1:10 ratios. Spin-coating was carried out at speeds ranging from 500-4000 RPM for 40 s with a spin acceleration of 80 %. Both “drop while spinning” and “drop before spinning” techniques were investigated.

Lift-Off Method

The dip method involved gently transferring 20-100 μL of 4:1 latex sphere:(1:400 Triton-X:methanol) mixture to the surface of a 15 cm diameter petri dish filled halfway with MilliQ water. Films of latex spheres were observed on the water surface and a silicon substrate was lifted through the film for coating. Substrates were dried in a vacuum desiccator before being transferred to vacuum chambers for deposition.

Gold Deposition

Gold was deposited by both evaporative and sputter deposition. Evaporative deposition was performed in a Denton bell jar chamber utilising a turbo pump. 99.99 % gold granules (AGR Matthey) were evaporated by a tungsten filament with base pressure ~10^{-7} Torr (1.3 x 10^{-5} Pa). Deposition rates were typically 0.1 $Ås^{-1}$ as monitored by a Maxtex T200 quartz crystal thickness monitor calibrated by AFM measurements. The distance between the sample and filament was 20 cm.

Sputter deposition was performed in an Edwards chamber utilising a diffusion pump. The chamber had a magnetron setup and had a target substrate separation distance of 15 cm with an argon partial pressure of 3×10^{-4} Torr (4×10^{-2} Pa). An Advanced Energy MDX 500 power supply (0.017 A, 20 V) was used to apply the potential. Deposition rates were typically 0.1 $Ås^{-1}$ as monitored by a Maxtex T100 quartz crystal thickness monitor calibrated by AFM measurements.

Metal Oxide Deposition

Where required, substrates were removed from the Denton bell jar chamber and transferred to the Edwards sputter equipped vacuum chamber and pumped to a base pressure ~10^{-6} Torr (~10^{-4} Pa). Argon was leaked into the chamber with a partial pressure of 3×10^{-4} Torr (4×10^{-2} Pa), and metal oxides were deposited with an advanced energy RFX-600 power supply (90 W) under slow rotation (~0.2 Hz). The distance between the sample and target was 15 cm. Deposition rates were typically 0.1 $Ås^{-1}$ as monitored by a Maxtex T100 quartz crystal thickness monitor calibrated by AFM measurements. Following metal oxide deposition, air was introduced into the chamber and the pressure equalised to atmosphere. Where required the gold evaporation procedure was then repeated.

Film Thickness Monitor Calibrations

Large area defect-free hcp regions will provide high levels of reproducibility in the x-y dimensions of triangular structures synthesised by NSL. Also of critical importance is the z dimension or height of the structures. Consequently steps must be taken to ensure accurate measurement of the height of any fabricated samples. Quartz crystal microbalances (QCMs) are used extensively in thin film deposition to measure the thickness of deposited films. These devices rely on the damping of an oscillating quartz crystal through inertial loading (deposition) to measure frequency shifts [314] (and if the density of the deposited material is known the thickness can be inferred [315]). While precise, careful calibration is essential to give accurate results. Of primary concern is the physical separation between the microbalance and the sample of interest (deposition rates differ depending on the solid angle between the deposition source and the area where the material is being deposited). To account for this, microbalances must be calibrated and great care must be taken to ensure experimental setup reproducibility.

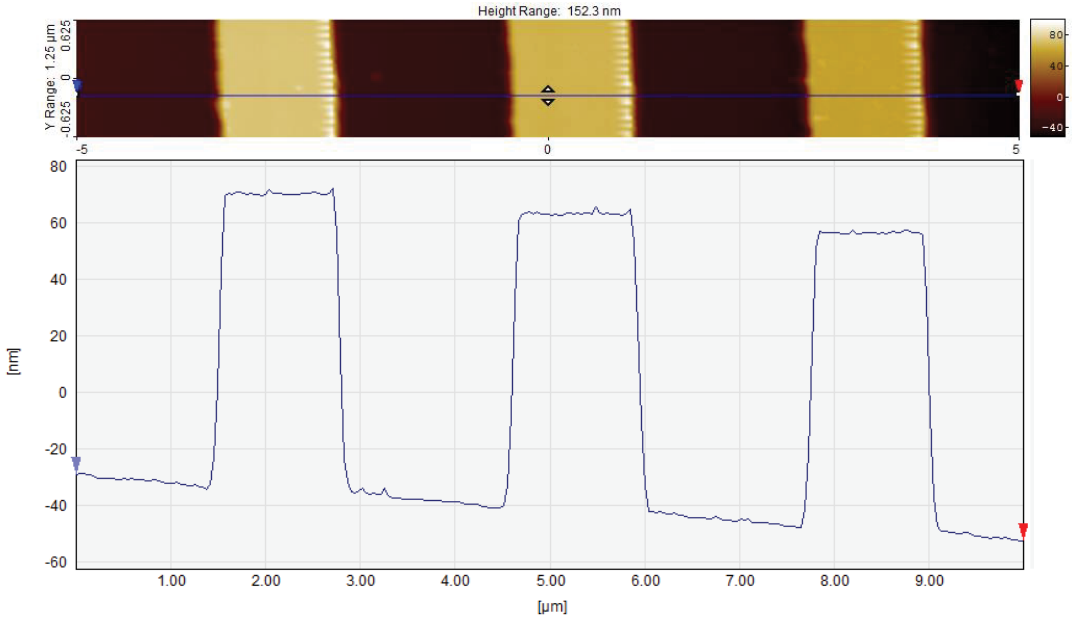

Figure 2-4. AFM image and line profile of calibration grating used for Atomic force microscope calibration.

Figure 2-4 shows atomic force microscope data for a calibration grating. The sensitivity of the piezoelectric scanner material decreases with an exponentially slowing rate as the material ages [316]. Recalibration is essential to account for this

and appropriate before recalibration of QCMs. The height of the features in the calibration grating is 110 nm with a feature wavelength of 3 µm.

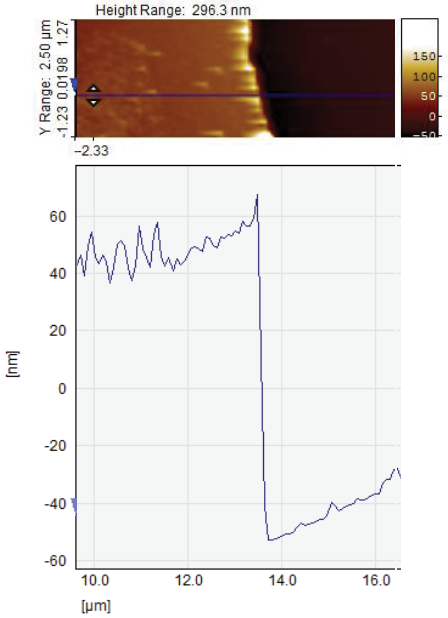

Figure 2-5 AFM image and line profile of gold step used for film thickness monitor calibration.

For Maxtek film thickness monitor calibrations glass slides were cleaned in Piranha solution and rinsed thoroughly with MilliQ water and dried in a stream of nitrogen gas. Lines were drawn on the slides with a felt tip pen and 100 nm films of gold (as measured by the deposition monitor) were deposited on the slide via evaporative or sputter deposition. After deposition slides were rinsed in DCM for one minute to remove the gold from the regions that were deposited on the ink. AFM measurements were subsequently performed on this region of the slide with a Digital Instruments Dimension 3100 Scanning Probe Microscope operating in tapping mode (measurements performed after microscope was calibrated to a standard grating). Calculation of the difference between the film thickness measured by the QCM and AFM was used to correct the tooling factor of the film thickness monitor.

Latex Sphere Removal

Latex spheres were removed by sonication of the silicon substrates dichloromethane (DCM) for 1 min followed by thorough rinsing with DCM and drying under a stream of nitrogen gas.

Vacuum annealing experiments

Annealing of samples under high vacuum conditions was performed in a Denton bell jar chamber utilising a turbo pump. The chamber was equipped with a resistive stage heater. Temperature was controlled by varying the applied potential and monitored by an *in-situ* k-type thermocouple.

Zinc Oxide Growth Experiments

Samples prepared by the NSL technique described above were heated for 3 h in a sealed tube containing 20 mL of a solution of zinc nitrate and hexamine (1:1 stoichiometry). Concentrations were varied from 0.1 mM up to 0.1 M. Important: samples were placed with the template side face down to minimize zinc oxide deposition from precipitates. After 3 h, samples were rinsed thoroughly with ethanol.

2-2.2 Characterisation

SEM Experiments

SEM measurements were obtained using a LEO Supra 55 VP microscope (Zeiss) equipped with an in-lens secondary-electron detector. For charging experiments an accelerating voltage of 0.3 keV was used and the scan rate was 44 s / image.

SEM Metrology

SEM area measurements were performed using ImageJ 1.50i. Distances were set in reference to the scale bar embedded in the image and area measurements were performed on regions chosen with the freehand selection tool.

AFM Measurements

For imaging a Digital Instruments Multimode Nanoscope III Scanning Probe Microscope was used. All imaging was conducted in the tapping mode, with 512 x 512 data acquisitions at a scan speed of 0.6 Hz at room temperature in air. Oxide-sharpened silicon nitride tips with integrated cantilevers with a nominal spring constant of 0.38 Nm^{-1} were used.

Monte Carlo Simulations

Monte Carlo simulations were performed on Casino v2.48 with 0.3, 1, 2 and 3 keV simulations performed with 2 000 000 simulated electrons. Beam radius = 1 nm. Database densities for silicon, gold, zinc oxide and alumina were utilised.

Fitting of Grey-Scale Data

Series of SEM images of an array of metal / metal oxide / metal devices collected over a time period at regular intervals were examined together with silicon-only substrates. Each SEM image was imported into Adobe Photoshop and individual triangular nanostructures in each array were defined using the Lasso function. The time interval between images was manually extracted from the image information bars. The mean grey-scale intensity of each nanostructure was calculated using the Histogram function in Adobe Photoshop with a value of 0 representing black and 256 representing white. The grey scale intensity of the silicon substrate was also measured using the Wand Tool with tolerances optimised on a case by case basis. The extracted data were subsequently converted to plots of mean grey-scale intensity *vs.* time. The data was fitted to the equation $I(t)=I(\infty)-Ae^{-t/RC}$ using FITYK 0.8.9 to obtain estimates and confidence intervals for *RC*.

EDS Measurements

EDS measurements were performed using a LEO Supra 55 VP microscope (Zeiss) equipped with an in-lens secondary-electron detector. EDS spectra were obtained with an Oxford instrument (INCA X-sight) X-ray detector.

Cathodoluminescence Experiments

Cathodoluminescence (CL) microscopy and spectroscopy was performed using a FEI Quanta 200 scanning electron microscope equipped with a Gatan MonoCL3 system. All CL spectra were corrected for the detection response of the system.

Chapter 3:

Formation of Periodic Arrays using Nanosphere Lithography

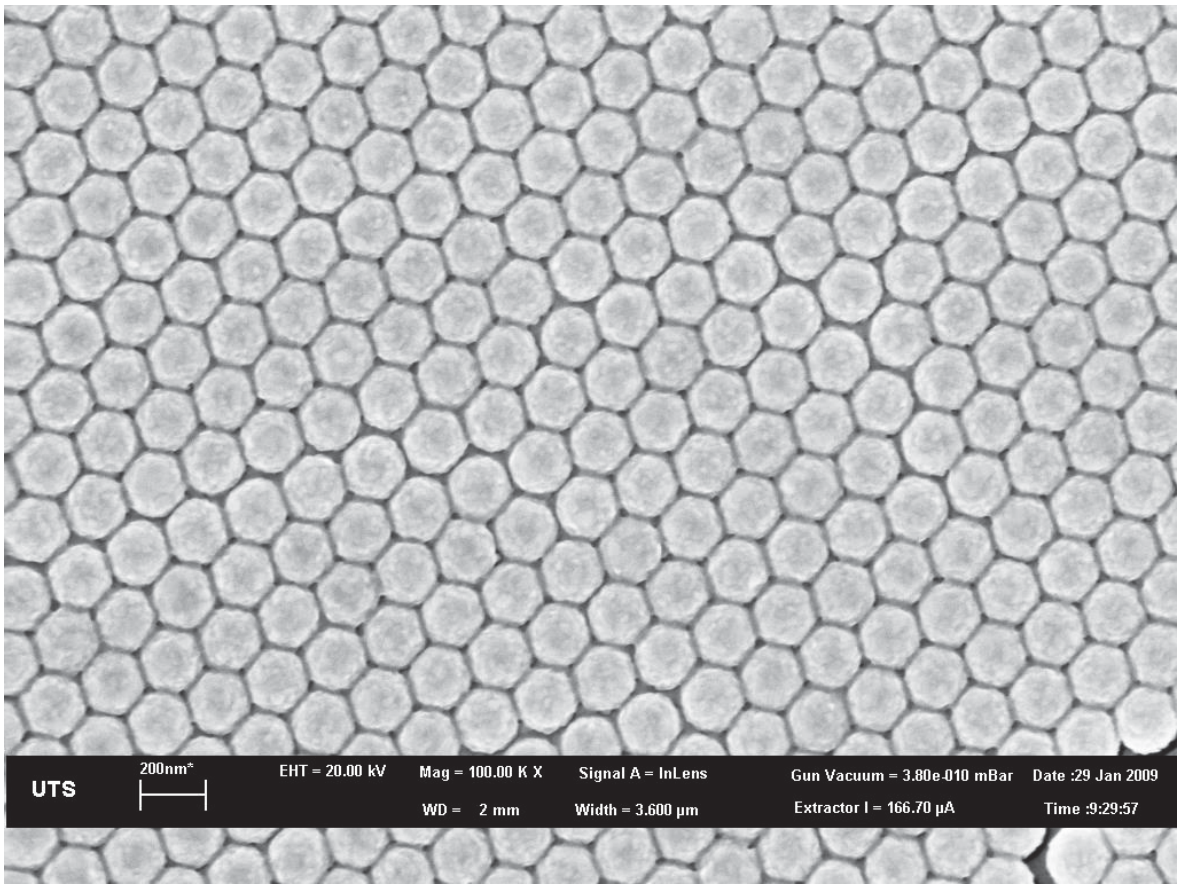

3 Formation of Periodic Arrays using Nanosphere Lithography

3-1 Introduction

The overall aim of the work presented in this thesis is to investigate techniques that enable the fabrication of arrays of nanoscale capacitor devices and their subsequent characterisation. Nanosphere lithography (NSL) is one technique that may be used to fabricate such periodic arrays of nanostructures.

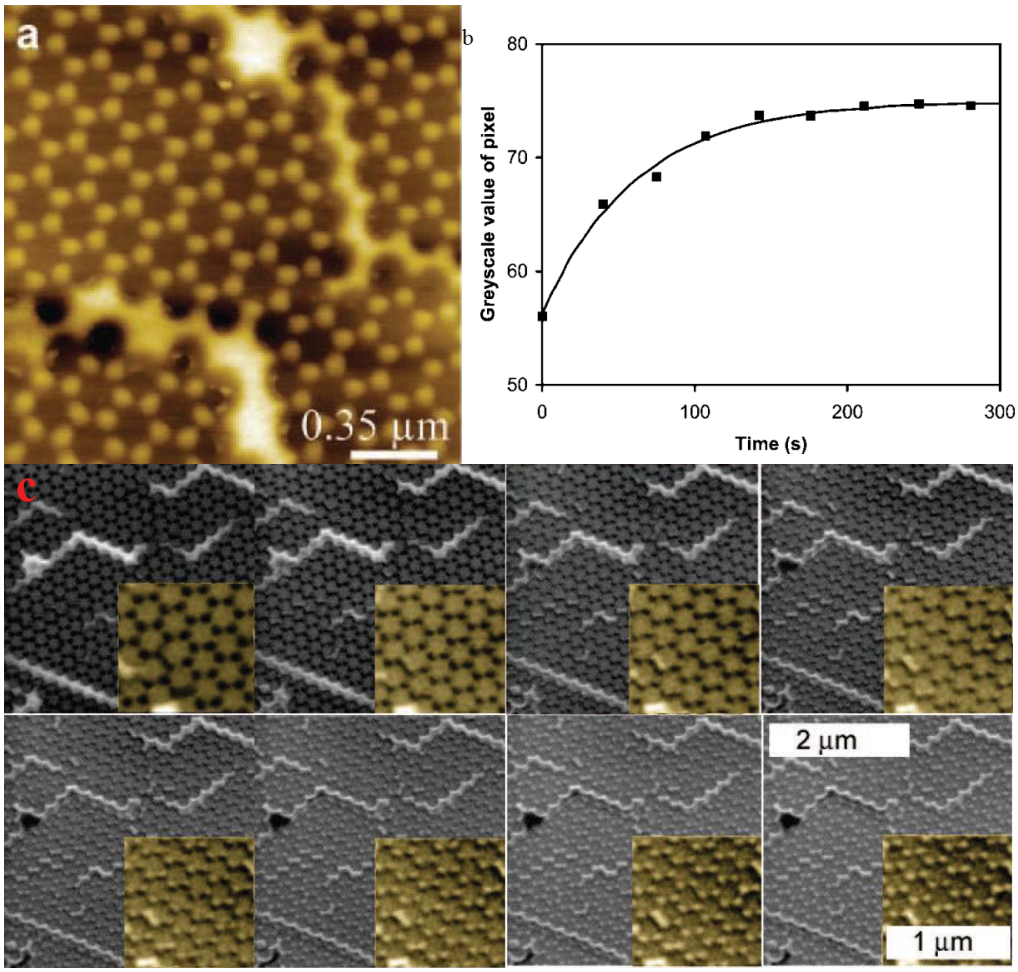

Figure 3-1. (a) AFM image of periodic structures fabricated using NSL. Large bright regions indicate mask defects where spheres did not form continuous hcp orientations. (b) grey-scale intensity *vs.* time data used to estimate the capacitance of structures produced in (a). (c) SEM images of nanostructures imaged over time. The greyscale intensity data is extracted from these images in (b). Data adapted from [19].

Gold / alumina / gold sandwich-type structures have been previously demonstrated as examples of nanocapacitors [18]. In previous work at UTS, it was found that experimental methods to produce periodic arrays of nanostructures using NSL gave results that at times were unreliable and problematic (see, for example, Figure 3-1 (a)). Defect regions, in which the spheres are not observed to be hexagonally close packed (hcp) can result in mask holes from missing spheres as well as dislocations where hcp regions do not align. Differences in the packing fraction of the spheres can also result in structures of different physical dimensions being deposited on the substrate. Minimising the presence of these defects is desirable as larger defect free regions will improve the reliability of experimental measurements by enabling simultaneous measurement of many identical structures under the same conditions. Structures produced by Zareie *et al.* [19] were also observed to charge rather rapidly (Figure 3-1 (b)) reaching a steady state value in four to five scans. Larger devices would take longer to charge under the same imaging conditions and have the potential to provide more information on the charging process.

The work presented in this chapter describes investigations into methods to produce hcp regions of PS spheres on silicon surfaces, which may be utilised as masks for metal and metal oxide depositions. It was hypothesised that adjustment of the NSL fabrication parameters could provide relatively large area defect-free masks that could be utilised to prepare discrete arrays of layered nanostructures. Ideally, a method could be found capable of producing structures of the same size that repeat periodically and enable the SEM characterisation of at least ten structures simultaneously.

It should be noted that this work is not (nor intended to be) a detailed investigation of the entire parameter space of NSL. Rather, it involves an exploration of materials and techniques such that a reliable method to produce uniform arrays of nanostructures with the desired spacing and feature sizes may be obtained. Several excellent reviews of the subject are available in the literature [310, 317-322].

PS latex spheres deposited electrostatically on surfaces were investigated as nanolithography masks [323]. This method was successful in attaching PS spheres to surfaces with no particular organisation [324-326]. Deckman and Dunsmuir were the first to report that PS latex spheres spin-coated onto substrates could form hcp domains under particular conditions [323]. Spin-coating parameters are numerous and

include: spin-speed, spin-acceleration, spin-time, solution concentration, solution volume, substrate type (including chemical modifications to alter a substrates hydrophobicity) and substrate size [327]. These interrelated variables make hcp optimisation challenging [328, 329] and the technique was initially unpopular. A decade after the initial reports, the synthetic procedure was refined by Hulteen and Van Duyne [311]. A surfactant was added to the spin-coating mixture and a significant increase in hcp domain sizes was observed. This modification made hcp structures with long range order facile and the technique became significantly more popular. The technique is also referred to as colloidal lithography, however when this is the case silica spheres are generally used [330, 331].

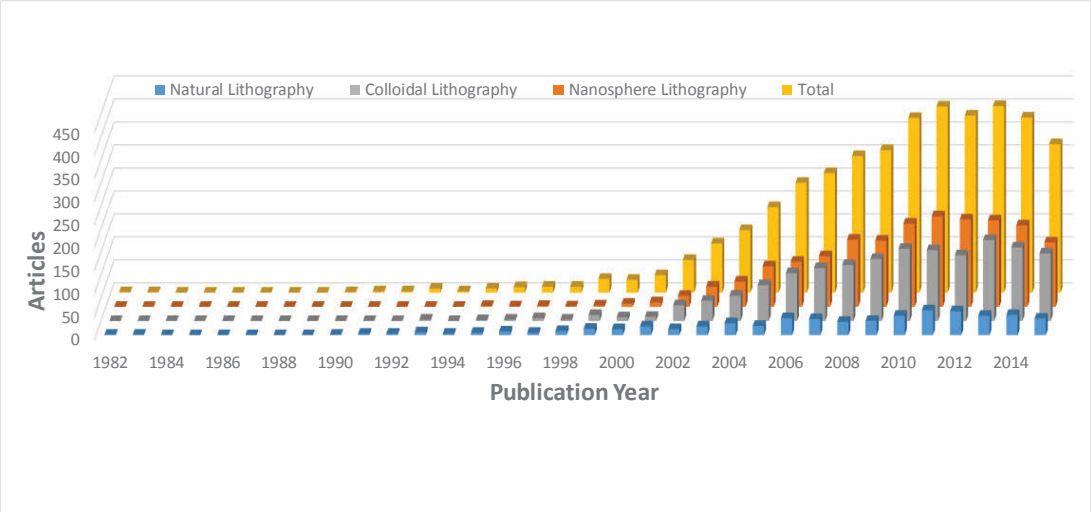

Figure 3-2. Column graph showing the number of papers containing the topics "natural lithography", "nanosphere lithography" and "colloidal lithography" between 1982 (first natural lithography paper published) and 2015. Data obtained from ISI Web of Knowledge (accessed 29th February 2016).

Figure 3-2 shows that from the publication of the first natural lithography paper in 1982 to the publication of the Hulteen nanosphere lithography paper in 1995 very few articles on this topic were published. After 1995, the publication rate increased, initially slowly, but then rather rapidly in the new millennium, peaking between 2011-2014. Today the technique has achieved widespread use.

As well as spin-coating, other techniques have been utilised to achieve hcp domains including; drop-casting [332-334], Langmuir-Blodgett [335-337] and other dip-type [338, 339] methods as well as electrophoresis [340], condensation on water

[341] and solid [342-344] surfaces. For clarity when referring to latex in this thesis, it is with respect to the IUPAC definition of "an emulsion or sol in which each colloidal particle contains a number of macromolecules" [345].

3-2 Results and Discussion

Figure 3-3 shows a schematic representation of the spin-coating process utilised in the current work where PS spheres were spin-coated onto a silicon substrate.

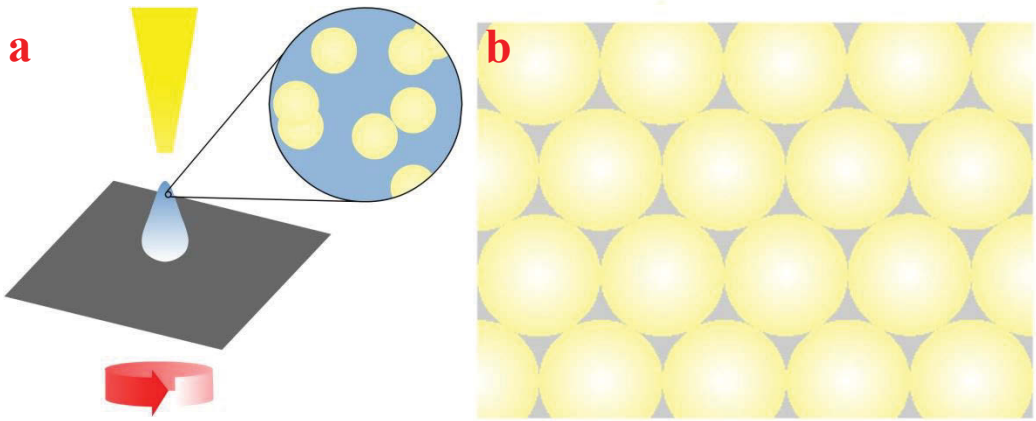

Figure 3-3. Schematic representing the spin-coating process being used to fabricate ordered arrays of close packed spheres for NSL. (a) Schematic depicting a solution of monodisperse PS latex being spin-coated onto a silicon substrate. (b) Schematic representing ordered array of hexagonally close packed PS spheres on silicon.

3-2.1 Effect of spin-coat volume

Initially, the spin-coating process was attempted using 10% w/v aqueous solutions of monodisperse 200 nm PS latex in a Triton-X / methanol mixture. Spheres were spin-coated onto p-type silicon substrates with dimensions ~ 1 cm^2. Substrates were cleaned by sonication in ethanol for 5 min, followed by thorough rinsing with ethanol and drying under a stream of nitrogen gas. Ratios of 10 % sphere solutions in water : (1:400 Triton-X : methanol) around 3:1 are widely reported in the literature [346]. Spin-coating speeds at or close to 3600 RPM are also commonly used, including by our research group [19]. As a first step an experiment was designed to optimise the effect of spin-coat solution volume on surface coverage of NSL masks. Solution

volumes ranging from 10-30 µL were investigated. Figure 3-4 shows initial results that were achieved using these parameters.

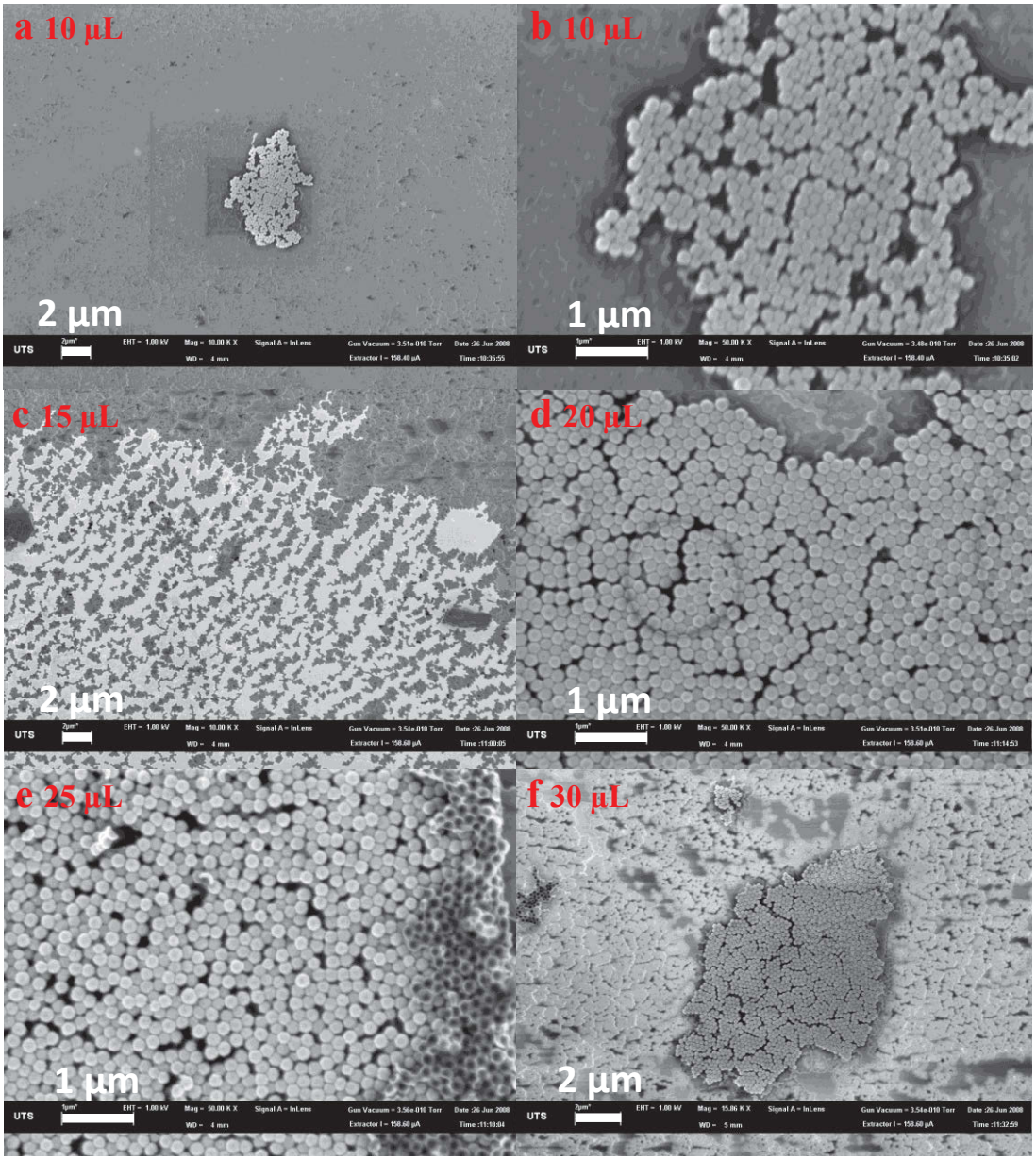

Figure 3-4. SEM micrographs of NSL masks used to investigate the effect of spin-coat volume on hcp ordering. Solutions were spin-coated onto silicon substrates with a "drop before spinning" method at 3600 RPM for 40s for mask formation. Subsequently, 20 nm of gold was deposited on the samples via evaporative deposition followed by thorough rinsing in dichloromethane (DCM).

It can be seen from Figure 3-4 that the method of mask removal (rinsing in DCM) failed to completely remove all spheres from the substrate. Large regions of spheres are prevalent in all samples investigated. A lack of contrast between deposited gold material and the substrate (highlighted in (b) and the region in (d) containing no

spheres) is also an indication that organic material is present on the surface. To prevent this occurring, sonication in conjunction with thorough rinsing of substrates in DCM was used in subsequent experiments where sphere removal is required. Evidence of charging effects are present in (f) with both dark and bright regions of gold visible. This is likely to be a consequence of beam electrons being trapped in the conducting gold deposits sitting atop the native oxide layer of the silicon substrate. With respect to surface coverage 20 µL solutions appeared to give the best initial results (d). A dark ring is also visible in panel (d), this is likely to be amorphous carbon left behind in the rinsing procedure. The ring structure is a consequence of capillary forces[347] present as carbon precipitated from the evaporating DCM solvent.

3-2.2 Effect of Triton-X - methanol mixture concentration

To combat the unwanted charging effects observed in Figure 3-4 silicon substrates were chemically treated by piranha etching. Prevalent in the semiconductor industry, piranha etching involves the immersion of the silicon substrate in a sulfuric acid / hydrogen peroxide mixture [348]. The highly concentrated sulfuric acid dehydrates the silicon substrate and greatly enhances the oxidising properties of the hydrogen peroxide removing all organic contaminants from the surface. This dehydration and subsequent oxidation occurs rather rapidly. Over time the sulfuric acid also etches the substrate removing contaminant metals and silicon dioxide leaving a silanised, oxide-free hydrophilic surface. A hydrophilic surface is highly desirable for NSL applications aiding in monolayer formation during the spin-coating procedure. An initially oxide free substrate will also greatly assist the reproducibility of capacitance measurements performed later in Chapter 4.

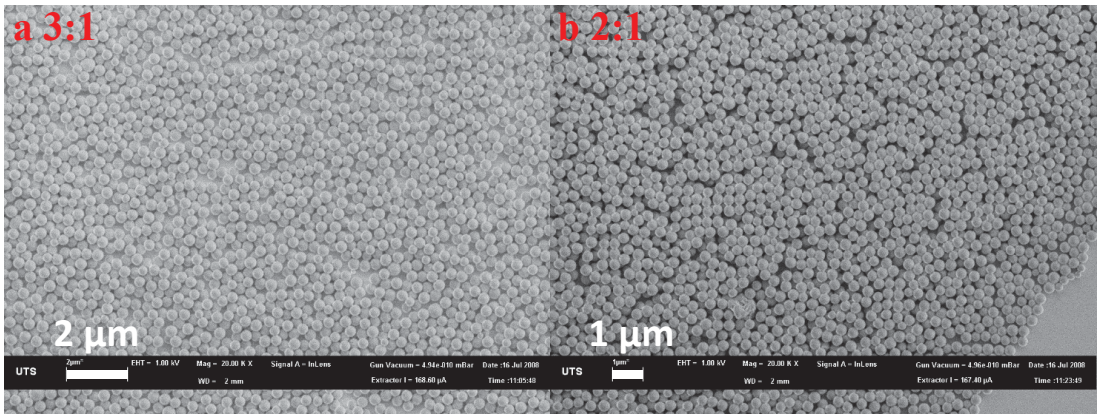

Figure 3-5. SEM micrographs of 200 nm latex sphere mixtures spin-coated onto silicon substrates with a (10 % w/v aqueous sphere solution) : (1:400 Triton-X : methanol) ratio of (a) 3:1 and (b) 2:1. Samples were prepared by spin-coating 20 µL mixtures on 1 cm^2 silicon substrates at 3600 RPM for 40 s in a "drop before spinning" method.

Figure 3-5 show SEM images of structures prepared using NSL with 200 nm PS spheres. Spheres were imaged with a relatively low accelerating voltage (1 KeV) to prevent charge 'flare-ups' or patch fields [349] on the electrically insulating PS spheres. Spheres were observed to form multilayers on the silicon substrate with little close packing observed on the uppermost layer. Double-layer NSL has been widely reported and is capable of forming a mask with periodic apertures for deposition. The phenomenon is generally observed when a higher concentration of nanospheres relative to Triton-X : methanol is spin-coated onto the substrate [311]. Double-layer NSL however is generally reported to be less reproducible than conventional NSL and does not occur over all regions of the substrate [310]. To minimise the potential of double-layers occurring in future experiments, lower concentration sphere mixtures were investigated.

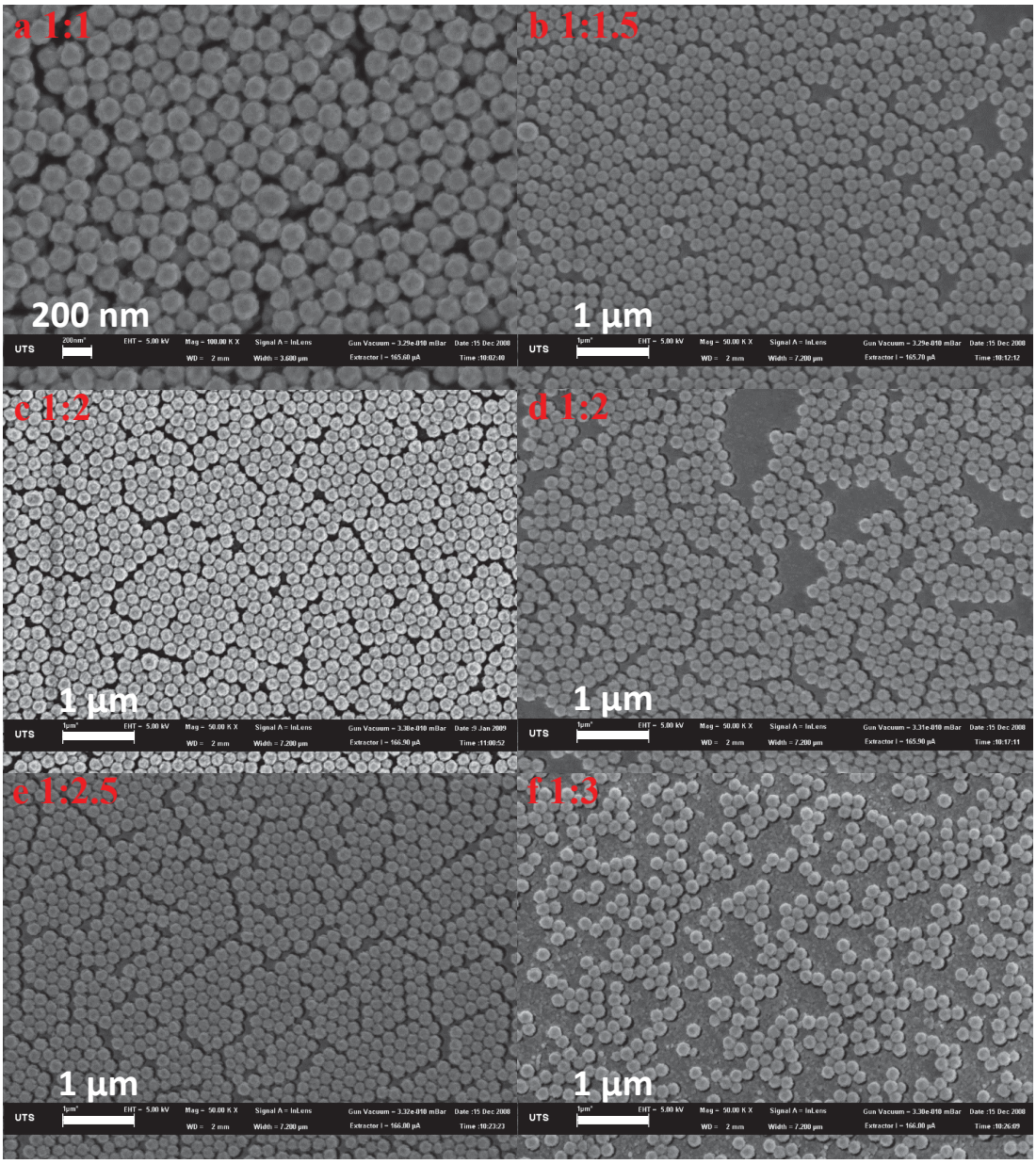

Figure 3-6. SEM micrographs of 200 nm latex sphere mixtures spin-coated onto silicon substrates with a (10 % w/v aqueous sphere solution) : (1:400 Triton-X : methanol) ratio of (a) 1:1, (b) 1:1.5, (c) and (d) 1:2, (e) 1:2.5 and (f) 1:3. Following spin-coating 20 nm of gold was deposited onto samples via evaporative deposition. Masks were prepared by spin-coating 20 µL mixtures on 1 cm^2 *p*-type silicon substrates at 3600 RPM for 40 s in a "drop before spinning" method.

Figure 3-6 shows a series of SEM micrographs obtained for lower concentration sphere mixtures ranging from 1:1 to 1:3 10 % aqueous sphere solution : (1:400 Triton-X : methanol) mixtures. Spheres in this series of experiments were coated with 20 nm of gold via evaporative deposition after spin-coating. This gold coating facilitates conduction of electrons to ground and allows for imaging at higher accelerating

voltages (5 KeV imaging could be performed without charge flare ups). Coating with 20 nm of gold introduces a surface roughness relative to both uncoated spheres (even when imaged at 1 KeV as in (e)) and an uncoated silicon substrate (particularly visible in (f)). This surface roughness is a consequence of the polycrystalline nature of gold films deposited by evaporative deposition. Gold coated PS spheres appear brighter than the gold coated silicon substrate as they are closer to the detector resulting in greater secondary electron signal during the raster scan. The concentrations investigated resulted in a transition from double-layer (1:1 ratio) to a sub-monolayer (1:3 ratio) packing of spheres. HCP regions with short range order and large defect boundaries were observed for mixture concentrations of 1:1.5, 1:2 and 1:2.5.

Having established a broad range for sphere concentrations that result in hcp regions (Figure 3-6, for example), the relatively small size of continuous areas was identified as problematic for future experiments. To address this, a “drop while spinning” technique [19] was employed during the spin coating process. This technique was investigated using the established concentration range as well as at higher sphere concentrations to account for the shorter interaction time with the substrate. Representative images of resultant surfaces are shown in Figure 3-7.

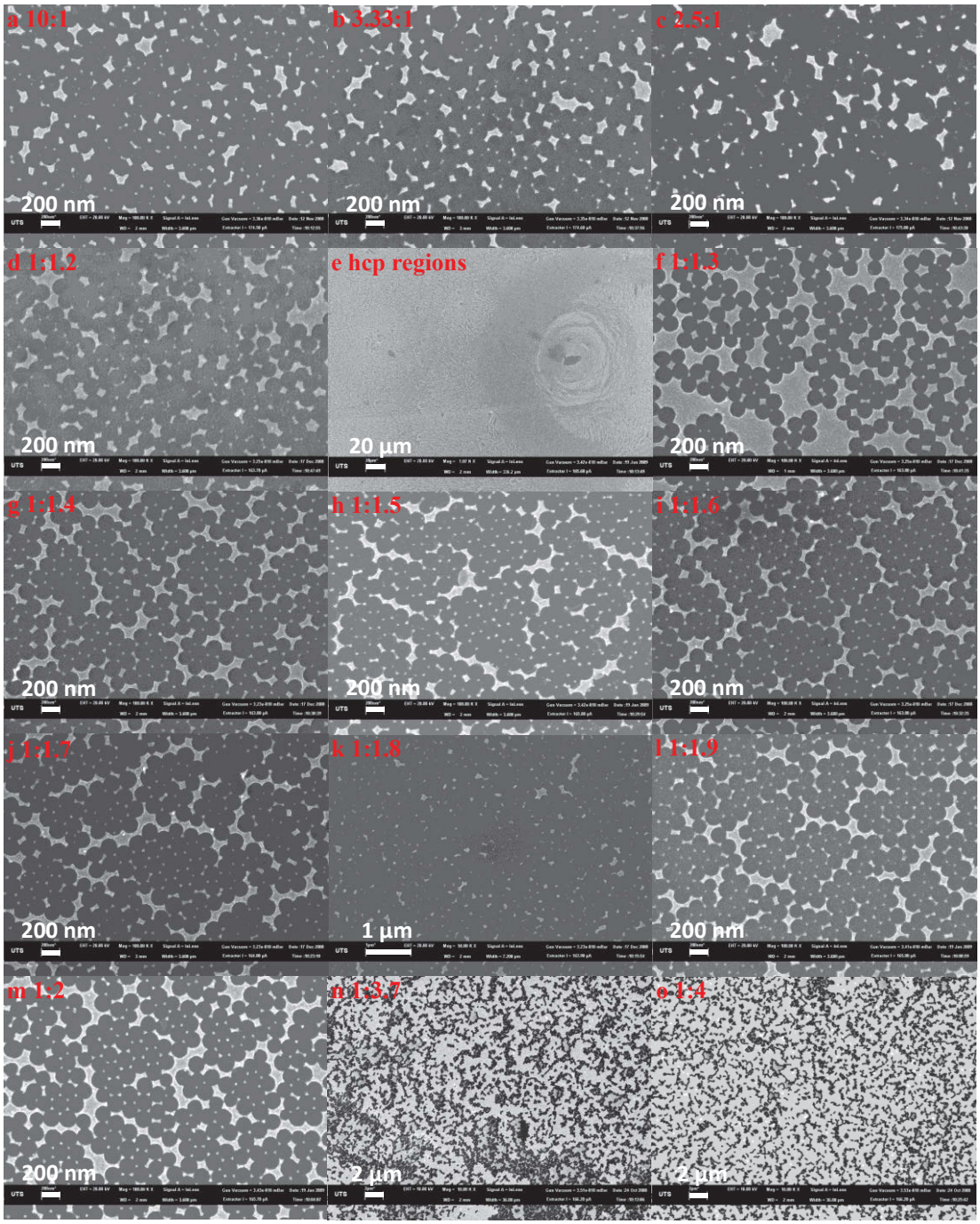

Figure 3-7. SEM micrographs of 200 nm latex sphere mixtures spin-coated onto silicon substrates with a (10 % w/v aqueous sphere solution) : (1:400 Triton-X : methanol) ratio of (a) 10:1, (b) 3.33:1, (c) 2.5:1, (d) 1:1.2, (f) 1:1.3, (g) 1:1.4, (h) 1:1.5, (i) 1:1.6, (j) 1:1.7, (k) 1:1.8, (l) 1:1.9, (m) 1:2, (n) 1:3.7 and (o) 1:4. (e) shows a low magnification image for areas that exhibit hcp regions. Following spin-coating 20 nm of gold was deposited on the samples via evaporative deposition and mask removal was facilitated by 1 min sonication and subsequent thorough rinsing in DCM. Samples were prepared by spin-coating 20 µL mixtures on 1 cm^2 *p*-type silicon substrates at 3600 RPM for 40 s in a "drop while spinning" method.

Figure 3-7 shows results obtained for a range of sphere concentrations with the implementation of the "drop while spinning" method. Bare silicon is present in regions that were previously covered with the mask. These regions appear darker than the gold structures due the difference in the work functions (Φ) and Fermi levels (E_F) of the two materials resulting in different probabilities of secondary electrons escaping the materials surface and reaching the detector [350]. Hcp regions were observed for sphere concentrations ranging between 1:1.4 and 1:2. Concentrations above this range resulted in disordered multilayers and below this range sub-monolayer regions were prevalent. Close packing however, only occurred in selected regions of the sample when the "drop while spinning" method was employed. These swirl shaped regions (see (e)) appeared selectively on substrates and were sometimes absent (k). Like the hcp regions in Figure 3-6 areas of close-packing are relatively small and many defects from incomplete mask formation are present. These results however are in complete agreement with those observed previously at UTS [19].

3-2.3 Effect of Spheres Size On hcp Domain Size and Reproducibility

Although limited satisfactory results were obtained using various parameters as outlined in Section 3-2.3, superior results could be obtained using fresh batches of PS latex spheres. The likely reason for this is the very small particles are highly susceptible to Brownian motion [351, 352] facilitating hydrophobic interactions resulting in particle aggregation. Sonication is capable of reversing this aggregation to a certain degree. Excessive sonication however results in the addition of thermal energy to the solution and has the potential to re-aggregate dispersed particles. Sonication of PS latex spheres was performed for 1 min at the beginning of every experiment where fresh mixtures of spheres : Triton-X : methanol were produced. How long particles were sonicated for by previous researchers was unable to be determined. Aggregation would explain the observed multilayer formation without close packing (Figure 3-5) and spheres appearing in a chain-like orientation (most visible in Figure 3-7 (o)) common for initial particle aggregation of this nature [353]. Freshly purchased PS latex spheres provided large regions of hcp for a broad range of sphere concentrations.

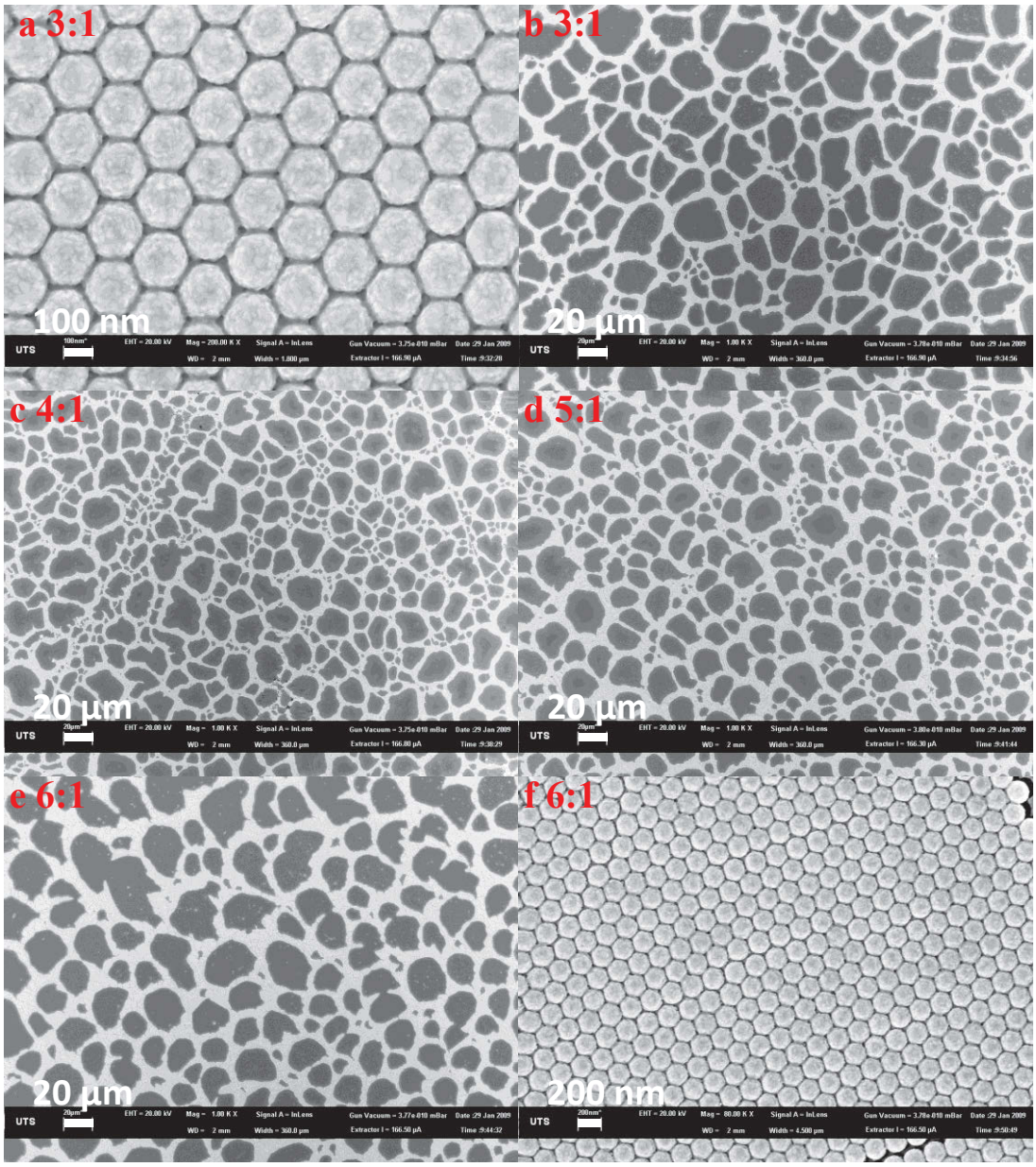

Figure 3-8. SEM micrographs of 200 nm latex sphere mixtures spin-coated onto silicon substrates with a (10 % w/v aqueous sphere solution) : (1:400 Triton-X : methanol) ratio of (a) and (b) 3:1, (c) 4:1, (d) 5:1, (e) and (f) 6:1. Following spin-coating 20 nm of gold was deposited on the samples via evaporative deposition. Samples were prepared by spin-coating 20 µL mixtures on 1 cm^2 *p*-type silicon substrates at 3600 RPM for 40 s in a "drop before spinning" method.

Figure 3-8 shows SEM micrographs of gold coated masks formed with NSL utilising fresh PS latex spheres with mixture concentrations of 3:1 ((a) and (b)), 4:1 (c), 5:1 (d) and 6:1 ((e) and (f)). It can be seen from the images that for all concentrations investigated spheres were observed to coat the substrate in a 'web-like' orientation ((b)-(e)) where large regions of hcp defect-free domains were present ((a)

and (f)). Areas where close packing did not occur on the substrate contained very few PS spheres. The sharp contrast of these results relative to those observed previously in the chapter are likely to be a strongly contributing factor to the reported unreliability of the technique experienced by other researchers in the field [354]. “Drop before spinning” of 20 μL solutions with a spin speed of 3600 RPM and a spin time of 40 s were chosen as suitable spin-coating parameters for all samples investigated from this point.

These findings enabled a more detailed examination of the effect of sphere size upon the quality of hcp regions produced during layer formation. It has been reported that larger PS latex can improve the reliability of NSL processes [308]. The effect of sphere size on hcp domain size and reproducibility was investigated.

Figure 3-9 shows SEM micrographs produced in an experiment to investigate the structural effects observed with the use of 500, 900 and 1500 nm PS latex spheres as masks for NSL. All spheres investigated were shown to form the same ‘web-like’ orientation on the silicon substrate observed with the 200 nm spheres in Figure 3-8 (Figure 3-9 (a), (c) and (e)). Again, relatively large area hcp regions were observed with dislocations and sphere voids still being present. Evidence of insufficient and excessive sonication is present in (c) and (e) respectively. Bright features in (c) are parts of the mask that have not been completely removed from the substrate. Dark areas in (e) indicate the removal of triangular structures as well as the NSL mask. The effect of sonication will be discussed further in Section 3-2.5. (d) and (f) show SEM micrographs of gold triangles with significantly different morphologies. This is a consequence of the different deposition methods employed. The 900 nm sphere templates used in (d) were coated in gold via sputter deposition, while the 1500 nm sphere templates in (f) utilised evaporative deposition. The effect of these different techniques on the nanostructure is discussed in more detail in Section 3-2.7.

It was demonstrated that 200, 500, 900 and 1500 nm spheres are satisfactory for use as NSL templates to form periodic arrays of discrete nanostructures. 1500 nm spheres also offer the advantage of producing relatively large triangular structures. Larger structures are desirable to assist in a more detailed understanding of the charging mechanism of synthesised devices in Chapter 4.

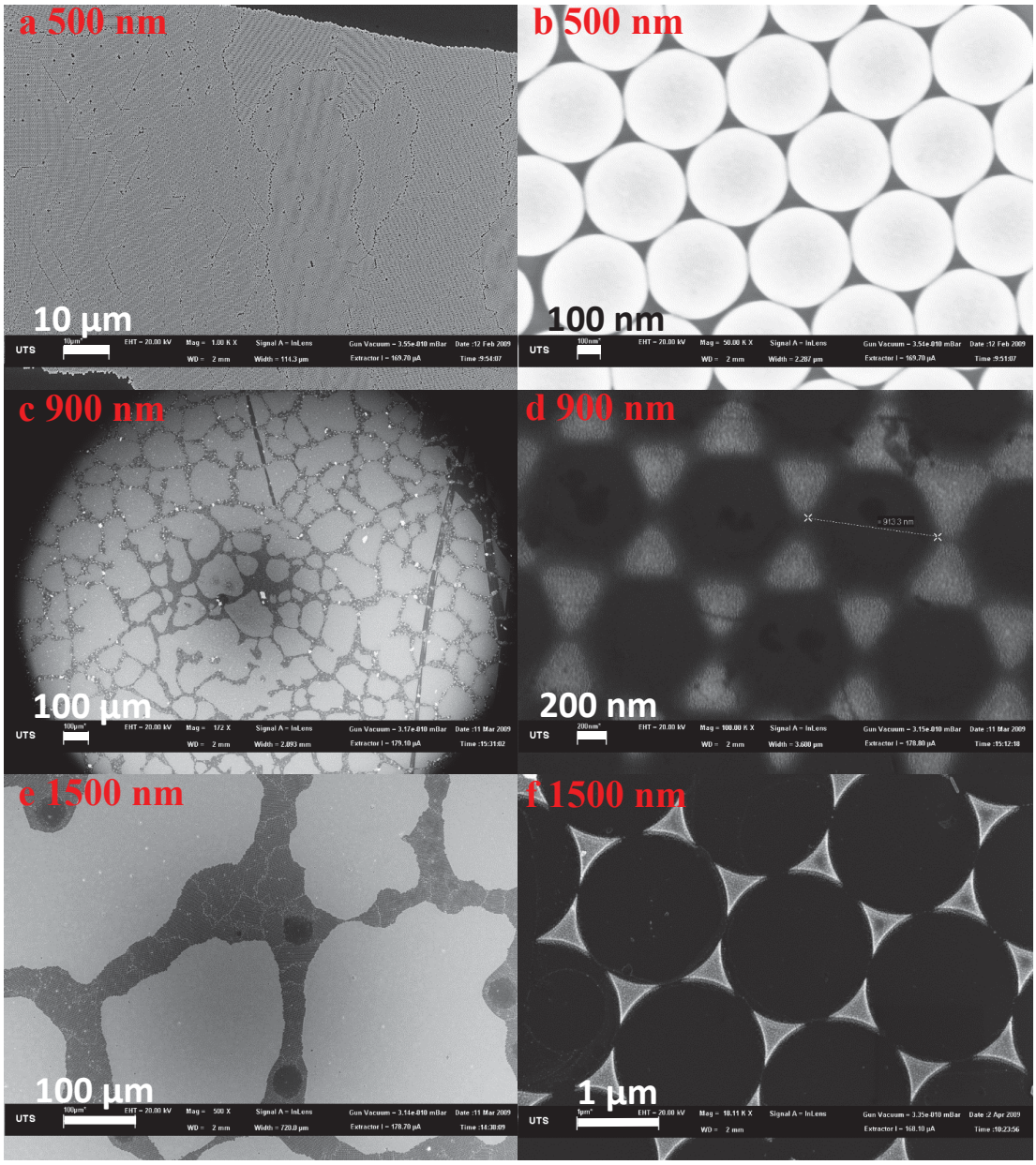

Figure 3-9. SEM micrographs of sphere mixtures spin-coated onto silicon substrates with a (10 % w/v aqueous sphere solution) : (1:400 Triton-X : methanol) ratio of 4:1. Size of the spheres are (a) and (b); 500 nm, (c) and (d); 900 nm, (e) and (f); 1500 nm. Following spin-coating 20 nm of gold was deposited on the samples via evaporative ((a), (b), (e) and (f) or sputter (c) and (d)) deposition. Mask removal (with the exception of (a) and (b)) was facilitated by 1 min sonication and subsequent thorough rinsing in DCM.

3-2.4 Effect of sonication time on the removal of the NSL mask.

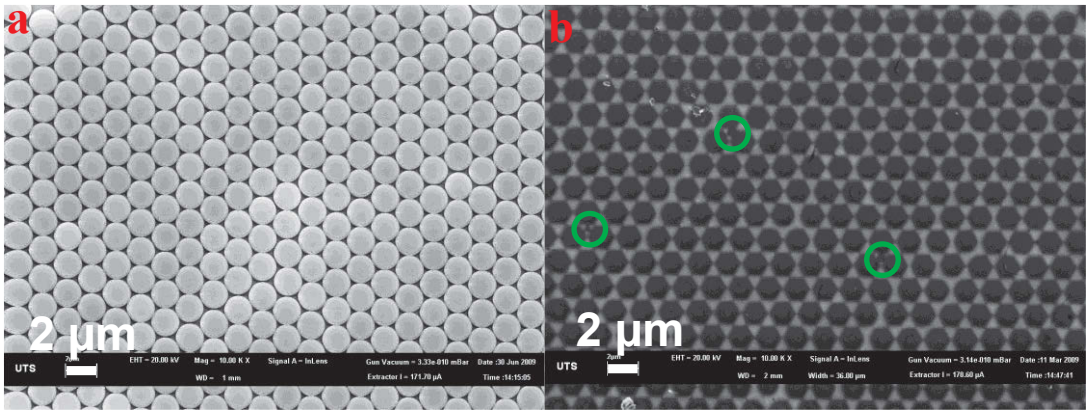

Figure 3-10. (a) Scanning electron micrograph of NSL mask composed of an array of close-packed 1500 nm PS spheres sputter coated with 20 nm of gold. (b) Gold triangular structures that remain after mask removal by sonication and rinsing in dichloromethane. Green circles highlight sections of gold triangles that have been displaced from the array.

In the literature, sonication in organic solvents is used almost exclusively to remove the PS latex mask from substrates in the NSL process. However, excessive sonication can lead to removal of deposited materials [355] (see Figure 3-10 (b) green circles). Insufficient sonication can also result in an incomplete mask removal (see Figure 3-9 (c)). During the optimisation process it was found that bath sonication of substrates in individual 20 mL glass sample tubes filled completely with DCM in a larger glass beaker half-filled with water for 1 min gave satisfactory results in terms of minimising the occasions where characteristics of excessive or insufficient sonication were observed.

Adhesive tape stripping has also been reported to be a suitable technique for NSL mask removal. The technique involves the application of adhesive tape to the surface of a silicon substrate after being used as a NSL mask. Removal of the tape has been reported to successfully displace the NSL without any damage occurring to materials deposited on the substrate [309]. This technique could minimise the problems observed with sonication. An experiment to determine the feasibility of tape stripping for mask removal was carried out.

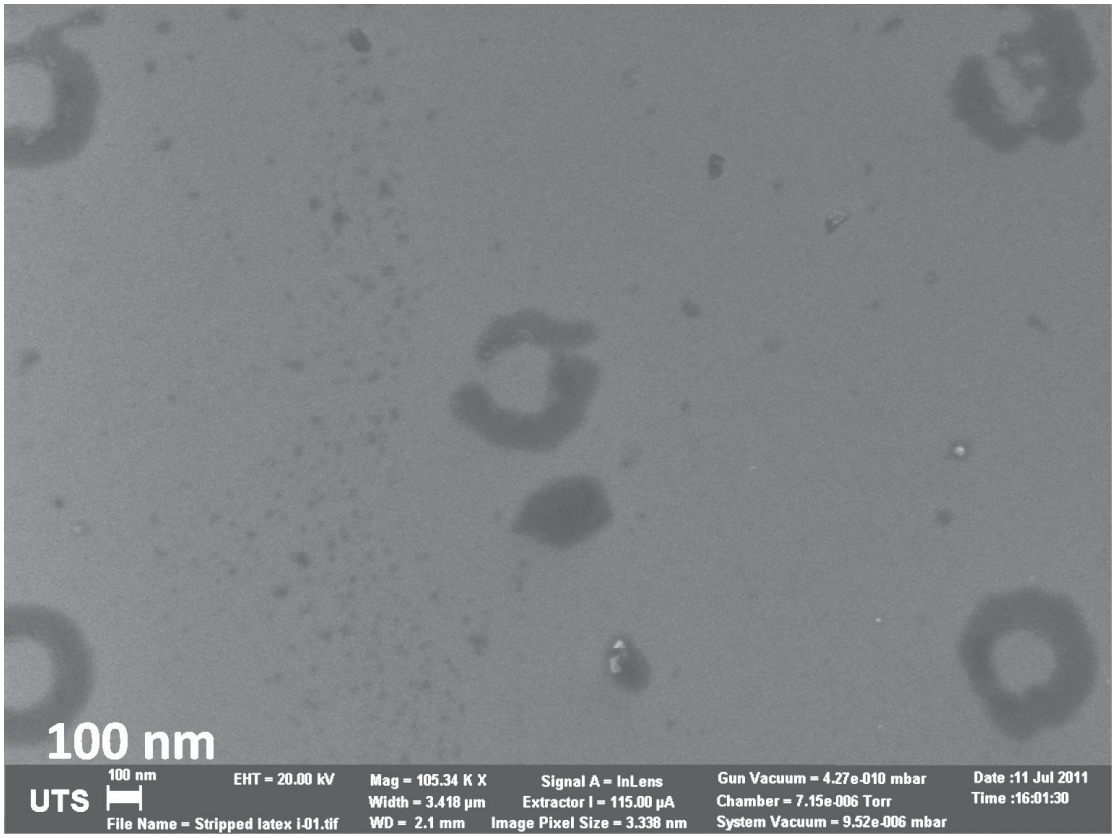

Figure 3-11. SEM micrograph of a silicon substrate after the removal of a 1500 nm PS latex sphere NSL mask via tape stripping. Contact patches where spheres resided before removal are clearly visible.

Figure 3-11 shows an SEM micrograph of a region of a sample where 1500 nm PS latex spheres were spin-coated onto a silicon substrate (no gold was deposited in this experiment) and subsequently removed via the tape strip method. Contact patches (from organic material) where the spheres resided before removal are clearly visible as dark rings in the image. These rings were less prominent in previous images as most of the organic material was removed during the rinsing procedure. As well as these contact patches significant amounts of organic material are also visible across the substrate (likely to be surfactant remaining from the spin coating process). This material is problematic as volatile organic materials in a SEM chamber can be reduced by the electron beam to form amorphous carbon deposits on the surface of any sample being imaged. These deposits are referred to as beam damage and are generally undesirable. With the aim of the experiments in Chapter 4 to estimate the capacitance of structures via SEM by measuring the change in brightness over time,

any darkening of the sample via contaminants should be avoided. Tape stripping was decided to be unsuitable for use in subsequent experiments.

3-2.5 The Lift-Off Method as an Alternative for Mask Formation

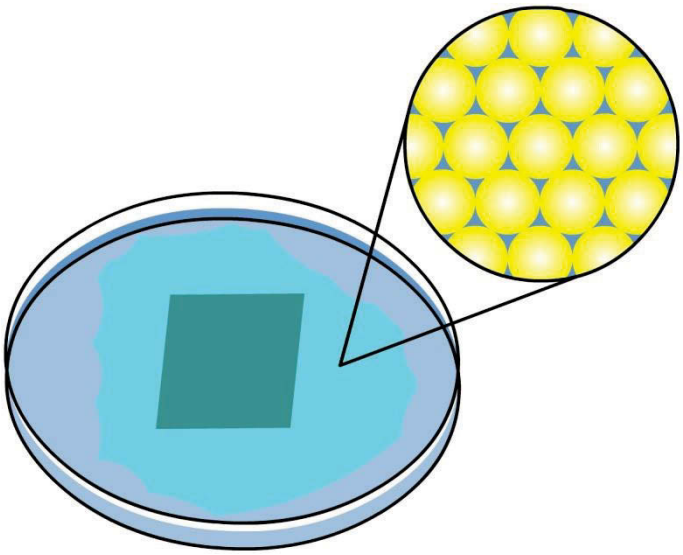

Figure 3-12. Schematic representing the experimental procedure used in the lift-off method. PS latex / surfactant mixtures are placed at the air-water interface of a petri dish and allowed to close pack via hydrophobic forces. A hydrophilic silicon substrate is then lifted through the floating film.

Rybczynski *et al.* reported the formation of large area hcp arrays by a water / air interface self-assembly of spheres followed by a subsequent lift-off with a silicon substrate through the interface [339]. This method was also investigated in the current work.

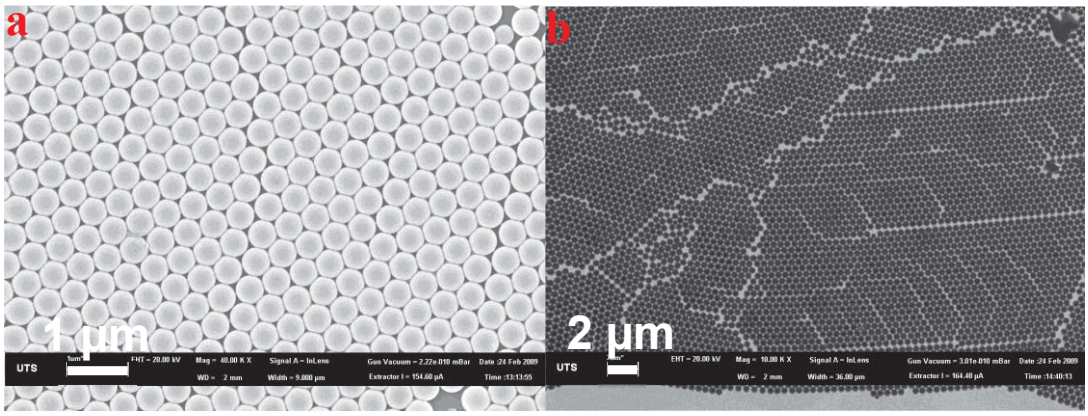

Figure 3-13. SEM micrographs of structures produced by the lift off process of 500 nm PS spheres, coated with 10 nm of gold (a) without and (b) with PS sphere removal.

Figure 3-13shows results obtained using the Rybczynski *et al.* solution lift off method. The primary modification relative to the published method was the continued use of piranha-etched silicon substrates (authors used 24 h immersion in 10% dodecylsodiumsulfate (SDS) solution). The use of a hydrophilic substrate required latex spheres to be deposited directly into the air / water interface rather than via the immersion of the sphere coated substrate. Another difference was the absence of surface tension modification by the addition of 4% SDS solution in ethanol to consolidate the particles. The use of Triton-X methanol mixtures to assist in self-assembled close-packing was maintained. The primary challenge with this method was the high levels of dexterity required to prevent substrate and tweezer movements causing turbulence in the petri dish and disturbing the close packing of the spheres at the air / water interface.

Regions of hcp spheres were obtained, however the size dispersion of these areas tended to be sporadic, with defect regions and grain boundaries prevalent throughout all samples. Reproducibility of samples is paramount for this investigation, so it was decided that the lift-off method in its investigated form was unsuitable for mask fabrication.

3-2.6 Effect of Metal Deposition Techniques on Nanostructure

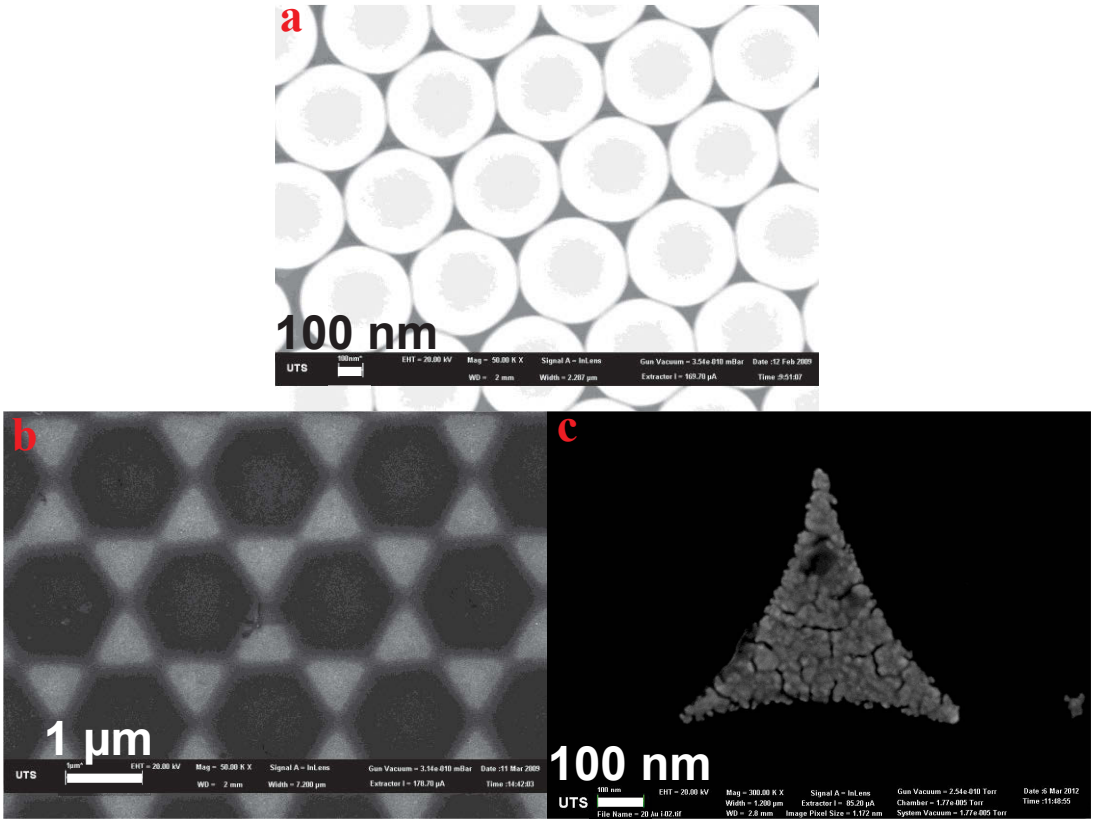

Figure 3-14. SEM micrographs of (a) 1500 nm close packed PS spheres. Triangular nanostructures formed by sputter deposition (b) and evaporative deposition (c) of gold.

Figure 3-14 shows that sputter deposition and evaporative deposition of gold result in different types of nanostructures being formed. Sputter deposition yields larger triangles with relatively low-curvature edges, smooth corners and a hill like topography (b). Conversely the nanostructures formed by evaporative deposition are smaller triangles with inwardly curved edges and sharper corners. The evaporated triangles also have a sharp step from film to substrate and more closely resemble the shape of the void in the mask (c). Surface roughness of the triangular structures produced by evaporative deposition is also observed to be high, with large grain boundaries clearly visible.

The mean free path of any deposited species in a vacuum deposition system can be given by the expression:

$$l = \frac{K_B T}{\sqrt{2}\pi\sigma^2 p}$$

Where K_B is the Boltzmann constant (1.38 x 10^{-23} JK^{-1}, T is the temperature of the system (K), σ is the Lennard-Jones parameter or effective radius of the gas molecule (m) and p is the pressure of the chamber (Pa).

Sputter deposition was carried out under higher pressure conditions (~10^{-3} Torr) relative to evaporation (~10^{-7} Torr), such that material travelling between the source and substrate has a shorter mean free path in the high pressure system (~ 20 cm relative to ~ 704 m calculated at 300 K using σ values of 0.35 nm for argon and 0.315 nm for the oxygen component of the water molecule). The greater probability of collisions with free gas molecules in the chamber will result in a higher chance of altered trajectories with increased angles of sputtered material passing through the mask apertures.

However the difference in morphologies is primarily driven by the higher surface mobility [356] of sputter deposited gold relative to evaporative deposition.

Evaporative deposition operates on a line-of-sight principle and is primarily driven by surface energy interactions initially with the substrate, transitioning to both the substrate and any deposited material and finally with the deposited film. Governed by an 'island growth' mechanism, there will be a sharp edge between areas in and out of line-of-sight of the material source (provided the deposited materials surface energy is higher than that of the substrate) [357]. It has been established that evaporative deposition of gold onto substrates where $T_s < 0.3T_m$ results in small-grained polycrystalline films that exhibit highly conductive, low stress characteristics [358, 359]. In the above experiments substrate temperatures were observed to reach a maximum of 55^{o}C (328.15 K as measured by an *in-situ* thermocouple). This would correspond to a substrate temperature ratio of less than 0.25 relative to 1337 K (T_M of gold).

The lower kinetic energy of evaporated materials striking the substrate relative to sputtered ones will also result in less surface diffusion [357].

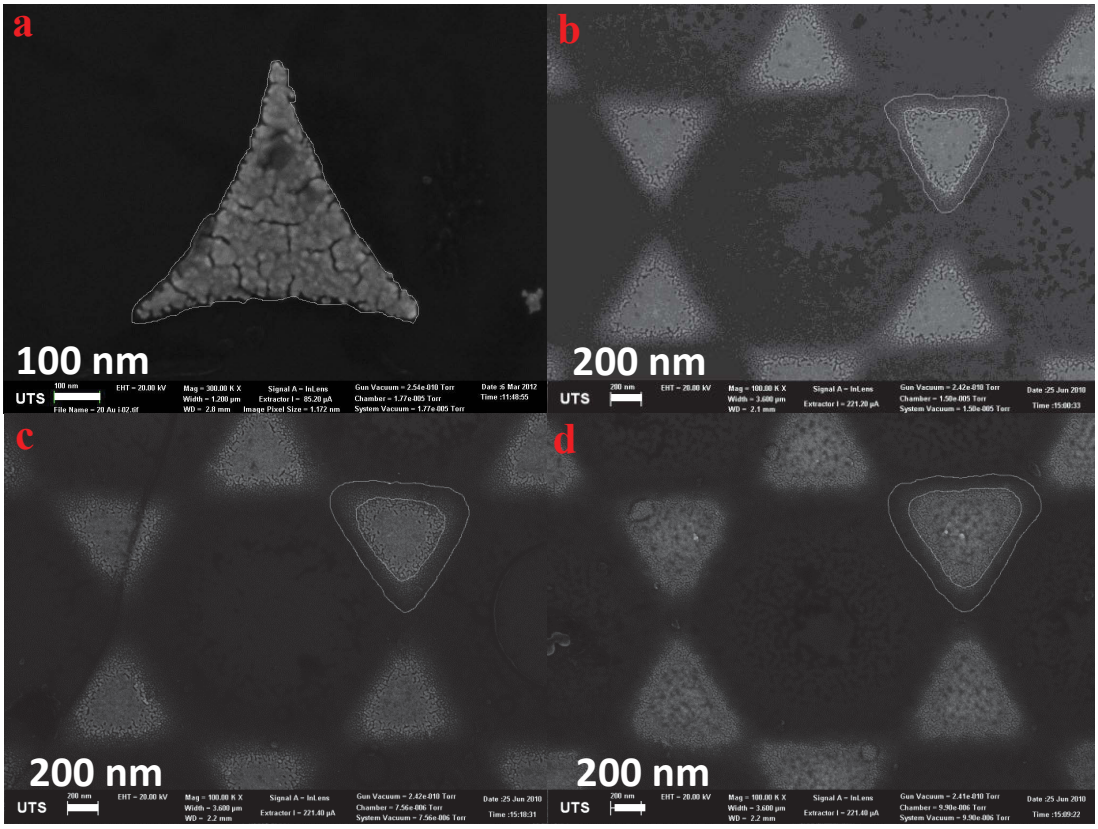

Figure 3-15. SEM micrographs of gold nanostructures produced by (a) evaporative coating or sputter coating 20 nm gold films on NSL templates utilising 1500 nm PS latex sphere masks. Sputtering argon partial pressure and power supply conditions were (b) 6 x 10^{-4} Torr, 0.017 A, 20 V, (c) 3 x 10^{-4} Torr, 0.017 A, 20 V and (d) 3 x 10^{-4} Torr, 0.020 A, 20 V.

Figure 3-15 shows the results for an experiment to investigate the effect of deposited materials kinetic energy on surface mobility. PS latex spheres with a diameter of 1500 nm were used as masks for NSL to fabricate 20 nm gold structures via (a) evaporative or (b-c) sputter deposition. Modifications were made to the argon partial pressure and power supply to control the kinetic energy of gold atoms during film growth. Increasing the partial pressure of argon in the chamber resulted in more collisions of sputtered material before reaching the substrate and hence an arrival with a lower kinetic energy. Modifying the power supply parameters alters the rate of acceleration of argon ions into the target. This directly influences the momentum transfer during sputtering. Triangular gold structures produced for sputter deposited samples show a changing morphology between their inner region (IR) where films are polycrystalline and relatively continuous, compared to their outer region where the height of the structures is observed to decrease (at a much lower gradient relative to

the sharp edge in structures produced by evaporative deposition) towards the edge of the structure. The surface roughness of the outer region is also significantly greater than the inner region indicating less dense thin film growth (especially evident in (b) where discrete island growth of gold is observed). Image metrology was used to calculate the area of these structures (indicated by the selected regions in Figure 3-15).

Table 3-1. Measured areas of gold structures using different gold deposition conditions.

Deposition method	Evaporative	Sputter 6 x 10^{-4} Torr (0.017 A, 20 V)	Sputter 3 x10^{-4} Torr (0.017 A, 20 V)	Sputter 3x10^{-4} Torr (0.020 A, 20 V)
IR area (nm^2)	137355	169529	187824	206722
Total area (nm^2)	137355	389695	474459	579748

Table 3-1 shows the measured areas of triangular gold structures produced under different deposition conditions. It can be seen that evaporative deposition resulted in the smallest x-y area gold structures followed by the higher pressure / lower power sputtering, next lower pressure / lower power sputtering and finally lower pressure / higher power sputtering resulting in increasingly larger area structures. For comparison the size of an ideal NSL aperture with 1500 nm PS latex spheres was measured to be 129750 nm^2 after 20 nm gold deposition. It is reasoned that the increased kinetic energy of gold deposited through the NSL mask results in larger x-y dimension triangular structures through higher surface mobility of deposited material.

To synthesise nanocapacitors, it is vital that the conducting electrodes are electrically isolated from each other; connection would create an electrical short which would prevent the device from storing charge. The production of lower x-y dimension triangles by evaporative deposition is advantageous when combined with a larger x-y dimension metal oxide in preventing shorts (see Chapter 4). Sputter deposition of gold films can however be useful in capping zinc oxide materials for use in salt solution growth experiments (Chapter 5).

3-3 Conclusions

A method to reliably produce arrays of nanostructures over a micron-scale range was developed. It should be noted that this work did not attempt to optimise for very

large area defect-free domain sizes. In this regard, micron-scale areas that were defect free were deemed sufficient for further fabrication and imaging experiments. Spin-coating of PS latex with a 4:1 ratio of 10 % w/v in aqueous solution with a 1:400 Triton-X:methanol mixture with a spin speed of 3600 RPM gave satisfactory hcp arrays. All PS spheres investigated gave long range close packing and reproducible results, provided spheres were not aged and were sonicated for 1 min prior to dilution. Masks formed with 1500 nm PS latex spheres were decided to be the most appropriate size for nanocapacitor synthesis experiments in Chapter 4 due to the longer times that will be required to charge the devices as a consequence of their larger surface area. Sputter and evaporative deposition produce different types of nanostructures which can be utilised in synthesising nanocapacitors. These findings are implemented in the subsequent chapter to synthesise periodic nanoscale capacitors.

Chapter 4:

Scanning Electron Microscope Charging of Gold-Metal Oxide- Gold Capacitors Synthesised by Nanosphere Lithography

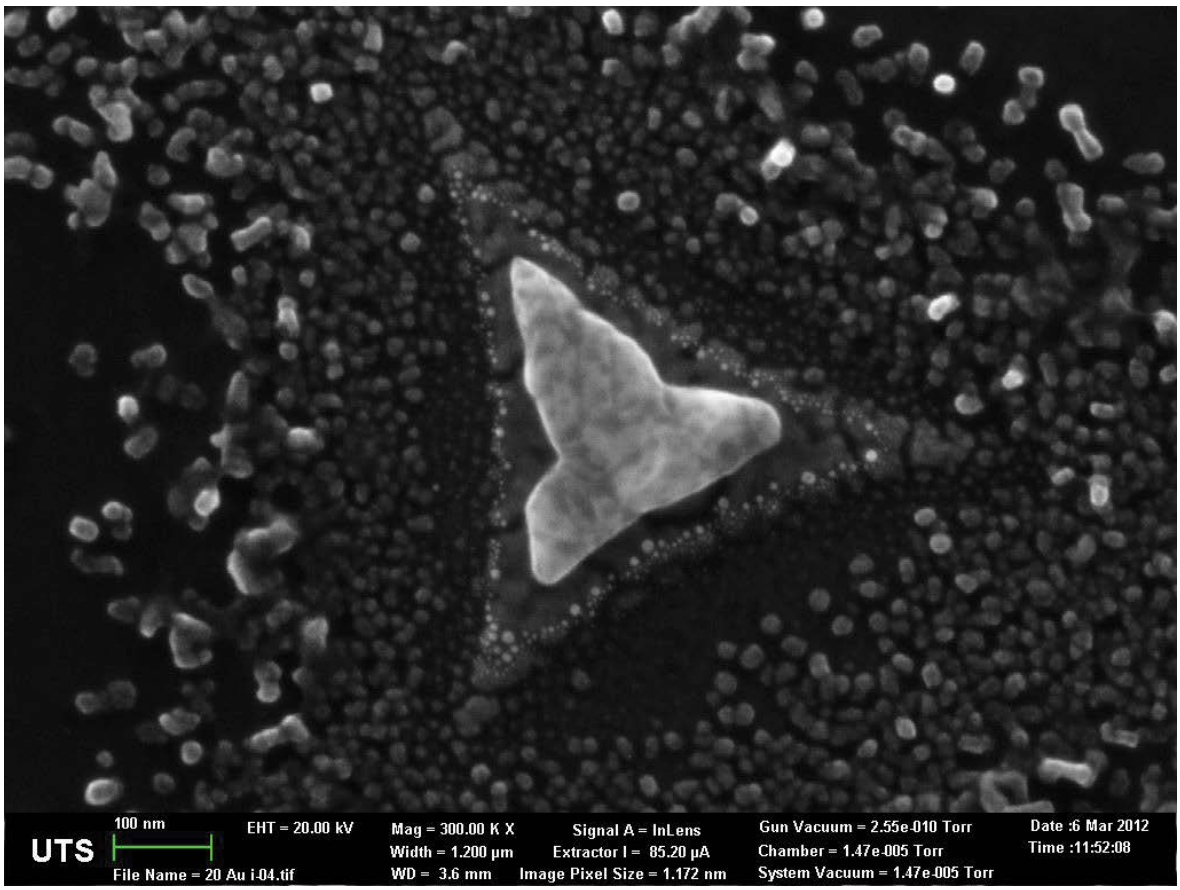

4 SEM Charging of Gold-Metal Oxide-Gold Capacitors Synthesised by NSL*

4-1 Introduction

As discussed in Chapter 1, there is significant interest in developing methods to fabricate macroscale capacitors comprised of nanoscale materials [360-362]. Popular approaches include synthesising electrochemical capacitors that incorporate carbon nanotubes [147] or graphene sheets [191] in electrodes. Functionalisation [143, 211], or incorporation of composite materials [113, 215], to exploit synergistic effects (such as improved power and energy densities) are also frequently investigated. Somewhat less attention has been paid to the soft lithographic fabrication of discrete nano- or mesoscale capacitors but, with the continuing miniaturisation of other circuit components, such tiny capacitors may become invaluable for future electronic devices.

Traditional MOS (metal / oxide / semiconductor) or MOM (metal / oxide / metal) capacitors are commonly characterised by capacitance-voltage measurements where a small AC voltage is applied to the device while measuring the current. The current can then be integrated with respect to time to determine the charge, and hence the capacitance. Continued miniaturisation of capacitance devices makes this type of measurement increasingly difficult because (1) the parasitic capacitance of any attached leads may eventually mask the measurement and (2) it may be challenging to attach such leads anyway. This is particularly the case for discrete nanocapacitors produced by self-assembly or soft lithography. Therefore, alternative methods to characterise the smallest capacitors are needed, especially those produced by non-traditional routes.

Monolayer-protected clusters and metal carbonyl clusters have been characterised by cyclic voltammetry or differential pulse voltammetry [265], while the pioneering Au@SnO_2 colloidal nanocapacitors of Mulvaney *et al*. [363] were probed by changes to the optical properties. However, these techniques probe particle ensembles rather

* A significant part of the work presented in this chapter has been published (see Coutts. M. J.; Zareie. H. M.; Cortie. M. B.; McDonagh. A. M., Nanotechnology. (2014) **25**(15): p. 155703.).

than individual particles. Scanning tunneling microscopy can be used to probe the charging of individual nano-devices [20], but only within a relatively narrow window of voltages and time-scales.

Scanning electron microscopy (SEM) is a versatile, powerful technique that has become indispensable in fields such as nanotechnology and materials science. The injection and emission of high energy electrons into samples allows information such as surface topography, sample composition and electrical conductivity to be extracted. In preliminary work, our group has demonstrated that SEM can also be used to experimentally estimate the capacitance of discrete nanocapacitors [19]. The basis of the capacitance measurement technique involves imaging arrays of discrete nanocapacitors at low accelerating voltages, and monitoring the increase in brightness of these devices over time. The increase in brightness is a consequence of an increasingly greater emission of secondary electrons and hence of an increasingly negative surface potential [364]. This change in brightness enables the time constant for charging to be measured and, consequently, the capacitance to be estimated. One limitation of this technique was the lack of long range order in the NSL lithography technique making the measurement of a large number of discrete devices simultaneously challenging. This limitation has been addressed in Chapter 3. While early work at UTS demonstrated a proof-of-concept, many questions remain about the fabrication processes as well as a detailed understanding of the device behaviour, especially concerning the role of various metals in the metal oxide layers.

In this chapter, the capability of SEM to charge and measure nanocapacitors devices is investigated as well as the effect of different materials on the charging behavior of the discrete nanocapacitors. The studied nanostructures consist of a metal oxide layer “sandwiched” between two layers of gold. Similar architectures using gold / silicon oxide “nanosandwiches” have been shown previously to exhibit interesting optical responses due to plasmonic interactions [309]. In this thesis the *RC* constants are extracted from the series of grey scale images and discussed in detail. Overall, the methods developed provide useful ways to fabricate and then characterise nano- or meso-scale charge-storage devices.

4-2 Results and Discussion

4-2.1 Fabrication of multi-layer metal / metal oxide / metal nanostructure arrays

Table 4-1. Properties of interest for metal oxides investigated to synthesise nanoscale capacitors.

Material	Relative Permittivity (ε_r)	Resistivity (Ωm)	Surface Energy (Jm^{-2})
Alumina	9.34 [365]	~10^{12} [366]	0.79 [367]
Silica	4.42 [261]	~10^{13} [368]	1.5 [369]
Zinc Oxide	7.5-8.6 [370]	~10^{12} [371]	1.42 [372]
Titania	86 [373]	10^{6}-10^{12} [374, 375]	1 [376]
Hafnia	25-50 [377, 378]	10^{8}-10^{11} [378, 379]	1.46 [380]

Table 4-1 shows data from the literature for the relative permittivity, resistivity and surface energy of the metal oxides investigated in this work. Having been demonstrated previously in the synthesis of nanoscale capacitors at UTS [19], alumina was a logical starting material for investigation. Silica is the semiconductor standard (primarily grown from silicon substrates in oxidising conditions, but also sputtered) and is used extensively for insulating applications [381]. Zinc oxide offers a relative permittivity between those of alumina and silica whilst maintaining a similar resistivity [382-387]. Titania is interesting in that deposited thin films have been shown to have a large range of reported resistivities [374, 375]. Finally, Hafnia's electrical properties have attracted much interest as a material for nanostructured devices [388]. With the continuing miniaturisation of semiconductor devices, research into high relative permittivity, high resistivity materials [389] for use as an alternative to silica (that are compatible with silicon) [390] which can suffer dielectric breakdown and current loss under the strong electric field densities becoming more prevalent with smaller feature sizes. Together, the selection of these materials has the potential to provide information on nanoscale capacitors fabricated with metal oxides that have a broad range of relative permittivities and resistivities.

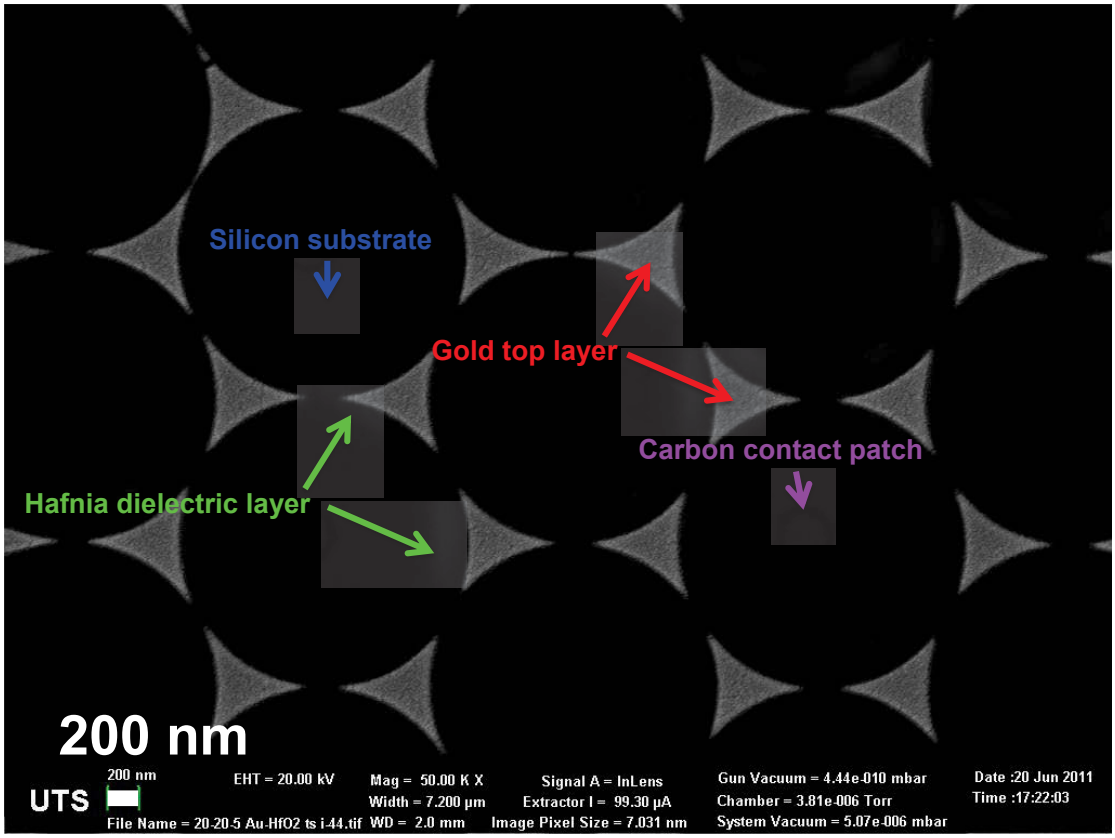

Figure 4-1. SEM micrograph of nanoscale capacitors fabricated NSL. Films consisting of gold (20 nm) / hafnia (20 nm) / gold (20 nm) layers were synthesised.

Figure 4-1 shows an array of gold (20 nm) / hafnia (20 nm) / gold (20 nm) nanostructures synthesised using NSL. The top gold layers are most visible in the image with sections of the hafnia layer also visible (where not covered by the top gold layer). It is evident that the top gold triangle and the hafnia layer have different morphologies and dimensions. This is a consequence of the different deposition techniques. Gold was deposited by evaporative deposition (discussed in detail in Chapter 3), while hafnia was deposited via RF magnetron sputtering. Insulating materials such as hafnia are notoriously difficult to deposit via evaporative deposition due to their generally very high T_M (2774^{o}C for hafnia [391]) and so sputtering is commonly employed. RF magnetron sputtering can overcome charge buildup from ionised gases colliding with the insulating target during the sputtering process. The polarity of the power supply is oscillated at radio frequencies [392]. As discussed in Chapters 2 and 3, sputter deposition results in materials being deposited onto substrates with a higher kinetic energy and surface mobility relative to evaporative deposition. Consequently, structures produced by RF sputtering through NSL masks

have larger x-y dimensions and somewhat different shapes to those deposited via evaporative deposition.

Also evident in Figure 4-1 is that the top gold triangle does not precisely centred relative to the hafnia triangle. This is a consequence of the angle between the inter-sphere void and the deposition source. This difference may be exploited in a technique known as Angle-Resolved NanoSphere Lithography (AR NSL) [321].

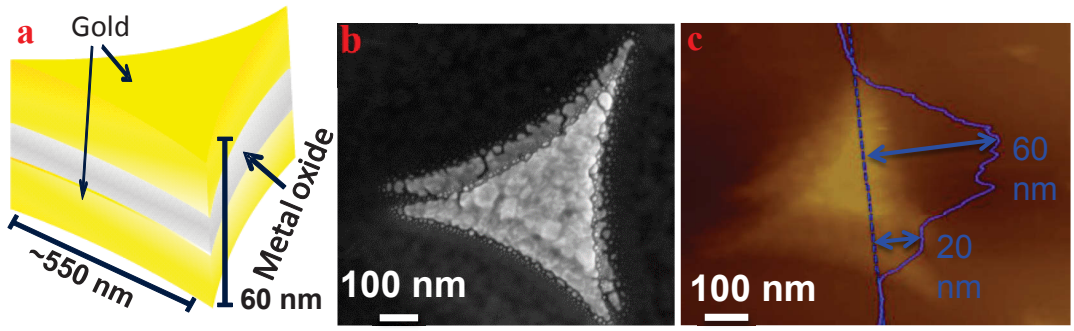

Figure 4-2. (a) Schematic representing the nanostructures produced for charging experiments. (b) Scanning electron micrograph of a nanostructure fabricated by depositing 20 nm of gold / 20 nm of alumina / 20 nm of gold (deposition of top layer of gold was offset in this example by tilting the sample during the last deposition cycle in order to facilitate visualisation of the uppermost gold layer. Image parameters: accelerating voltage, 20 keV, working distance, 1.8 mm. (c) AFM image and section line profile overlay of 20 nm gold / 20 nm hafnia / 20 nm gold nanostructure (structure synthesised with a larger offset of bottom gold layer to aid film thickness measurements).

The geometry of the fabricated nanostructures is shown in Figure 4-2 (a) together with the nanostructure dimensions. (b) shows a scanning electron micrograph of a gold (20 nm) / alumina (20 nm) / gold (20 nm) structure. AR NSL is employed to illustrate the sandwich-type structure (the alumina layer in this image is not visible due to low contrast under the imaging conditions used). AFM measurements (c), revealed that the overall height of the nanostructures is 60 nm (the sum of the three 20 nm thick films). The thickness of the bottom gold triangle was also measured to be 20 nm.

4-2.2 SEM imaging of multi-layer metal / metal oxide / metal nanostructure arrays

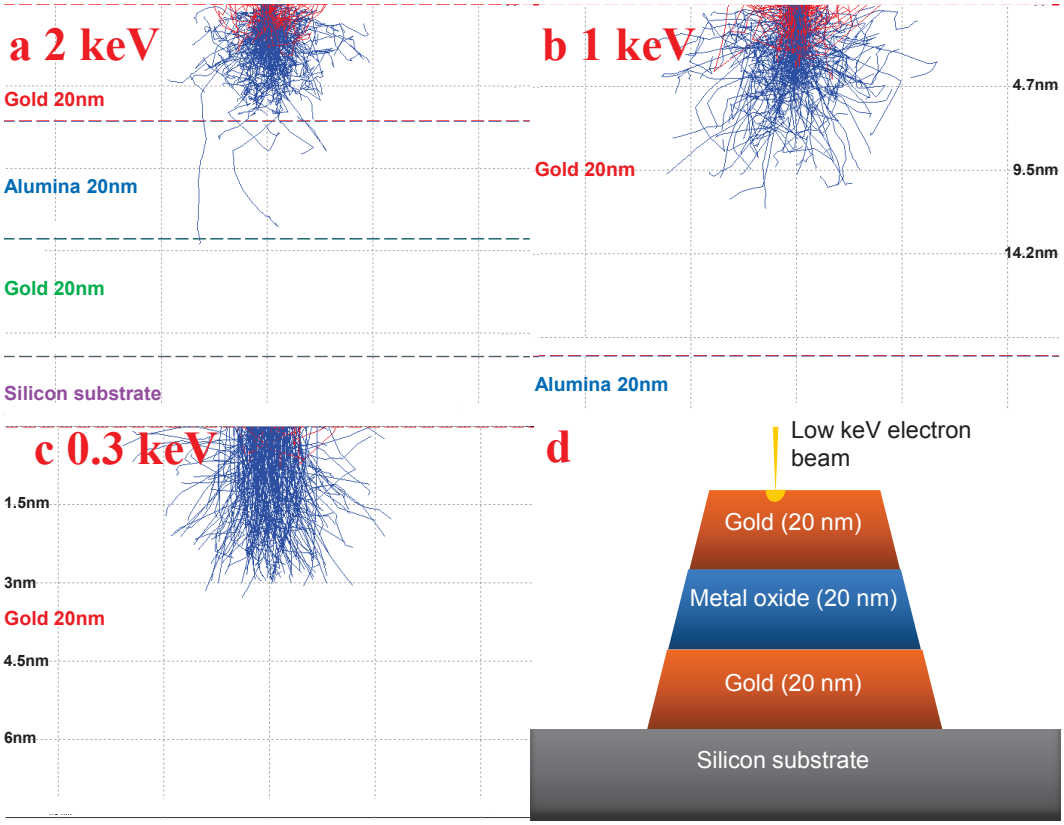

Figure 4-3. Monte Carlo simulation results for an electron beam irradiating a gold (20 nm) / alumina (20 nm) / gold (20 nm) film on a silicon substrate with different accelerating voltages. (a); 2 keV, (b); 1 keV and (c); 0.3 keV. The trajectories of electrons that generate secondary and backscattered electrons are represented by blue and red lines respectively. Horizontal dashed lines represent material interfaces. (d) Schematic representing the interaction of a low accelerating voltage electron beam with fabricated nanoscale devices.

An accelerating voltage of 0.3 keV was used for imaging. This voltage is critical to the experiments described here. Monte Carlo simulations were carried out for the structures investigated in this chapter. If an accelerating voltage of 2 keV is used (Figure 4-3 (a)) the vast majority of the electrons injected into the sample will interact exclusively with the top gold layer. However, it is probable that some electrons will penetrate the top gold layer and interact with metal oxide regions of the structures. Lower accelerating voltages, such as 1 keV or 0.3 keV (Figure 4-3 (b) and (c)) have interaction volumes with the gold film of ~10 nm and ~3 nm, respectively. Imaging with 1 keV enables better discrimination of fine features compared to imaging using

0.3 keV beam energies, however a 0.3 keV beam offers a distinct advantage. At this voltage, the initial induced surface potential should be close to zero because the accelerating voltage is very close to the first critical energy (E_{c1} ≈0.3 keV) of gold [364, 393] and thus changes in contrast (i.e. changes in surface potential) during imaging may be attributed to the charging behavior attributable to the various nanostructures.

Aluminium oxide as dielectric material

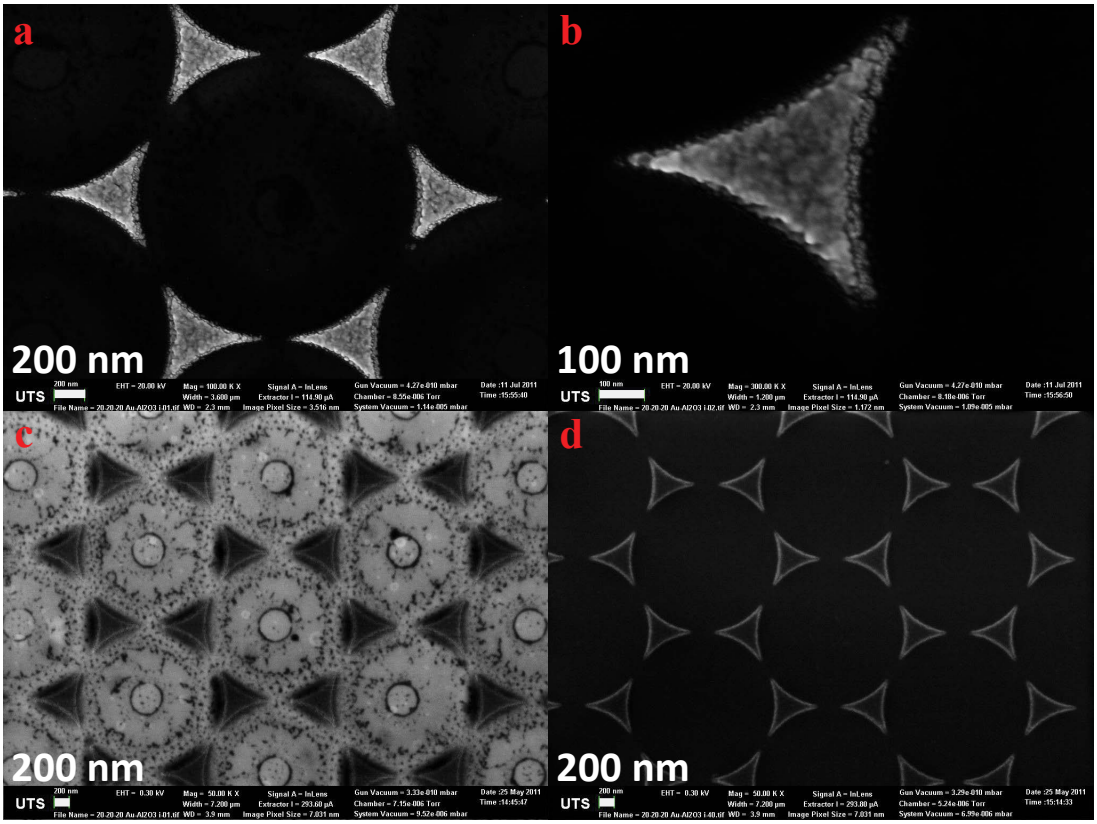

Figure 4-4. SEM micrographs of nanoscale capacitors fabricated utilising NSL. Films consisting of gold (20 nm) / alumina (20 nm) / gold (20 nm) layers were synthesised. (a); image of six discrete structures. (b); image of an individual structure. (c); low accelerating voltage image of an array of structures at the beginning of the charging process. (d); low accelerating voltage image of the same array at the completion of the charging process.

Figure 4-4 Shows SEM images of nanoscale capacitors composed of gold (20 nm) / alumina (20 nm) / gold (20 nm) layers. Panels (a) and (b) show the microstructure of the fabricated devices. The top gold triangle appears to "float" above the bottom triangle. This is a consequence of the deposited alumina layer being invisible under 20 keV imaging conditions. Panel (c) shows the structures imaged under the very low

(0.3 keV) accelerating voltage used for charging experiments. Imaging with a low accelerating voltage reveals the alumina layer. Dark carbon deposits are ubiquitous throughout the sample. These deposits are seen to adhere differently to the silicon surface compared to the alumina film. Small, isolated deposits are visible on the low surface energy alumina film (this may have occurred when the DCM solvent evaporated after the rinsing process). The top gold triangles are observed to be relatively dark with a bright region visible around the edges of the structure. The silicon substrate is relatively bright, indicating a high secondary electron signal relative to the gold triangular structure. This is unusual for SEM, where gold has a higher secondary electron yield relative to silicon [394] and normally appears brighter during imaging. Very dark regions are also visible on the alumina film in close proximity to the edges of the top gold triangle. The structures in (d) are the same array as in (c) but have undergone charging via repeated imaging at the 0.3 keV accelerating voltage. The most striking change from this charging process is that the substrate has undergone a contrast inversion and is now darker than the top gold layer, which has increased in brightness and now has a more pronounced edge effect. The alumina layer and carbon deposits are no longer visible. The results of an experiment to continually image an array of discrete nanostructures over an extended period of time is shown in Figure 4-5.

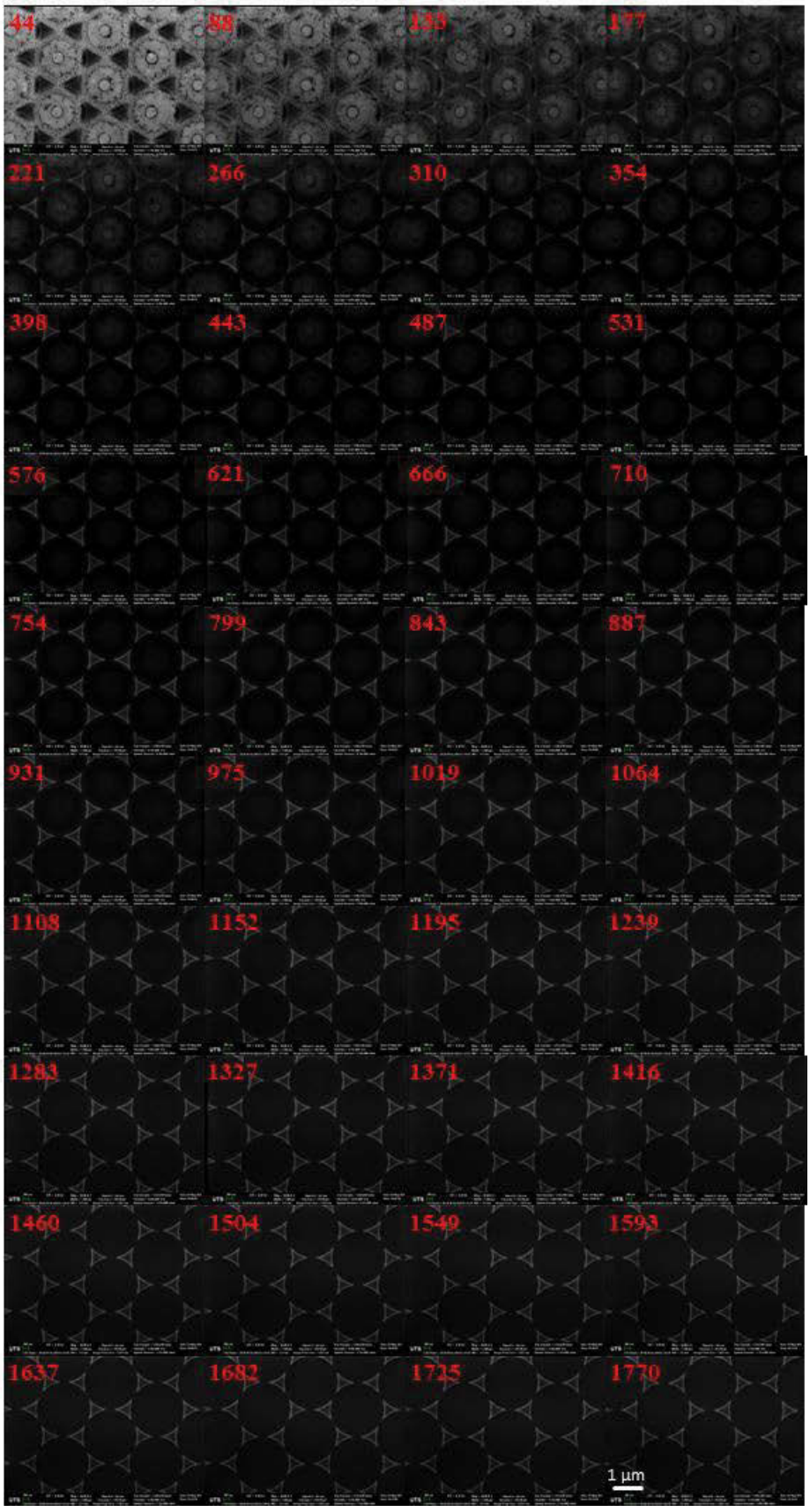

Figure 4-5. SEM micrographs of a gold (20 nm) / alumina (20 nm) / gold (20 nm) nanosandwich array collected under a 0.3 keV accelerating voltage. Time data overlayed on the images is in s.

Figure 4-5 shows an example of a series of SEM images that have been acquired sequentially of the same area of an array of gold (20 nm) / alumina (20 nm) / gold (20 nm) nanostructures. As discussed above, secondary electrons are generated only in the topmost layer of the tri-layered structure using an accelerating voltage of 0.3 keV and at this voltage the initial induced surface potential should be close to zero. However, as electrons flow into the electrically floating top gold electrode, the surface potential becomes negative as the capacitor charges. Figure 4-5 reveals that the initially dark triangular nanostructures increase in brightness upon continuous imaging due to an accumulation of electrons in the topmost gold layer.

Over the same period, the silicon substrate darkens. The mechanism of darkening on the silicon involves a build-up of positive charge on the silicon surface, which has the effect of retarding the escape of secondary electrons [364]. The positive charge arises due to the need to balance the floating negative charge on the uppermost gold electrode. The very dark region adjacent to the top gold triangular layer becomes less visible with the progression of time.

The evolution of mean grey-scale intensity for each nanocapacitor was measured as well as that of their silicon substrates to quantify the dynamics of the charging process. The grey-scale intensity correlates with charging whereby higher intensity values (equating to brighter regions) indicate greater negative surface charge densities.

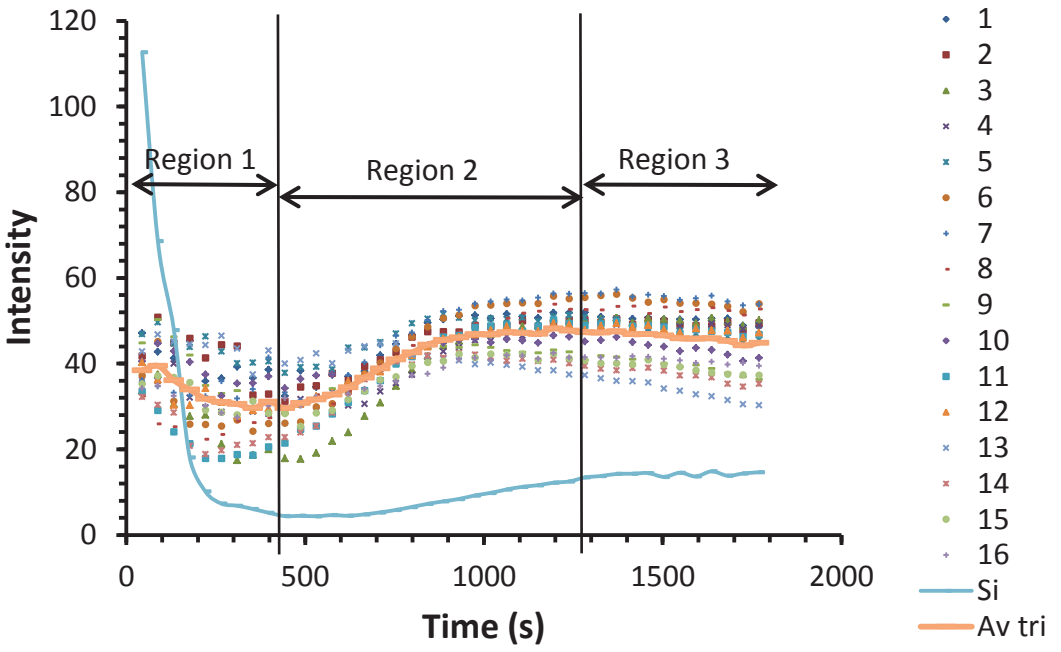

Figure 4-6. Plot of grey-scale intensity *vs.* time, for the charging of sixteen gold (20 nm) / alumina (20 nm) / gold (20 nm) nanosandwiches. Average grey-scale intensity of silicon substrate and an average value for the top gold triangular structures (blue and orange traces respectively) are also presented.

Figure 4-6 shows a plot of the mean grey-scale intensity *vs.* imaging time for each of the triangular gold (20 nm) / alumina (20 nm) / gold (20 nm) nanostructures shown in Figure 4-5 together with that of the nearby silicon substrate. These data provide insight into the charging profiles for individual devices. The mean intensities vary somewhat for individual structures, which reflects the effect of small changes in structure geometries that can be attributed to inter-sphere void size differences in the masking phase of fabrication. The structures undergo three relatively distinct brightness changes during continuous imaging. Between 0 and ~ 450 s, Region 1, the intensity varies somewhat erratically for each structure but in general rises briefly in the first few images, then diminishes somewhat. Between ~ 450 and 1200 s, Region 2, the intensity increases with an initially high, but slowing rate. After 1200 s, Region 3, the intensity remains relatively constant although for some structures it decreases marginally with time. It should be pointed out that this data provides much more information on the charging process than was achievable with the smaller nanocapacitors synthesised previously at UTS [19].

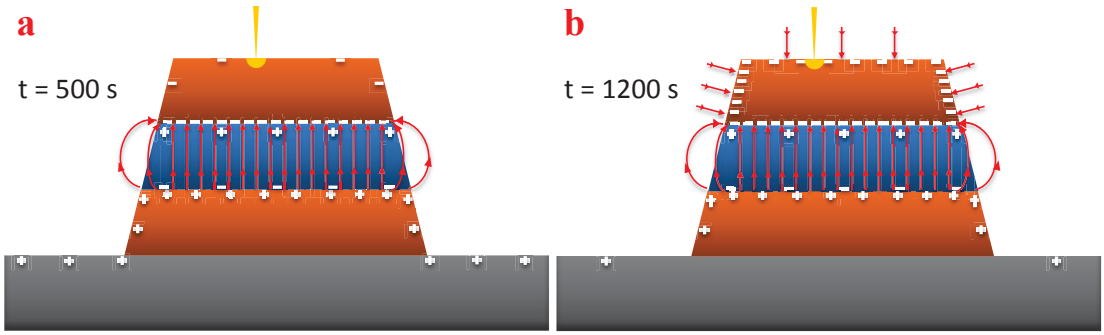

Figure 4-7. Schematic representation of the charge configuration of an individual gold (20 nm) / alumina (20 nm) / gold (20 nm) nanostructure at *t* ~ 500 s (a) and ~ 1200 s (b). Surface charges are displayed in white, electric field lines in red and electrons injected into the sample by the focused electron beam in yellow.

It can be seen from the schematic representation in Figure 4-7 that the gold / dielectric interface is not directly probed in these experiments, but rather only the uppermost few nanometers of the various surfaces. Therefore, in Region 1 the triangles darken due to the applied potential of the electron beam resulting in a charge build-up at the gold / dielectric interface, attracted there by a need to compensate the growing positive charge in the substrate. This results in fewer electrons at the surface of the triangles (Figure 4-7 (a)). The polarisation of the dielectric also results in the observed darkening on the metal oxide film close to the top gold triangle. This decreases as a function of time as the dielectrics rate of polarisation decreases and the continued irradiation by the electron beam results in a build-up of surface charge. In Region 2, brightening of the electrically isolated metallic parts is associated with an increase in negative potential of the surface of the gold top electrode. This we associate with a saturated dielectric and thus an increasing electron density at the surface as more electrons are injected from the beam. From ~ 1200 seconds onwards, Region 3, the devices are fully charged throughout and little further change occurs (i.e. a steady state of electron flux in and out of the uppermost triangle). It is noteworthy that the behaviour seen in Region 1 was not observed in previous research [19]. It is reasoned that the dielectric of the significantly smaller devices (synthesised via NSL with 200 nm PS spheres and a 5 nm thick alumina layer) is saturated rather quickly and only charge accumulation on the uppermost region of the top gold electrode is observed. The smaller sizes of the devices also made features such as the brighter edges during imaging harder to discern.

For the purpose of determining the charging rates of the capacitors, changes in the brightness of the gold surfaces do not provide a direct probe of charging at the gold / metal oxide interface since there is a latency period before the charge on the upper surface starts to become appreciably negative (in any case, this change in surface potential occurs when the dielectric approaches a saturated polarisation). However, the change in brightness of the silicon surface provides immediate information about the charging of the interface without the complications associated with the gold surface. Thus, the change in the grey-scale intensity of the silicon surfaces for each of the device arrays during the charging phase (Region 1) was used to measure the time constants of the devices. The charging of a capacitor obeys a first-order rate law and can be modeled by the equation:

$$V(t) = V_{max}\left(1 - e^{\frac{t}{\tau}}\right)$$

Where the time constant (τ) represents the time for a device to charge / discharge to 63.2% of the difference between its initial and final values, voltage $V(t)$=0 at t=0, $V(t)$=V_{max} at very long times, and

$$\tau = RC$$

Where R is the resistance and C is the capacitance of the device. Experimental time constants were extracted from plots of greyscale intensities of the silicon substrates *vs*. time (t) fitted using

$$I(t) = I_{\infty} + Ae^{\frac{-t}{RC}}$$

Where $I(t)$ is the greyscale intensity at time t, I_{∞} is the minimum greyscale intensity in Region 1.

Fitting of the silicon data for the curve in Figure 4-6 gave an experimental time constant of 70 ± 8 s. This data is collated with the results from other metal oxides in Table 4-2.

Spatial effects

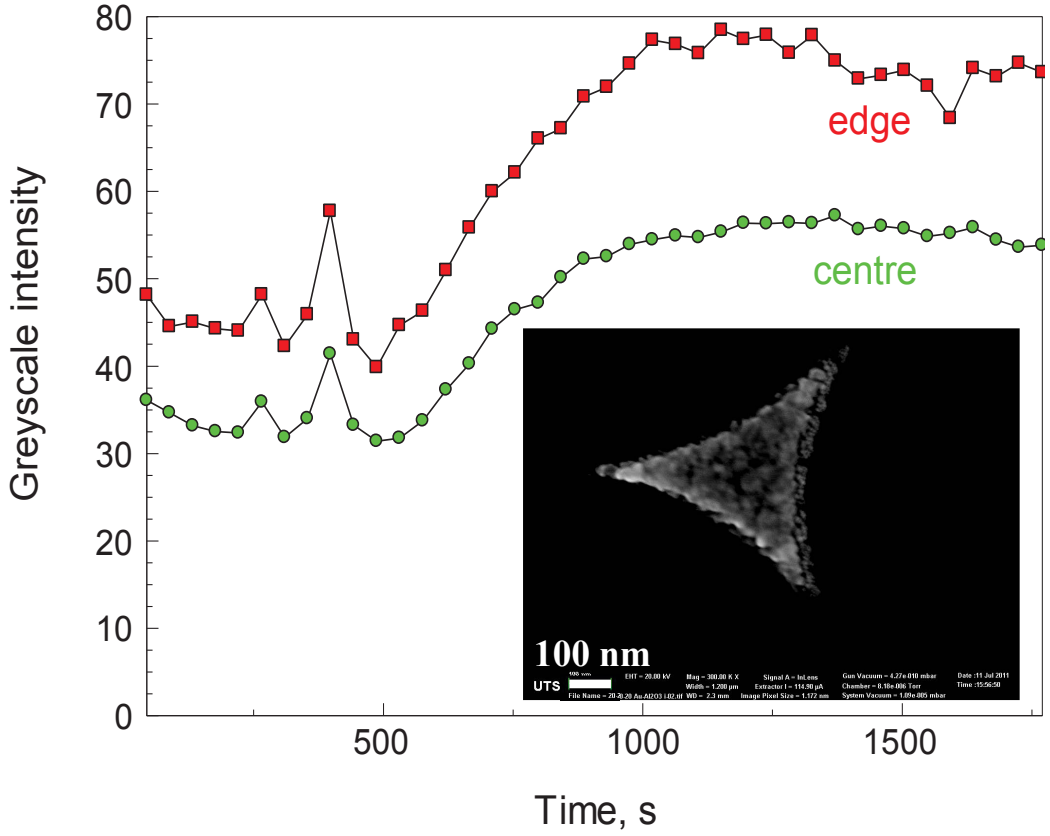

Figure 4-8. Graphs of mean grey-scale intensities *vs.* time for edge (red) and middle (blue) regions of the top gold layer of a single gold (20 nm) / alumina (20 nm) / gold (20 nm) structure ('Triangle #7').

Throughout the charging experiments, SEM images of the edges of the individual nanostructures were significantly brighter than the central regions and, although both regions exhibited a brightness increase in the 500-1200 s period, the centers showed significantly less change and were less bright overall (Figure 4-8). The edge effect is well known in scanning electron microscopy where a reduced escape distance results in a greater number of secondary electrons reaching the detector. However, this effect should only be visible at displacements of less than 3 nm from the edge (within the beam's interaction volume). Interestingly, analysis of Figure 4-4 (d) and other SEM images show that the edge is significantly brighter for displacements of up to ~ 20 nm. This is a likely consequence of the electron distribution which is constrained to the gold surface (to prevent any electric field inside to gold material) being highest in regions with the greatest area of curvature (Gauss's law).

Carbon contamination

A significant risk in these charging experiments is the potential of organic material in the vapour state to be reduced by the electron beam and deposited on any areas imaged. The presence of organic material in these samples is undesirable, however is unlikely to contribute to beam damage because the accelerating voltages typically used in SEM (generally up to 30 keV) are insufficient to displace materials such as PS into the vacuum chamber [395]. Very low accelerating voltages (such as the 0.3 keV beam energy used in the charging experiments described in this chapter) do not pose a risk of inducing this phenomenon. Other potential sources of volatilised organic material are DCM used in NSL mask removal and the organic solvents present in the silver epoxy used to make an electrical connection between the silicon substrate and the SEM stub. DCM is used so prevalently in NSL mask removal because of its ability to solute PS, as well as its low boiling point (39.8^{o}C at standard pressure [396]) making the removal of the solvent very facile. To minimise the potential of both DCM and silver epoxy contributing to SEM carbon contamination, samples were dried in a desiccator for an hour after SEM preparation (i.e. silver epoxy application), prior to SEM experiments.

Samples were also imaged in a scanning electron microscope (Zeiss Supra 55VP) utilising an oil-less scroll pump and regularly plasma cleaned to further minimise the risk of carbon contamination.

Silicon dioxide as dielectric material

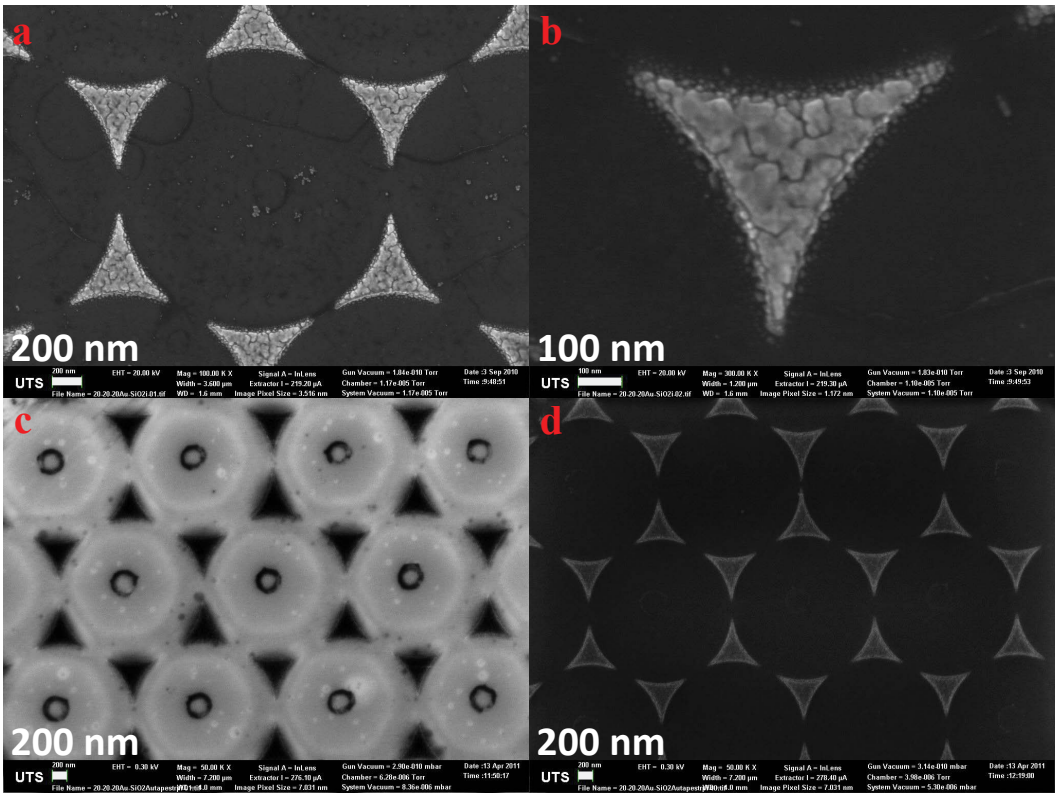

Figure 4-9. SEM micrographs of nanoscale capacitors fabricated utilising NSL. Films consisting of gold (20 nm) / silica (20 nm) / gold (20 nm) layers were synthesised. (a); image of six discrete structures. (b); image of an individual structure. Low accelerating voltage images of an array of structures at the beginning (c) and completion (d) of the charging process.

Figure 4-9 shows SEM images of nanoscale capacitors with gold (20 nm) / silica (20 nm) / gold (20 nm) layers. Panels (a) and (b) show the microstructure of the fabricated devices. The microstructure is very similar to that produced with alumina dielectrics. Again, the top gold triangle "floats" above the bottom triangle. Small isolated gold islands are visible around the edges of the gold triangles. It is unclear from these images whether the islands are beside the top, bottom or both gold layers. The low accelerating voltage in (c) allows the faint visualisation of the silica layer. Carbon deposits are clearly visible on the sample. The top gold triangles are very dark (more so than was observed with the alumina devices) with no visible edge effect. The silicon substrate is bright and actually appears brighter than the surface in the alumina dielectric experiments due to the low carbon contamination in this sample. Very dark regions close to the edges of the top gold triangle are visible. The structures in (d) are almost identical to those observed in Figure 4-4 (d). The only difference being a slightly less pronounced edge effect in the silica dielectric samples.

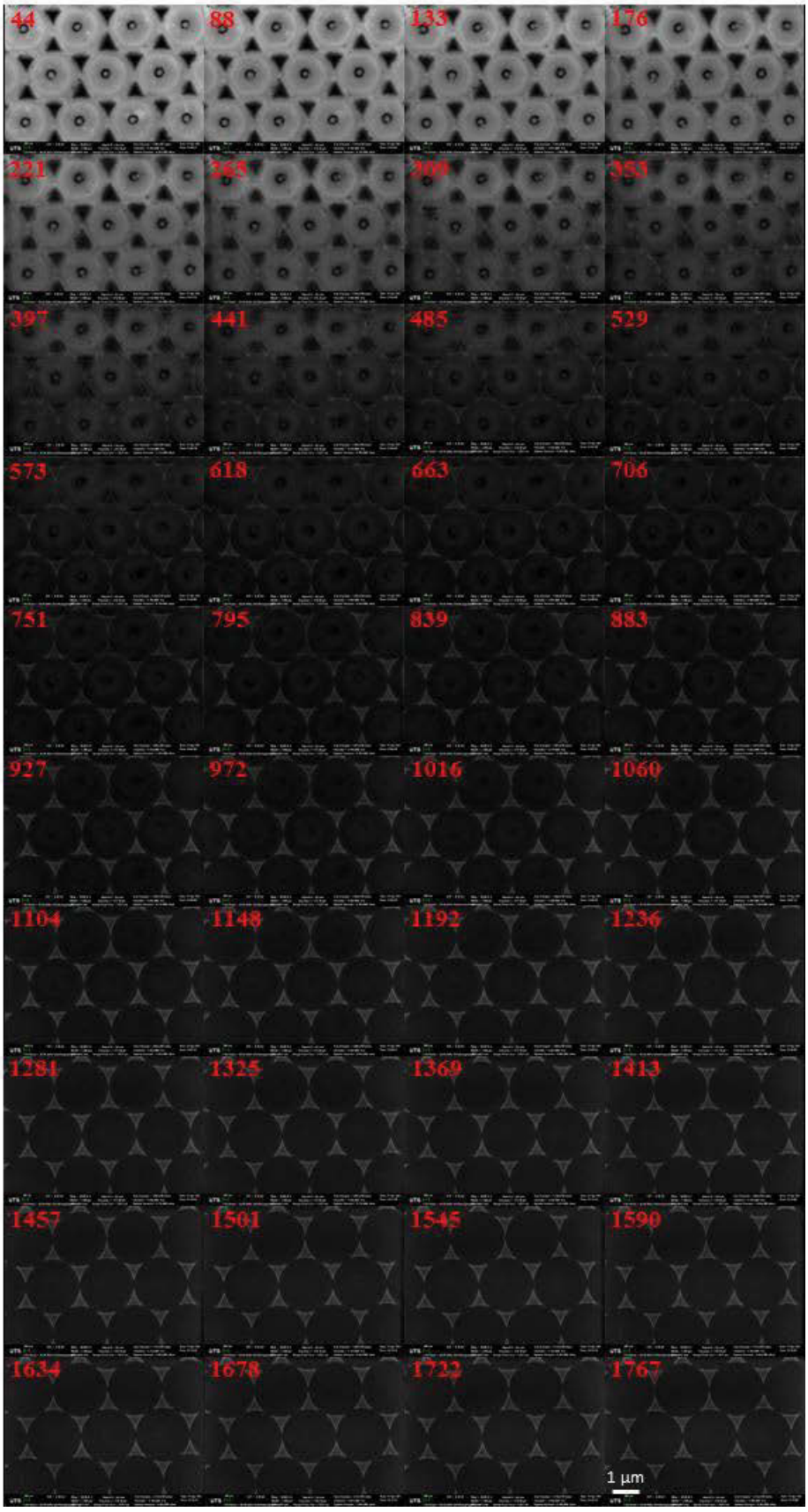

Figure 4-10. SEM micrographs of a gold (20 nm) / silica (20 nm) / gold (20 nm) nanosandwich array collected under a 0.3 keV accelerating voltage. Time data overlayed on the images is in s.

Figure 4-10 shows a series of SEM images for gold (20 nm) / silica (20 nm) / gold (20 nm) nanostructures. As with the alumina structures, the initially dark triangular top layers increase in brightness upon continuous imaging. The same silicon darkening effect is observed with an initially rapid decrease in brightness before stabilisation.

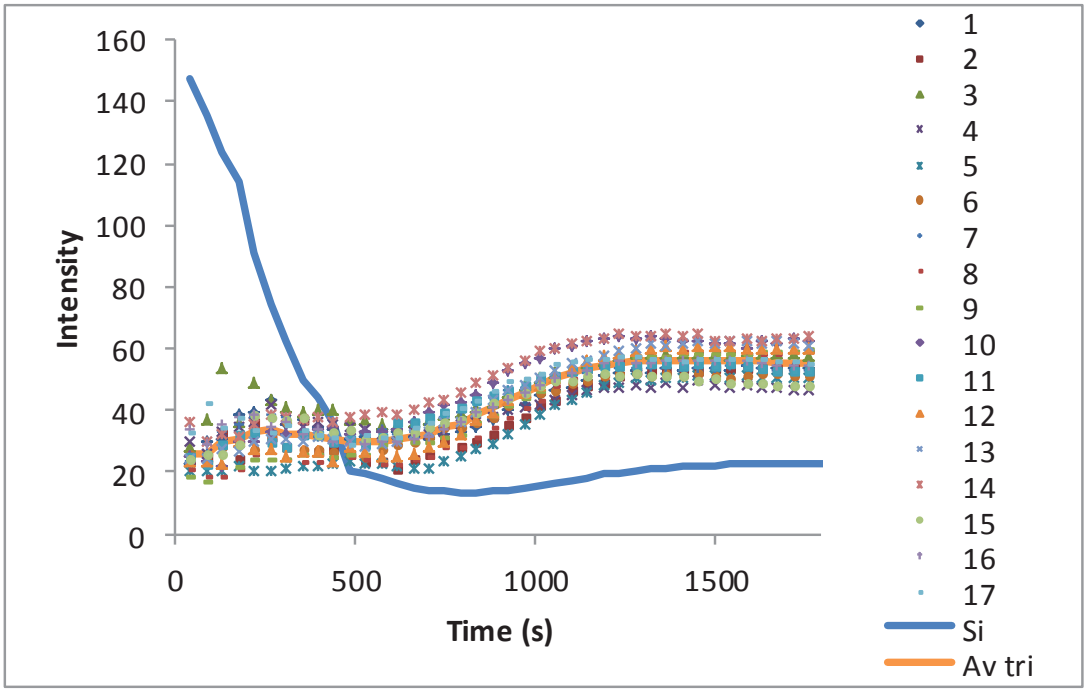

Figure 4-11. Plot of grey-scale intensity *vs.* time, for the charging of seventeen gold (20 nm) / silica (20 nm) gold (20 nm) nanosandwiches. Average grey-scale intensity of silicon substrate and an average value for the top gold triangular structures (blue and orange traces respectively) are also presented.

Figure 4-11 shows a graph of the mean greyscale intensity *vs.* imaging time for each of the triangular gold (20 nm) / silica (20 nm) / gold (20 nm) nanostructures shown in Figure 4-10 together with that of the nearby silicon substrate. The structures undergo similar changes to those observed for the alumina dielectric samples with Region 1 slightly longer, now between 0 and ~ 550 s, with the initial slight increase observed in Figure 4-6 occurring in this experiment over a longer time. This is consistent with a longer time constant, which may be expected from the higher resistivity of silica compared to alumina. Region 2, now between ~ 550 and 1300 s, increases in intensity at a similar rate to the devices with an alumina dielectric. In Region 3, the intensity of the triangles demonstrates less divergence relative to the

alumina structures. This divergence is likely to be a result of some structures leaking charge after extended periods of beam irradiation.

Fitting the silicon grey-scale data obtained from Figure 4-11 to the time constant expression gave an experimental time constant of 248 ± 27 s.

Zinc oxide as dielectric material

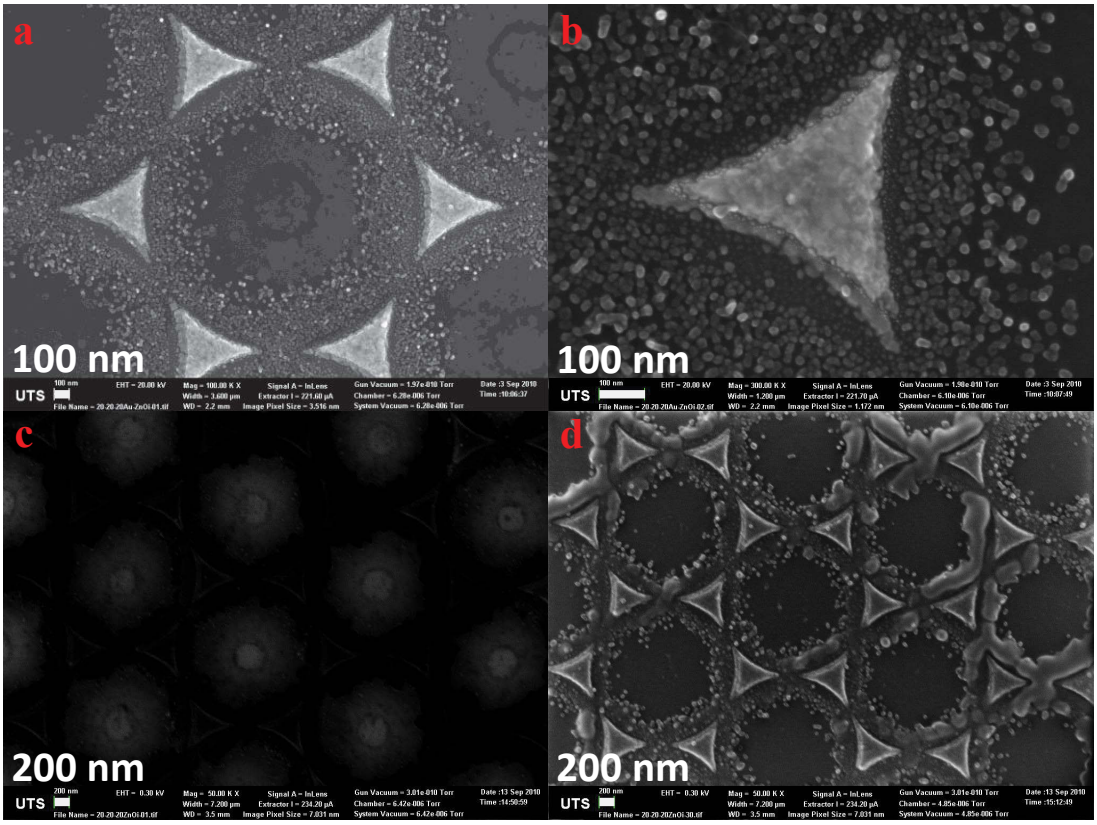

Figure 4-12. SEM micrographs of nanoscale capacitors fabricated utilising NSL. Films consisting of gold (20 nm) / zinc oxide (20 nm) / gold (20 nm) layers were synthesised. (a); image of six discrete structures. (b); image of an individual structure. (c); low accelerating voltage image of an array of structures at the beginning of the charging process. (d); low accelerating voltage image of the same array at the completion of the charging process.

Figure 4-12 shows SEM images of nanoscale capacitors with gold (20 nm) / zinc oxide (20 nm) / gold (20 nm) layers. Panels (a) and (b) show the microstructure of the fabricated devices. Structures synthesised with a zinc oxide dielectric appear strikingly different to those observed for both alumina and silica. Large amounts of nanoparticulate material are visible surrounding the gold layers. This phenomenon is investigated in detail in Chapter 5 and is found to be zinc oxide re-emitted during the RF sputter deposition process. Zinc oxide particles lie around (but not touching) the

gold layers with particle size increasing with increasing distance from the gold. While the zinc oxide deposits are significantly different to silica and alumina deposits, the gold layers appear very similar to those observed with alumina and silica dielectrics. The top gold triangle “floats” and some islands of material are apparent around the edges of the gold triangles. From panel (b) it is unclear whether the islands are gold or deposited zinc oxide. Panel (c) is also quite different to corresponding images in Figures 4-4 and 4-9 (c). The image is significantly darker with regions of nanoparticulate zinc oxide the darkest in the image. Similar to alumina and silica however, the silicon substrate is brighter than the top gold layer. The gold triangles also demonstrate an edge effect. Panel (d) reveals significant carbon deposits on this zinc oxide sample. These deposits are seen to concentrate on the high surface area and relatively high surface energy [397] zinc oxide.

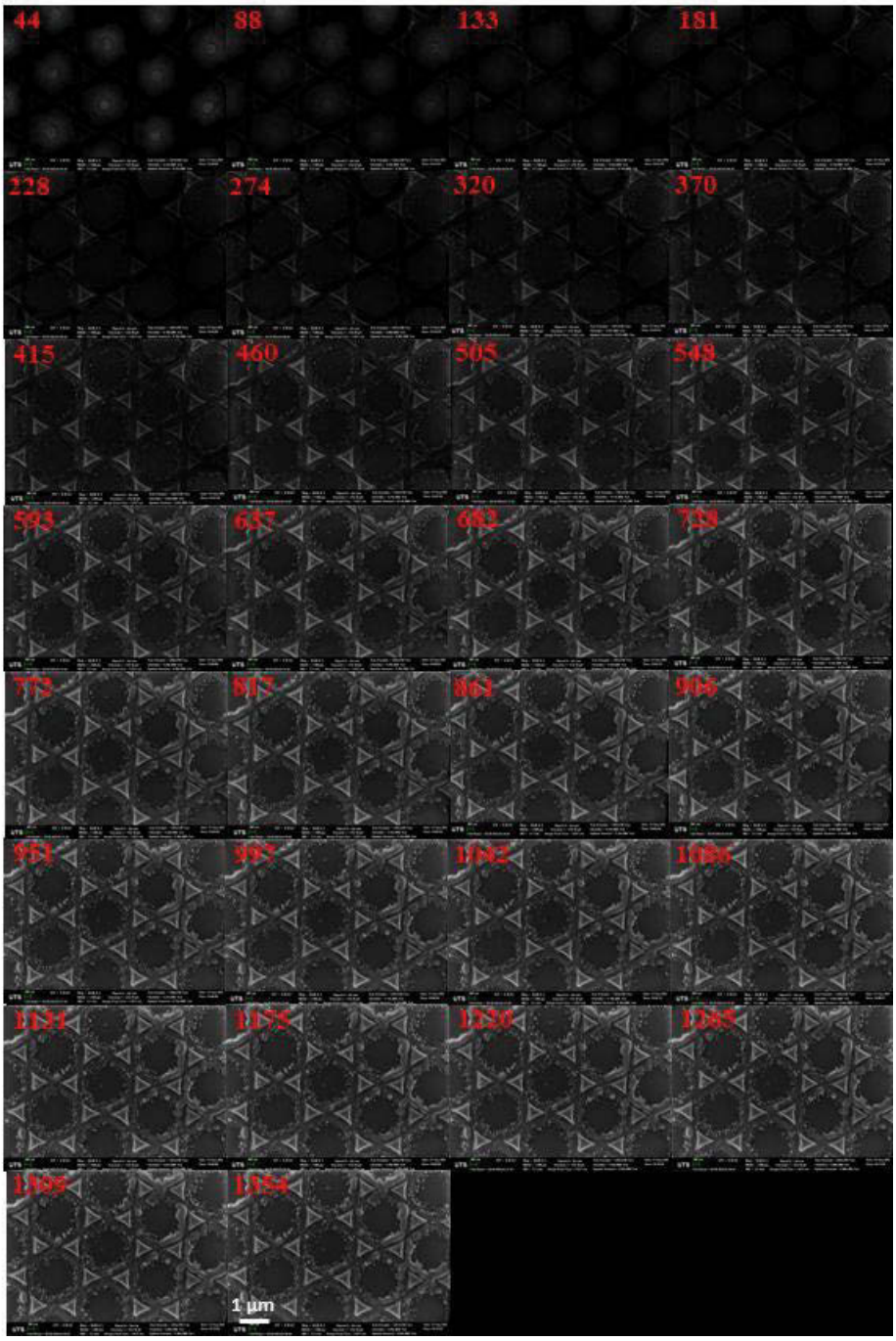

Figure 4-13. SEM micrographs of a gold (20 nm) / zinc oxide (20 nm) / gold (20 nm) nanosandwich array collected under a 0.3 keV accelerating voltage. Time data overlayed on the images is in s.

Figure 4-13 shows the SEM time series for gold (20 nm) / zinc oxide (20 nm) / gold (20 nm) nanostructures. The initially dark triangular top layers increase in brightness upon continuous imaging. The silicon darkening effect is observed with an initially rapid decrease in brightness before stabilisation, similar to the other metal oxide-containing devices. The differences in contrast are however, not as significant

as was observed for alumina and silica dielectrics. At the completion of the charging process, the silicon substrate is much brighter than with previous results.

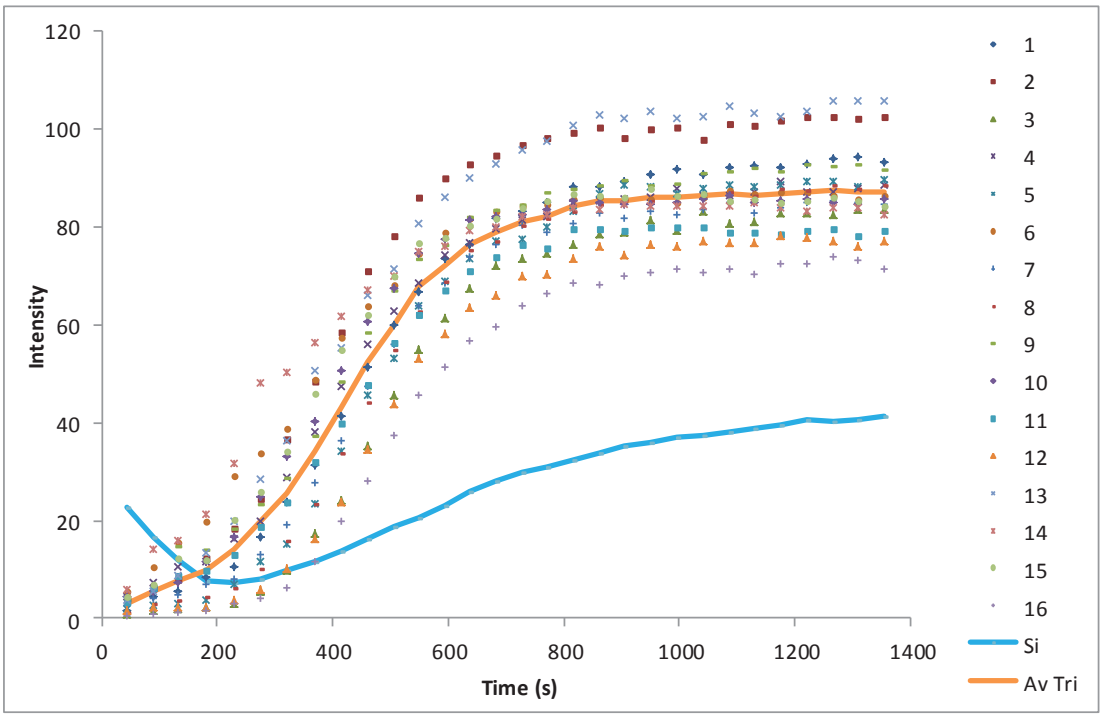

Figure 4-14. Plot of grey-scale intensity *vs.* time for the charging of sixteen gold (20 nm) / zinc oxide (20 nm) gold (20 nm) nanosandwiches. Average grey-scale intensity of silicon substrate and an average value for the top gold triangular structures (blue and orange traces respectively) are also included.

Figure 4-14 shows a graph of the mean greyscale intensity *vs.* imaging time for each of the triangular gold (20 nm) / zinc oxide (20 nm) / gold (20 nm) nanostructures shown in Figure 4-13 together with that of the nearby silicon substrate. The structures undergo very much shorter transitions between regions than observed for the structures containing alumina and silica dielectrics. Region 1 now occurs either before or at the first image, i.e. < 44 s, indicating a fast dielectric saturation. The initial intensity values of the silicon substrate are significantly lower than those observed in structures containing alumina or silica dielectrics. Region 2, between ~44 and ~1000 s, and Region 3 (> 1000 s) behave in a similar manner to alumina and silica as expected for charge accumulation on the topmost region of the upper gold electrode and the achievement of a steady state charge transfer. The change in intensity for the top gold electrode is more pronounced than observed in the structures where silica and alumina were the dielectric materials. Little divergence is observed in Region 3.

The experimental time constant obtained by fitting the silicon greyscale data from Figure 4-14 is 56 ± 30 s.

Titanium dioxide as dielectric material

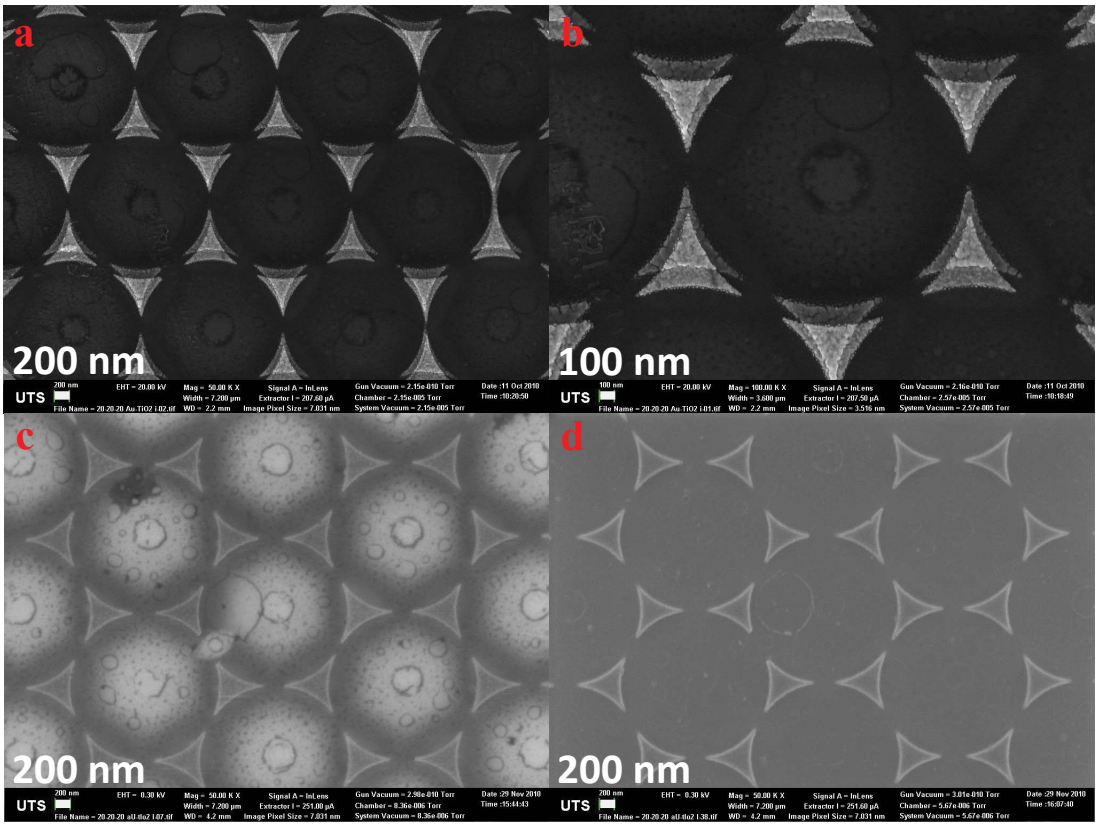

Figure 4-15. SEM micrographs of nanoscale capacitors fabricated utilising NSL. Films consisting of gold (20 nm) / titania (20 nm) / gold (20 nm) layers were synthesised. (a); image of twenty discrete structures. (b); image of five discrete structures. (c); low accelerating voltage image of an array of structures at the beginning of the charging process. (d); low accelerating voltage image of the same array at the completion of the charging process.

SEM images of nanoscale capacitors with gold (20 nm) / titania (20 nm) / gold (20 nm) layers are shown in Figure 4-15. These structures clearly have a misalignment of the top and bottom gold electrode and were not used for charging experiments (panels (a) and (b)). This misalignment is a result of the gold being deposited with the substrate orientations relative to the deposition source being changed inadvertently during the fabrication of the bottom and top gold layers. They are included here for an analysis of microstructure only. The microstructure is similar to those produced with alumina and silica dielectrics with an absence of the nanoparticulate material that was observed with zinc oxide samples. Gold islands are not seen at the magnification

presented in these images. Panel (c) reveals extensive carbon deposits and shows that the titania layer have a similar morphology to alumina and silica. The top gold triangles are much brighter than those observed for any of the previous dielectrics with a visible edge effect. The silicon substrate is not as bright as was observed with alumina and silica, however is brighter than the results for zinc oxide. The very dark regions close to the edges of the top gold triangle observed with alumina and silica but undeterminable in zinc oxide are not present. The structures in (d) are almost identical to those observed in (c), little change is observed on the top gold electrode upon extended imaging. The silicon substrate is observed to darken, less than observed with alumina and silica, however more than zinc oxide.

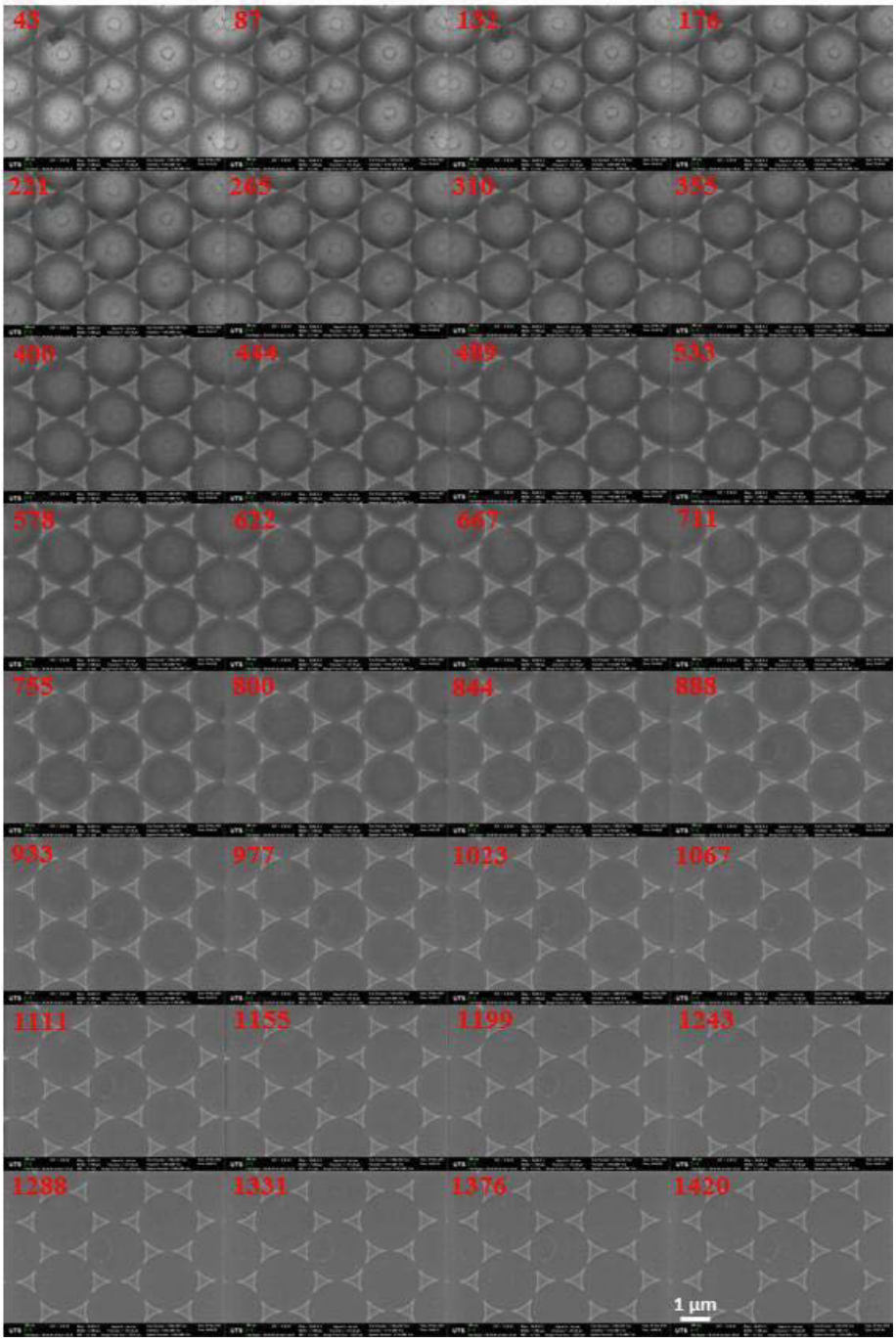

Figure 4-16. SEM micrographs of a gold (20 nm) / titania (20 nm) / gold (20 nm) nanosandwich array collected under a 0.3 keV accelerating voltage. Time data overlayed on the images is in s.

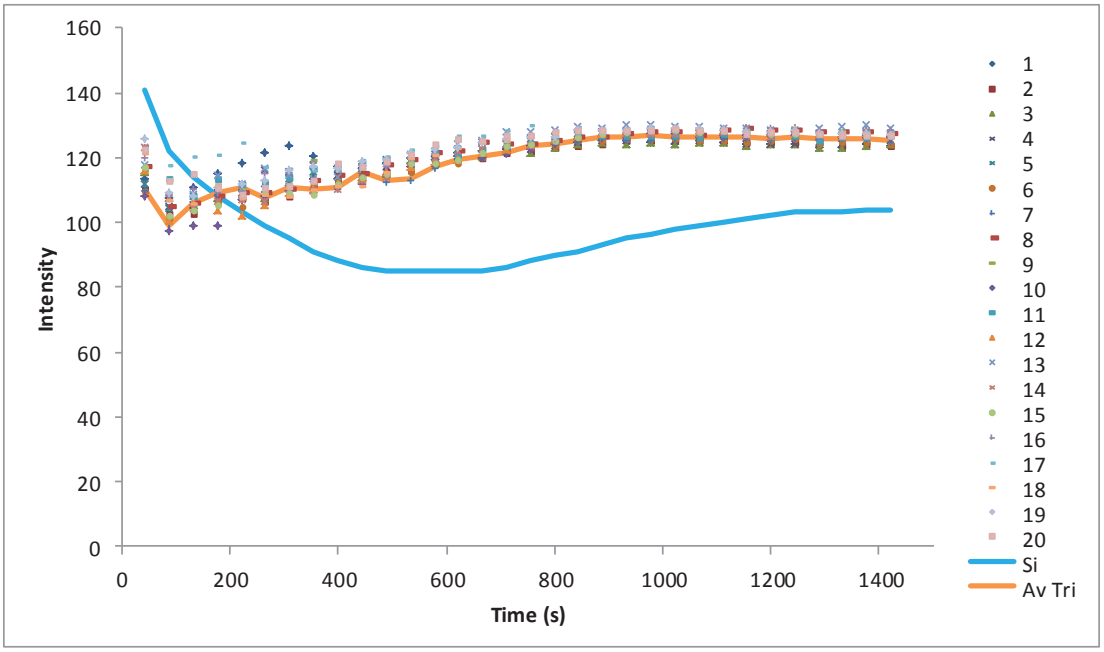

Figure 4-17. Plot of grey-scale intensity *vs.* time for the charging of twenty gold (20 nm) / titania (20 nm) / gold (20 nm) nanosandwiches. Average grey-scale intensity of silicon substrate and an average value for the top gold triangular structures (blue and orange traces respectively) are also presented.

Figure 4-17 shows a graph of the mean grey-scale intensity *vs.* imaging time for each of the triangular gold (20 nm) / titania (20 nm) / gold (20 nm) nanostructures shown in Figure 4-16 together with that of the nearby silicon substrate. Similar to the zinc oxide-containing examples, the structures undergo shorter transitions between regions than observed for the alumina and silica dielectrics. Region 1 now occurs between 0 ~ 100 s, indicative of a fast dielectric saturation. The initial intensity value of the silicon substrate is comparable to results obtained for alumina and silica dielectrics. The titania-containing devices exhibits significantly lower changes in contrast between Region 2 (~100 - 800 s) and Region 3 (>800 s) relative to alumina, silica and zinc oxide. Little divergence is observed in Region 3. In contrast, the intensity values for titania dielectric nanocapacitors are observed to converge slightly.

Fitting the silicon data in Figure 4-17 to the same expression as for alumina, silica and zinc oxide gave an experimental time constant of 168 ± 79 s. The relatively large margin for error is a consequence of the shorter region 1 providing less data points for curve fitting.

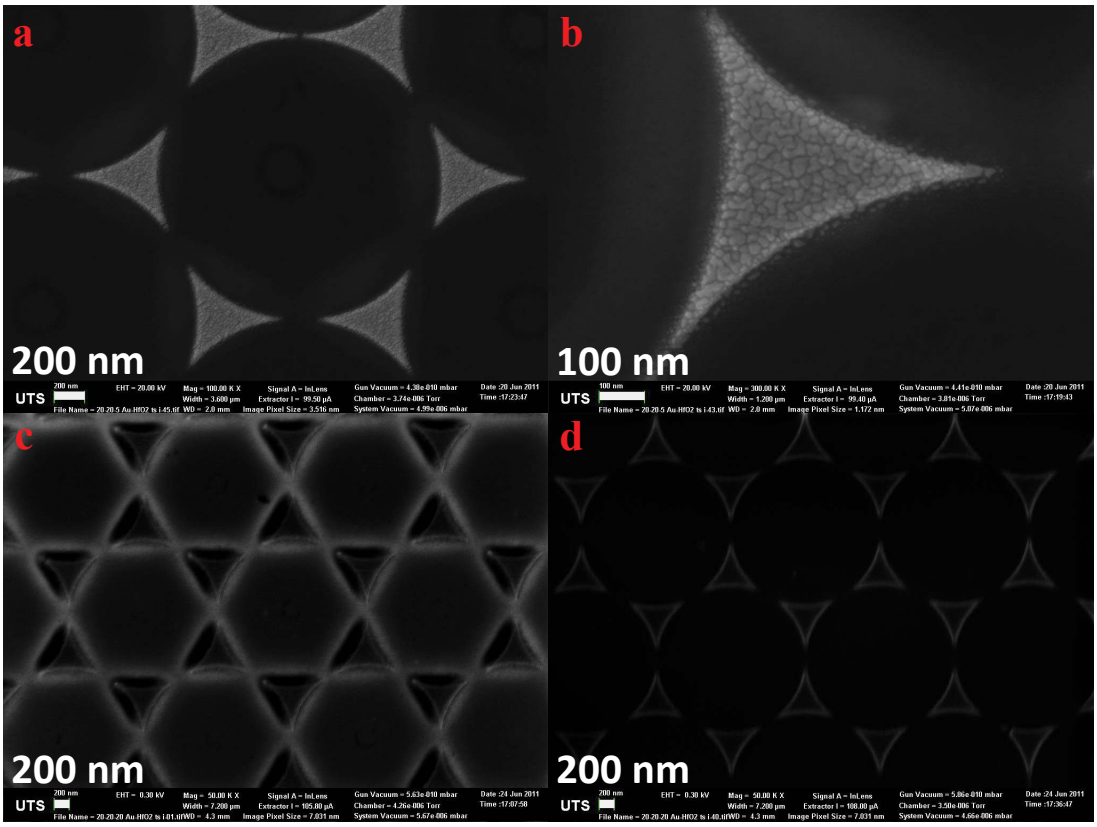

Figure 4-18. SEM micrographs of nanoscale capacitors fabricated utilising NSL. Films consisting of gold (20 nm) / hafnia (20 nm) / gold (20 nm) layers were synthesised. (a); image of six discrete structures. (b); image of an individual structure. (c); low accelerating voltage image of an array of structures at the beginning of the charging process. (d); low accelerating voltage image of the same array at the completion of the charging process.

SEM images of nanoscale capacitors with gold (20 nm) / hafnia (20 nm) / gold (20 nm) layers are shown in Figure 4-18. Deposited hafnia can be seen faintly in panels (a) and (b). It is evident that it is not directly aligned with the gold triangular structures, however the larger x-y dimensions of the RF sputter deposited hafnia means that the gold structures remain isolated from each other. The microstructure is otherwise very similar to those produced with alumina, silica and titania dielectrics with an absence of the nanoparticulate material that was observed with zinc oxide samples. Small isolated gold islands surrounding the top or bottom gold triangles in (b) are clearly visible. Panel (c) reveals small amounts of carbon deposits. The top gold layers are dark at the beginning of the charging process, though not as dark as was observed for alumina, silica or zinc oxide and exhibit a moderate edge effect. The silicon substrate is not as bright as was observed with alumina and silica, however is

brighter than the results for zinc oxide. The very dark regions close to the edges of the top gold triangle that give an indication to the dielectrics polarisability are strongly present, more so than with any dielectric studied previously. The structures in (d) are also darker than those in all other dielectrics with a moderate edge effect. The silicon substrate is observed to be darker than with all other observed materials.

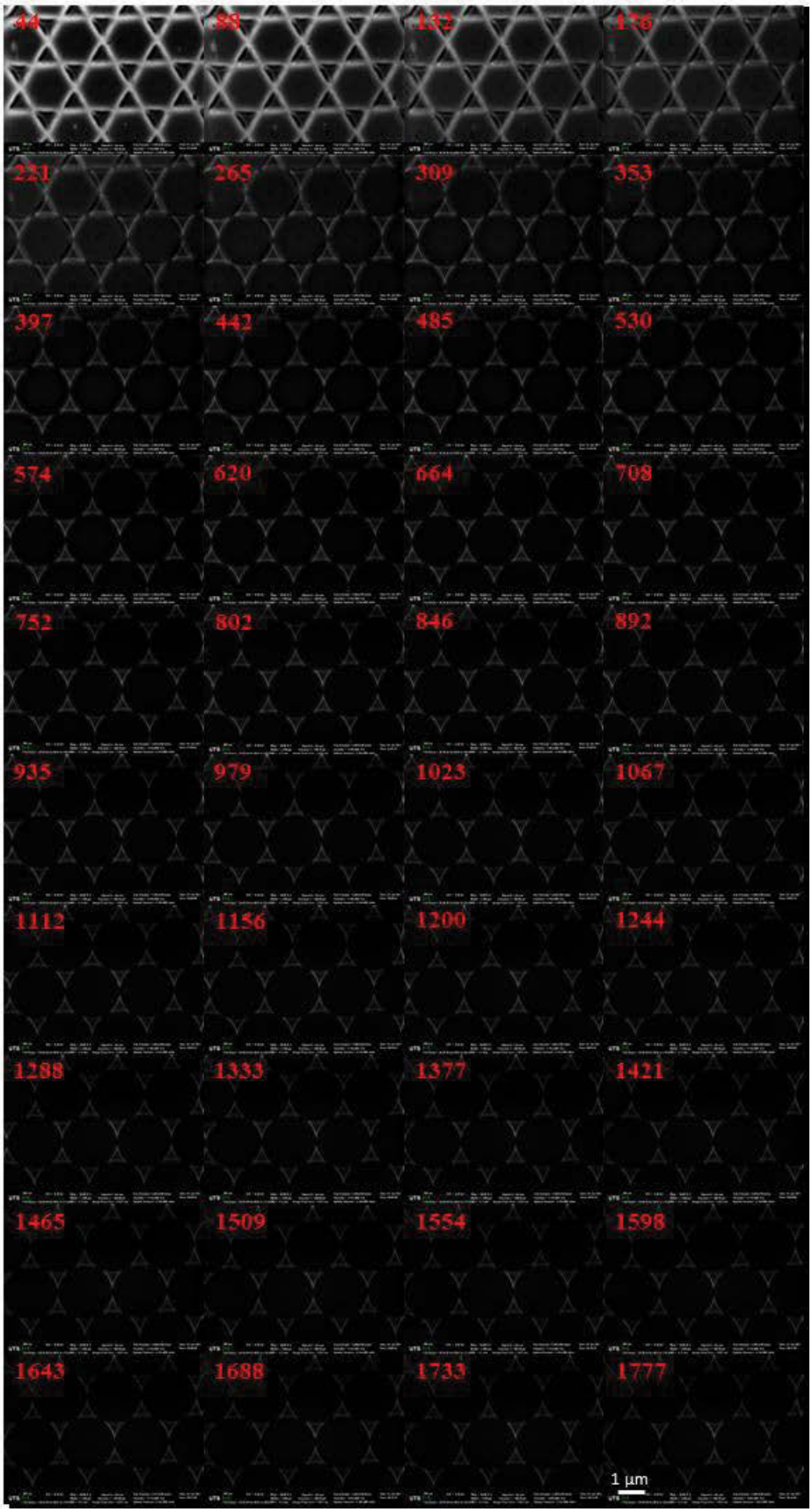

Figure 4-19. SEM micrographs of a gold (20 nm) / hafnia (20 nm) / gold (20 nm) nanosandwich array collected under a 0.3 keV accelerating voltage. Time data overlayed on the images is in s.

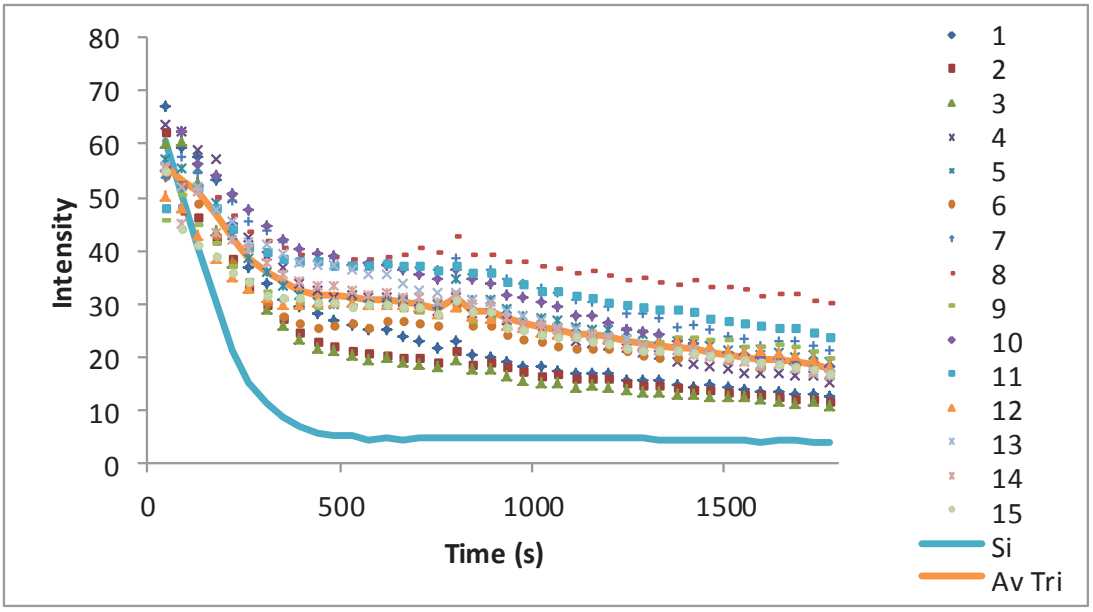

Figure 4-20. Plot of grey-scale intensity *vs.* time for the charging of fifteen gold (20 nm) / hafnia (20 nm) gold (20 nm) nanosandwiches. Average grey-scale intensity of silicon substrate and an average value for the top gold triangular structures (blue and orange traces respectively) are also presented.

Figure 4-20 shows a graph of the mean grey-scale intensity *vs.* imaging time for each of the triangular gold (20 nm) / hafnia (20 nm) / gold (20 nm) nanostructures shown in Figure 4-19 together with that of the nearby silicon substrate. The results observed for hafnia are vastly different from those observed for any other dielectric. Region 1 now occurs throughout the entire imaging process i.e. 0 ~ 1800 s. The grey scale intensity of the top gold layer is observed to continually decrease throughout the experiment. Likewise, the grey-scale intensity of the silicon substrate darkens and "bottoms out" of the defined contrast parameters. Little convergence or divergence is observed throughout the charging process.

Fitting the silicon data from Figure 4-20 to the time constant equation gave an experimental time constant of 125 ± 13 s. However, it is hypothesised that the capacitors synthesised with a hafnia dielectric are not fully charged using this methodology, possibly due to the very high resistivity of the hafnia film. The resistivity of hafnia differs significantly depending on the method of deposition. Values for deposited hafnium oxide films range between 10^6 [398] and 10^{14} [399] Ωm. Characteristics of Region 2, which we assign to be the end of the charging

process and subsequent build-up of charge on the upper surface of the top gold triangle, were not observed. The grey-scale intensity of the silicon background decreases with time, but reaches the lower limit of the measurable contrast parameters and is not observed to rise. The gold triangles are also observed to continually decrease in brightness and not undergo the observed increase in brightness of other dielectric materials.

4-2.3 Comparison of different dielectric materials

Table 4-2. Calculated time constants and capacitance

Material	Relative Permittivity (ε_r)	Resistivity (Ωm)	Est Time Constant (s)[a]	Exp Time Constant (s)
Alumina	9.34 [365]	~10^{12} [366]	80	70 ± 8
Silica	4.42 [261]	~10^{13} [368]	390	248 ± 27
Zinc Oxide	7.5-8.6 [370]	~10^{12} [371]	70-80	56 ± 30
Titania	86 [373]	10^{6}-10^{12} [374, 375]	0.0076-7600	168 ± 79
Hafnia	25-50 [377, 378]	10^{8}-10^{11} [378, 379]	0.02- 40	125 ± 13

[a] Estimated time constants, τ, were calculated using $\tau = RC = \rho L/A \times \varepsilon_0\varepsilon_r A/L = \rho\varepsilon_0\varepsilon_r$ where ρ is the resistivity of the dielectric, L is the thickness and A is the cross sectional area of the device, ε_0 is the permittivity of free space and ε_r is the relative permittivity of the dielectric (or the material's dielectric constant).

Table 4-2 shows data and calculations for the various metal oxide dielectrics. Zinc oxide, silica, alumina, and hafnia show theoretical time constants that are in the region of tens to hundreds of seconds and are quite amenable to measurement with the experimental setup described here. Titania was also shown to fall within its very broad range of expected values. This is a significant advance in the measurement of nanoscale capacitance as the technique is non-destructive, able to probe multiple devices, requires no additional specialised equipment (other than the scanning electron microscope) and is useful across a range of dielectrics.

The experimental time constants of the devices containing zinc oxide, silica and alumina and titania are all in agreement with those predicted based upon the relative

permittivities and resistivities of these materials. For hafnia, the reported resistivity values are quite sensitive to the deposition conditions and so comparison with time constants based on these data is approximate at best.

4-2.4 Other experiments/observations

Nanostructures with no dielectric material

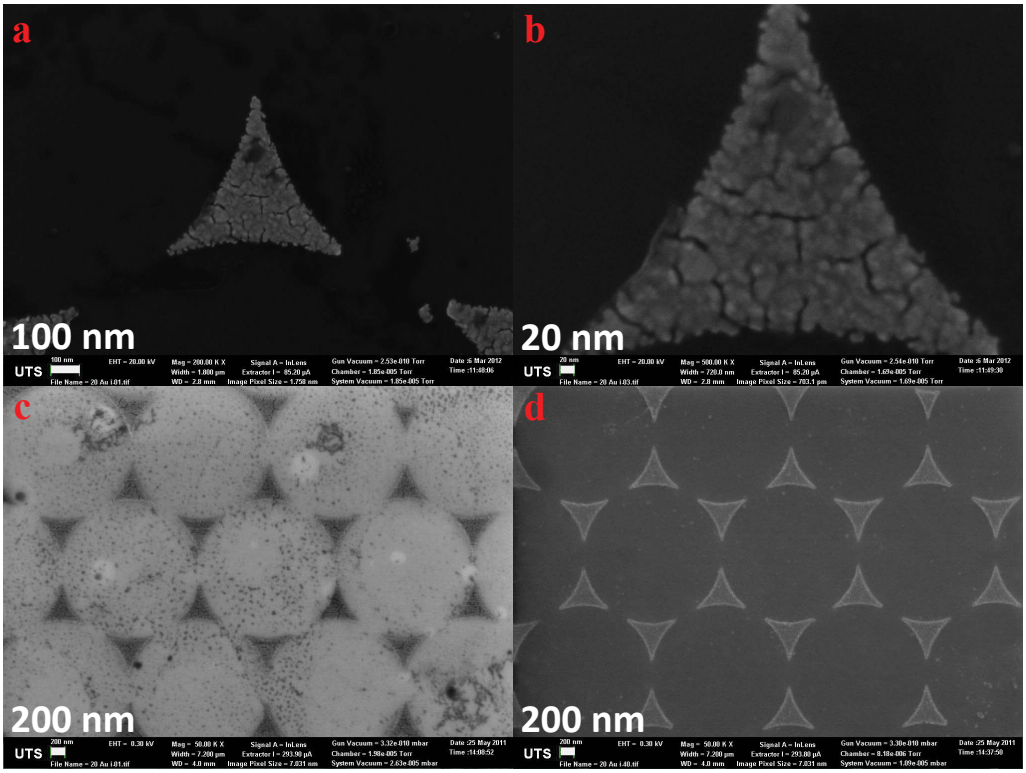

Figure 4-21. SEM micrographs of nanoscale capacitors fabricated utilising NSL. Triangular structures consisting of gold (20 nm) layers were synthesised. (a); image of an individual structure. (b); high-magnification image of an individual structure. (c); low accelerating voltage image of an array of structures at the beginning of the charging process. (d); low accelerating voltage image of the same array at the completion of the charging process.

As a control experiment and to determine if the gold triangle would undergo charging with the absence of deposited dielectric material, the effect of charging gold only structures was studied. Figure 4-21 shows SEM images of nanoscale gold (20 nm) structures. Panels (a) and (b) show the microstructure of the gold triangles, which is similar to the top gold layers observed in synthesised nanocapacitors. No isolated gold islands are visible around the edges of the structure. Panel (c) reveals some carbon deposits on the surface. The gold triangles are dark at the beginning of the

charging experiment with a faint edge effect. The silicon substrate is not as bright as was observed with alumina, silica and titania, however is brighter than the results for zinc oxide and hafnia. No very dark regions are visible close to the edges of the gold triangle. The structures shown in panel (d) are almost identical to those observed with titania dielectric devices. The silicon substrate is observed to darken, less than observed with alumina, silica and hafnia, however more than zinc oxide.

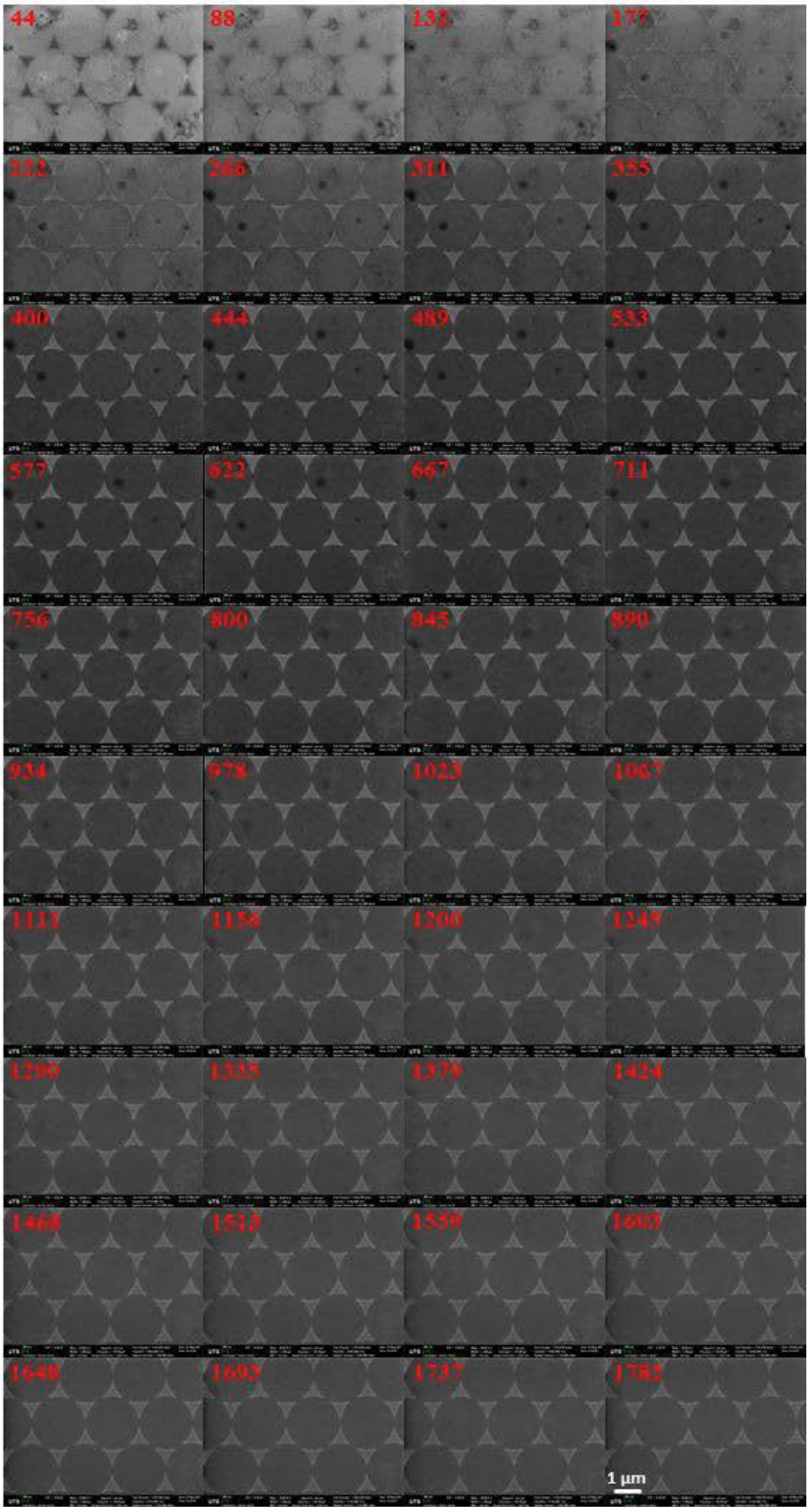

Figure 4-22. SEM micrographs of a gold (20 nm) array collected under a 0.3 keV accelerating voltage. Time data overlayed on the images is in s.

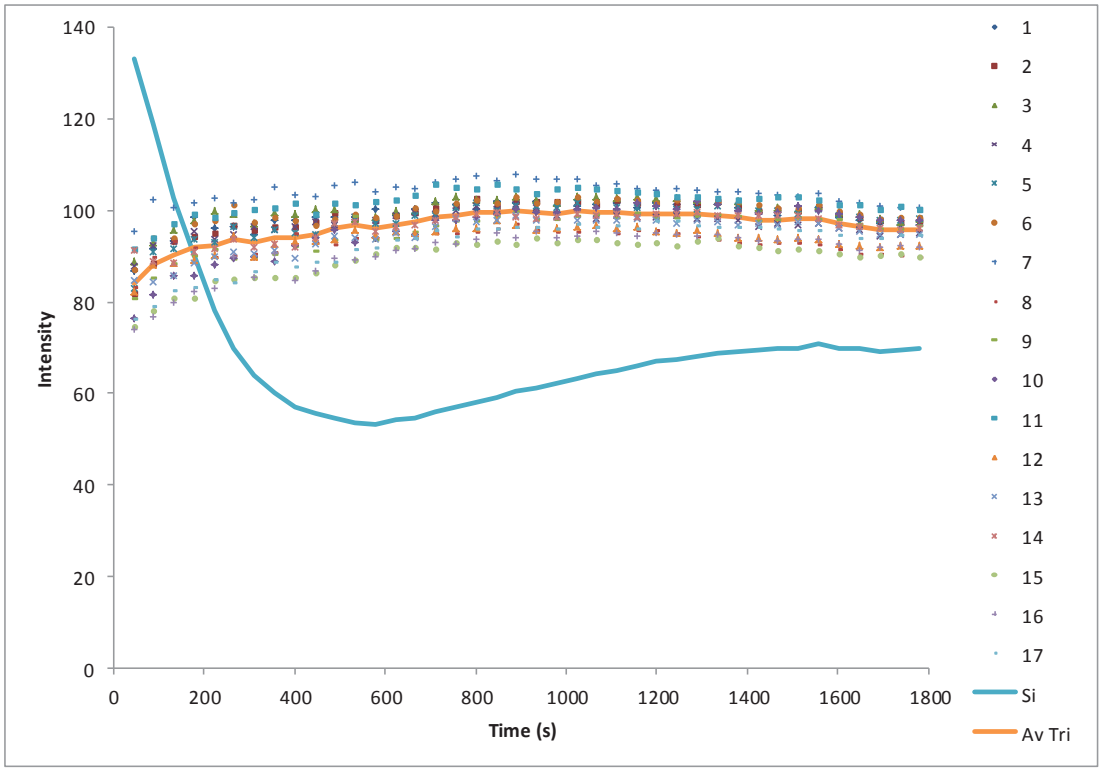

Figure 4-23. Plot of grey-scale intensity *vs.* time for the charging of seventeen gold (20 nm) nanostructures. Average grey-scale intensity of silicon substrate and an average value for the top gold triangular structures (blue and orange traces respectively) are also presented.

Figure 4-23 shows a graph of the mean grey-scale intensity *vs.* imaging time for each of the triangular gold (20 nm) nanostructures shown in Figure 4-22 together with that of the nearby silicon substrate. In this control experiment, Region 1, where the gold triangles are observed to decrease in intensity, is absent. The gold structures increase in brightness steadily between 44 ~900 s (Region 2). The build-up of charge on the gold structure still occurs without a deposited dielectric, however the effect is far less pronounced than that observed for alumina, silica or zinc oxide. The silicon substrate initial intensity value decreases over time, and then rises after ~600s and then flattens out. Convergence is observed in Region 3 (> 900 s).

The relatively small intensity changes upon scanning indicate very little capacitance within the structures, as expected. The small τ is attributed to a very small R caused by electron tunneling and leakage through the nanoscale native oxide film. In this case, charge on the top (and only) electrode drains relatively rapidly to ground.

Substrate only measurements

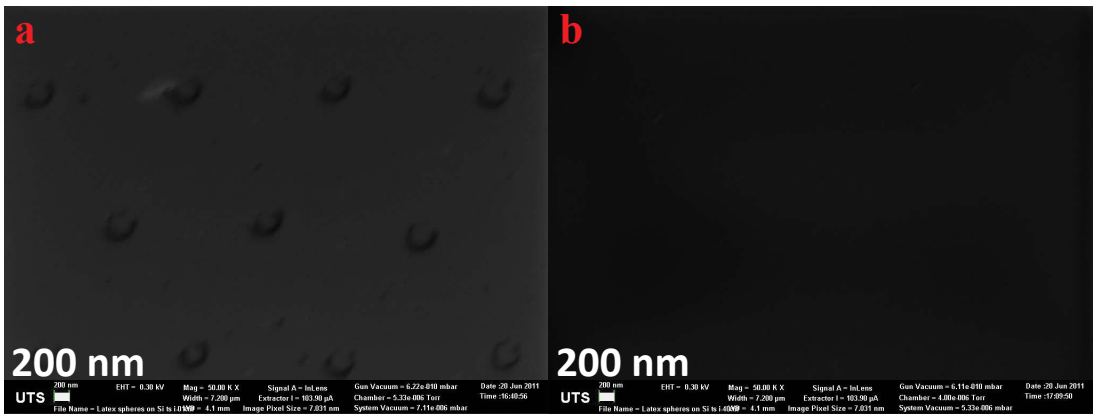

Figure 4-24. SEM micrographs of silicon substrate after NSL mask fabrication and subsequent removal without metal /metal oxide deposition. (a); low accelerating voltage image of substrate at the beginning of the electron beam irradiation process. (b); low accelerating voltage image of the same substrate at the completion of the electron beam irradiation process.

In another control experiment, the effect of charging silicon substrates was investigated that had undergone NSL mask formation and subsequent removal without any metal or metal oxide deposition. Figure 4-24 shows SEM images of the silicon substrate before (a) and after (b) a charging experiment. Carbon deposits are clearly visible in panel (a). After charging (panel (b)), the substrate has become noticeably darker, but far less so than when gold / metal oxide structures are present.

Figure 4-25. SEM micrographs of a silicon surface with latex spheres removed collected under a 0.3 keV accelerating voltage. Time data overlayed on the images is in s.

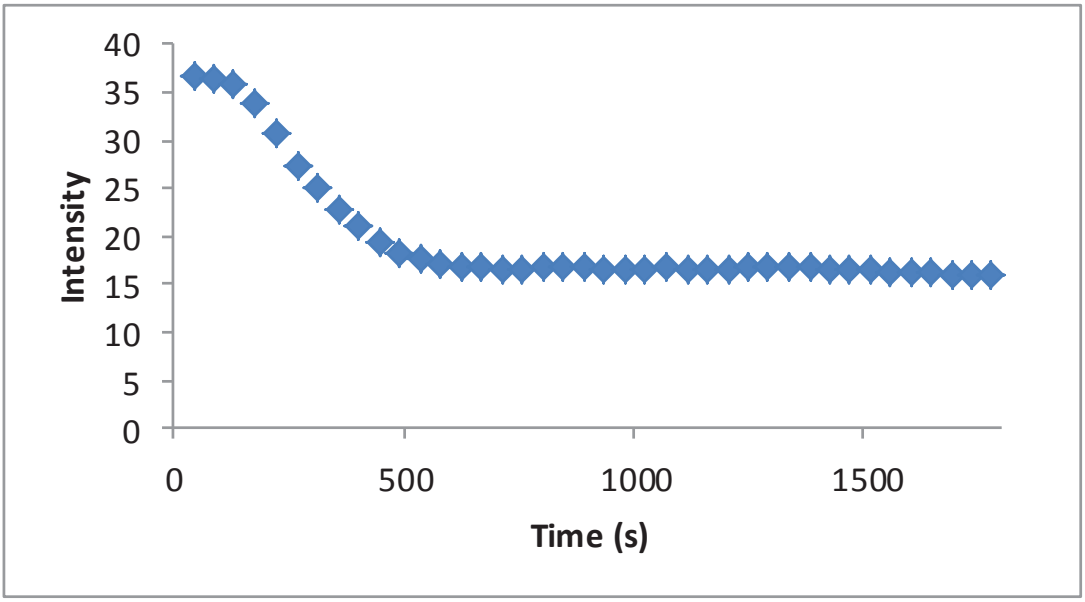

Figure 4-26. Plot of grey-scale intensity *vs.* time for the charging of a silicon substrate. Average grey-scale intensity of silicon substrate is presented.

Figure 4-26 shows a graph of the mean grey-scale intensity *vs.* imaging time for the silicon only substrate shown in Figure 4-25. The grey-scale intensity decreases at an initially slow, then accelerating rate before levelling out ~ 600 s. This implies that while substrate darkening occurs with the absence of deposited material, the change in brightness however is significantly lower than observed on substrates with capacitive devices.

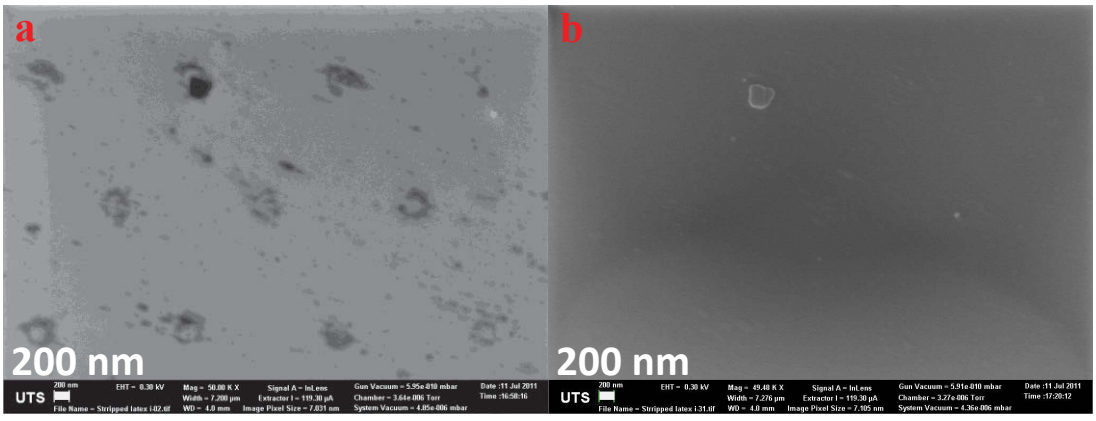

Figure 4-27. SEM micrographs of silicon substrate after NSL mask fabrication and subsequent removal without metal /metal oxide deposition. Subsequently, the substrate was left in a desiccator for three weeks. (a); low accelerating voltage image of substrate at the beginning of the electron beam irradiation process. (b); low accelerating voltage image of the same substrate at the completion of the electron beam irradiation process.

To test the effect of native oxide on the silicon substrate upon charging, the above experiment was repeated with the same silicon substrate after three weeks of storage in a desiccator. Figure 4-27 shows SEM images of the silicon substrate before (a) and after (b) the charging experiment. In panel (a), carbon deposits are clearly visible and after charging, panel (b), the substrate has become slightly darker.

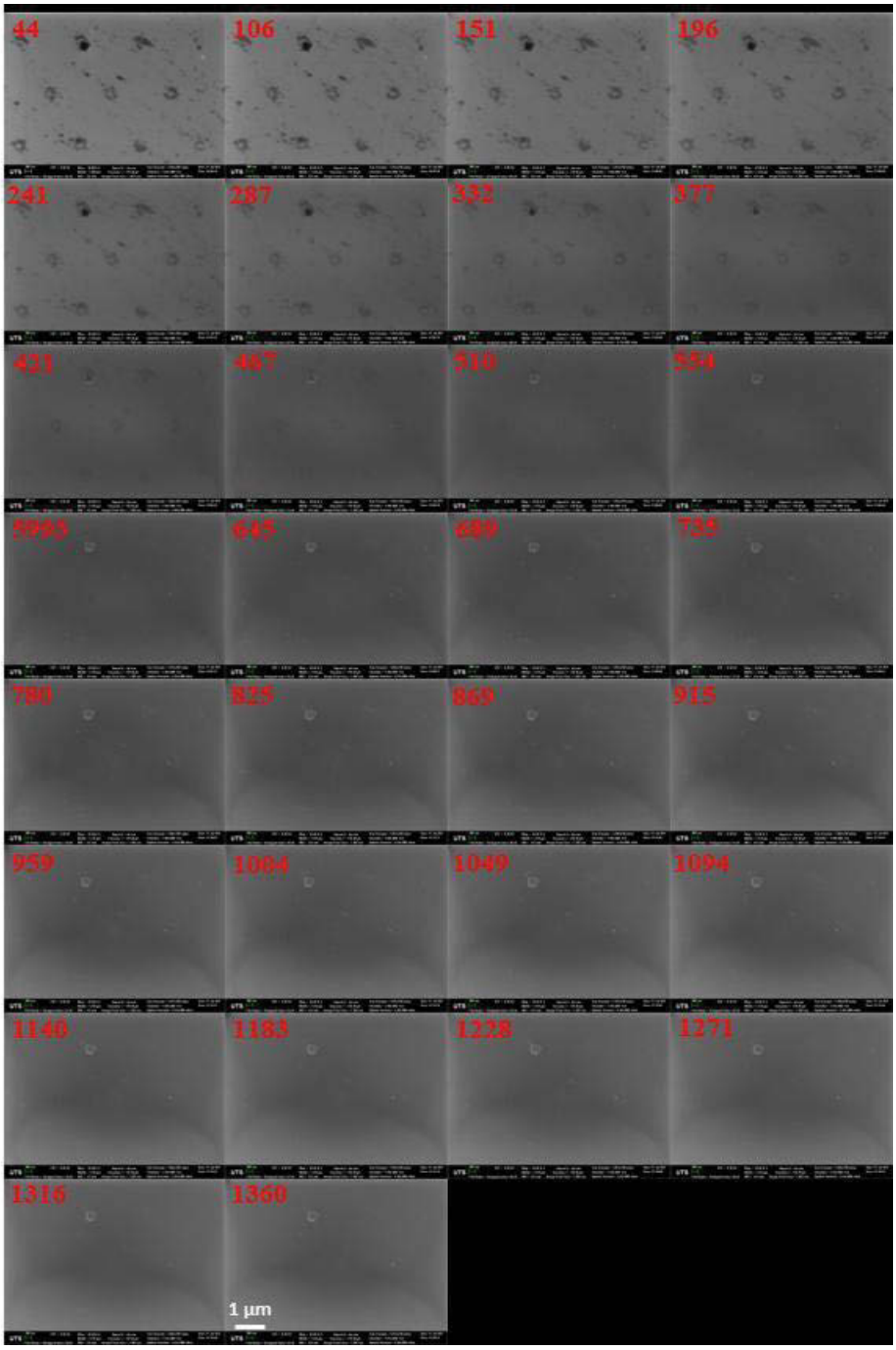

Figure 4-28. SEM micrographs of a silicon surface with latex spheres removed, imaged after three weeks. Imaging was performed under a 0.3 keV accelerating voltage. Time data overlayed on the images is in s.

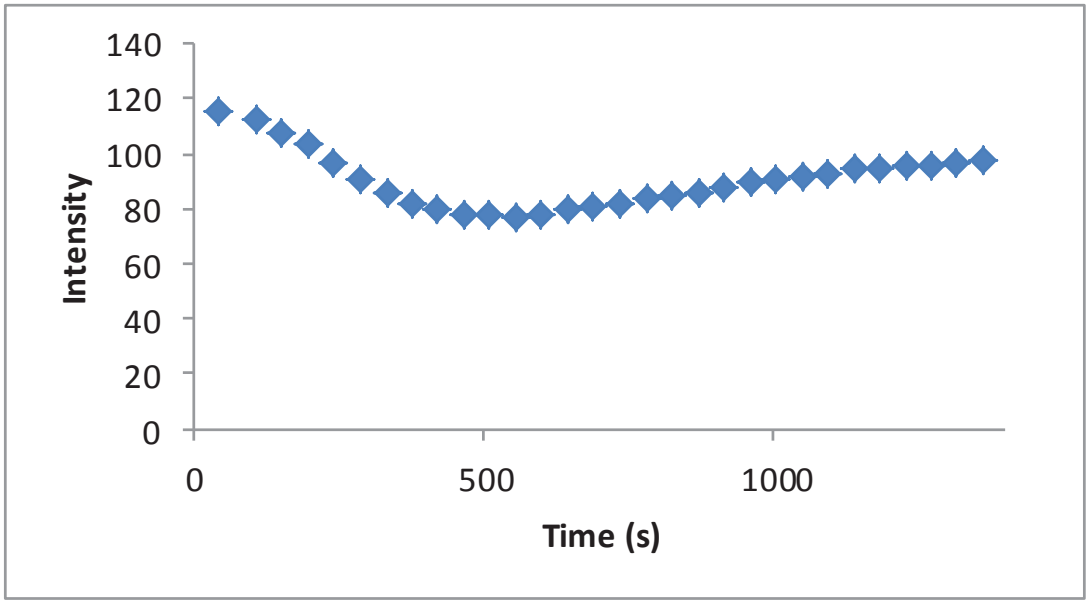

Figure 4-29. Plot of grey-scale intensity *vs.* time for the charging of silicon comparator without deposited nanostructures left in desiccator conditions for three weeks after initial measurement.

Figure 4-29 shows a graph of the mean grey-scale intensity *vs.* imaging time for the silicon only substrate aged for three weeks (data from Figure 4-28). The grey-scale intensity decreases at an initially slow, then accelerating rate before steadily increasing ~600 s. This behaviour may be attributed to a layer of native oxide becoming thick enough to retain some surface charge in the scanning electron microscope. For capacitance measurements of fabricated devices such as those reported here, SEM experiments should be performed as soon as possible to the completion of the deposition process.

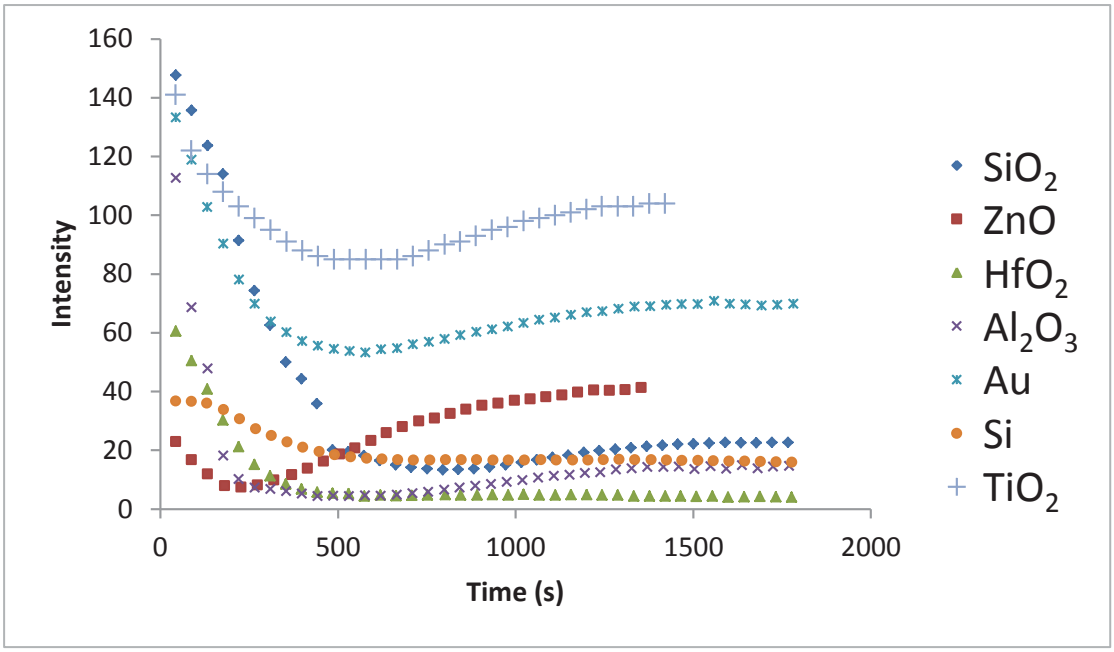

Figure 4-30. Graphs of grey-scale intensity *vs.* time for the silicon background for arrays of devices as well as unmodified silicon and gold-only arrays.

A relatively minor degree of darkening of silicon was observed in the absence of any nanocapacitors. Such darkening is ubiquitous during SEM imaging in general and is due to the deposition of carbonaceous contaminants from the SEM chamber. To examine the influence of this darkening, the intensity changes of the silicon background for each of the different arrays of nanostructures were compared, Figure 4-30. These data reveal that the rate of silicon darkening is, as expected, dependent upon the type of adjacent nanostructure and darkening due to in-chamber carbon deposition is quite small.

Retention of charge

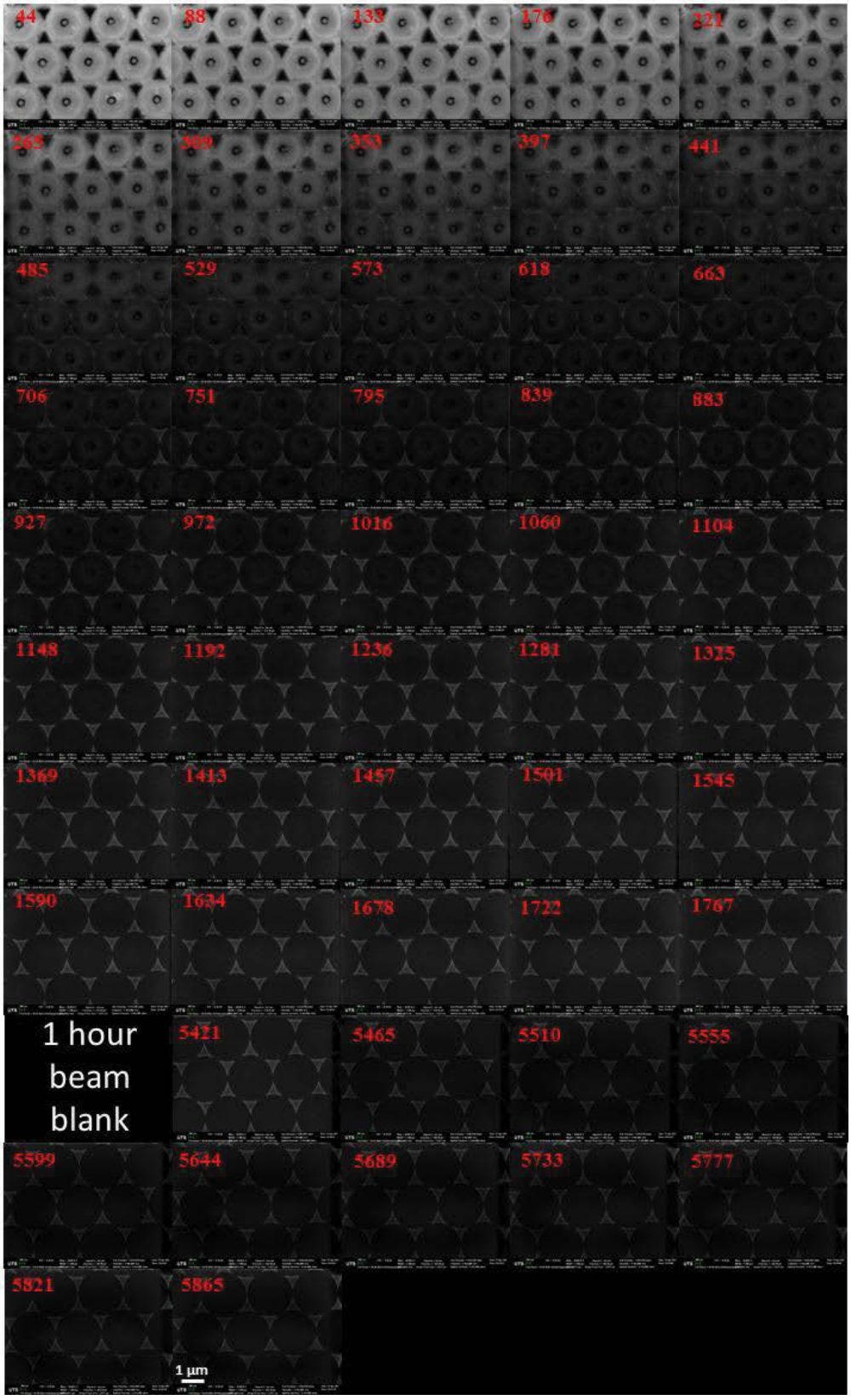

Figure 4-31. SEM micrographs of a gold (20 nm) / silica (20 nm) / gold (20 nm) nanosandwich array collected under a 0.3 keV accelerating voltage. After extended imaging the electron beam was blanked for 1 h before resumption of imaging. Time data overlayed on the images is in s.

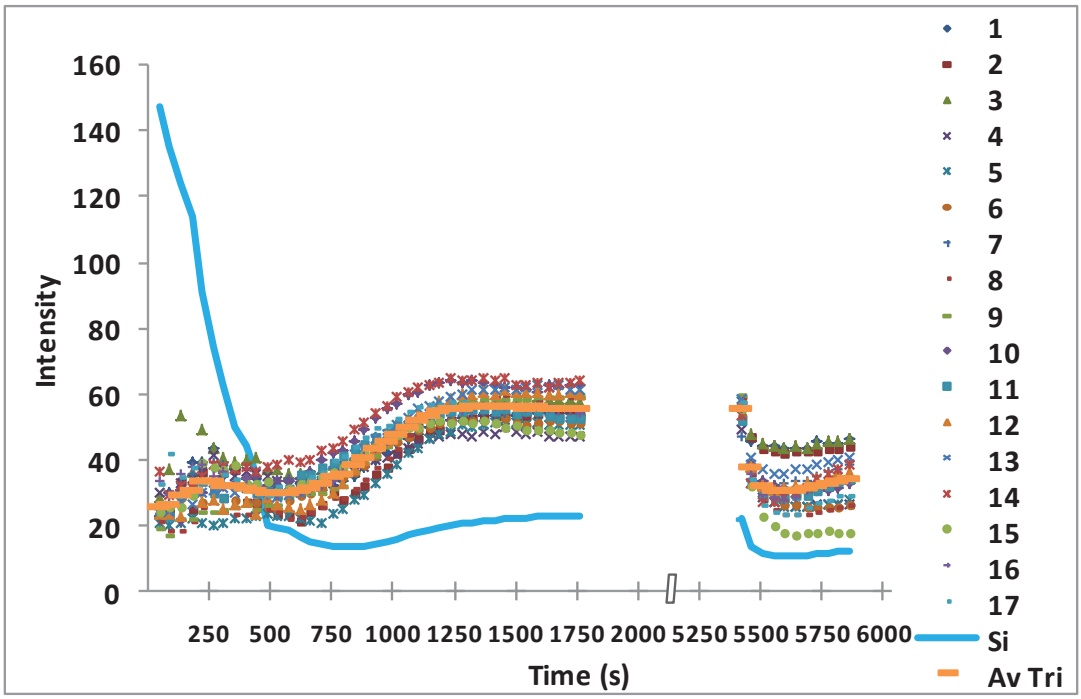

Figure 4-32. Plot of grey-scale intensity *vs.* time for the charging of gold (20 nm) / silica (20 nm) / gold (20 nm) nanosandwiches with 1 h of no electron irradiation. Average grey-scale intensity of silicon substrate and an average value for the top gold triangular structures (blue and orange traces respectively) are also included.

A prolonged charging experiment was conducted with gold (20 nm) / silica (20 nm) / gold (20 nm) nanostructures, which included an hour during which time the electron beam was blanked. The results are shown in Figures 4-31 and 4-32. It is evident that the charged state of the capacitors was substantially maintained during the hour in which the electron beam was absent. When the electron beam was re-introduced, a rapid redistribution of electrons occurred to return the device to the point near that at the end of Region 1. That is, the point where the dielectric is fully polarised.

Sputter deposition and charging experiments

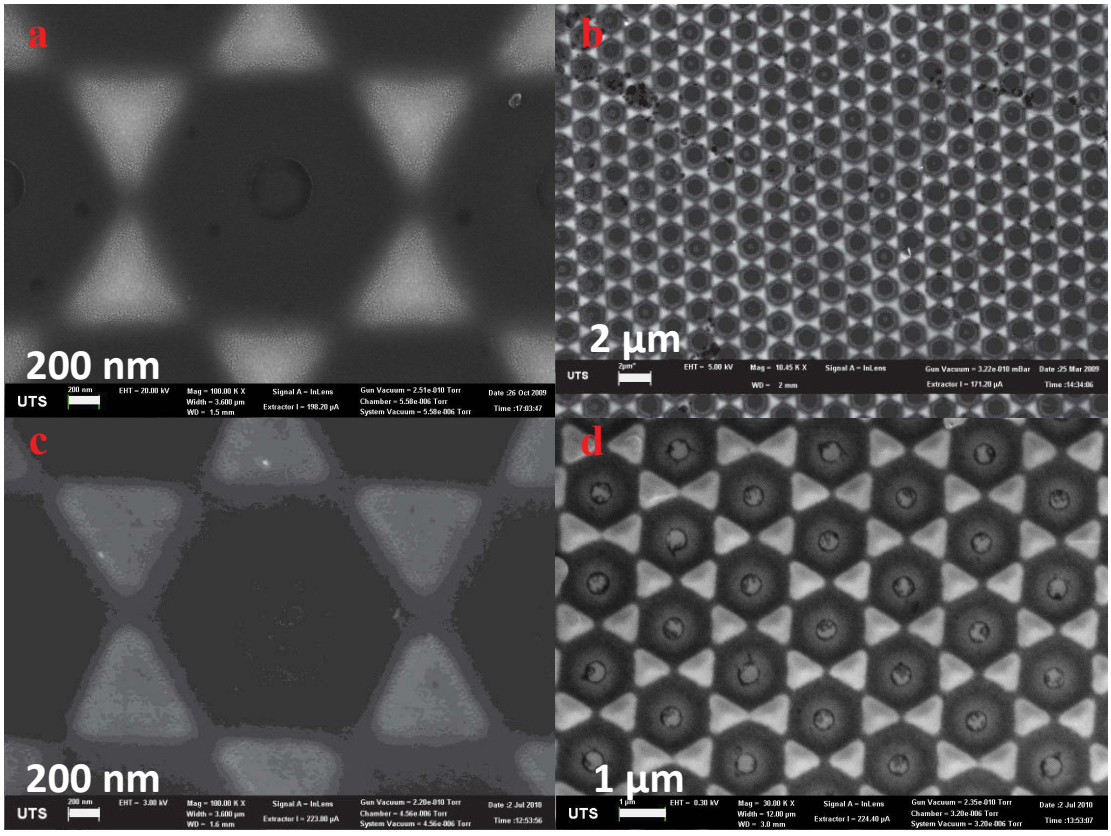

Figure 4-33. SEM micrographs of nanoscale structures fabricated using NSL. Films consisting of (a); gold (20 nm) / hafnia (20 nm) / gold (20 nm), (b); gold (20 nm) / zinc oxide (20 nm) / gold (20 nm), (c) and (d) gold (20 nm) / alumina (20 nm) / gold (20 nm) were deposited via sputter deposition. All structures failed to demonstrate charging characteristics under imaging with a low energy electron beam (d).

While it was determined in Chapter 3 that evaporative deposition of gold electrodes would provide higher quality, electrically isolated devices relative to those prepared using sputter deposited gold, experiments to confirm this were carried out. Nanostructures (see Figure 4-33) prepared with (a); hafnia, (b) zinc oxide and (c); alumina dielectrics resulted in structures that when imaged under a 0.3 keV accelerating voltage initially had bright gold triangles on a dark silicon substrate (d) and no change in brightness was observed over extended imaging. This indicates that it is likely that the large x-y area gold structures are in electrical contact with each other and no capacitive charging of individual structures occurs.

Carbon minimisation on samples

Carbon deposits were found to be ubiquitous in samples. While satisfactory capacitance data were obtained using the procedures described above, some investigations into methods to remove, or at least reduce, deposited carbon were undertaken. Such methods may be useful for future work where specimens may be heavily contaminated with carbon and thus grey-scale intensity changes may be obscured. The methods included prolonged exposure of samples to DCM and a vacuum annealing technique. Structures containing zinc oxide showed the most carbon contamination and so this dielectric was chosen as the most appropriate material for these experiments.

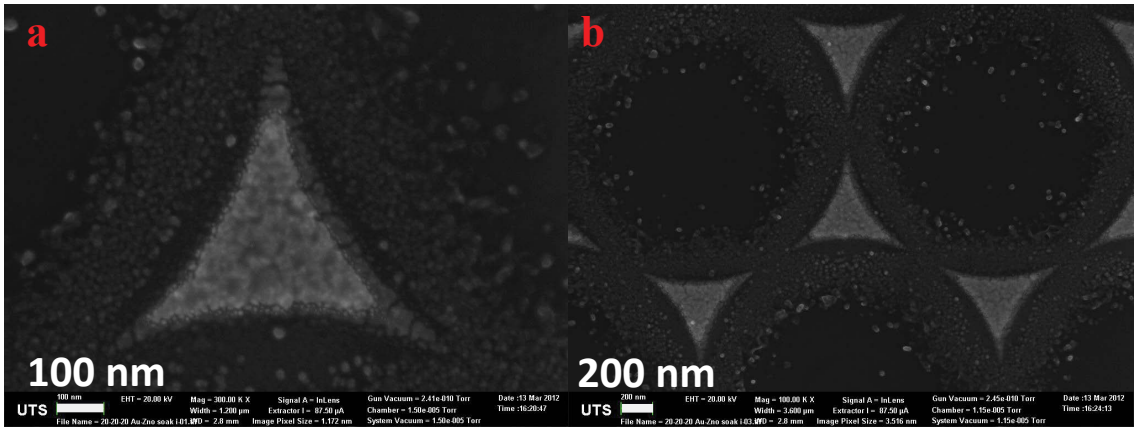

Figure 4-34. SEM micrographs of nanoscale structures fabricated utilising NSL. Films consisting of gold (20 nm) / zinc oxide (20 nm) / gold (20 nm) layers were deposited via evaporative (gold) and sputter (zinc oxide) deposition. After the removal of the mask by 1 min sonication and subsequent rinsing in DCM, samples were left in a sample tube filled with DCM overnight before removal and thorough rinsing again in DCM.

Figure 4-34 shows nanostructures obtained via NSL utilising evaporative deposition of gold and sputter deposition of zinc oxide. Following mask removal sonication and rinsing in DCM, the samples were soaked in DCM overnight, rinsed again with DCM and dried in a stream of nitrogen gas. Large regions of carbon visible in previous experiments (see for example, Figure 4-12 (d)) are absent. The extended immersion in DCM appeared to have no impact on the adhesion of the deposited material to the silicon substrate with no evidence of displaced material.

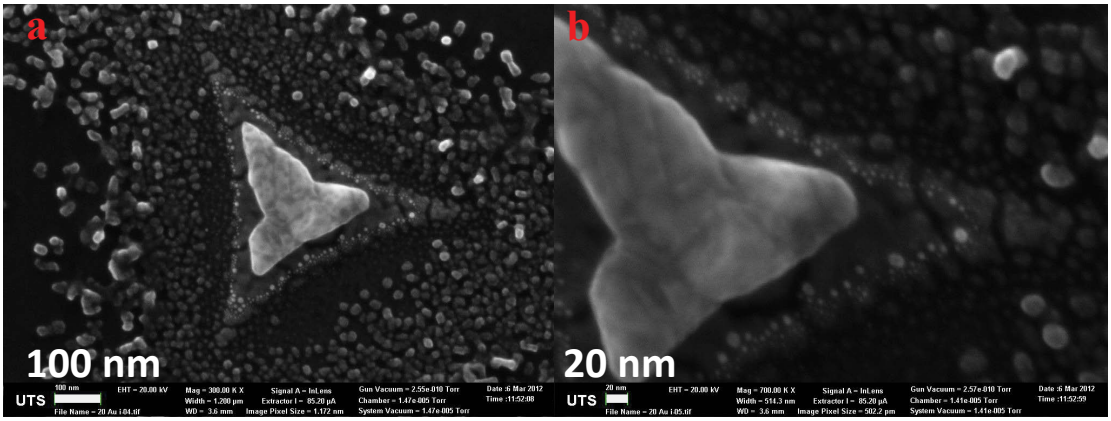

Figure 4-35. SEM micrographs of a nanoscale structure fabricated utilising NSL. After the removal of the mask by 1 min sonication and subsequent rinsing in DCM, samples were annealed at 300°C for 3 hr under high vacuum conditions (~10^{-7} Torr (1.3 x 10^{-5} Pa)). Films consisting of gold (20 nm) / zinc oxide (20 nm) / gold (20 nm) were deposited via evaporative (gold) and sputter (metal oxide) deposition.

Figure 4-35 shows results obtained from vacuum annealing experiments. The T_M for PS is 240°C, however, the polymer commonly decomposes below this temperature [400]. Under high vacuum conditions, decomposition is less likely with evaporation the more likely route of polymer removal [401]. After the standard NSL procedure, samples were annealed under high vacuum conditions at 300°C for 3 hr. No carbon deposits are visible on the surface. However, the uppermost gold triangle was observed to reduce in area and contract under the annealing conditions. Furthermore, the crystalline structure of the triangle appears to alter, with larger grain boundaries and a decrease in apparent surface roughness. Vacuum annealing has been shown to minimise the surface energy of gold thin films by increasing the proportion of (111) orientated regions [402]. The effect of annealing gold structures is widely reported to be surface energy driven and exhibits strong size dependence [296, 403]. The top gold triangle is also brighter as a consequence of the increased height of the contracted structure and decreased carbon present.

Small gold islands (within the top layer) not in contact with the top gold triangle remain isolated after annealing. These islands are formed during evaporative deposition and indicate that the surface energy of the layer that the gold is being deposited onto is very low [404]. The surface energies of gold and silicon are reported to be 4.45 [405] and 2.13 [406] Jm^{-2}, respectively. The bottom gold triangle

undergoes little physical change with respect to both x-y dimensions and polycrystalline structure.

4-3 Conclusions

Nanocapacitors have been fabricated containing a range of dielectric materials. Nanosphere lithography coupled with RF magnetron sputtering and evaporative deposition reliably gave relatively large area arrays of devices. Estimates of the time constant τ associated with the charging of the nanocapacitors were extracted by fitting grey-scale data obtained using a scanning electron microscope. The τ (=RC) values were 248 ± 27 s for silica, 70 ± 8 s for alumina, 56 ± 30 s for zinc oxide, 168 ± 79 for titania and 125 ± 13 s for hafnia. The RC values measured by this technique are consistent with those anticipated from the material properties of the dielectric interlayer.

During the nanocapacitor fabrication process, devices containing a zinc oxide dielectric exhibited metal oxide deposition in regions out of line-of-sight of the deposition source. This phenomenon was investigated further and results are described in Chapter 5.

Chapter 5:

Templated Zinc Oxide Structures Grown from Salt Solution

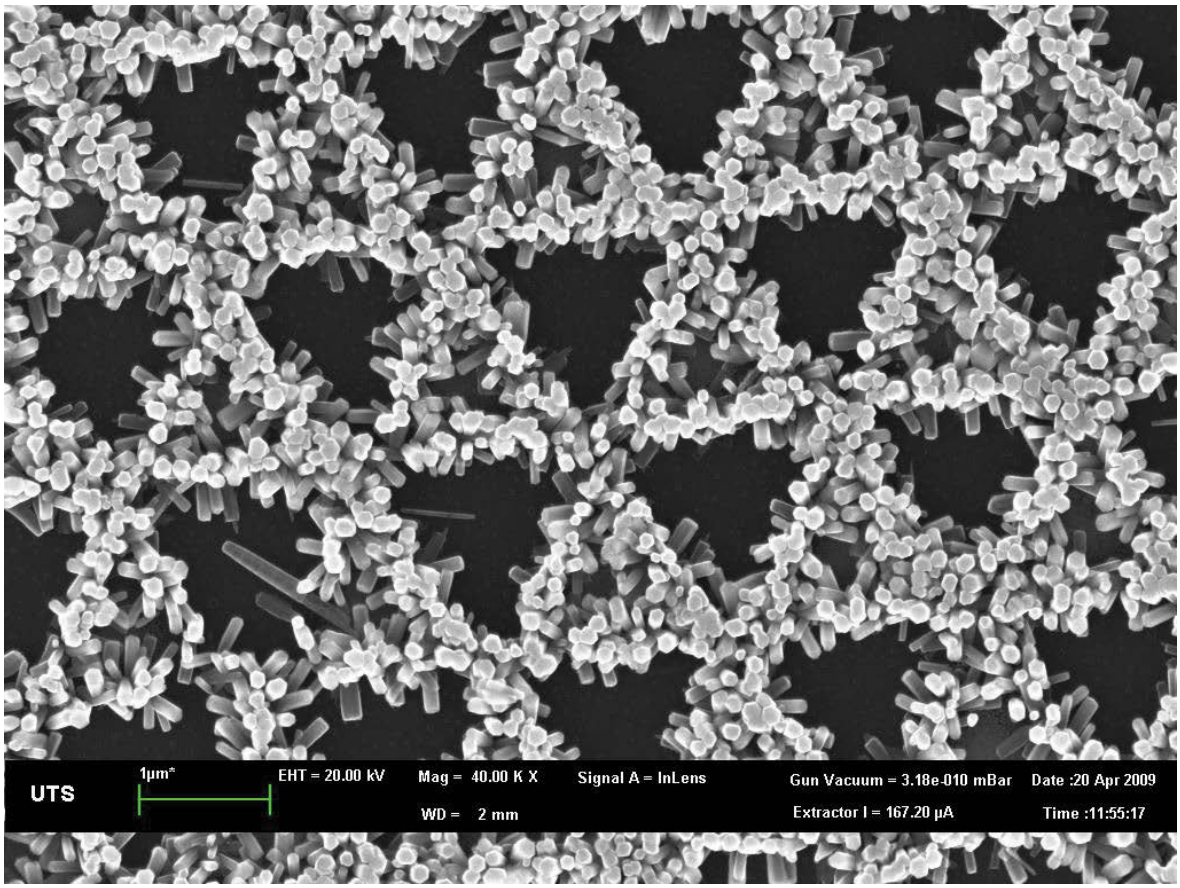

5 Templated Zinc Oxide Structures Grown from Salt Solution*

5-1 Introduction

During the course of the investigations outlined in Chapter 4, it was noted that structures prepared using zinc oxide as the dielectric layer showed unusual deposition behaviour. Closer examination of the structures revealed deposits in regions not expected to contain any material, that is, in regions lying outside of the line-of-sight of the sputtering trajectory. The deposited material formed remarkable hexagonal ring-shaped structures. This chapter presents a detailed investigation into the unusual deposition properties of zinc oxide deposited on gold using NSL. The new nanostructures were also examined as templates to promote the growth of zinc oxide nanostructures from solution.

Zinc oxide nano and microstructures have attracted a large amount of interest in research due largely to their optoelectronic properties and high emission efficiency for applications such as lighting [407] and in detectors [408, 409]. More specific applications include low-loss surface acoustic wave (SAW) filters [410], transparent conductive oxides (TCOs) [411] as well as UV photo-emitters [412]. A considerable amount of research has focused on the synthesis of these nanostructures by a variety of techniques including electrodeposition [411, 413] epitaxial growth of thin films [408, 409], and high temperature vapour deposition for nanowires [414, 415]. Solution deposition of nanostructures including nanowires [312, 416-419], nanotubes [413], and "pine-nanotrees" [420] is a promising technique due to its low cost and flexibility of structures offered by altering the growth conditions.

It was hypothesised that the ordered arrays of triangular nanostructures could be used to prepare more complex metal oxide structures. This chapter examines the results of experiments designed to test this hypothesis and the associated mechanism.

* A significant part of the work presented in this chapter has been published (see Coutts et al. ACS Applied Materials & Interfaces, 2010. **2**(6): p. 1774-1779).

5-2 Results and Discussion

5-2.1 Fabrication and structural characterisation of zinc oxide structures

Characterisation by SEM

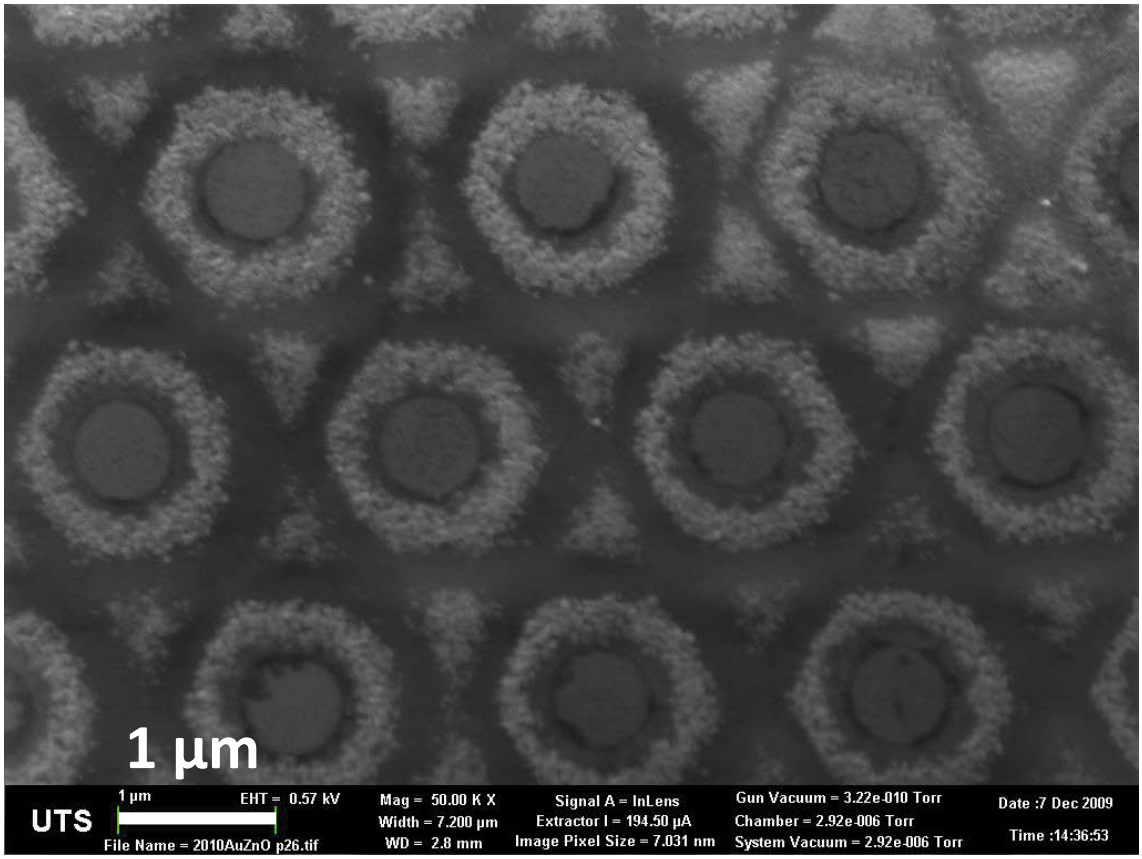

Figure 5-1. SEM micrograph of triangular pyramids and zinc oxide rings that result from the metal / metal oxide sputtering of gold (20 nm) followed by zinc oxide (10 nm) on a NSL mask fabricated with 1500 nm PS latex spheres. PS latex sphere mask has been removed. Image is acquired with a 0.57 keV potential (relatively low accelerating voltage) to maximise SE emission from the surface enhancing the contrast from the differences in zinc oxide morphology.

Figure 5-1 shows an SEM image of an array of gold / zinc oxide structures. The array consists of two shapes: compact composite triangles made from a layer of zinc oxide on top of a layer of gold, and loosely packed granular rings of zinc oxide. The rings have a degree of hexagonal symmetry. Remarkably, the rings were deposited in regions that were shaded by the latex spheres. The edges of the triangles are ~750 nm in length while the hexagonal rings are ~1.3 µm from face to face as indicated in Figure 5-2.

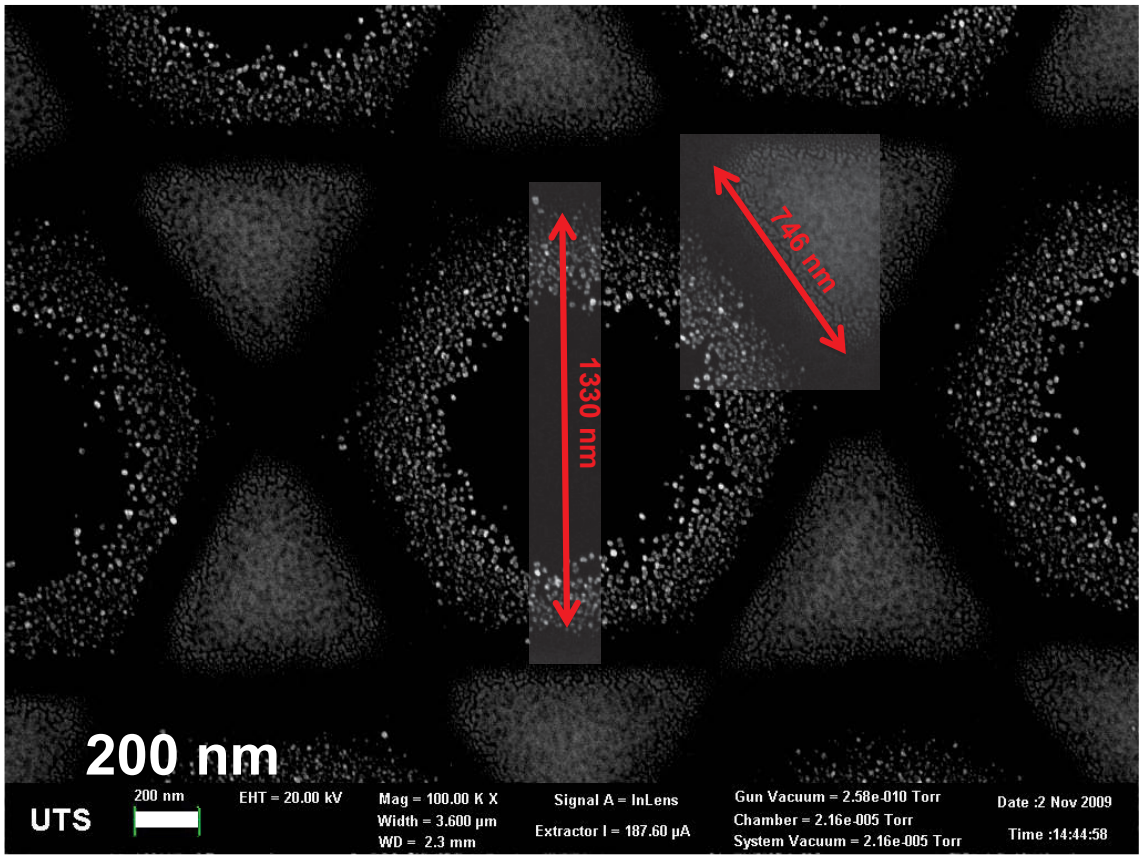

Figure 5-2. SEM micrograph of gold (20 nm) / zinc oxide (10 nm) / nano-structures.

The arrays of the nanostructures were prepared using NSL and DC/RF magnetron sputtering (Discussed in Chapters 2, 3 and 4). Briefly, an aqueous suspension of PS spheres (diameter 1500 nm) was spin-coated onto a cleaned silicon substrate. Gold was then deposited by DC magnetron sputtering followed by zinc oxide deposited by RF sputtering. The latex spheres were then removed by sonication and rinsing in DCM. Figure 5-3 shows the regions where zinc oxide has been deposited. As well as being deposited in the tops of the spheres and the inter-sphere voids, zinc oxide is deposited in regions away from normal line-of-sight deposition.

Figure 5-3. Schematic showing the procedure to prepare the new structures. (a) Spheres are deposited on silicon surface. (b) Gold is deposited on spheres and onto silicon through the inter-sphere voids. (c) Zinc oxide is deposited on gold spheres and nanostructures, however small

amounts of zinc oxide are also deposited on the silicon substrate in between the nanostructures and the latex spheres.

Importantly, a gold layer is critical to ring formation; only triangular structures of zinc oxide were formed when no gold was deposited first (Figure 5-4). It can be seen from the figure that when zinc oxide only is deposited onto a silicon substrate via NSL, triangular regions are visible in a periodic pattern. A faint outline of zinc oxide is also visible around the thicker triangular region. Carbon deposits are extensive throughout the sample and as observed for structures such as the gold / alumina / gold nanoscale capacitors in Chapter 4 (see Figure 4-4), carbon is seen to deposit differently on the lower surface energy zinc oxide and silicon regions.

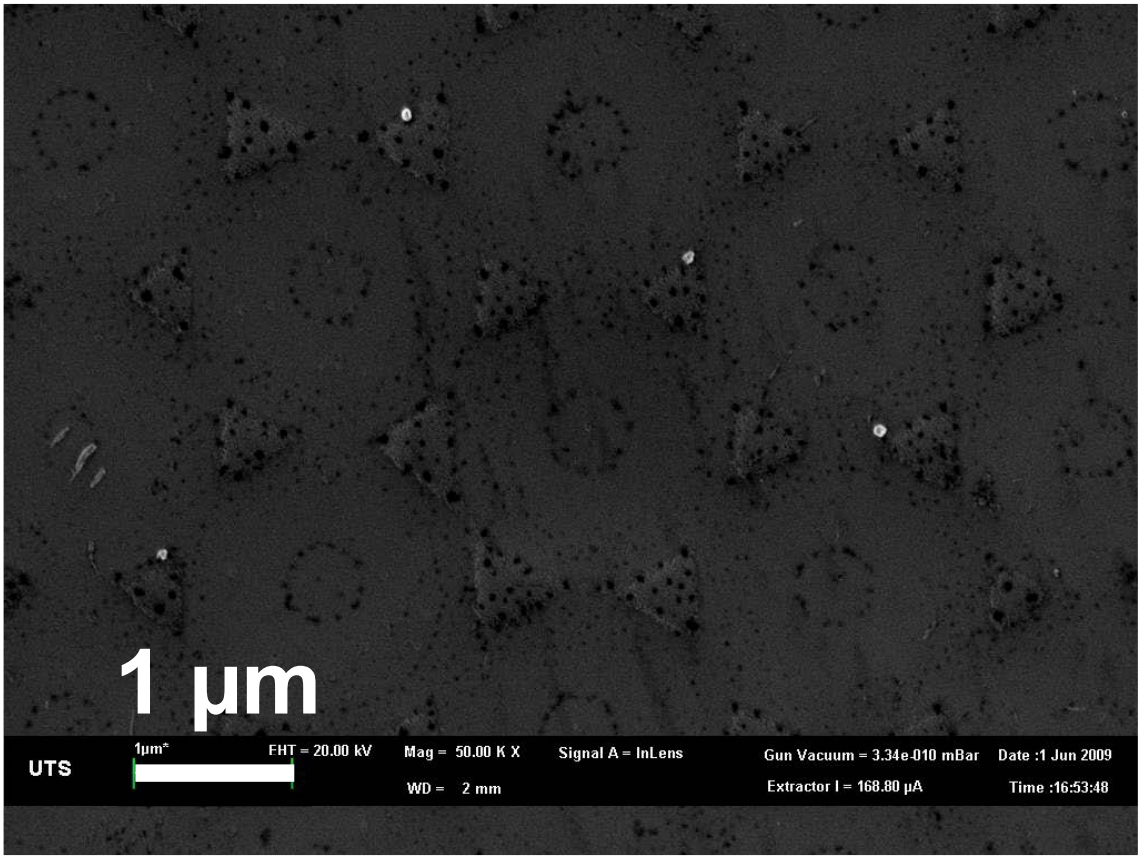

Figure 5-4. SEM micrograph of the triangular pyramids fabricated by the deposition of 10 nm of zinc oxide through a 1500 nm PS latex sphere mask.

AFM Characterisation

AFM was utilised to experimentally determine if the presence of zinc oxide rings affect the thickness of the deposited gold / zinc oxide structures.

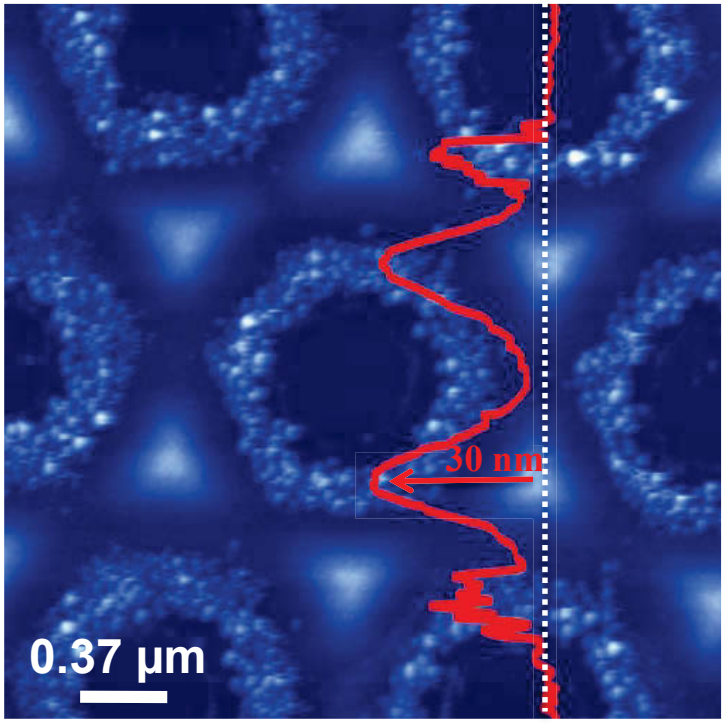

Figure 5-5. AFM image of gold (20 nm) / zinc oxide (10 nm) structures with corresponding line profile (red trace) of indicated section (white dashed line).

The atomic force microscope (AFM) data shown in Figure 5-5 reveals the topography of a 3 µm x 3 µm region of an array. A line profile shows that the peak-height of the triangular structures is ~30 nm, which is in agreement with 20 nm of gold and 10 nm of zinc oxide as measured by a quartz crystal microbalance during the deposition process. The hexagonal rings have a peak-height of ~15 nm.

EDS Characterisation

Energy dispersive X-ray spectroscopy (EDS) was utilised to determine the chemical atomic composition of the different regions of the sample. An accelerating voltage of 3 keV was employed for these experiments (see Figure 5-6).

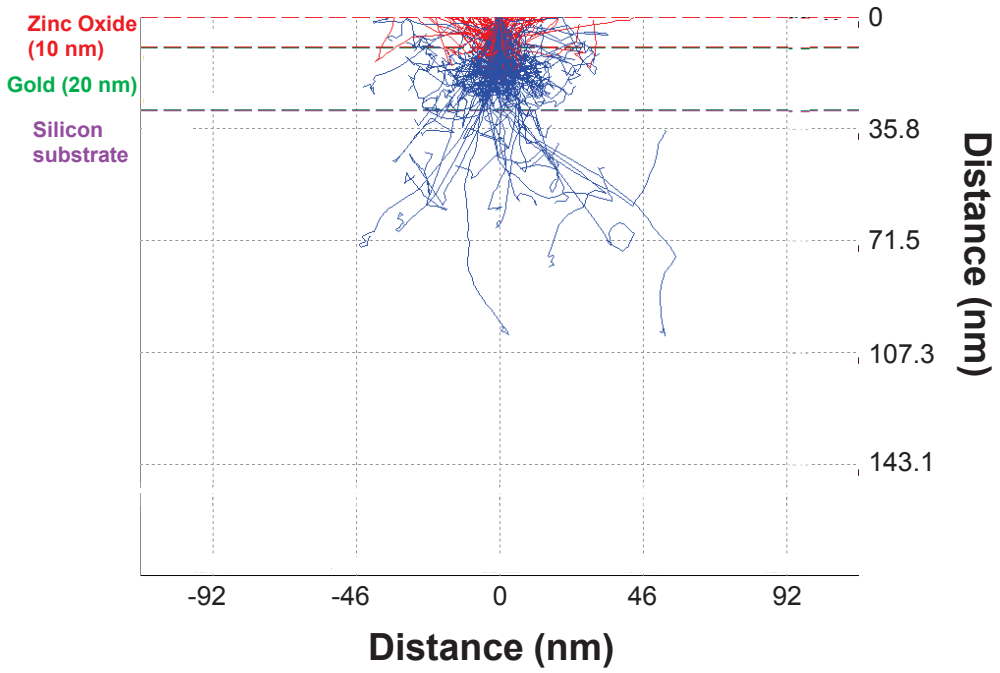

Figure 5-6. Monte Carlo simulation results for a 3 keV electron beam irradiating a gold (20 nm) / zinc oxide (10 nm) film on a silicon substrate. The trajectories of electrons that generate secondary and backscattered electrons are represented by blue and red lines respectively. Coloured horizontal dashed lines represent material interfaces.

Figure 5-6 shows the results obtained for a Monte Carlo simulation of a 3 keV electron beam interacting with gold (20 nm) / zinc oxide (10 nm) film on a silicon substrate. It can be seen from the figure that SEs are generated primarily in the gold and zinc oxide regions of the sample. EDS measurements at this accelerating voltage will prevent results being "washed out" by silicon signals which would occur if higher accelerating voltages were employed.

Data obtained by EDS measurements are shown in Figure 5-7. These experiments confirm that the rings contain zinc and oxygen, with gold being absent, while the triangular structures contain gold, zinc and oxygen. Carbon was detected across each of these regions and was found to be ubiquitous in all samples investigated.

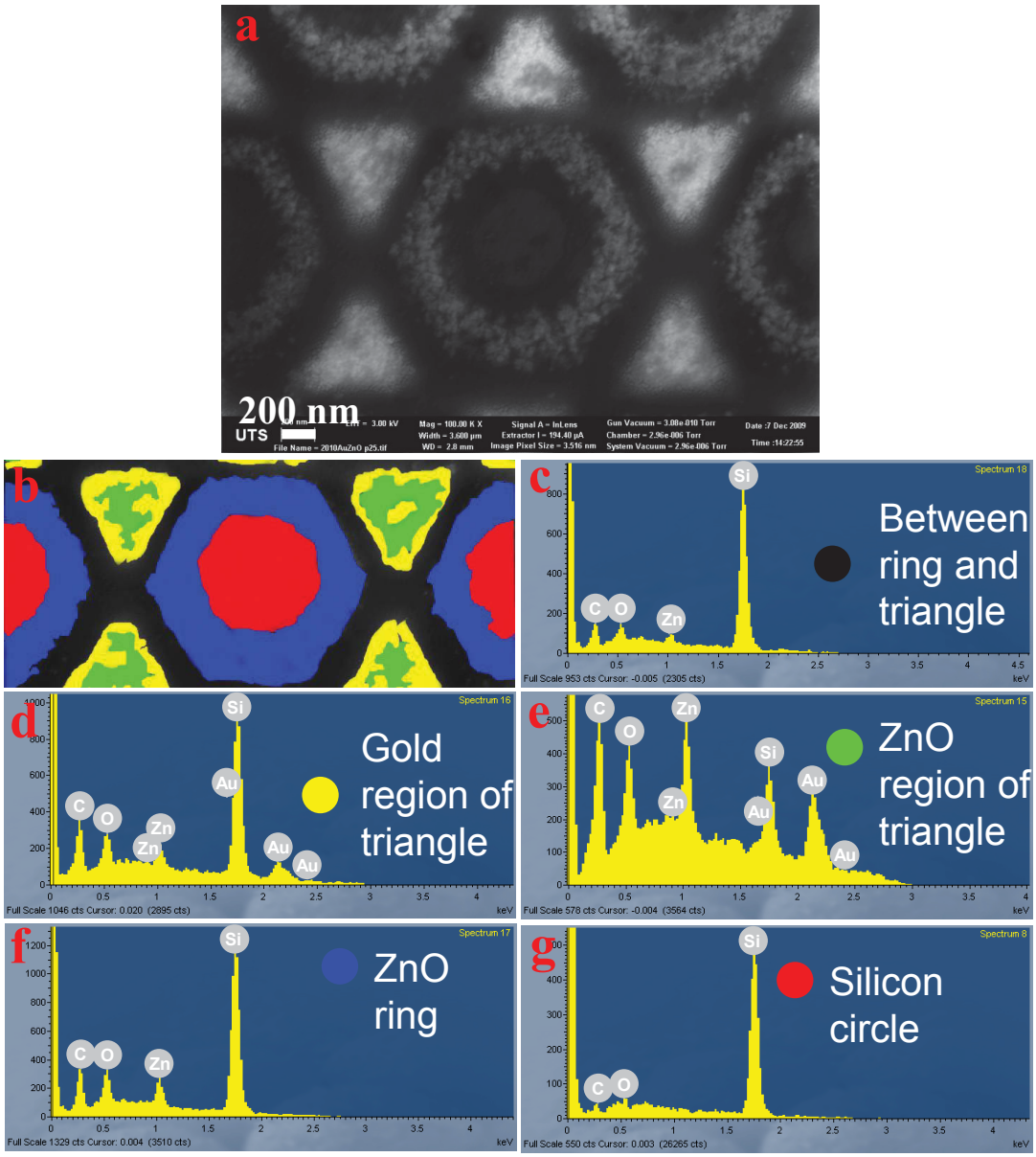

Figure 5-7. Scanning electron micrograph and energy-dispersive X-ray spectroscopy of gold (20 nm) / zinc oxide (10 nm) template. Performed with a 3.0 keV accelerating voltage (a) SEM micrograph of array sample, (b) colour map representing the different regions of the array (made from (a)), (c-g) X-ray spectra of the different regions of the sample.

The silicon ((SiKα_1 1.74 keV Relative Intensity (RI) 100), (SiKα_2 1.7394 keV RI 50), and (SiKβ_1 1.8359 keV RI 2)) signals representing emission energies from electron hole recombination's are present in all samples, however the intensity is relatively lower in spectra acquired on the gold triangle; this is a consequence of the shielding effect of the deposited gold / zinc oxide materials resulting in very low signals generated from the silicon substrate. The ZnL$\alpha_{1,2}$ (1.0117 keV RI 111) and ZnL$_1$ (0.884 keV RI 7) peak

representing zinc recombination is strongly detected in the zinc oxide ring and on the zinc oxide regions of the triangle, it is also detected with lower relative intensity on the gold region of the triangle and between the triangle and the ring, however no zinc is detected in the silicon circle. Gold ($AuM\alpha_1$ 2.1229 keV RI 100) is detected only on the triangle, with no evidence on any presence on the silicon substrate. Both carbon ($CK\alpha_1$ 0.277 keV RI 147) and oxygen ($Ok\alpha_{1,2}$ 0.5249 keV RI 151) are detected in all regions of the sample. The carbon can be attributed to trace amounts of dissolved latex spheres remaining, while oxygen is from the thin surface oxide layer formed on silicon as well as the zinc oxide. Carbon is found to be more present in regions containing the zinc oxide rings than on silicon only regions. This is in complete agreement with results observed in Chapter 4 (see Figure 4-12 (d)).

Re-Emission in thin film deposition

The dimensions of the hexagonal ring structures indicate that they form in a region that was shaded by the latex sphere NSL mask from direct "line-of-sight" of the sputter target. To deposit in these shaded areas the sputtered zinc oxide must either have been deflected from its trajectory in-flight or have been re-emitted from the surface of the triangles. In fact, re-sputtering (originally reported as bias sputtering [421]) is a known phenomenon where materials condensed onto a film during its growth phase are ejected by bombardment of deposited materials. Re-sputtering coefficients for zinc oxide are reported to be as high as 0.3 [422]. This means that approximately 30 % of the total material deposited on a film will be subsequently ejected during the deposition process. Any re-emission that occurs on the substrate will also occur on the film thickness monitors used in experiments, meaning accurate film thickness measurements are maintained. While re-emitted material from the film thickness monitor will move away from the new "target" and likely deposit somewhere on a chamber wall, the NSL mask present during deposition constrains any material re-emitted from fabricated gold / zinc oxide triangular regions. Under appropriate conditions and geometries, significant quantities of material can be deposited in areas not in line-of-site of the source [423-429] and the deposits are reportedly loosely packed [422], as is the case in the current work. However, re-emission from the surface is not sufficient on its own to explain the ring-shaped deposits of zinc oxide described here because the rings were not formed when the gold under-layer was absent. Clearly, the gold plays a vital role in the process.

5-2.2 Mechanism of zinc oxide structure formation

Proposed mechanism

It is known that zinc oxide and gold can form a Schottky diode [430], with the oxide serving as an n-type semiconductor. A barrier height of 1.02 eV was reported [431]. This phenomenon is not unique to gold, silver and platinum have also been reported with barrier heights of 0.84 [409] and 0.43 eV [432] respectively. In this situation, negative charge may accumulate on the zinc oxide that overlies the gold in the triangles, with the charge induced by electric fields and / or charged species within the sputter chamber. Once sufficient charge had developed, negatively charged zinc oxide species may be deflected away from the triangles. However, deflection of *incoming* charged species is unlikely as their concentrations are reportedly less than a few percent because of the strong magnetic fields around the target [433, 434]. Furthermore, the kinetic energy of the incoming zinc oxide is high, as evidenced by the compact nature of the zinc oxide on the triangle.

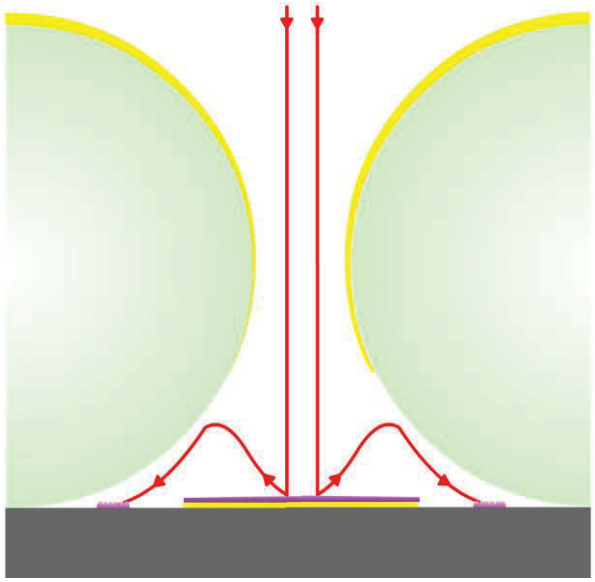

Figure 5-8. Schematic for the proposed mechanism for the formation of zinc oxide rings. The green circles are latex spheres, yellow indicates deposited gold, purple deposited zinc oxide and the red lines indicate deposited zinc oxide trajectory.

On the other hand, re-emission of zinc oxide from a deposit is an effective process and is known to be enhanced by negatively charged surfaces [426] as they can attract

positively charged argon ions. The deposition of zinc oxide at the significantly reduced kinetic energies relative to sputtering at the target (in the order of 10's of eV's for deposited materials at the substrate while typically hundreds of eV for target [295]) while capable of producing re-emission of zinc oxide species, is unlikely to overcome the binding energy of gold (84.0 eV [435]). Consequently gold is not expected to be re-emitted. Support for this is provided in the EDS measurements (Figure 5-7).

It is proposed that it is the diodic characteristics of the composite zinc oxide / gold triangles that are responsible for the directed deposition of the re-emitted zinc oxide to form the unusual hexagonal ring structures (see Figure 5-8). SEs generated during the re-sputtering process [436] are likely to accumulate on the surface of zinc oxide as well as in the depletion region at the zinc oxide / gold interface.

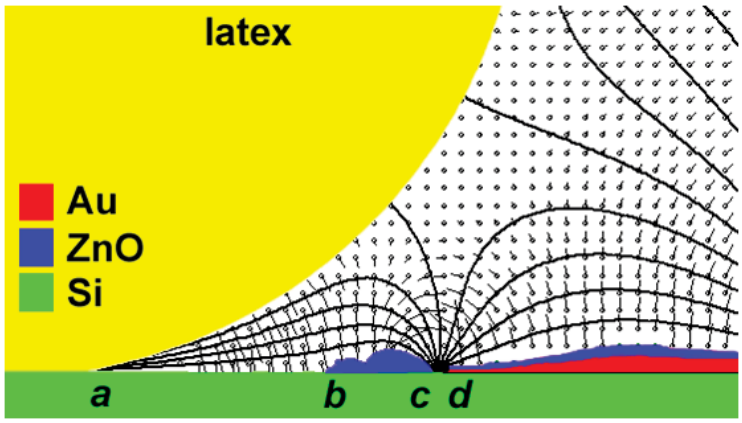

Figure 5-9. Proposed mechanism for the formation of the zinc oxide rings. Distribution of electric equipotentials (solid lines) and direction of field lines (vectors) for the case where the triangle has accumulated a negative potential relative to the silicon substrate (the latex sphere is treated as an insulator in this simulation). The drawing is to scale and uses the experimental AFM topography in the calculation. The zinc oxide is the blue phase. Modelling and image provided by Professor Michael Cortie.

Support for this mechanism may be deduced from the location of the re-emitted deposit. Figure 5-9 shows the results of modelling the electric field in the vicinity of the substrate using the Poisson equation. In the simulation shown, a charge of 0 V was allocated to the latex sphere, -1 V to the triangle, and 0 V to the silicon substrate. Simulations for other situations, and for the case in which the polymer sphere is considered to be an insulator, produced similar results; the only important criterion for ring formation is that the triangles should be at a more negative potential than the

surrounding material. In all cases, any negatively charged zinc oxide species re-emitted from the triangular surface can be propelled along the electric field lines into the space lying under the polymer sphere in the region between points *b* and *c*. However, very few species are likely to settle in the zone between points *c* and *d* because the electric field lines in that region of the sample are directed parallel to the surface of the silicon substrate (Gauss's law). Furthermore, few species will travel to the region between points *a* and *b* because the electric field lines in that regions point back to the under-surface of the latex sphere. It can be seen by following the field vectors that little or no charged, remitted material would deposit in this region. The regions between points *a* and *b*, and between *c* and *d*, correspond to the regions free of zinc oxide observed in experiments, while the region *b*-*c* corresponds to the experimentally observed zinc oxide ring.

The absence of a ring in the case where no gold layer was present is readily explained as any charge on the zinc oxide triangles drains through the silicon substrate to ground, resulting in no local electric fields. Although re-emission of zinc oxide would still occur, very little material would be preferentially deflected into the region *b*-*c* because of the absence of a local electric field.

Effect of surface composition on ring formation

The gold can form a Schottky diode with silicon [437] and in the case of a p-type silicon substrate this would preferentially channel negative charge from the substrate to the gold and from there through the gold / zinc oxide junction into the overlying zinc oxide. In contrast, an n-type silicon substrate should channel holes into the gold and this in turn reduces the rectification on the gold / zinc oxide junction by promoting a greater reverse current of electrons from zinc oxide to gold and hence reduces the negative charge on the zinc oxide. Experimentally, we found that the ring formations could be produced on either n- or p-type silicon, Figure 5-10, but the density of that on n-type silicon was lower than on p-type, in agreement with the proposed mechanism.

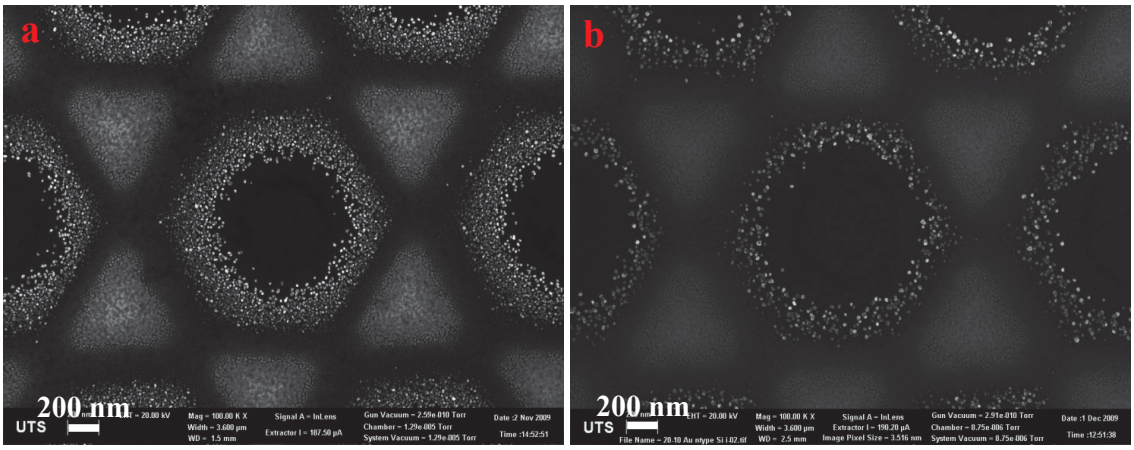

Figure 5-10. SEM micrographs of gold (20 nm) / zinc oxide (10 nm) deposited on (a) p-type (100) and (b) n-type (111) Silicon.

Clearly, an underlying gold layer was critical to ring formation in the experiments described above. To investigate if other metals could give rise to the same effect, zinc oxide re-emission onto platinum containing NSL structures was investigated.

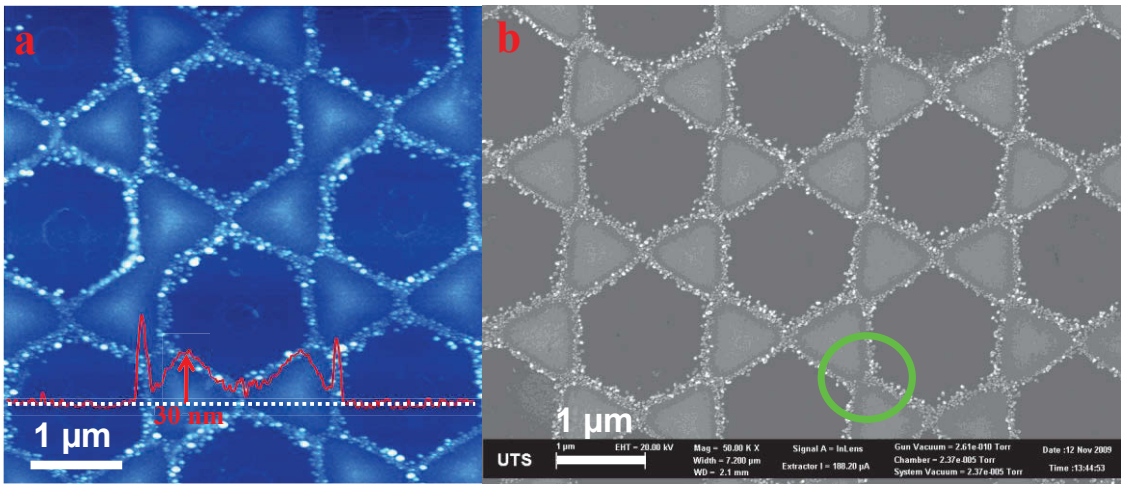

Figure 5-11. (a) AFM data of arrays fabricated by deposition of platinum (20 nm) / zinc oxide (10 nm) through NSL masks with corresponding line profile (red trace) for the specified section (white dashed line). (b) SEM micrograph of the sample shown in panel (a). Green circle indicates a region of between two platinum triangles that are seen to be in physical contact.

When zinc oxide was deposited on platinum triangular structures, the re-emitted zinc oxide almost entirely resided on the silicon substrate in very close proximity to the deposited platinum (Figure 5-11). Platinum is capable of forming a Schottky diode with n-type zinc oxide [438], so the deflection of negatively charged re-emitted zinc oxide

species by the electric field induced in the platinum conductor is to be expected. However, the difference of this result relative to gold in terms of where the zinc oxide species is directed is striking.

AFM data (Figure 5-11 (a)) show that the platinum triangles have a larger x-y area than the gold triangles deposited under similar conditions. Line profile data reveal that re-emitted zinc oxide is actually thicker than the deposited triangular structures. This is in contrast to the AFM data obtained with gold triangles (Figure 5-5). With gold triangles however, the re-emitted zinc oxide deposits over larger x-y dimensions. It appears that re-emitted material is more tightly directed by electric fields arising from the platinum structures. Line profile traces reveal that the platinum triangles are either touching or are very close to each other. In Figure 5-11 (b), an example of two touching platinum triangles is highlighted by the green circle.

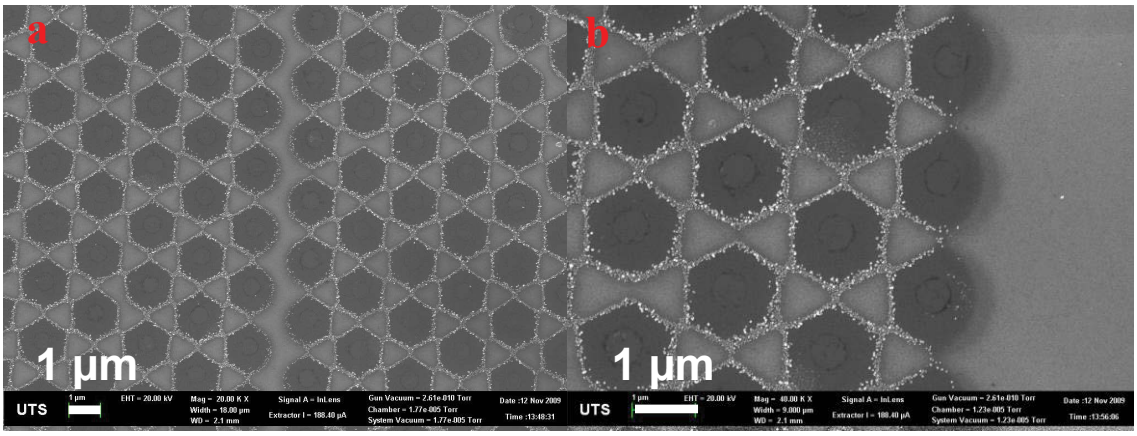

Figure 5-12. SEM micrographs of different regions of arrays produced from the re-emission of 10 nm zinc oxide films on platinum (20 nm) triangles. (a) Large grain boundary between hcp regions. (b) Area near the edge of a hcp region.

Figure 5-12 shows SEM images of the same platinum-containing array as shown in Figure 5-11 but in a region containing defects (arising from a misaligned or incomplete NSL mask). Panel (a) shows regions where spheres were not close packed and the resultant platinum film is continuous. Significantly less zinc oxide was re-emitted from this region. Panel (b) shows that no re-emitted zinc oxide deposited on a larger continuous platinum layer. A proposed mechanism for the different results observed with platinum compared to gold structures involves the formation of a Faraday cage by the electrically continuous platinum triangles, which form a lattice. The resultant

electric fields direct negatively charged re-emitted zinc oxide onto the silicon substrate as well as away from the triangular structures.

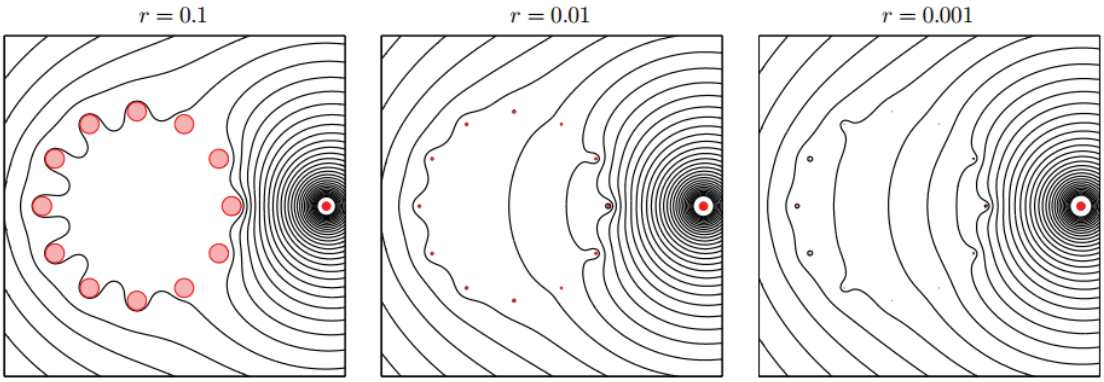

Figure 5-13. Results of modelling carried out to determine the resultant equipotential distribution from a point source charge (solid red circle) on a mathematical representation of a faraday cage composed of various wire thicknesses. Figure reproduced from [439].

Figure 5-13 shows the results of work carried out by Chapman *et al.* [439] to mathematically determine the resultant equipotental line distribution induced by a point charge in close proximity to a simple Faraday cage model. Of primary interest in this figure is the region between the point source and its closest conductive points (right-most red outlined circles). Electric field lines in close proximity to conductive regions enter the shielded region. It is proposed here that a similar interaction occurs for the negatively charged zinc oxide film sitting atop the conductive platinum lattice. During deposition, some negatively charged re-emitted zinc oxide (less than with gold) is deflected onto the silicon substrate in regions very close to the deposited platinum lattice by electric fields. Material also deflects away from the deposited film.

Further evidence for this proposed mechanism can be discerned from the results of experiments where zinc oxide was deposited onto structures consisting of a conducting surface (continuous gold film) and an insulator (hafnia). It may be expected that on a conductive surface, negatively charged re-emitted zinc oxide material will deflect away from the substrate (due to Gauss's law). In the case of an insulator, accumulated charge at the zinc oxide surface will deflect negatively charged re-emitted zinc oxide species away from the zinc oxide layer, resulting in deposition onto the substrate and away from the deposited films.

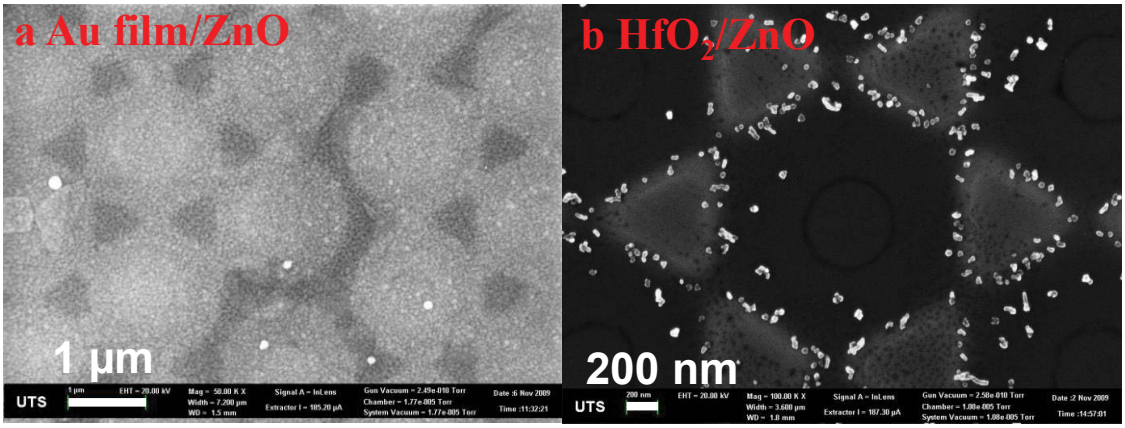

Figure 5-14. SEM micrographs of arrays produced from the re-emission of 10 nm zinc oxide films on a continuous gold film (100 nm) (a) and hafnia (20 nm) triangular structures (b).

Figure 5-14 shows SEM images for the different morphologies of zinc oxide obtained when deposited on a continuous gold film and on hafnia structures. Panel (a) shows zinc oxide deposited on a continuous gold film where zinc oxide triangular structures (darker regions) are formed on the polycrystalline gold. Defects from the NSL mask are prevalent throughout the sample and reflect the fact that the technique has not been optimised for gold surfaces. No zinc oxide rings were deposited. Re-emitted zinc oxide is present (white particles) and is reasoned to have been removed from the underside of the PS latex spheres during mask removal (or possibly during re-emission if a critical mass could no longer adhere to the undersides of spheres). Alternatively, the gold film may contain pinholes which could result in negatively charged re-emitted zinc oxide being directed there, however as re-emitted zinc oxide is also visible in the centre of one of the zinc oxide triangles, this is unlikely.

In panel (b), re-emitted zinc oxide is visible on the substrate and the edges of the hafnia / zinc oxide triangles. Less material is present than observed using gold or platinum triangles. The deposits are seen to reside primarily at the transition point between the deposited film and the silicon substrate. Material is also present (though less prevalent) on the silicon substrate. No zinc oxide is visible close to the latex sphere contact patch and very little can be seen on the centre regions of the deposited gold triangles. It is reasoned that when negatively charged zinc oxide is re-emitted it is deflected away from the triangular structures primarily to the undersides of the latex sphere mask but also out of the masks inter-sphere voids and onto the silicon substrate.

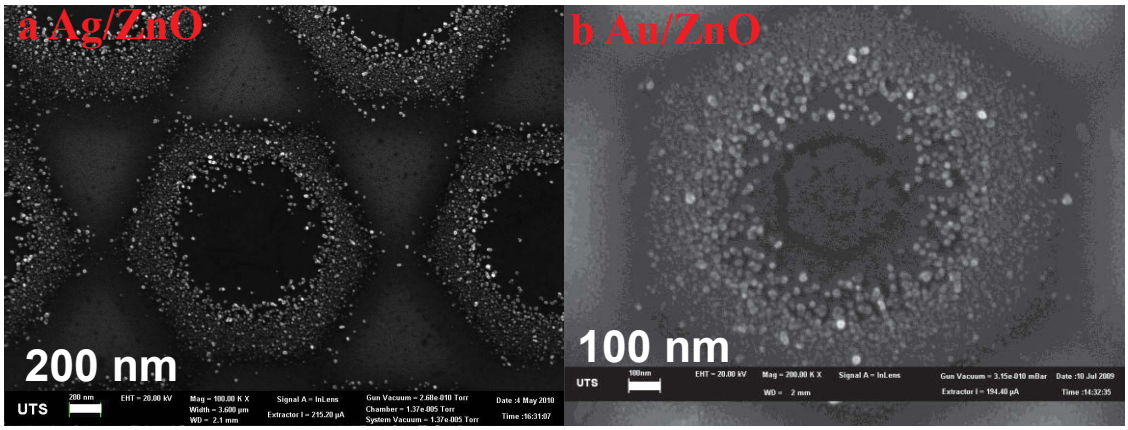

Figure 5-15. SEM micrographs of arrays produced from the re-emission of 10 nm zinc oxide films on structures consisting of connected silver (20 nm) (a) and connected gold (20 nm) triangular structures (b). Gold deposition parameters: Argon partial pressure 3×10^{-4} Torr (4×10^{-2} Pa). Power supply settings (0.030 A, 20 V).

Figure 5-15 confirms that when continuous triangular structures of gold and silver are used as conductors for re-emission experiments, zinc oxide deposits directly beside the conductor in a similar fashion to that observed for platinum. Significantly more material is seen to be deposited than in the case of platinum. This can be attributed to the higher barrier heights of the Schottky contacts formed relative to platinum. The understanding of this mechanism means that the amount and indeed, the regions where negatively charged re-emitted zinc oxide is deposited can be controlled to a large degree.

These results agree with the proposed mechanism whereby negatively charged surfaces of zinc oxide (induced by the SEs generated during the re-sputtering process) induce electric field lines to maintain Gauss's law and ensure that the electric field inside the underlying conductor is close to zero. These electric fields deflect any negatively charged re-emitted zinc oxide species along trajectories dependant on the microstructure of the discrete or continuous conductive regions.

5-2.3 Templates for hydrothermal growth of new zinc oxide structures

Having demonstrated that NSL can be successfully employed to produce arrays of zinc oxide nanostructures, and that these materials occur in regions that lie out of the "line-of-sight" of the deposition source, it was proposed that the fabricated nanostructures could be used to seed the growth of zinc oxide. Zinc oxide is grown by gas [440] or solution [441] phase methods. Gas phase synthesis methods typically require high temperatures (temperatures of 900^{o}C for example are commonly employed [442]). These temperatures have the potential to alter the morphology of our fabricated structures (see for example Figure 4-35). Solution phase synthesis methods however are performed at significantly lower temperatures (typically below 100^{o}C [443], however reactions in sealed vessels can be used for higher temperatures [444]) and therefore considered appropriate for investigation. Precursors for zinc oxide solution growth are numerous and include zinc acetate, zinc hydroxide acetate [445], zinc hydroxide carbonate [446], zinc hydroxide sulfate [445] and zinc nitrate [447]. Zinc nitrate is the most prevalent precursor for template growth methods and was considered appropriate for investigation [448]. Methods for seeding templated growth include growth on zinc substrates [449], solution precipitation [450], spin coating [443], sputter deposition [448], atomic layer deposition [451] and NSL fabrication [452]. While NSL has been used for seeding template growth before (the most similar being the work of Cheng *et al.* where colloidal lithography was used to shield regions of a zinc film for subsequent growth in the ring regions [312]), this is the first time it has been used with re-emitted zinc oxide material in the ring region. This technique also offers the advantage of enabling greater control of where the zinc oxide is deposited with options of ring only, triangle only and ring and triangle being available.

Effect of template composition

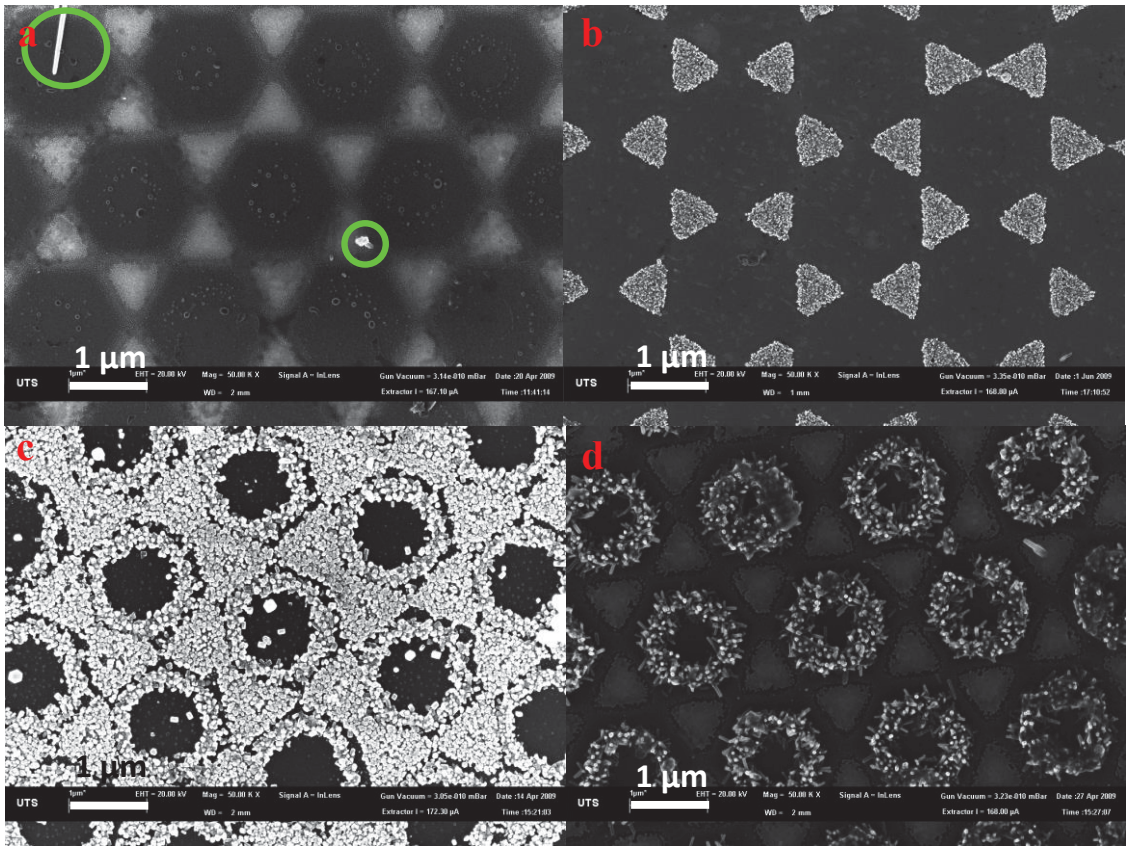

Figure 5-16. SEM micrographs of arrays of fabricated triangular structures by deposition of zinc oxide from zinc nitrate / hexamine solutions onto templates with various compositions. Samples were all incubated for 3 hrs at 90°C in aqueous solution containing equimolar concentrations of zinc nitrate and hexamine (10 mM). (a) Gold (20 nm), green circles indicate zinc oxide material. (b) Zinc oxide (10 nm). (c) Gold (20 nm) / zinc oxide (10 nm). (d) Gold (20 nm) / zinc oxide (20 nm) / gold (20 nm).

The new nanostructured arrays were investigated as templates to seed the hydrothermal growth of zinc oxide. The templates were immersed in aqueous solutions of zinc nitrate and hexamine (10 mM equimolar solutions were reacted at 90°C for 3 hrs) [312]. Gold / zinc oxide / gold sandwich-type array structures were prepared with different thicknesses of gold and zinc oxide to investigate their role in the subsequent zinc oxide growth. The reaction temperature, reactant concentration and template array structure were each found to have a significant influence on the type of zinc oxide structures that formed. Figure 5-16 shows the results of zinc oxide growth experiments using various template structures. Gold-only triangles, zinc oxide-only triangles, triangles consisting of gold capped with zinc oxide, as well as gold / zinc oxide / gold

sandwiches with the associated hexagonal ring structures were investigated. The growth conditions were identical for each substrate used. Importantly, during immersion in the growth solution the substrates were placed face-down to minimise settling of precipitates onto the surface. Figure 5-16 (a) reveals that almost no zinc oxide growth occurs when gold-only arrays are used. Some growth is seen and is highlighted by the green circles. This is in contrast to some reported experiments performed with the substrate facing up where growth is presumably seeded by settled precipitates [419] and also in contrast to physical vapour growth methods where only gold is required to catalyse growth but at significantly elevated temperatures [453]. Figure 5-16 (b) shows that limited growth occurs when zinc oxide templates are used without gold and that growth occurs only directly on top of the triangles. Significantly more zinc oxide growth is seen in Figure 5-16 (c) both on top of and around the edges of the triangular structures, which consist of 10 nm of zinc oxide on top of 20 nm of gold. It is apparent that the NSL-deposited zinc oxide seeds the subsequent growth but the combination of gold and zinc oxide in the triangles significantly increases zinc oxide growth. Interestingly, as well as growth on the triangular template surfaces, the ring-shaped zinc oxide deposits formed in the hexagonal voids between the triangles also facilitated growth. Figure 5-16 (d) shows zinc oxide growth using gold / zinc oxide / gold sandwich-type templates, here the top layer of gold caps the triangular pyramid limiting zinc oxide growth to the ring shaped regions.

Effect of solution concentration

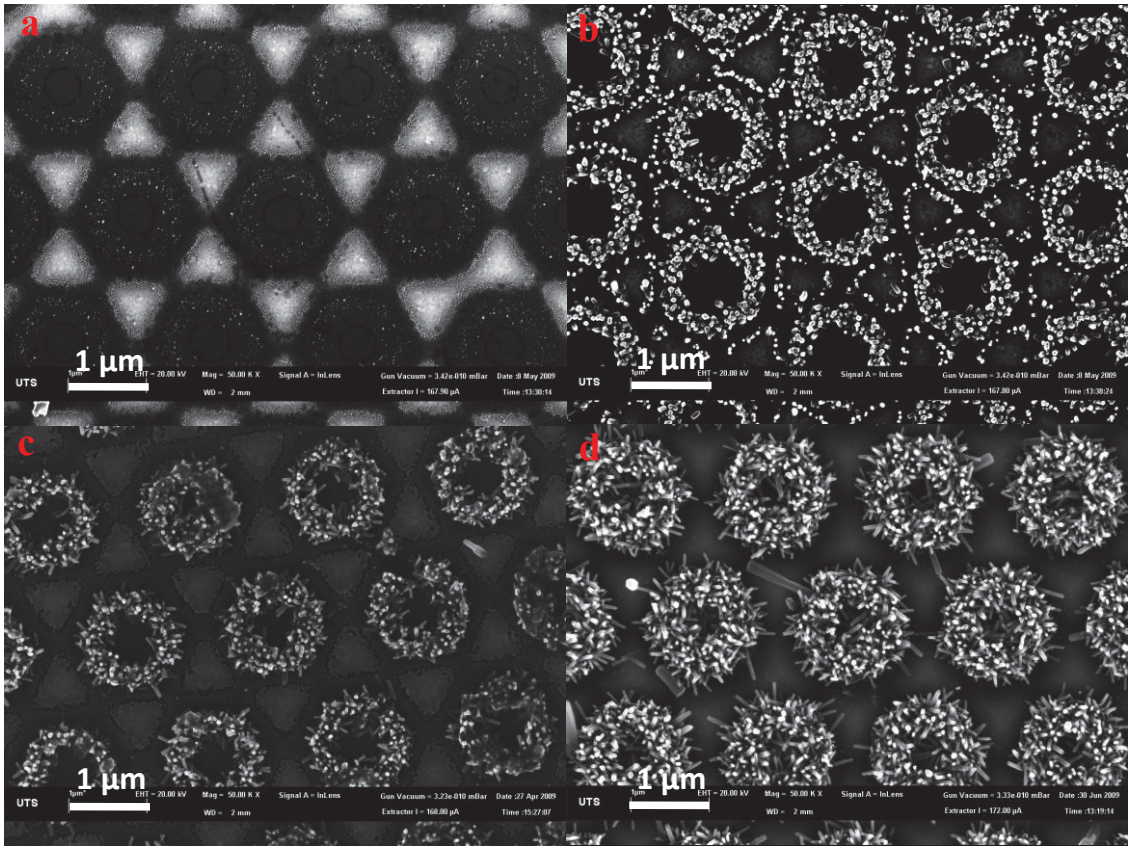

Figure 5-17. SEM micrographs of arrays fabricated by deposition of zinc oxide from zinc nitrate solutions of various concentrations onto templates consisting of gold (20 nm) / zinc oxide (20 nm) / gold (20 nm) and incubated at 90°C for 3hrs. Concentrations of zinc nitrate / hexamine are; (a) 0.1 mM. (b) 1 mM. (c) 10 mM. (d) 0.1 M.

Increasing the concentration of zinc nitrate and hexamine in the growth solution resulted in amplified zinc oxide growth on the templates. Figure 5-17 (a)-(d) shows examples of gold (20 nm) / zinc oxide (20 nm) / gold (20 nm) templates immersed in zinc nitrate and hexamine solutions of concentrations ranging from 0.1 mM to 0.1 M. As well as the amplification in coverage, higher concentrations resulted in rod-like structures with increasing diameters. These results are in agreement with those published recently by Xu *et al*. [454].

Evolution of solution growth during incubation

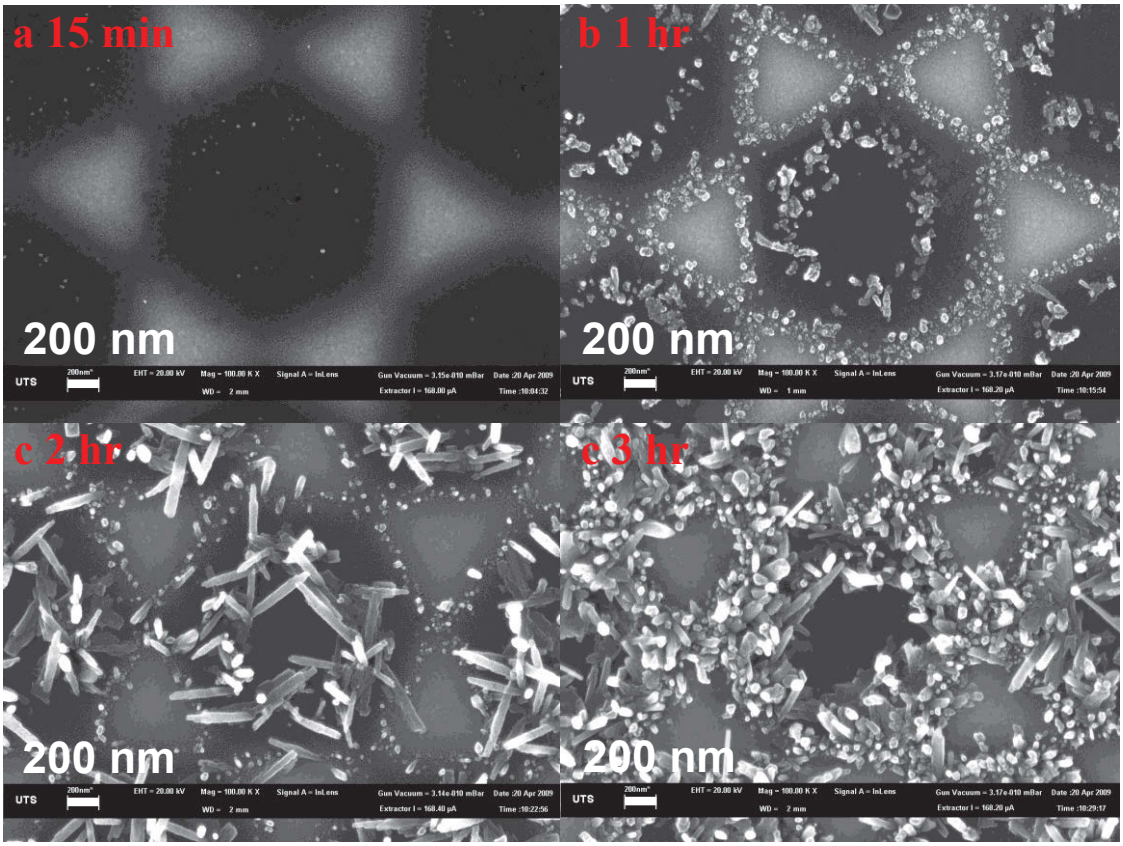

Figure 5-18. SEM micrographs of arrays fabricated by deposition of zinc oxide from zinc nitrate solutions of various incubation times onto templates consisting of gold (20 nm) / zinc oxide (20 nm) / gold (20 nm) nanostructures. 10 mM concentrations of zinc nitrate / hexamine were incubated at 90^{o}C for; (a) 15 min. (b) 1 hr. (c) 2 hrs. (d) 3 hrs.

Figure 5-18 shows the evolution of solution deposited zinc oxide morphology over time. It can be seen from the images that there is a latency period before solution growth begins to occur with no visible growth in (a). Over time the structures are observed to develop from initially granular type structures (b) to higher aspect ratio, faceted, rod-like structures (c) and (d).

Effect of incubation temperature

The template growth of zinc oxide on samples incubated at 80, 90 and 150^{o}C was also examined. Amplified growth was observed with increasing temperature (Figure 5-19) in agreement with previous studies [454-456]. At 150^{o}C, many of the zinc oxide rods formed tube-shaped structures with clean, hexagonal facets (Figure 5-20). Such structures have been reported to form at 85^{o}C [457] and 90^{o}C [458, 459] reaction

temperatures. The zinc oxide tubes were synthesised by both electrochemical (She *et al.* [457]) and hydrothermal (Tong *et al.* [458] and Ashfold *et al* [459]) methods. She *et al.* performed electrodeposition from a zinc chloride solution to produce rods and the subsequent reversal of the applied potential which etched preferentially into the centre of the zinc oxide tubes via a proposed defect selective method. Tong *et al.* observed tube and volcano-like structures from extended reaction times which they attributed to the Ostwald ripening process occurring favourably on the polar region of the zinc oxide surface. Ashfold *et al.* reported tube formation from extended reaction times where the pH of the reaction solution passed a critical value and the formation of the zinc hydroxide intermediate became thermodynamically unfavourable. It is reasoned that at elevated temperatures the reaction proceeds at a higher rate, and the formation of these tubes normally observed at longer reaction times is observed here.

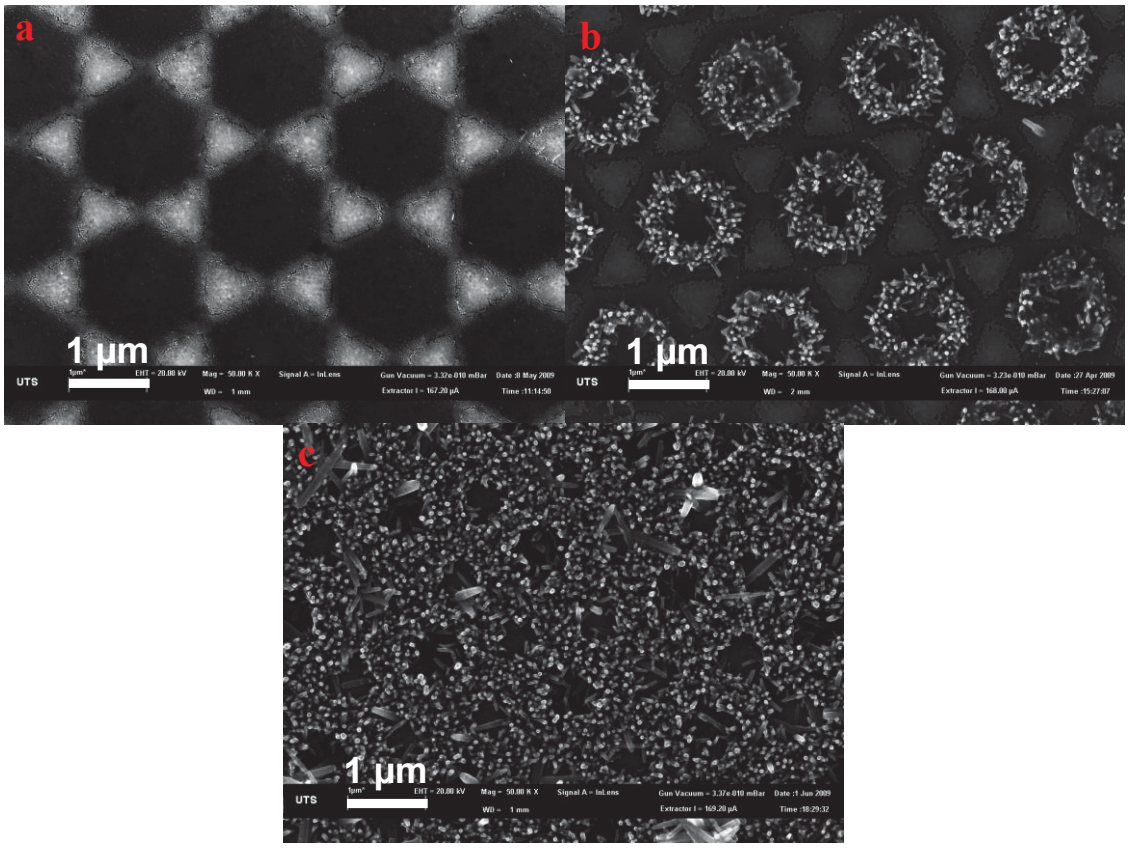

Figure 5-19. Scanning electron micrographs of 20 nm gold / 10 nm zinc oxide / 20 nm gold nano-sandwiches grown hydrothermally in 10mM $ZnNO_3$ and hexamine solutions for 3h. Incubation temperatures were varied from (a) 80°C, (b) 90°C and (c) 150°C. These images show significant change in the amount and diameter of zinc oxide nanorods produced.

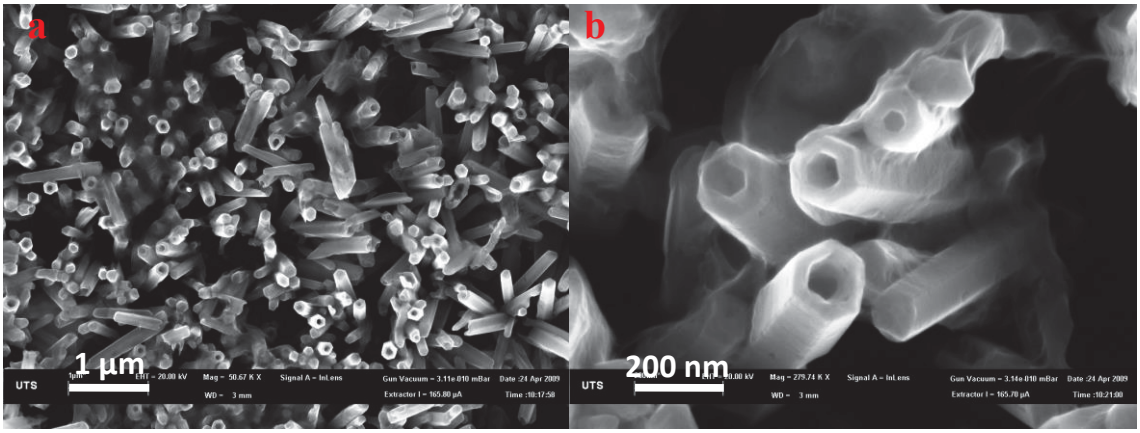

Figure 5-20. Low (a) and high (b) magnification scanning electron micrographs show that at elevated temperatures (150°C) of growth solution, zinc oxide exhibits hexagonally-faceted tubes with ~200 nm diameter and ~1-2 µm length.

Effect of an applied potential

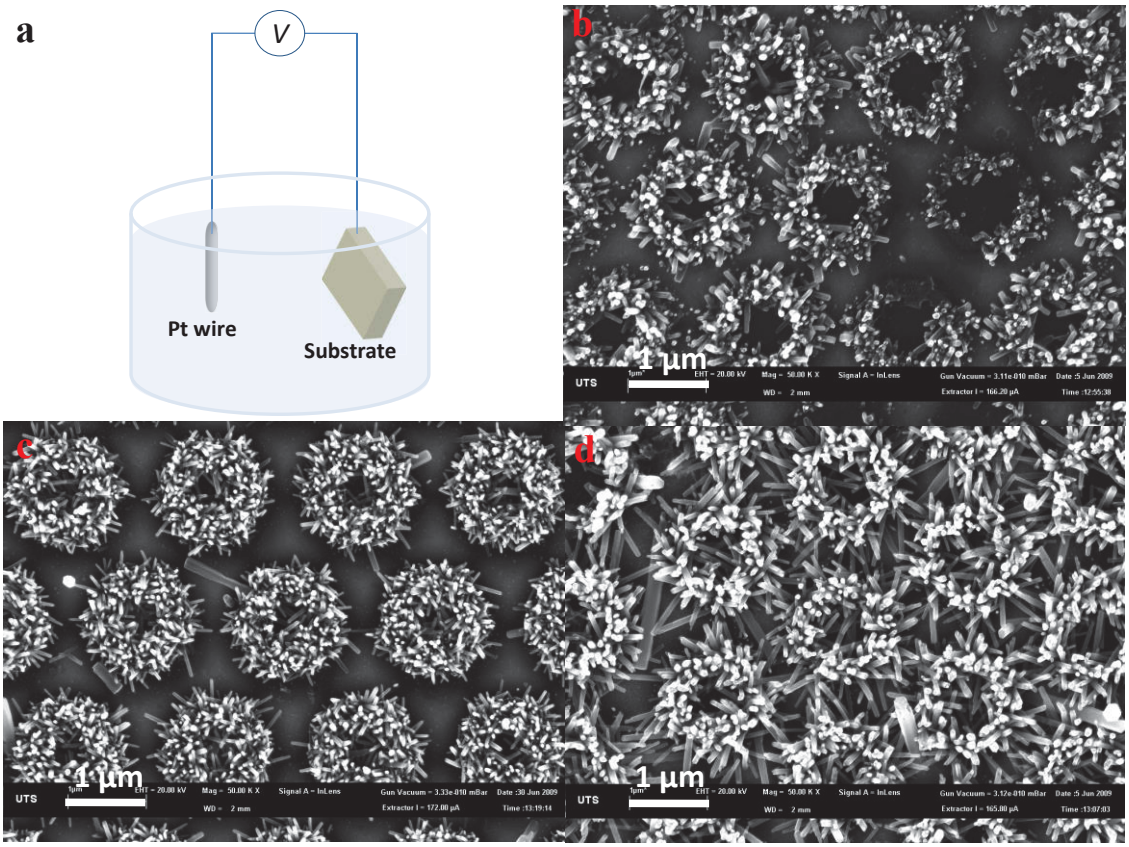

Figure 5-21. (a) Schematic illustration showing the apparatus used to apply bias during zinc oxide growth. (b)-(d) SEM micrographs of arrays fabricated by growth of zinc oxide from zinc nitrate solution on templates consisting of gold (20 nm) / zinc oxide (20 nm) / gold (20 nm) at 90°C for 3hrs with various applied potentials; (b) -0.5V. (c) 0V. (d) +0.5V potentials.

An applied bias has been reported to affect the rate of growth of zinc oxide structures, which deposit on the cathode [418, 460]. To examine the effect of applied bias on the zinc oxide growth templates, the experimental set up shown in Figure 5-21 (a) was assembled. Substrates were immersed in a growth solution and a potential of either 0, +0.5 or -0.5 V (with respect to the counter-electrode, where +0.5V indicates that the substrate was cathodic) was applied. The SEM micrographs shown in Figure 5-21 (b)-(d) reveal that applying a potential to the samples during growth had a significant impact on resultant structures. An applied potential of -0.5 V diminished growth while a potential of +0.5 V resulted in amplified growth relative to the sample with 0 V applied. This indicates that, in this environment, zinc can be conveyed to the surface of a growing crystal in some positively charged complex.

Cathodoluminescence experiments

Cathodoluminescence (CL) measurements confirmed the composition and highlighted some local stress properties [461, 462] of some zinc oxide nanostructures grown by template and solution precipitation. CL spectra from the ring-shaped zinc oxide deposits reveal a weak excitonic ultra-violet peak located at 3.22 eV (385 nm) along with a slightly stronger green luminescence peak at around 2.5 eV (~495 nm), which is generally attributed to oxygen related surface and bulk recombination centres in zinc oxide [463]. A typical CL spectrum exhibited by the zinc oxide nanostructures is shown in Figure 5-22 (c) and (f). The CL emission is comprised of a strong red luminescence peak centred at 1.6 eV (~775 nm) and a weak excitonic near band edge emission at 3.22 eV. The red luminescence peak has been assigned to a donor-acceptor pair transition between neutral effective mass donors and V_{Zn}^{-} acceptors [464]. CL imaging (Figure 5-22 (e)) reveals that the red luminescence increases from the base of the nanowire and is strongest at its tip, suggesting that the donor-acceptor pair concentration is highest at the growth ends. These data indicate that the template structure as well as the zinc oxide growth times and temperatures have a significant effect on the type of native defect and their distribution within the zinc oxide nano-structures.

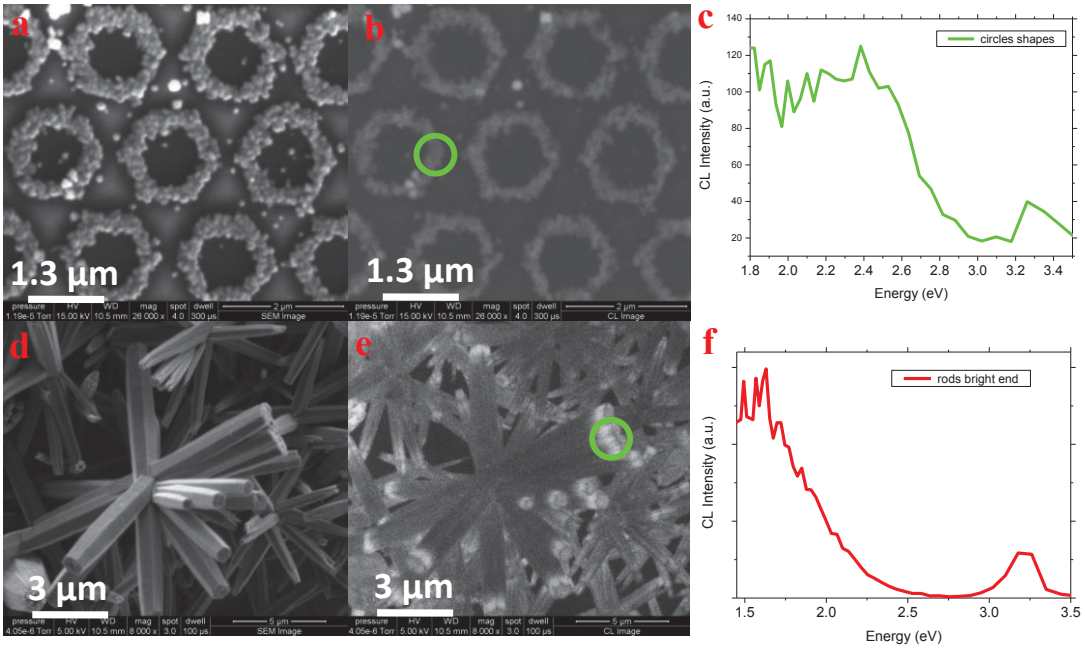

Figure 5-22. SEM micrographs of (a) zinc oxide ring and (d) solution precipitate with their corresponding cathodoluminescence (CL) images ((b) and (e) respectively). Cathodoluminescence (CL) spectra of the ring (c) and precipitate (f). Green circles indicate regions were spectra were acquired. Spectra and images acquired by Professor Matthew Phillips.

5-3 Conclusions

In summary, arrays of gold / zinc oxide triangles and zinc oxide rings were fabricated on silicon substrates using nanosphere lithography. The rings, which possess a degree of hexagonal symmetry, are evidently formed by the re-emission of negatively charged zinc oxide from the upper surfaces of the triangles. This phenomenon required the presence of an underlying layer of conducting material capable of forming a Schottky barrier with the deposited zinc oxide. The barrier height of the Schottky contact formed directly affected the amount of negatively charged re-emitted zinc oxide deposited. The morphology of the conducting layer was found to control the trajectories of negatively charged re-emitted zinc oxide species. The rings of zinc oxide can, in turn, serve as nuclei for the subsequent development of the zinc oxide crystals from an aqueous growth solution. Where the zinc oxide growth occurs as well as the amount of growth can be controlled by the type and the amount of materials present in the template.

Further control of the growth could be exercised by varying the growth solution concentration or temperature, as well as by applying an external potential.

Chapter 6:

General Conclusions / Future Directions

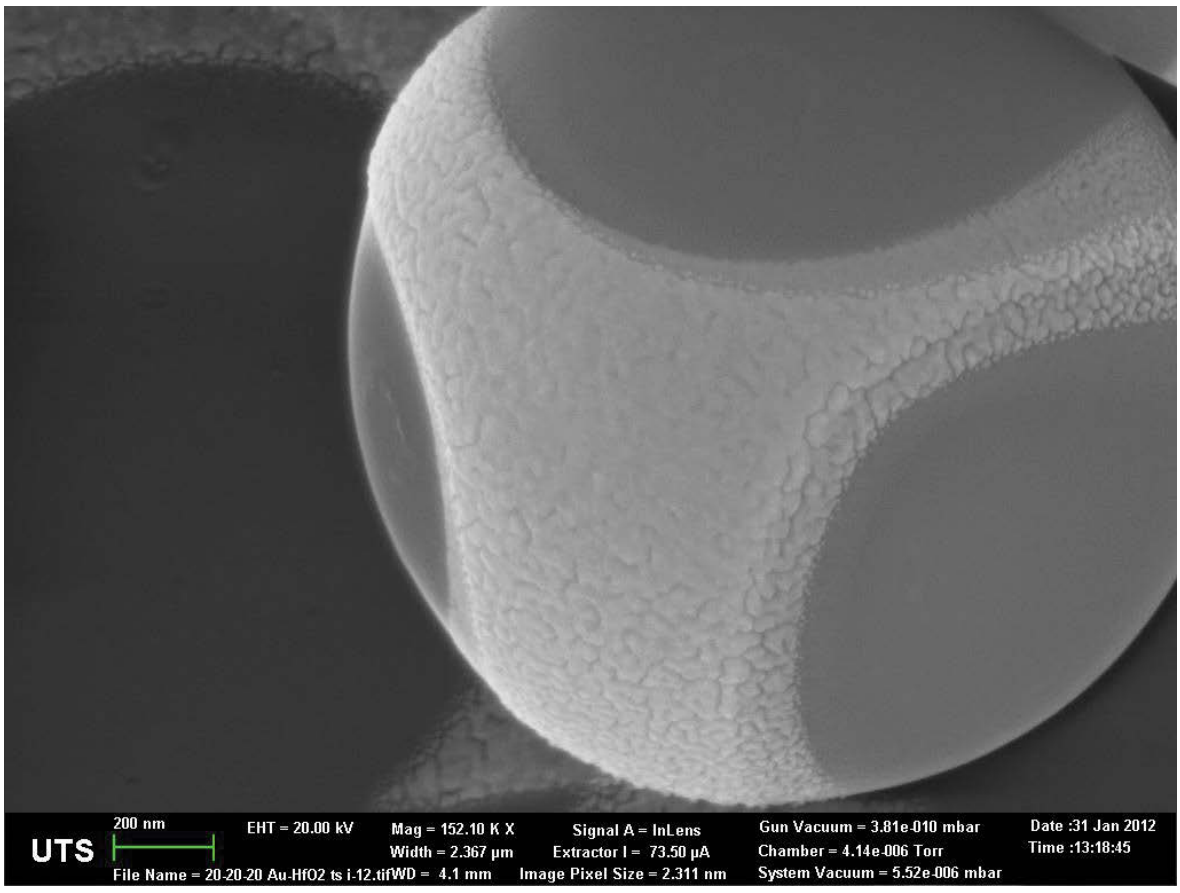

6 General conclusions

6-1 General discussions and conclusions

The primary aim of this project was to fabricate novel nanoscale capacitor devices and characterise their charge storage capabilities. This aim was achieved, along with some unanticipated findings.

With regard to the fabrication of nanoscale capacitors, the use of PS spheres together with metal / metal oxide deposition was found to be entirely feasible. Experimental conditions were developed such that PS spheres with diameters from 200 – 1500 nm demonstrated long range close packing and gave reproducible results. The size of the nanocapacitor devices could be adjusted by use of larger or smaller spheres. The use of 1500 nm diameter PS sphere gave ~550 nm edge length devices while 200 nm and 900 nm diameter spheres gave ~50 nm and ~250 nm edge length devices, respectively.

The metal / metal oxide deposition method (sputter or evaporative deposition) was found to have an effect on the structure of the resultant nanostructures. Control of the kinetic energy of the deposited materials resulted in different surface mobilities during film growth and as a consequence, the size and morphologies of the devices can be controlled to a certain extent.

The developed nanofabrication techniques enabled the construction of nanocapacitors containing a range of dielectric materials. The newly developed larger devices had charging timescales that enabled the various phases of charging to be examined by SEM techniques while the smaller devices (developed prior to this work) charged rapidly and so time constant measurements were impossible using this technique. Estimates of the time constant of the nanocapacitors were made using SEM images acquired during charging and subsequent fitting of the grey-scale intensity data extracted from the images.

The *RC* values measured by this technique are consistent with those anticipated from the material properties of the dielectric interlayer. Importantly, this work shows that nanoscale capacitor devices may be characterised without the need to attach any wires or leads.

During the fabrication of nanoscale capacitors it was found that unusual arrays of gold / zinc oxide triangles and zinc oxide rings could be formed on a silicon substrate. This process depended on the re-emission of zinc oxide from the upper surfaces of the triangles. It was found that an underlying layer of conducting material on the base of the triangle was necessary for re-emission. The rings of zinc oxide proved to be useful as nuclei for the subsequent development of the zinc oxide crystals from an aqueous growth solution.

6-2 Future directions

6-2.1 Nanosphere Lithography

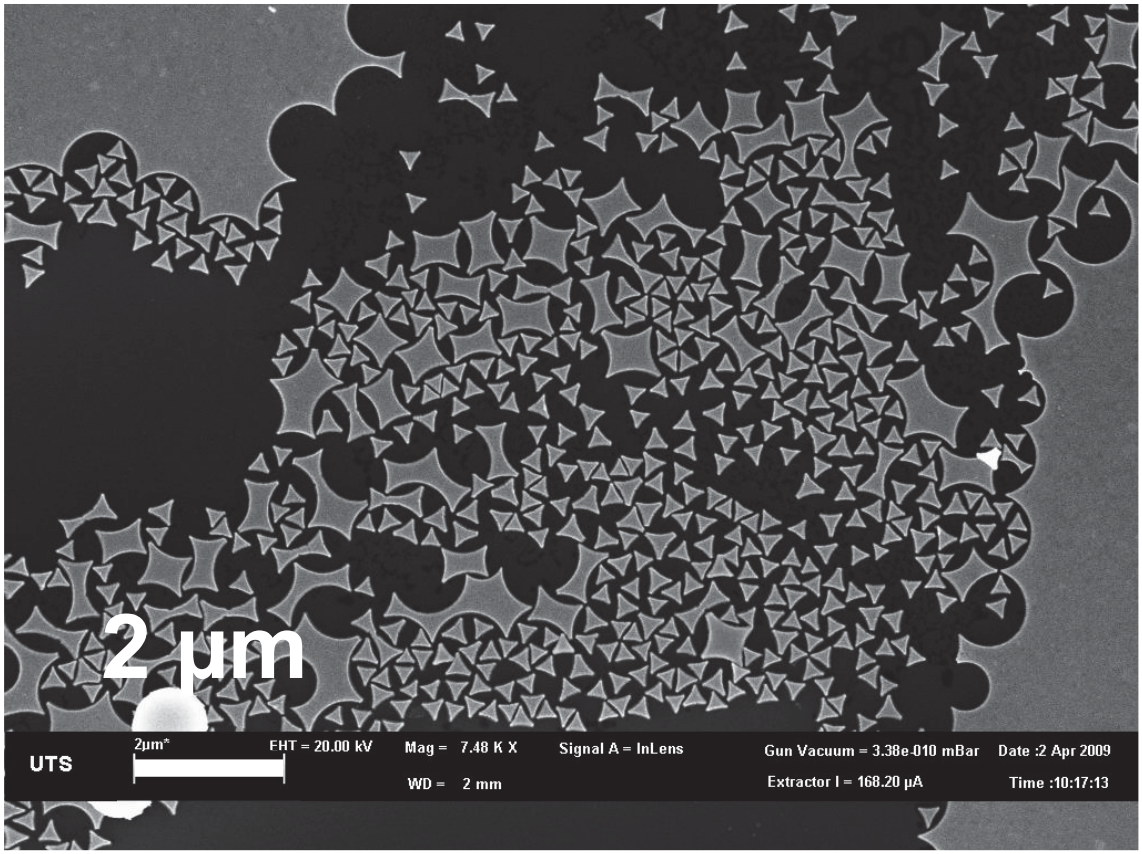

Figure 6-1. SEM micrograph of structures produced with 900 nm PS spheres coated with 20 nm of gold following substrate sonication in dichloromethane for 5 min.

During work conducted to optimise NSL parameters (Chapter 3), an unusual phenomenon was observed and is depicted in Figure 6-1.

The image is of a silicon surface that had been coated with 900 nm PS spheres and then 20 nm of gold followed by sonication in DCM for 5 minutes. However, this sonication period proved to not only remove most of the spheres but also dislocated a large portion of gold deposited thorough the mask voids. Other researchers have highlighted the importance of short sonication times [332-334]. The area in the image shows a high concentration of mobile structures collected together during the rinsing procedure. While undesirable for the current project, a fabrication technique where gold (or other metallic) structures are fabricated via the standard NSL method described in Chapter 3 and subsequently isolated by extended sonication could be used to produce solutions of discrete metallic particles for optical [465] or catalytic [466] applications.

Different electrode materials and deposition powers were shown to produce electrically continuous arrays of materials. This approach could also be used to fabricate arrays of electrically connected capacitors. These arrays could form nanoscale "batteries" similar to the electrically connected Leyden Jars that were prevalent before the Galvanic Cell became popular.

6-2.2 SEM charging of nanoscale capacitors

The nanocapacitors synthesised in Chapter 4 could be characterised via STS or CAFM. This characterisation would allow comparison to the results from the SEM charging experiments. This work has not been done before as very few research groups use NSL to fabricate discrete nanoscale capacitors.

Carbon contamination was found to be ubiquitous. Several techniques were explored to minimise this with extended soak times in DCM and vacuum annealing showing promising results. Figures 4-34 and 4-35 show that a reduction in surface carbon is possible. Further work (for example, EDS experiments) would be required to obtain more quantitative data on the degree of carbon remaining after these carbon reduction techniques.

Capacitors made with larger or smaller sphere masks than those investigated here could be fabricated and examined. Changing the physical size of the capacitors would increase or decrease the length of time required to fully charge the devices (for this reason relatively large latex spheres were used in this thesis). The differences in physical sizes, however, should result in the measured time constants being identical.

Nanocapacitors with hafnia dielectrics demonstrated different characteristics during the charging process compared to the other metal oxides investigated. Plots of grey-scale intensity *vs.* time gave very different results relative to other investigated dielectrics with an extended time for Region 1 (charge build-up at the conductor / dielectric interface). Changing parameters such as the charging time, thickness of the deposited dielectric, or size of the devices may shed light on the different behaviour of this material.

As described above, vacuum annealing experiments were investigated to remove carbon from samples synthesised via NSL. These experiments resulted in the surface area minimisation of the top gold electrode. This contraction should alter the capacitive properties of the device by decreasing the area of dielectric polarisation. This can provide another method of altering the electrical properties of devices fabricated in the future.

Of all of the essential components of electronic circuitry, the capacitor appears to be the least studied with regard to miniaturisation to the nanoscale. An expansion of the work presented here would be to extend the techniques developed in this project to the characterisation of capacitive properties of other nanoscale materials where the formation of nanoscale contacts is problematic. For example, gold nanoparticles attached to insulators (as shown schematically in Figure 6-2) could be probed using the SEM charging / grey-scale imaging technique.

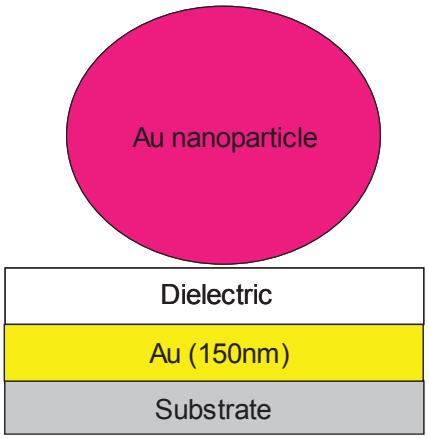

Figure 6-2. Attachment of a gold particle to a grounded dielectric for SEM investigation into the capacitive properties of the particle / dielectric / metal system.

Furthermore, utilising the sintering of gold nanoparticles (discussed in appendix), various sizes of gold particle-based capacitors may be investigated. Examples of different sized gold particles obtained during the current work are shown in Figure 6-3. Citrate stabilised gold nanoparticles attached to a silicon substrate via a self-assembled monolayer of thiol-terminated silane molecules and shown in panel (a). Subsequent sintering of the sample by vacuum annealing the substrate at 200^{o}C for three hours removed the citrate stabilising molecules and resulted in some cases in the coalescence of neighbouring particles (panel (b)).

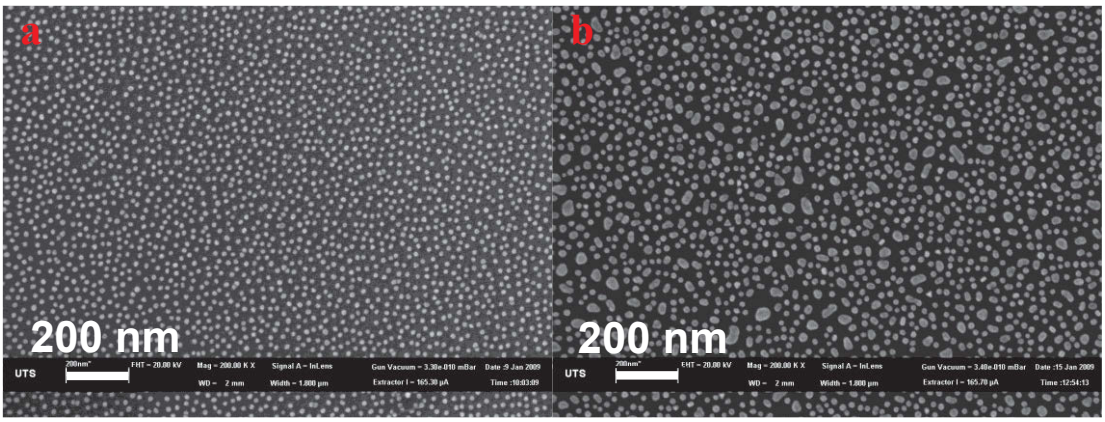

Figure 6-3. SEM micrographs of citrate stabilised gold nanoparticles attached to a silicon substrate via a silane / thiol thin film both before (a) and after (b) sintering. Particles were sintered by vacuum annealing at 200^{o}C for three hours.

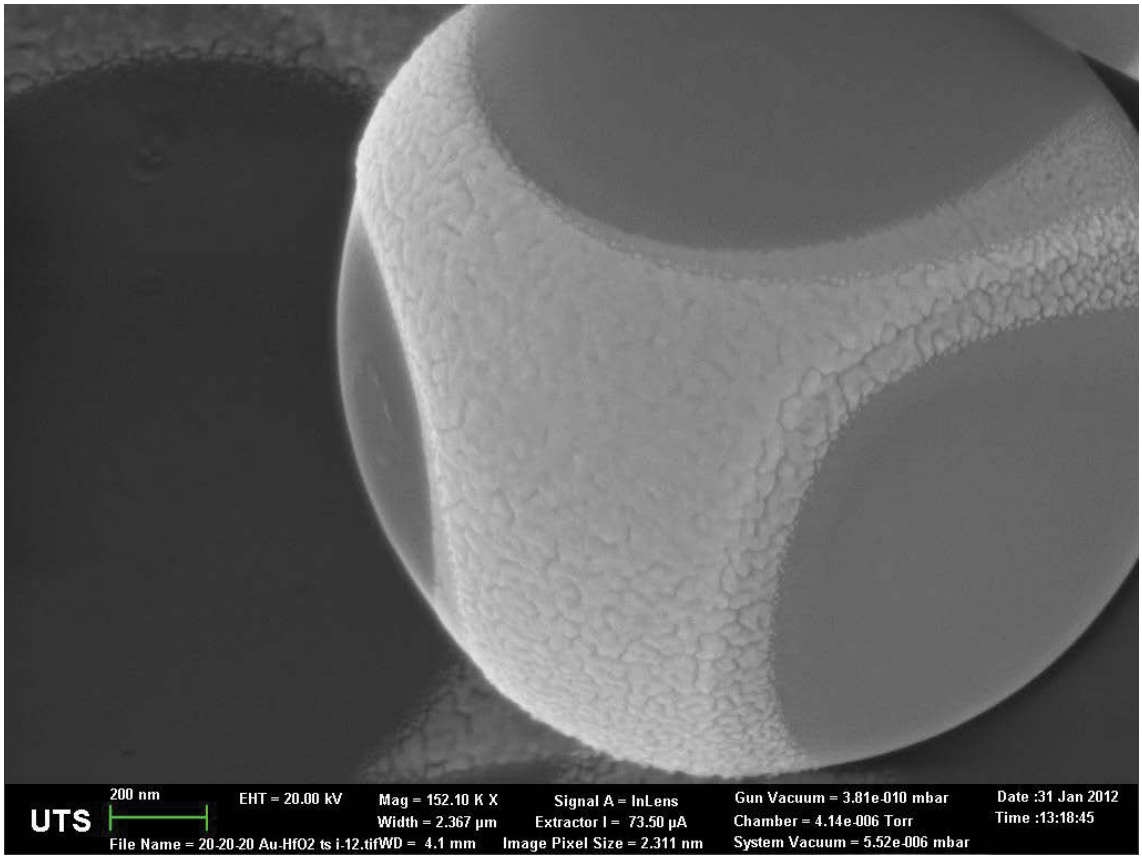

Figure 6-4. SEM micrograph of 20 nm gold / 20 nm hafnia / 20 nm gold nanostructured thin films deposited on a 1500 nm PS sphere (gold layers have been offset for clarity).

During the course of this project, it was found that metal / metal oxide / metal structures could be synthesised on curved surfaces. Figure 6-4 depicts a gold / hafnia / gold multilayer structure formed on the surface of a PS sphere. This demonstrates that, in principle, capacitors can be synthesised on curved surfaces. Furthermore, the SEM charging techniques demonstrated in this project could be used to characterise capacitors on spheres.

In future studies, a nano-circuit could be constructed consisting of a capacitor, switch, and some form of nanoscale material that undergoes a detectable change from the electrons supplied by the capacitor. This would provide a proof of concept for a device that can perform meaningful work. The capacitors described here could serve as electron sources and materials such as gold nanoparticles (see Appendix) could be sintered to form conductive wires.

6-2.3 Re-emission of Zinc Oxide and Solution Growth Experiments

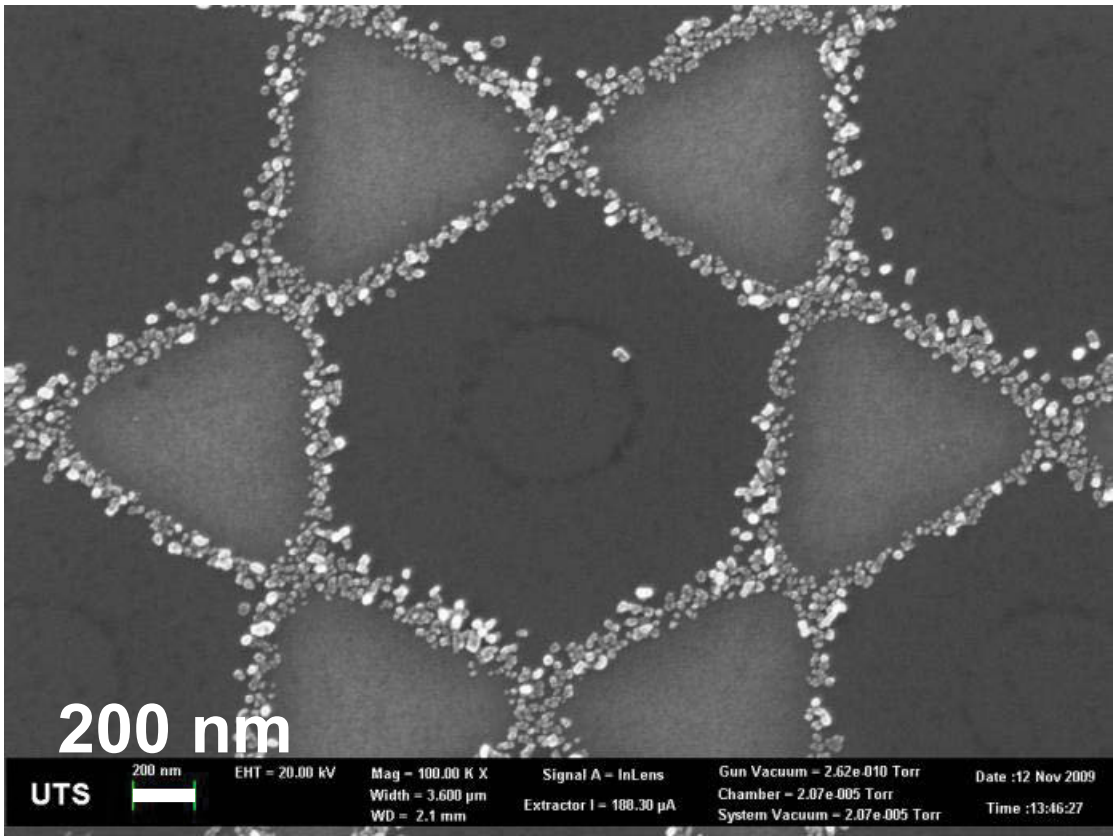

Figure 6-5. SEM micrograph of continuous structures fabricated by deposition of platinum (20 nm) / zinc oxide (10 nm) through a NSL mask composed of hcp 1500 nm PS latex spheres.

Re-emitted zinc oxide materials have been deposited on regions very close to or touching the conducting triangular lattice structure (in this case, platinum see Figure 6-5). These structures may be applied to solution growth experiments to fabricate arrays of zinc oxide microstructures connected to a long range electrically continuous electrode. The improvement of the electrical conductivity of produced samples (by fabricating conducting triangular structures that are in electrical contact) has the potential to enhance the properties of the material and potentially aid future applications. Experiments to alter the physical size of the platinum triangles similar to those performed in Chapter 3 (see Figure 3-15), possibly improving the conductivity further, could aid in future development for applications such as ultraviolet lasing of nanowire arrays [467].

Appendix

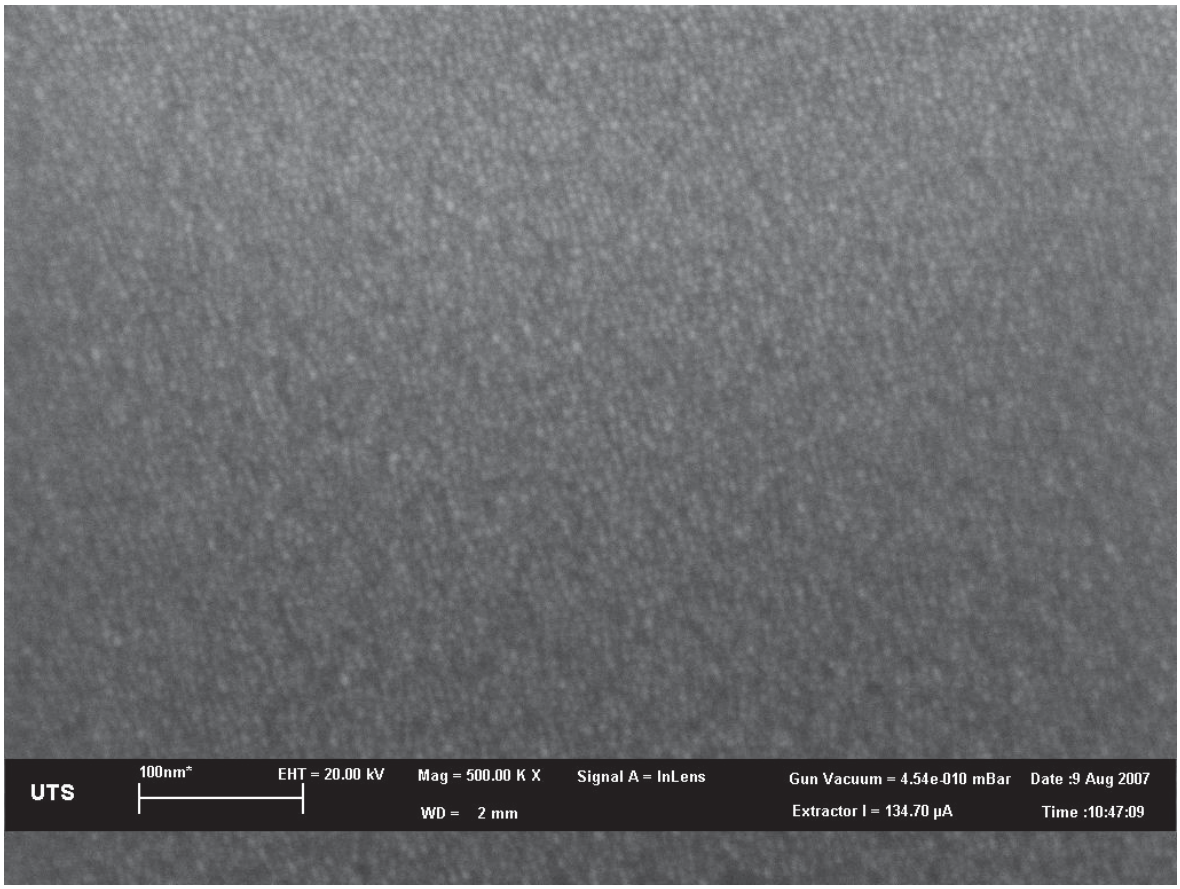
UTS
100nm*
EHT = 20.00 kV
Mag = 500.00 K X
Signal A = InLens
WD = 2 mm
Gun Vacuum = 4.54e-010 mBar
Extractor I = 134.70 µA
Date :9 Aug 2007
Time :10:47:09

Appendix

7 Gold Nanoparticles for Charge Transport

7-1 Introduction

Isolated nanoparticles of gold, as well as alternate metals such as silver and copper are capable of storing small amounts of charge. The relatively thin and non-polarisable dielectric of alkanethiol chains restricts large amounts of charge being stored before the electronic surface potential of the particles become too large and quantum tunnelling to nearby objects occurs.

The plasmon resonance of gold and silver nanoparticles also lends to their use in photonic applications [468-473]. This plasmon resonance is a consequence of electrons oscillating inside the conducting region of the particle. The energy required to excite an electron into this oscillation is proportional to the size of the particle. Consequently photonic applications use nanoparticles of specific sizes to absorb light of specific wavelengths.

While large collections of thiol, amine or alkyne stabilised particles in the solid state are normally semiconducting / insulating, they can undergo a process known as "sintering", where stabilising ligands are removed from particles and surface energy minimisation forces drive the formation of continuous, conducting metallic films. Inkjet-printing-like techniques as well as stamp-like methods of depositing nanoparticle inks followed by their subsequent sintering to conducting films has been proposed as a route towards ultra-low cost electronic devices.

Particles can be sintered to form conducting features i.e. wires and interconnects for applications such as thin film transistors (TFTs) and photovoltaics [474-476]. Direct heating is the most prevalent method for sintering particles, however the mechanism behind the sintering process has been investigated previously at UTS [477], and oxidation of the stabilising ligand has been shown to drive the sintering process. Room temperature sintering of alkanethiol stabilised particles was demonstrated in a strongly oxidising environment. Questions however still remain about the molecular form of the species sublimated during the sintering process, and

what remains on the gold surface after sintering has occurred. Further investigations into the thiol oxidation during the sintering process are required

Aggregations of precious metal nanoparticles such as gold, platinum or silver may be readily sintered to provide electrically continuous materials. A number of applications and scientific investigations have been reported [478-485] but the interest in this phenomenon relevant to this thesis lies in the application of such sintered materials as nanoscale change transporters (i.e. wires). Some efforts have been directed toward developing formulations that sinter at the lowest practicable temperatures to enable inks made from these nanoparticles to be applied to polymer or other heat-sensitive substrates [479, 486]. In work performed prior to PhD studies, it was shown that sintering can be facilitated by an oxidising environment and the temperature at which it occurs can be brought down to 25ºC by these means [486]. The 5 nm diameter gold nanoparticles are susceptible to the onset of sudden, exothermic sintering. The marked exothermicity of the process is primarily due to the high specific surface area of the nanoparticles and the consequent rapid release of this energy as heat when the surfaces are consumed during sintering. The mechanism by which the protective thiol ligands are removed from the particles is therefore important but not fully understood.

Here, X-ray Photoelectron Spectroscopy (XPS), Thermogravimetric Analysis (TGA), Differential Scanning Calorimetry (DSC) and mass spectrometry (MS) are used to elucidate the mechanism by which sintering in very small, 1-butanethiol-stabilised, gold nanoparticles is accelerated in oxidising environments and the role of the protecting ligand in this process.

7-2 Experimental Methods

7-2.1 Techniques Used In This Work

Thermal Gravimetric Analysis / Differential Scanning Calorimetry

TGA records sample mass as a function of temperature. Samples are placed in a crucible (usually platinum / rhodium alloys or alumina), attached to a thermocouple (thermistors are generally not used due to their relatively low temperature ranges) as well as a high precision balance (e.g. microbalance or torsion balance). Samples are loaded into sealed programmable furnaces (capable of accepting gas flows for

atmospheres such as nitrogen, argon, air etc) which performs functions such as heating samples at a constant rate or holding samples at isotherms for a set period of time. TGA can provide information about sample changes such as oxidation, sublimation or decomposition.

In this work, TGA was used to study the mass loss (corresponding to the removal of the stabilising ligand) of 1-butanethiol stabilised gold nanoparticles.

Figure 7-1. Photographic image of the sample holder configuration of a SDT 2960 with simultaneous TGA-DSC. The sample under analysis is in the left crucible, the right crucible is a reference used for DSC measurements

Differential scanning calorimetry is an associated technique where sample-containing crucibles are heated in parallel with a reference crucible (Figure 7-1) so that thermodynamic information about the sample can be extracted. For example, upon heating, a sample may undergo a recrystallization, which is an endothermic process. This process would not result in a mass loss, and consequently would not be measurable by TGA. Endothermic reactions, however, extract heat from the system (in this case the platinum crucible) which lowers the temperature of the sample holder (and the thermocouple attached to it) relative to that of the reference. Therefore a difference in thermal energy will be recorded at temperatures where thermodynamic processes occur. Other examples of thermodynamic processes measurable by DSC are sublimations, combustions and dehydrations.

DSC was used here to study the exothermic surface area minimisation and endothermic sublimation of stabilising ligands that occurs during the sintering of 1-butanethiol stabilised gold nanoparticles.

Mass Spectrometry

MS measures the charge to mass ratio of an ionised material. Species are ionised by electron or chemical ionisation (for gases and vapours), while electrospray ionisation is common for solids and liquids. Once ionised, atomic species or molecular fragments are accelerated by an electric field and subsequently deflected by a magnetic field. The magnetic field deflects species depending on their charge to mass ratio. The amount of deflection can be mathematically expressed by the combination of the Lorentz force law and newtons second law of motion. For organic materials (especially large ones), ionisation commonly results in fragmentation of the original structure.

In this work, MS was utilised in conjunction with TGA in both air and argon atmospheres. Electron ionisation was also used in a residual gas analyser MS system in HV sintering experiments.

X-Ray Photoelectron Spectroscopy

XPS is a quantitative spectroscopy technique used to measure the atomic composition of samples. Samples are irradiated with photons of X-ray energies and the kinetic energy and number of electrons ejected from the sample is recorded. XPS is generally performed in HV or ultra-high vacuum (UHV) conditions. XPS can also provide information on a materials chemical state by measuring shifts in a materials binding energy (eV).

In this work, XPS is used to measure the change in intensity of the carbon / gold and sulfur / gold ratios, as well as to measure the chemical shifts of the sulfur species during the sintering process.

7-2.2 Experimental details

General.

Tetrachloroauric acid was prepared using a literature procedure [487]. 1-Butanethiol (Aldrich), tetraoctylammonium bromide (Aldrich), toluene (Fluka),

sodium borohydride (98% Ajax), sodium sulphate (99% Aldrich), cyclohexane (99.5% Lab Scan), methanol (99.9% Aldrich), dichloromethane (99.5% Lab Scan), gold (99.99%, AGR Matthey, Australia), and chromium (99.99% Fluka) were all used as received. MilliQ water (18 MΩ cm^{-1}) was used in all procedures.

Synthesis of Gold Nanoparticles.

Butanethiol-stabilised gold nanoparticles were synthesised by a modified Brust procedure [488] similar to that of Wu *et al.* [479]. Tetraoctylammonium bromide (8.75 g, 16 mmol) was dissolved in toluene (300 mL). A solution of tetrachloroauric acid ($HAuCl_4 \cdot 3H_2O$, 1.57 g, 4 mmol) in water (150 mL) was then added to the toluene with rapid stirring. The organic phase changed in colour from yellow to dark orange upon formation of a gold/surfactant complex. After 2 minutes, a solution of 1-butanethiol (0.36 g, 4 mmol in 50 mL of toluene) was added with vigorous stirring. After stirring for 10 minutes, the solution mixture was cooled in an ice-water bath. A freshly prepared solution of sodium borohydride (1.51 g, 40 mmol) in 100 mL of water was added over a period of 30 seconds whereupon the mixture became dark brown/black in colour. The mixture was stirred vigorously for 3 h and then the organic phase was separated, washed three times with water, dried with anhydrous sodium sulfate and filtered. The filtrate was reduced to a volume of ~50 mL using a rotary evaporator and 50^{o}C water bath. The solution was then added drop-wise to 200 mL of vigorously stirred methanol. The precipitated particles were isolated by centrifugation. The particles were purified by redissolving in 20 mL of cyclohexane followed by re-precipitation in 200 mL of methanol, centrifuging and drying. 0.755 g of a black powder was collected.

Mass spectrometry and Thermal Analysis.

MS of samples heated in vacuum was carried out at a facility at the Taiwan Synchrotron. The overall pressure of the chamber was in the 10^{-8} mbar range and increased to around 10^{-6} mbar from outgassing during the sintering process.

Thermogravimetric analysis (TGA) experiments were performed using SETRAM setsys TG-DSC 15 with simultaneous differential thermal analysis (DTA)−TGA. A heating rate of 2 °C.min^{-1} was used in an argon gas stream of cylinder purity. Simultaneous TGA−MS experiments were conducted using a Quadrupole mass

spectrometer (model Thermostar QMS 200 M3) from Balzers Instruments in a platinum crucible. Survey scans were performed and the current intensities of the most prominent masses were examined.

Synchrotron XPS Experiments.

Silicon substrates (~1 cm^2, *p*-type(*100*)) were prepared by sonication in ethanol for 10 minutes followed by thorough rinsing with water and then drying in a stream of nitrogen. A chromium film (100 nm) was deposited by evaporative deposition using a Denton bell jar DV-502 vacuum chamber equipped with a tungsten filament for heating. Film thickness was monitored by a calibrated Maxtek TM-100 film thickness monitor.

A solution of gold nanoparticles (10 mg in 200 μL of dichloromethane) was prepared and 50 μL drops were deposited onto substrate to completely cover the surface with particles.

Photoelectron spectroscopy was performed using a wide-range spherical grating monochromator (WR-SGM) beamline at the National Synchrotron Radiation Research Centre (Taiwan, ROC). XPS data were collected using a VG CLAM2 Triple-Channeltron electron energy analyser. Specimens were heated in an adjacent chamber equipped with a heating stage and heated for 2 minutes (either under UHV or air) and then re-introduced to the XPS chamber for data collection. Scans recorded on the same regions to monitor X-ray beam damage revealed no significant changes within the measurement time (~10 mins). The XPS binding energy scale was referenced to the Au $4f_{7/2}$ peak (84.0 eV) of a clean gold film.

7-3 Results and discussion

When sintering occurs in the presence of oxygen, a range of oxidised sulfur species were detected in TGA / MS experiments (Figure 7-2) indicating cleavage of the gold-thiol bond. The MS data are consistent with the generation of alkane fragments such as C_3H_8 (44 amu), C_2H_5 (29 amu) and C_2H_2 (26 amu), H_2S (34 amu), thiol fragments such as CH_4S, C_2S, C_2H_2S, C_2H_4S,C_3H_4S, C_4H_8S, C_2HS, and oxidized sulfur-containing species such as SO, SO_2, CSO, CH_4SO, CH_5SO, C_2SO and CH_4SO.

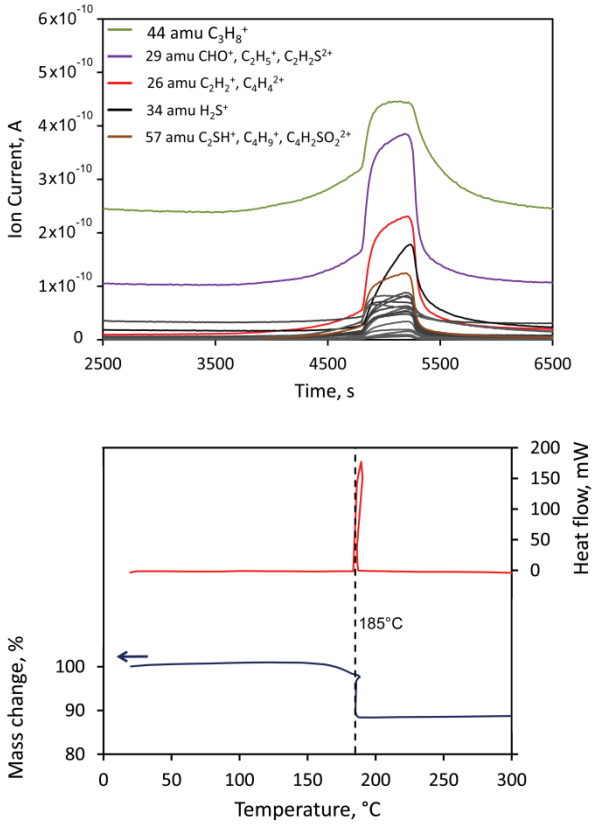

Figure 7-2. Top: MS data for gold nanoparticles heated in air/argon at 2°C.min^{-1}. The possible identities of five significant fragments are indicated. Data for nitrogen and argon are not shown. Bottom: TGA and DSC curves. Data are slightly asymmetrical during sinter ignition because the rapid rate of heat release temporarily increases the samples temperature above the furnace setpoint.

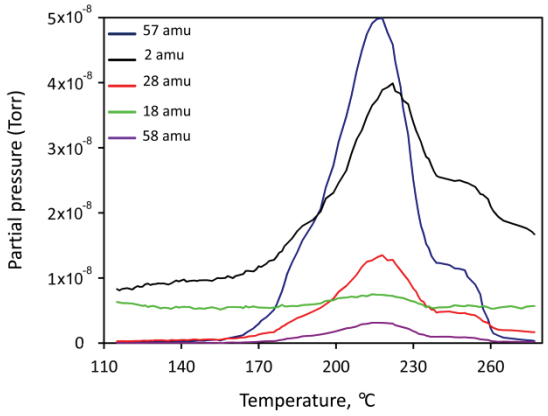

Figure 7-3. MS data collected for gold nanoparticles heated in a vacuum (10^{-4} – 10^{-6} Pa).

Figure 7-3 shows MS data obtained upon heating the 1-butanethiol-stabilised particles under vacuum (10^{-4} – 10^{-6} Pa) up to 275ºC. The pressure of the vacuum chamber was observed to increase during heating experiments as a result of the outgassing that occurred during the sintering process. The concentrations of species detected in the instrument (and thus released by the particles) begins to increase significantly at ~160ºC. The data are consistent with the evolution of species such as C_4H_9 and/or C_2SH (57 amu), H_2 (2 amu), C_4H_{10} and/or C_2SH_2 (58 amu) and C_2H_4 and/or N_2 and/or CO (28 amu). There is also a constant background of H_2O (18 amu). Figure 7-3 shows that, in vacuum, evolution of desorbed material reaches a maximum at ~210 - 220ºC, a temperature that agrees closely with previous work showing that these particles sinter in an exothermic manner at ~220ºC when heated in vacuum at 5 ºC.min^{-1} [486]. Another feature evident in Figure 7-3 is a second stage of material release at ~250ºC. Considering work reported by Tilley *et al.* [482], the current data indicate that desorption of stabilising ligand begins at an appreciable rate at ~160ºC until sufficient material has been removed to allow the sintering event (here at ~220ºC), which results in a large release of organic material. Subsequent defect removal and/or grain coarsening leads to a further release of organic material at ~250ºC.

The above data provide useful insights into the reaction and / or desorption of the protective ligand, but do not directly provide insight into the material remaining on the gold surface. To examine this, the XPS spectra of samples heated in UHV and air were examined.

The intensity ratios, S 2p:Au 4f and C 1s:Au 4f, recorded by XPS at room temperature after heating gold nanoparticles to various temperatures are shown in Figure 7-4. The data follow significantly different trends that depend upon the atmosphere in which the particles were heated. When heated under ultra-high vacuum conditions, the carbon and sulfur signals increase relative to the gold signal as the temperature is increased beyond the sintering temperature. The nanoparticles have a calculated starting surface area of over a hundred m^2g^{-1} (based on a particle diameter of ~2.5 nm) but the surface area diminishes considerably upon sintering. Both sulfur and carbon have negligible solubility in solid gold and so any carbon and sulfur not lost to the atmosphere should be concentrated on the surface. This is clearly the case for the material sintered in vacuum. However, a different behavior is observed for

particles heated in air. In this case, the ratios of carbon and sulfur to gold are similar to those obtained under UHV up to ~220ºC after which there is a significant *decrease* in the carbon and sulfur to gold ratios. These data show that a chemical interaction took place between air and sample, the net effect of which was to volatilise the adsorbates. It is not clear from these data if carbon is cleaved from sulfur during this event or if the adsorbate leaves intact. Removal of the stabilising adsorbates (that is, 1-butanethiolate) may be deemed necessary to sintering [479, 489] but the acquired data suggest that the fate of the stabilising butanethiolate ligands differs depending on the environment.

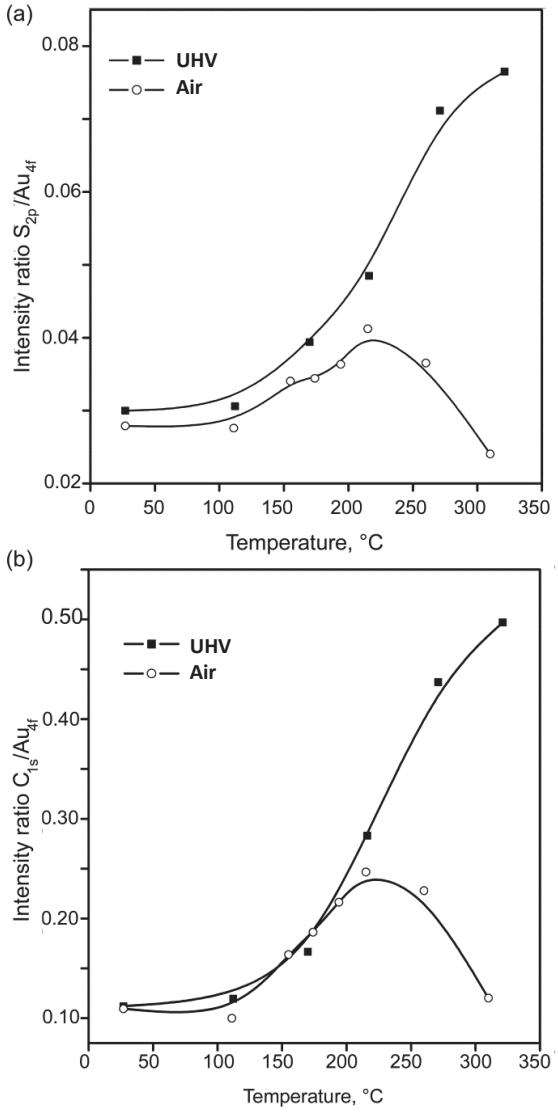

Figure 7-4. Graphs of XPS data showing intensity ratios for (a) S_{2p} / Au_{4f} and (b) C_{1s} / Au_{4f}, measured on 1-butanethiol-stabilised gold nanoparticles as a function of annealing temperature and surrounding environment.

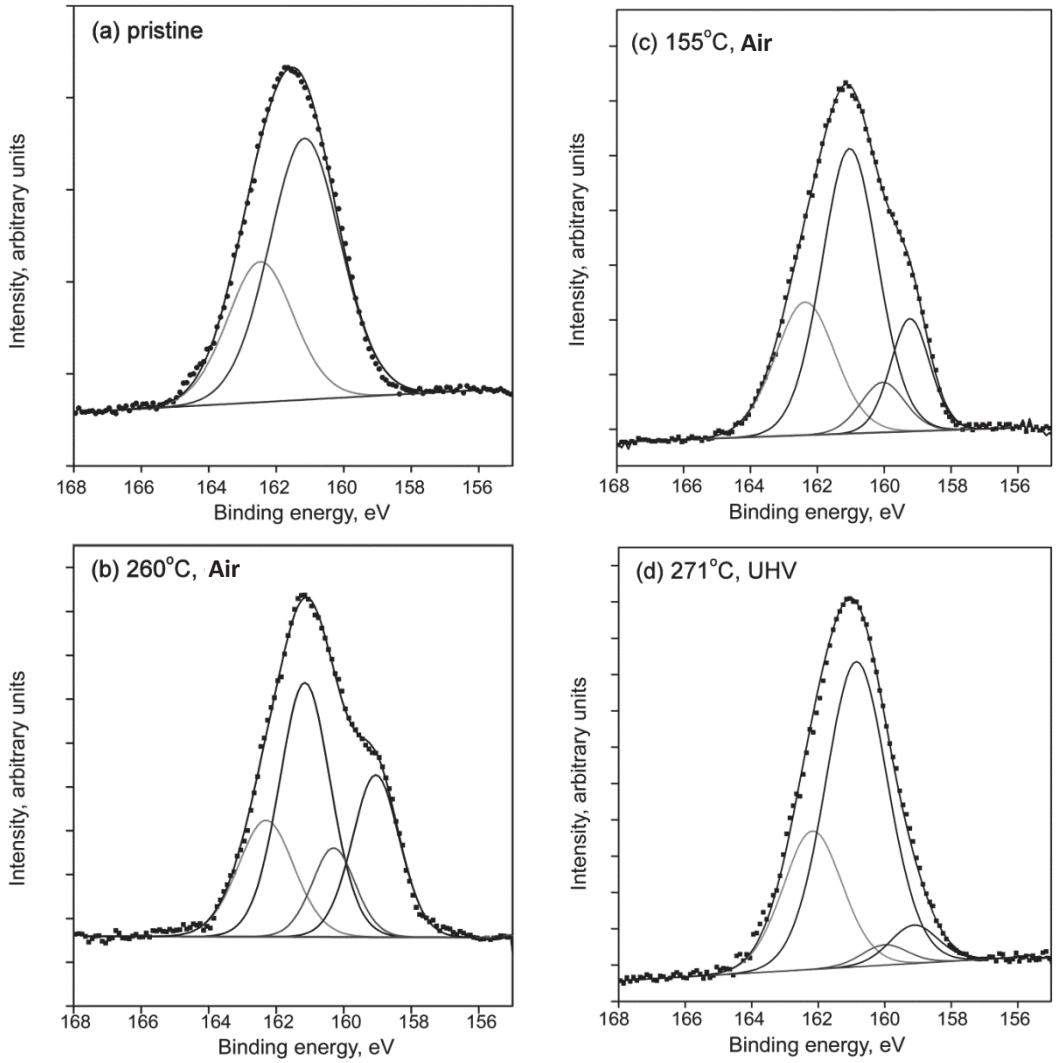

Figure 7-5. Peak shape analysis of the S_{2p} envelope for (a) pristine nanoparticles, (b) nanoparticles heated in air at 155°C, (c) nanoparticles in air at 260°C, and (d) nanoparticles heated in ultra-high vacuum at 271°C.

The chemical environment of the sulfur atoms in the various samples was probed by deconvoluting the binding energy spectra*. Figure 7-5 (a) shows the analysis of the S_{2p} signal for as-synthesised particles. The spectrum can be fitted with one doublet accounting for spin-orbit split $2p_{3/2}$ and $2p_{1/2}$ levels, which are separated by 1.2 eV and have a branching ratio of 1/2. After heating in air at 155 and 260ºC, deconvolution of the signals requires two doublets Figure 7-5 (b) and (c). The doublet

* Dr Cuong Ton-That (UTS) is acknowledged for deconvoluting the acquired data.

at lower binding energies (~159 eV) may be assigned to individual sulfur atoms bonded to the gold surface, with the slightly reduced binding energy relative to sulfur atoms on a planar gold surface due to the highly curved and strained surface of the nanoparticle. The doublet at higher binding energies (~162 eV) is assigned to sulfur atoms forming a bridge between gold and some other moity, presumably the butyl chain (although a polymeric sulfur moiety cannot be excluded on the basis of peak energies alone). Heating in air produced proportionately more signal at ~159 eV from the individual sulfur atoms. This suggests that while the untreated sample contains its sulfur mainly in the form of covalently bound thiols, a significant portion of it decomposes to sulfur when heated (and sintered) in air. In contrast, removal of chemisorbed thiol by simple volatilisation is unlikely to occur at temperatures up to 260ºC, as shown by the spectrum of the sample heated in vacuum. In that case, heating to 271ºC did not result in any marked development of doublets at the lower (~159 eV) binding energy, Figure 7-5 (d), and the resulting spectrum was not dissimilar to that of the pristine sample. This suggests that there was only 'bound' thiol present even though this temperature is past that where sintering occurs. Not surprisingly, there is no peak in any of the samples at 164 eV due to unbound thiols or sulfur as excess thiol from the synthetic procedure is removed during purification and if any had formed during heat treatment, it would have been rapidly volatilised.

The process of sintering was also examined by Professor Michael Cortie, UTS, in a series of *in situ* XRD experiments, which provide useful and complementary insights into the sintering mechanism. A number of structural changes occur in the sample as it is heated. Initially, the particles were measured to be separated by a distance of 2.74 nm. As the sample was heated, the inter-particle spacing expands gradually until ~80°C (at ramp rate of 2.5^{o}Cmin^{-1}) or ~100°C (at ramp rate of 6^{o}Cmin^{-1}), after which it enters a period of rapid expansion so that by 120^{o}C the particle-to-particle peak has moved out of the range of the detector. This rapid interparticle distance increase suggests a change in the state of the sample although the MS data show no release of molecular species during this transition, so the ligand evidently remains tightly bound to the nanoparticles. After several crystallographic changes, a sudden and rapid transition in the shape of XRD peaks at 195 ºC (at a nominal ramp rate of 2.5°Cmin^{-1} or 185°C at 1°Cmin^{-1}) corresponds to the onset of the exothermic sinter process. The nanoparticles coalesce into a polycrystalline mass. Particle-to-particle scattering

disappears because the gold nanoparticles are now fused together. A grain size of at least 100 nm was calculated.

7-4 Conclusions

The sintering of gold nanoparticle inks requires that their protective ligand shell be disrupted and removed. This occurs at a much lower temperature in oxygen-containing environments than in vacuum, and we have confirmed here that this difference is due to the oxidation and removal of the protective ligands which leave the surface as a volatile thiolate, or fragments thereof. In vacuum, the protective ligand must either be displaced by the reduction in surface area that occurs driven by the high surface tension of gold, or the gold / sulfur bond between ligand and gold nanoparticle must be cleaved by heat, either of which requires temperatures that are in excess of 200ºC. During heating the material undergoes a series of structural transitions, with particle growth and recrystallisation setting in at about 80°C, which is well before sintering occurs. The transition at 80°C may also correspond to the change of the material from colloidal glass to loosely packed powder, due to the van der Waals bonding of the colloidal glass being overcome at this temperature.

References

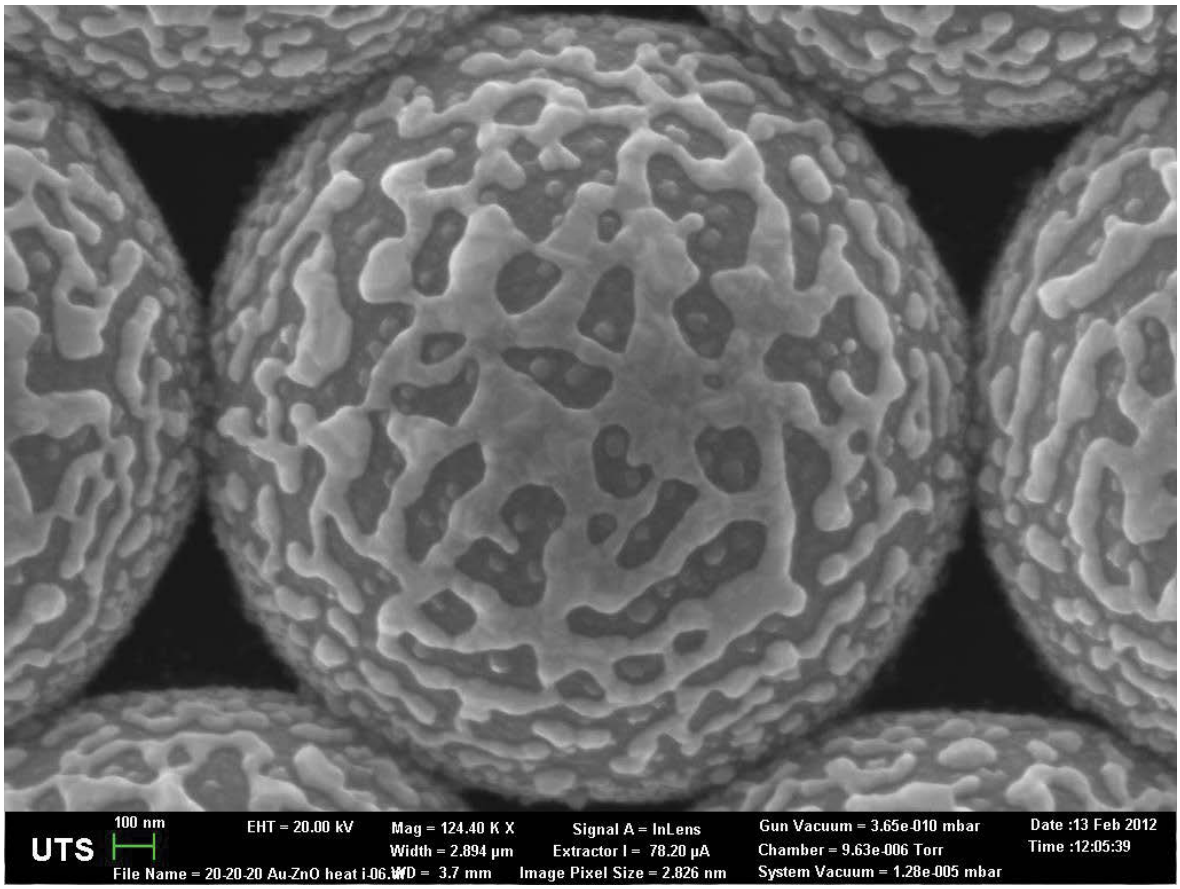
UTS
100 nm
EHT = 20.00 kV
Mag = 124.40 K X
Width = 2.894 µm
WD = 3.7 mm
Signal A = InLens
Extractor I = 78.20 µA
Image Pixel Size = 2.826 nm
Gun Vacuum = 3.65e-010 mbar
Chamber = 9.63e-006 Torr
System Vacuum = 1.28e-005 mbar
Date :13 Feb 2012
Time :12:05:39
File Name = 20-20-20 Au-ZnO heat i-06.tif

References

1. Ekanayake, S.R., M.B. Cortie, and M.J. Ford, *Design of nanocapacitors and associated materials challenges.* Current Applied Physics, 2004. **4**(2-4): p. 250-254.
2. Korotkov, A.N., *Intrinsic Noise of the Single-Electron Transistor.* Physical Review B, 1994. **49**(15): p. 10381-10392.
3. Lu, W. and C.M. Lieber, *Nanoelectronics from the bottom up.* Nature Materials, 2007. **6**(11): p. 841-850.
4. Armstrong, N., R.C. Hoft, A. McDonagh, M.B. Cortie, and M.J. Ford, *Exploring the performance of molecular rectifiers: Limitations and factors affecting molecular rectification.* Nano Letters, 2007. **7**(10): p. 3018-3022.
5. Yang, K.J. and C.M. Hu, *MOS capacitance measurements for high-leakage thin dielectrics.* Ieee Transactions on Electron Devices, 1999. **46**(7): p. 1500-1501.
6. Lewis, N.D. *E.G. Von Kliest & Pieter van Musschenbroek - The Leyden jar*. Available from: http://itp.nyu.edu/~ndl5/electricity/pages/leyden.html.
7. Zhang, L. and S.J. Watkins, *Capacitor voltage balancing in multilevel flying capacitor inverters by rule-based switching pattern selection.* Iet Electric Power Applications, 2007. **1**(3): p. 339-347.
8. Ramasamy, N., *Power System Capacitors*. 2005, Boca Raton: Taylor and Francis Group.
9. Trembley, M., *Part of a Letter from Mr. Trembley, F.R.S. to Martin Folkes, Esq; Pres. R. S. concerning the Light Caused by Quicksilver Shaken in a Glass Tube, Proceeding from Electricity.* Philosophical Transactions. **44**(478-484): p. 58-60.
10. Williams, H.S., *A Prefatory Characterization of The History of Italy*, in *The Historians' History of the World*. 1904: London and New York. p. 6.
11. Williams, E.H., AND Williams, Henry Smith, *A History of Science*. Vol. Volume 2: The beginnings of modern science
12. Ramasamy, N., *Power System Capacitors*. 2005: CRC Press. 576.
13. Volta, A. and H. George, *Del Modo di Render Sensibilissima la piu Debole Elettricita sia Naturale, sia Artificiale. By Mr. Alexander Volta, Professor of*

Experimental Philosophy in Como, &c. &c.; Communicated by the Right Hon. George Earl Cowper, F. R. S. Philosophical Transactions of the Royal Society of London, 1782. **72**(ArticleType: research-article / Full publication date: 1782 /): p. 237-xxxiii.

14. Faraday, M., *Experimental Researches in Electricity. Seventh Series.* Philosophical Transactions of the Royal Society of London, 1834. **124**: p. 77-122.
15. Pollak, C., *Process of Producing Plates for Secondary Batteries*, U.S.P. Office, Editor. 1897.
16. Helmholtz, *On the Modern Development of Faraday's Conception of Electricity.* Science (New York, N.Y.), 1881. **2**(44): p. 182-5.
17. Burke, A., *Ultracapacitors: why, how, and where is the technology.* Journal of Power Sources, 2000. **91**: p. 37 - 50.
18. Skunik, M., M. Chojak, I.A. Rutkowska, and P.J. Kulesza, *Improved capacitance characteristics during electrochemical charging of carbon nanotubes modified with polyoxometallate monolayers.* Electrochimica Acta, 2008. **53**: p. 3862-3869.
19. Zareie, H.M., S.W. Morgan, M. Moghaddam, A.I. Maaroof, M.B. Cortie, and M.R. Phillips, *Nanocapacitive Circuit Elements.* ACS Nano, 2008. **2**(8): p. 1615-1619.
20. Cortie, M.B., M.H. Zareie, S.R. Ekanayake, and M.J. Ford, *Conduction, storage, and leakage in particle-on-SAM nanocapacitors.* Ieee Transactions on Nanotechnology, 2005. **4**(4): p. 406-414.
21. Tipler, P.A. and G. Mosca, *Physics for scientists and engineers*. 5th ed. 2004, New York: Freeman. 2 v. (various pagings).
22. An, K.H., W.S. Kim, Y.S. Park, J.-M. Moon, D.J. Bae, S.C. Lim, Y.S. Lee, and Y.H. Lee, *Electrochemical properties of High-Power Supercapacitors Using Single-Walled Carbon Nanotube Electrodes.* Advanced Functional Materials, 2001. **11**(5): p. 387-392.
23. Carlberg, J.C. and O. Inganas, *Poly(3,4-ethylenedioxythiophene) as Electrode Material in Electrochemical Capacitors.* Journal of the Electrochemical Society, 1997. **144**(4): p. L61-L64.

24. Rolison, D.R. and L.F. Nazar, *Electrochemical energy storage to power the 21st century.* MRS Bulletin, 2011. **36**(7): p. 486-493.
25. Pandolfo, A.G. and A.F. Hollenkamp, *Carbon Properties and their role in supercapacitors.* Journal of Power Sources, 2006. **157**: p. 11-27.
26. Murugan, A.V., A.K. Viswanath, G. Campet, C.S. Gopinath, and K. Vijayamohanan, *Enhancement of double layer capacitance behaviour and its electrical conductivity in layered poly (3,4-ethylenedioxythiophene)-based nanocomposites.* Applied Physics Letters, 2005. **87**: p. 243511.
27. Chen, J.H., W.Z. Li, D.Z. Wang, J.G. Yang, J.G. Wen, and Z.F. Ren, *Electrochemical characterization of carbon nanotubes as electrode in electrochemical double-layer capacitors.* Carbon, 2002. **40**: p. 1193-1197.
28. Raymundo-Pinero, E., F. Leroux, and F. Beguin, *A high-performance carbon for supercapacitors obtained by carbonization of a seaweed biopolymer.* Advanced Materials, 2006. **18**(14): p. 1877-+.
29. Frackowiak, E. and F. Beguin, *Carbon materials for the electrochemical storage of energy in capacitors.* Carbon, 2001. **39**(6): p. 937-950.
30. Ito, Y. and T. Nohira, *Non-conventional electrolytes for electrochemical applications.* Electrochimica Acta, 2000. **45**(15-16): p. 2611-2622.
31. Pandolfo, A.G. and A.F. Hollenkamp, *Carbon properties and their role in supercapacitors.* Journal of Power Sources, 2006. **157**(1): p. 11-27.
32. Sarangapani, S., B.V. Tilak, and C.P. Chen, *Materials for electrochemical capacitors - Theoretical and experimental constraints.* Journal of The Electrochemical Society, 1996. **143**(11): p. 3791-3799.
33. Simon, P. and Y. Gogotsi, *Materials for electrochemical capacitors.* Nature Materials, 2008. **7**(11): p. 845-854.
34. Leonard, F. and A.A. Talin, *Electrical contacts to one- and two-dimensional nanomaterials.* Nature Nanotechnology, 2011. **6**(12): p. 773-783.
35. Miles, D.T. and R.W. Murray, *Temperature-dependent quantized double layer charging of monolayer-protected gold clusters.* Analytical Chemistry, 2003. **75**(6): p. 1251-1257.
36. Kim, S.K., S.W. Lee, J.H. Han, B. Lee, S. Han, and C.S. Hwang, *Capacitors with an Equivalent Oxide Thickness of < 0.5 nm for Nanoscale Electronic*

Semiconductor Memory. Advanced Functional Materials, 2010. **20**(18): p. 2989-3003.

37. Podpirka, A., B. Viswanath, and S. Ramanathan, *Active low temperature oxidation as a route to minimize electrode-oxide interface reactions in nanoscale capacitors.* Journal of Applied Physics, 2010. **108**(2).
38. Mendes, P.M., A.H. Flood, and J.F. Stoddart, *Nanoelectronic devices from self-organized molecular switches.* Applied Physics a-Materials Science & Processing, 2005. **80**(6): p. 1197-1209.
39. Oliver, R.A., *Advances in AFM for the electrical characterization of semiconductors.* Reports on Progress in Physics, 2008. **71**(7).
40. Subramanian, V., H.W. Zhu, R. Vajtai, P.M. Ajayan, and B.Q. Wei, *Hydrothermal synthesis and pseudocapacitance properties of MnO_2 nanostructures.* Journal of Physical Chemistry B, 2005. **109**(43): p. 20207-20214.
41. Chen, S.W. and R.W. Murray, *Electrochemical quantized capacitance charging of surface ensembles of gold nanoparticles.* Journal of Physical Chemistry B, 1999. **103**(45): p. 9996-10000.
42. Hou, J.G., B. Wang, J.L. Yang, X.R. Wang, H.Q. Wang, Q.S. Zhu, and X.D. Xiao, *Nonclassical behavior in the capacitance of a nanojunction.* Physical Review Letters, 2001. **86**(23): p. 5321-5324.
43. Zhang, S.L., Y. Lv, Z.M. Jiang, and X.J. Yang, *Electrical properties of individual self-assembled GeSi quantum rings.* Journal of Applied Physics, 2011. **110**(9).
44. Toh, S.L., P.K. Tan, Y.W. Goh, E. Hendarto, J.L. Cai, H. Tan, Q.F. Wang, Q. Deng, J. Lam, L.C. Hsia, and Z.H. Mai, *In-depth electrical analysis to reveal the failure mechanisms with nanoprobing.* Ieee Transactions on Device and Materials Reliability, 2008. **8**(2): p. 387-393.
45. Grutzner, M., *Advanced electrical analysis of embedded memory cells using Atomic Force Probing.* Microelectronics Reliability, 2005. **45**(9-11): p. 1509-1513.
46. Heyrovsky, J., *Researches with the dropping mercury cathode Part I General introduction.* Recueil Des Travaux Chimiques Des Pays-Bas, 1925. **44**: p. 488-495.

47. Heyrovsky, J., *Researches with the dropping mercury cathode Part III A theory of over-potential.* Recueil Des Travaux Chimiques Des Pays-Bas, 1925. **44**: p. 499-502.
48. Heyrovsky, J. and M. Shikata, *Researches with the dropping mercury cathode Part II The polarograph.* Recueil Des Travaux Chimiques Des Pays-Bas, 1925. **44**: p. 496-U7.
49. Watanabe, M.O. and Y. Ohba, *Interface properties for GaAs/InGaAlP heterojunctions by the capacitance-voltage profiling technique.* Applied Physics Letters, 1987. **50**(14): p. 906-908.
50. Patil, S., S. Datar, N. Rekha, S.K. Asha, and C.V. Dharmadhikari, *Charge storage and electron transport properties of gold nanoparticles decorating a urethane-methacrylate comb polymer network.* Nanoscale, 2013. **5**(10): p. 4404-4411.
51. Suganuma, Y., P.E. Trudeau, and A.A. Dhirani, *Probing correlated current and force effects of nanoparticle charge states by hybrid STM-AFM.* Physical Review B, 2002. **66**(24).
52. Thomson, R.E. and J. Moreland, *Development of Highly Conductive Cantilevers for Atomic-Force Microscopy Point-Contact Measurements.* Journal of Vacuum Science & Technology B, 1995. **13**(3): p. 1123-1125.
53. Bugg, C.D. and P.J. King, *Scanning Capacitance Microscopy.* Journal of Physics E-Scientific Instruments, 1988. **21**(2): p. 147-151.
54. Williams, C.C., W.P. Hough, and S.A. Rishton, *Scanning Capacitance Microscopy On A 25 nm Scale.* Applied Physics Letters, 1989. **55**(2): p. 203-205.
55. Matey, J.R. and J. Blanc, *Scanning Capacitance Microscopy.* Journal of Applied Physics, 1985. **57**(5): p. 1437-1444.
56. Zheng, J.P., P.J. Cygan, and T.R. Jow, *Hydrous Ruthenium Oxide as an Electrode Material for Electrochemical Capacitors.* Journal of the Electrochemical Society, 1995. **142**(8): p. 2699-2703.
57. Zheng, J.P. and T.R. Jow, *A new charge storage mechanism for electrochemical capacitors.* Journal of the Electrochemical Society, 1995. **142**(1): p. L6-L8.

58. Zheng, J.P. and T.R. Jow, *High energy and power density electrochemical capacitors.* Journal of Power Sources, 1996. **62**: p. 155-159.

59. Jeong, Y.U. and A. Manthiram, *Amorphous Ruthenium-Chromium Oxides for Electrochemical Capacitors.* Electrochemical and Solid-State Letters, 2000. **3**(5): p. 205-208.

60. Long, J.W., K.E. Swider, C.I. Merzbacher, and D.R. Rolison, *Voltammetric Characterization of Ruthenium Oxide-Based Aerogels and Other RuO_2 Solids: The Nature of Capacitance in Nanostructured Materials.* Langmuir, 1999. **15**(3): p. 780-785.

61. Kim, I.-H., J.-H. Kim, and K.-B. Kim, *Electrochemical Characterisation of Electrochemically Prepared Ruthenium Oxide/Carbon nanotube Electrode for Supercapacitor Application.* Electrochemical and Solid-State Letters, 2005. **8**(7): p. A369-A372.

62. Kim, I.-H., J.-H. Kim, Y.-H. Lee, and K.-B. Kim, *Synthesis and Characterization of Electrochemically prepared Ruthenium Oxide on Carbon Nanotube film substrate for Supercapacitor Applications.* Journal of the Electrochemical Society, 2005. **152**(11): p. A2170-A2178.

63. Lee, B.J., S.R. Sivakkumar, J.M. Ko, J.H. Kim, S.M. Jo, and D.Y. Kim, *Carbon nanofibre/hydrous RuO_2 nanocomposite electrodes for supercapacitors.* Journal of Power Sources, 2007. **168**: p. 546-552.

64. Ragupathy, P., H.N. Vasan, and N. Munichandraiah, *Synthesis and Characterisation of Nano-MnO_2 for Electrochemical Supercapacitor Studies.* Journal of the Electrochemical Society, 2008. **155**(1): p. A34-A40.

65. Hunter, D.N., S.L. Pickering, and D. Jia, *Thin-film nanocapacitor and its characterization.* European Journal of Physics, 2007. **28**: p. 161-170.

66. Kang, H.K., J. Seo, D.D. Carlo, Y.-K. Choi, and L.P. Lee, *Planar Nanogap Capacitor Arrays on Quartz for Optical and Dielectric Bioassays.* 7th Internation Conference on Miniaturized Chemical and Biochemical Analysis Systems, 2003. **October 5-9**: p. 697-700.

67. Li, Q., S. Surthi, G. Mathur, S. Gowda, V. Misra, T.A. Sorenson, R.C. Tenent, W.G. Kuhr, S.-i. Tamaru, J.S. Lindsey, Z. Liu, and D.F. Bocian, *Electrical characterization of redox-active molecular monolayers on SiO_2 for memory applications.* Applied Physics Letters, 2003. **83**(1): p. 198-200.

68. Li, Q., S. Surthi, G. Mathur, S. Gowda, Q. Zhao, T.A. Sorension, R.C. Tenent, K. Muthukamaran, J.S. Lindsey, and V. Misra, *Multiple-bit storage properties of porphyrin monolayers on SiO_2.* Applied Physics Letters, 2004. **85**(10): p. 1829 - 1831.

69. Sohn, J.I., Y.-S. Kim, C. Nam, B.K. Cho, T.-Y. Seong, and S. Lee, *Fabrication of high-density arrays of individually isolated nanocapacitors using anodic aluminum oxide templates and carbon nanotubes.* Applied Physics Letters, 2005. **87**(12): p. 123115-3.

70. Zhao, D., Y. Zhu, and J. Liu, *Charge storage in a metal-oxide-semiconductor capacitor containing cobalt nanocrystals.* Solid-State Electronics, 2006. **50**(2): p. 268-271.

71. Spassov, D., E. Atanassova, and D. Virovska, *Electrical characteristics of Ta_2O_5 based capacitors with different gate electrodes.* Applied Physics a-Materials Science & Processing, 2006. **82**(1): p. 55-62.

72. Atanassova, E., D. Spassov, A. Paskaleva, M. Georgieva, and J. Kopninarova, *Electrical characteristics of Ti-doped Ta_2O_5 stacked capacitors.* Thin Solid Films, 2008. **516**(23): p. 8684-8692.

73. Seki, S., T. Unagami, and B. Tsujiyama, *P-Channel TFTs Using Magnetron-Sputtered Ta_2O_5 Films as Gate Insulators.* Ieee Electron Device Letters, 1984. **5**(6): p. 197-198.

74. Chaneliere, C., J.L. Autran, R.A.B. Devine, and B. Balland, *Tantalum pentoxide (Ta_2O_5) thin films for advanced dielectric applications.* Materials Science & Engineering R-Reports, 1998. **22**(6): p. 269-322.

75. Paskaleva, A., E. Atanassova, and N. Novkovski, *Constant current stress of Ti-doped Ta_2O_5 on nitrided Si.* Journal of Physics D-Applied Physics, 2009. **42**(2).

76. Atanassova, E., A. Paskaleva, and N. Novkovski, *Effects of the metal gate on the stress-induced traps in Ta_2O_5/SiO_2 stacks.* Microelectronics Reliability, 2008. **48**(4): p. 514-525.

77. Choi, D. and P.N. Kumta, *Chemically Synthesized Nanostructured VN for Pseudocapacitor Application.* Electrochemical and Solid-State Letters, 2005. **8**(8): p. A418 - A422.

78. Shelimov, K.B., D.N. Davydov, and M. Moskovits, *Template-grown high-density nanocapacitor arrays.* Applied Physics Letters, 2000. **77**(11): p. 1722-1724.

79. Emmenegger, C., P. Mauron, A. Zuttel, C. Nutzenadel, A. Schneuwly, R. Gallay, and L. Schlapbach, *Carbon nanotube synthesized on metallic subtrates.* Applied Surface Science, 2000. **162-163**: p. 452-456.

80. Frackowiak, E. and F. Beguin, *Carbon materials for the electrochemical storage of energy in capacitors.* Carbon, 2001. **39**: p. 937-950.

81. Xu, B., F. Wu, F. Wang, S. Chen, G.P. Cao, and Y.S. Yang, *Single-walled carbon nanotubes as electrode materials for supercapacitors.* Chinese Journal of Chemistry, 2006. **24**(11): p. 1505-1508.

82. Kim, Y.T., Y. Ito, K. Tadai, T. Mitani, U.S. Kim, H.S. Kim, and B.W. Cho, *Drastic change of electric double layer capacitance by surface functionalization of carbon nanotubes.* Applied Physics Letters, 2005. **87**(23).

83. Hughes, M., G.Z. Chen, M.S.P. Shaffer, D.J. Fray, and A.H. Windle, *Electrochemical capacitance of a nanoporous composite of carbon nanotubes and polypyrrole.* Chemistry of Materials, 2002. **14**(4): p. 1610-1613.

84. Frackowiak, E. and F. Beguin, *Electrochemical storage of energy in carbon nanotubes and nanostructured carbons.* Carbon, 2002. **40**(10): p. 1775-1787.

85. Frackowiak, E., K. Metenier, V. Bertagna, and F. Beguin, *Supercapacitor electrodes from multiwalled carbon nanotubes.* Applied Physics Letters, 2000. **77**(15): p. 2421-2423.

86. Jurewicz, K., S. Delpeux, V. Bertagna, F. Beguin, and E. Frackowiak, *Supercapacitors from nanotubes/polypyrrole composites.* Chemical Physics Letters, 2001. **347**(1-3): p. 36-40.

87. Chen, J.H., W.Z. Li, D.Z. Wang, S.X. Yang, J.G. Wen, and Z.F. Ren, *Electrochemical characterization of carbon nanotubes as electrode in electrochemical double-layer capacitors.* Carbon, 2002. **40**(8): p. 1193-1197.

88. An, K.H., W.S. Kim, Y.S. Park, Y.C. Choi, S.M. Lee, D.C. Chung, D.J. Bae, S.C. Lim, and Y.H. Lee, *Supercapacitors using single-walled carbon nanotube electrodes.* Advanced Materials, 2001. **13**(7): p. 497-+.

89. Liu, C.G., H.T. Fang, F. Li, M. Liu, and H.M. Cheng, *Single-walled carbon nanotubes modified by electrochemical treatment for application in*

electrochemical capacitors. Journal of Power Sources, 2006. **160**(1): p. 758-761.

90. Zhang, C., X. Bin Zhang, X.Y. Tao, S.M. Zhou, L. Ma, H. Zhang, and Ieee, *Study of activated bamboo-shaped multiwall carbon nanotubes as supercapacitor electrodes*. 2006 1st IEEE International Conference on Nano/Micro Engineered and Molecular Systems, Vols 1-3. 2006. 603-606.
91. Xu, B., F. Wu, Y.F. Su, G.P. Cao, S. Chen, Z.M. Zhou, and Y.S. Yang, *Competitive effect of KOH activation on the electrochemical performances of carbon nanotubes for EDLC: Balance between porosity and conductivity.* Electrochimica Acta, 2008. **53**(26): p. 7730-7735.
92. Endo, M., Y.J. Kim, T. Chino, O. Shinya, Y. Matsuzawa, H. Suezaki, K. Tantrakarn, and M.S. Dresselhaus, *High-performance electric double-layer capacitors using mass-produced multi-walled carbon nanotubes.* Applied Physics a-Materials Science & Processing, 2006. **82**(4): p. 559-565.
93. Zhang, Y., C.G. Liu, B. Wen, X.Y. Song, and T.J. Li, *Preparation and electrochemical properties of nitrogen-doped multi-walled carbon nanotubes.* Materials Letters, 2011. **65**(1): p. 49-52.
94. Frackowiak, E., S. Delpeux, K. Jurewicz, K. Szostak, D. Cazorla-Amoros, and F. Beguin, *Enhanced capacitance of carbon nanotubes through chemical activation.* Chemical Physics Letters, 2002. **361**(1-2): p. 35-41.
95. Kim, Y.J., Y.A. Kim, T. Chino, H. Suezaki, M. Endo, and M.S. Dresselhaus, *Chemically modified multiwalled carbon nanotubes as an additive for supercapacitors.* Small, 2006. **2**(3): p. 339-345.
96. Jiang, Q., M.Z. Qu, G.M. Zhou, B.L. Zhang, and Z.L. Yu, *A study of activated carbon nanotubes as electrochemical super capacitors electrode materials.* Materials Letters, 2002. **57**(4): p. 988-991.
97. Frackowiak, E., K. Jurewicz, K. Szostak, S. Delpeux, and F. Beguin, *Nanotubular materials as electrodes for supercapacitors.* Fuel Processing Technology, 2002. **77**: p. 213-219.
98. Li, C.S., Y.J. Qiao, J.J. Wu, D.Z. Wang, and D.B. Yuan, *Enhancing the capacitances of electric double layer capacitors based on carbon nanotube electrodes by carbon dioxide activation and acid oxidization.* Science China-Technological Sciences, 2010. **53**(5): p. 1234-1239.

99. Zhao, X., B.T.T. Chu, B. Ballesteros, W.L. Wang, C. Johnston, J.M. Sykes, and P.S. Grant, *Spray deposition of steam treated and functionalized single-walled and multi-walled carbon nanotube films for supercapacitors.* Nanotechnology, 2009. **20**(6).

100. Pico, F., J.M. Rojo, M.L. Sanjuan, A. Anson, A.M. Benito, M.A. Callejas, W.K. Maser, and M.T. Martinez, *Single-walled carbon nanotubes as electrodes in supercapacitors.* Journal of The Electrochemical Society, 2004. **151**(6): p. A831-A837.

101. Seo, M.K. and S.J. Park, *Influence of air-oxidation on electric double layer capacitances of multi-walled carbon nanotube electrodes.* Current Applied Physics, 2010. **10**(1): p. 241-244.

102. Hu, C.C., J.H. Su, and T.C. Wen, *Modification of multi-walled carbon nanotubes for electric double-layer capacitors: Tube opening and surface functionalization.* Journal of Physics and Chemistry of Solids, 2007. **68**(12): p. 2353-2362.

103. Li, C.S., D.Z. Wang, T.X. Liang, X.F. Wang, J.J. Wu, X.Q. Hu, and J. Liang, *Oxidation of multiwalled carbon nanotubes by air: benefits for electric double layer capacitors.* Powder Technology, 2004. **142**(2-3): p. 175-179.

104. Kim, Y.T., K. Tadai, and T. Mitani, *Highly dispersed ruthenium oxide nanoparticles on carboxylated carbon nanotubes for supercapacitor electrode materials.* Journal of Materials Chemistry, 2005. **15**(46): p. 4914-4921.

105. Jang, I.Y., H. Muramatsu, K.C. Park, Y.J. Kim, and M. Endo, *Capacitance response of double-walled carbon nanotubes depending on surface modification.* Electrochemistry Communications, 2009. **11**(4): p. 719-723.

106. Kim, Y.T. and T. Mitani, *Competitive effect of carbon nanotubes oxidation on aqueous EDLC performance: Balancing hydrophilicity and conductivity.* Journal of Power Sources, 2006. **158**(2): p. 1517-1522.

107. Liu, C.G., M. Liu, F. Li, and H.M. Cheng, *Frequency response characteristic of single-walled carbon nanotubes as supercapacitor electrode material.* Applied Physics Letters, 2008. **92**(14).

108. Yamada, Y., O. Kimizuka, O. Tanaike, K. Machida, S. Suematsu, K. Tamamitsu, S. Saeki, and H. Hatori, *Capacitor Properties and Pore Structure*

of Single- and Double-Walled Carbon Nanotubes. Electrochemical and Solid State Letters, 2009. **12**(3): p. K14-K16.

109. Shiraishi, S., M. Kibe, T. Yokoyama, H. Kurihara, N. Patel, A. Oya, Y. Kaburagi, and Y. Hishiyama, *Electric double layer capacitance of multi-walled carbon nanotubes and B-doping effect.* Applied Physics a-Materials Science & Processing, 2006. **82**(4): p. 585-591.
110. Lee, K.Y., Y.S. Lin, Y.M. Chen, and Y.S. Huang, *Influence of the nitrogen content on the electrochemical capacitor characteristics of vertically aligned carbon nanotubes.* Physica E-Low-Dimensional Systems & Nanostructures, 2010. **42**(10): p. 2799-2803.
111. Lee, J.Y., K.H. An, J.K. Heo, and Y.H. Lee, *Fabrication of supercapacitor electrodes using fluorinated single-walled carbon nanotubes.* Journal of Physical Chemistry B, 2003. **107**(34): p. 8812-8815.
112. Zhou, C.F., S. Kumar, C.D. Doyle, and J.M. Tour, *Functionalized single wall carbon nanotubes treated with pyrrole for electrochemical supercapacitor membranes.* Chemistry of Materials, 2005. **17**(8): p. 1997-2002.
113. Gupta, V. and N. Miura, *Polyaniline/single-wall carbon nanotube (PANI/SWCNT) composites for high performance supercapacitors.* Electrochimica Acta, 2006. **52**(4): p. 1721-1726.
114. Zhou, Y.K., B.L. He, W.J. Zhou, J. Huang, X.H. Li, B. Wu, and H.I. Li, *Electrochemical capacitance of well-coated single-walled carbon nanotube with polyaniline composites.* Electrochimica Acta, 2004. **49**(2): p. 257-262.
115. Liu, J.L., J. Sun, and L.A. Gao, *A Promising Way To Enhance the Electrochemical Behavior of Flexible Single-Walled Carbon Nanotube/Polyaniline Composite Films.* Journal of Physical Chemistry C, 2010. **114**(46): p. 19614-19620.
116. Gupta, V. and N. Miura, *Influence of the microstructure on the supercapacitive behavior of polyaniline/single-wall carbon nanotube composites.* Journal of Power Sources, 2006. **157**(1): p. 616-620.
117. Oh, J., M.E. Kozlov, B.G. Kim, H.K. Kim, R.H. Baughman, and Y.H. Hwang, *Preparation and electrochemical characterization of porous SWNT-PPy nanocomposite sheets for supercapacitor applications.* Synthetic Metals, 2008. **158**(15): p. 638-641.

118. An, K.H., K.K. Jeon, J.K. Heo, S.C. Lim, D.J. Bae, and Y.H. Lee, *High-Capacitance Supercapacitor Using a Nanocomposite Electrode of Single-Walled Carbon Nanotube and Polypyrrole.* Journal of the Electrochemical Society, 2002. **149**(8): p. A1058-A1062.

119. Frackowiak, E., K. Jurewicz, S. Delpeux, V. Bertagna, S. Bonnamy, and F. Beguin, *Synergy of components in supercapacitors based on nanotube/polypyrrole composites.* Molecular Crystals and Liquid Crystals, 2002. **387**: p. 297-302.

120. Frackowiak, E., K. Jurewicz, S. Delpeux, and F. Beguin, *Nanotubular materials for supercapacitors.* Journal of Power Sources, 2001. **97-8**: p. 822-825.

121. Xiao, Q.F. and X. Zhou, *The study of multiwalled carbon nanotube deposited with conducting polymer for supercapacitor.* Electrochimica Acta, 2003. **48**(5): p. 575-580.

122. Lin, X.Q. and Y.H. Xu, *Facile synthesis and electrochemical capacitance of composites of polypyrrole/multi-walled carbon nanotubes.* Electrochimica Acta, 2008. **53**(15): p. 4990-4997.

123. Sharma, R.K., A. Karakoti, S. Seal, and L. Zhai, *Multiwall carbon nanotube-poly(4-styrenesulfonic acid) supported polypyrrole/manganese oxide nano-composites for high performance electrochemical electrodes.* Journal of Power Sources, 2010. **195**(4): p. 1256-1262.

124. Pieta, P., G.M. Venukadasula, F. D'Souza, and W. Kutner, *Preparation and Selected Properties of an Improved Composite of the Electrophoretically Deposited Single-Wall Carbon Nanotubes, Electrochemically Coated with a $C_{(60)}$-Pd and Polybithiophene Mixed Polymer Film.* Journal of Physical Chemistry C, 2009. **113**(31): p. 14046-14058.

125. Chen, P.C., H.T. Chen, J. Qiu, and C.W. Zhou, *Inkjet Printing of Single-Walled Carbon Nanotube/$RuO_{(2)}$ Nanowire Supercapacitors on Cloth Fabrics and Flexible Substrates.* Nano Research, 2010. **3**(8): p. 594-603.

126. Park, J.H., J.M. Ko, and O.O. Park, *Carbon nanotube/RuO_2 nanocomposite electrodes for supercapacitors.* Journal of The Electrochemical Society, 2003. **150**(7): p. A864-A867.

127. Yan, S.C., H.T. Wang, P. Qu, Y. Zhang, and Z.D. Xiao, *$RuO_{(2)}$/carbon nanotubes composites synthesized by microwave-assisted method for electrochemical supercapacitor.* Synthetic Metals, 2009. **159**(1-2): p. 158-161.

128. Arabale, G., D. Wagh, M. Kulkarni, I.S. Mulla, S.P. Vernekar, K. Vijayamohanan, and A.M. Rao, *Enhanced supercapacitance of multiwalled carbon nanotubes functionalized with ruthenium oxide.* Chemical Physics Letters, 2003. **376**(1-2): p. 207-213.

129. Lee, J.K., H.M. Pathan, K.D. Jung, and O.S. Joo, *Electrochemical capacitance of nanocomposite films formed by loading carbon nanotubes with ruthenium oxide.* Journal of Power Sources, 2006. **159**(2): p. 1527-1531.

130. Zhou, Y.K., B.L. He, F.B. Zhang, and H.L. Li, *Hydrous manganese oxide/carbon nanotube composite electrodes for electrochemical capacitors.* Journal of Solid State Electrochemistry, 2004. **8**(7): p. 482-487.

131. Wang, G.X., B.L. Zhang, Z.L. Yu, and M.Z. Qu, *Manganese oxide/MWNTs composite electrodes for supercapacitors.* Solid State Ionics, 2005. **176**(11-12): p. 1169-1174.

132. Wu, Y.T. and C.C. Hu, *Effects of electrochemical activation and multiwall carbon nanotubes on the capacitive characteristics of thick MnO_2 deposits.* Journal of The Electrochemical Society, 2004. **151**(12): p. A2060-A2066.

133. Fan, Z., J.H. Chen, B. Zhang, F. Sun, B. Liu, and Y.F. Kuang, *Electrochemically induced deposition method to prepare gamma-MnO_2/multi-walled carbon nanotube composites as electrode material in supercapacitors.* Materials Research Bulletin, 2008. **43**(8-9): p. 2085-2091.

134. Ma, S.B., K.W. Nam, W.S. Yoon, X.Q. Yang, K.Y. Ahn, K.H. Oh, and K.B. Kim, *Electrochemical properties of manganese oxide coated onto carbon nanotubes for energy-storage applications.* Journal of Power Sources, 2008. **178**(1): p. 483-489.

135. Okamura, K., R. Inoue, T. Sebille, K. Tomono, and M. Nakayama, *An Approach to Optimize the Composition of Supercapacitor Electrodes Consisting of Manganese-Molybdenum Mixed Oxide and Carbon Nanotubes.* Journal of The Electrochemical Society, 2011. **158**(6): p. A711-A717.

136. Zhao, X., C. Johnston, and P.S. Grant, *A novel hybrid supercapacitor with a carbon nanotube cathode and an iron oxide/carbon nanotube composite anode.* Journal of Materials Chemistry, 2009. **19**(46): p. 8755-8760.

137. Fan, Z., J.H. Chen, K.Z. Cui, F. Sun, Y. Xu, and Y.F. Kuang, *Preparation and capacitive properties of cobalt-nickel oxides/carbon nanotube composites.* Electrochimica Acta, 2007. **52**(9): p. 2959-2965.

138. Lee, J.Y., K. Liang, K.H. An, and Y.H. Lee, *Nickel oxide/carbon nanotubes nanocomposite for electrochemical capacitance.* Synthetic Metals, 2005. **150**(2): p. 153-157.

139. Chen, P.C., G. Shen, S. Sukcharoenchoke, and C. Zhou, *Flexible and transparent supercapacitor based on $In_{(2)}O_{(3)}$ nanowire/carbon nanotube heterogeneous films.* Applied Physics Letters, 2009. **94**(4).

140. Ahn, H.J., W.B. Kim, and T.Y. Seong, *$Co(OH)_{(2)}$-combined carbon-nanotube array electrodes for high-performance micro-electrochemical capacitors.* Electrochemistry Communications, 2008. **10**(9): p. 1284-1287.

141. Masarapu, C., H.F. Zeng, K.H. Hung, and B.Q. Wei, *Effect of Temperature on the Capacitance of Carbon Nanotube Supercapacitors.* ACS Nano, 2009. **3**(8): p. 2199-2206.

142. Niu, C.M., E.K. Sichel, R. Hoch, D. Moy, and H. Tennent, *High power electrochemical capacitors based on carbon nanotube electrodes.* Applied Physics Letters, 1997. **70**(11): p. 1480-1482.

143. Hiraoka, T., A. Izadi-Najafabadi, T. Yamada, D.N. Futaba, S. Yasuda, O. Tanaike, H. Hatori, M. Yumura, S. Iijima, and K. Hata, *Compact and Light Supercapacitor Electrodes from a Surface-Only Solid by Opened Carbon Nanotubes with 2 200 $m^{(2)}$ $g^{(-1)}$ Surface Area.* Advanced Functional Materials, 2010. **20**(3): p. 422-428.

144. Izadi-Najafabadi, A., S. Yasuda, K. Kobashi, T. Yamada, D.N. Futaba, H. Hatori, M. Yumura, S. Iijima, and K. Hata, *Extracting the Full Potential of Single-Walled Carbon Nanotubes as Durable Supercapacitor Electrodes Operable at 4 V with High Power and Energy Density.* Advanced Materials, 2010. **22**(35): p. E235-+.

145. Barisci, J.N., G.G. Wallace, D. Chattopadhyay, F. Papadimitrakopoulos, and R.H. Baughman, *Electrochemical properties of single-wall carbon nanotube*

electrodes. Journal of The Electrochemical Society, 2003. **150**(9): p. E409-E415.

146. Yu, C.J., C. Masarapu, J.P. Rong, B.Q. Wei, and H.Q. Jiang, *Stretchable Supercapacitors Based on Buckled Single-Walled Carbon Nanotube Macrofilms.* Advanced Materials, 2009. **21**(47): p. 4793-+.
147. An, K.H., W.S. Kim, Y.S. Park, J.M. Moon, D.J. Bae, S.C. Lim, Y.S. Lee, and Y.H. Lee, *Electrochemical properties of high-power supercapacitors using single-walled carbon nanotube electrodes.* Advanced Functional Materials, 2001. **11**(5): p. 387-392.
148. Barisci, J.N., G.G. Wallace, D.R. MacFarlane, and R.H. Baughman, *Investigation of ionic liquids as electrolytes for carbon nanotube electrodes.* Electrochemistry Communications, 2004. **6**(1): p. 22-27.
149. Shiraishi, S., H. Kurihara, K. Okabe, D. Hulicova, and A. Oya, *Electric double layer capacitance of highly pure single-walled carbon nanotubes (HiPco (TM) Buckytubes (TM)) in propylene carbonate electrolytes.* Electrochemistry Communications, 2002. **4**(7): p. 593-598.
150. Izadi-Najafabadi, A., T. Yamada, D.N. Futaba, M. Yudasaka, H. Takagi, H. Hatori, S. Iijima, and K. Hata, *High-Power Supercapacitor Electrodes from Single-Walled Carbon Nanohorn/Nanotube Composite.* ACS Nano, 2011. **5**(2): p. 811-819.
151. Kaempgen, M., C.K. Chan, J. Ma, Y. Cui, and G. Gruner, *Printable Thin Film Supercapacitors Using Single-Walled Carbon Nanotubes.* Nano Letters, 2009. **9**(5): p. 1872-1876.
152. Li, X., J.P. Rong, and B.Q. Wei, *Electrochemical Behavior of Single-Walled Carbon Nanotube Supercapacitors under Compressive Stress.* ACS Nano, 2010. **4**(10): p. 6039-6049.
153. Futaba, D.N., K. Hata, T. Yamada, T. Hiraoka, Y. Hayamizu, Y. Kakudate, O. Tanaike, H. Hatori, M. Yumura, and S. Iijima, *Shape-engineerable and highly densely packed single-walled carbon nanotubes and their application as super-capacitor electrodes.* Nature Materials, 2006. **5**(12): p. 987-994.
154. Xu, B., F. Wu, R.J. Chen, G.P. Cao, S. Chen, G.Q. Wang, and Y.S. Yang, *Room temperature molten salt as electrolyte for carbon nanotube-based*

electric double layer capacitors. Journal of Power Sources, 2006. **158**(1): p. 773-778.

155. Kaempgen, M., J. Ma, G. Gruner, G. Wee, and S.G. Mhaisalkar, *Bifunctional carbon nanotube networks for supercapacitors.* Applied Physics Letters, 2007. **90**(26).
156. Tahhan, M., N. Barisci, G.G. Wallace, and Ieee, *Conducting polymer-carbon nanotubes composites*. Proceedings of the 2001 1st Ieee Conference on Nanotechnology. 2001. 229-232.
157. Roldan, S., Z. Gonzalez, C. Blanco, M. Granda, R. Menendez, and R. Santamaria, *Redox-active electrolyte for carbon nanotube-based electric double layer capacitors.* Electrochimica Acta, 2011. **56**(9): p. 3401-3405.
158. Frackowiak, E., S. Delpeux, K. Jurewicz, K. Szostak, D. Cazorla-Amoros, and F. Beguin, *Enhanced Capacitance of carbon nanotubes through chemical activation.* Chemical Physics Letters, 2002. **361**: p. 35-41.
159. Kim, J.H., K.W. Nam, S.B. Ma, and K.B. Kim, *Fabrication and electrochemical properties of carbon nanotube film electrodes.* Carbon, 2006. **44**(10): p. 1963-1968.
160. Gao, Y., L.K. Pan, Y.P. Zhang, Y.W. Chen, and Z. Sun, *Electrosorption of $FeCl_3$ solutions with carbon nanotubes and nanofibers film electrodes grown on graphite substrates.* Surface Review and Letters, 2007. **14**(6): p. 1033-1037.
161. Emmenegger, C., P. Mauron, P. Sudan, P. Wenger, V. Hermann, R. Gallay, and A. Zuttel, *Investigation of electrochemical double-layer (ECDL) capacitors electrodes based on carbon nanotubes and activated carbon materials.* Journal of Power Sources, 2003. **124**(1): p. 321-329.
162. Chatterjee, A.K., M. Sharon, R. Baneriee, and M. Neumann-Spallart, *CVD synthesis of carbon nanotubes using a finely dispersed cobalt catalyst and their use in double layer electrochemical capacitors.* Electrochimica Acta, 2003. **48**(23): p. 3439-3446.
163. Du, C.S., J. Yeh, and N. Pan, *High power density supercapacitors using locally aligned carbon nanotube electrodes.* Nanotechnology, 2005. **16**(4): p. 350-353.

164. Du, C.S. and N. Pan, *High power density supercapacitor electrodes of carbon nanotube films by electrophoretic deposition.* Nanotechnology, 2006. **17**(21): p. 5314-5318.

165. Zhang, H., G.P. Cao, Y.S. Yang, and Z.N. Gu, *Comparison between electrochemical properties of aligned carbon nanotube array and entangled carbon nanotube electrodes.* Journal of The Electrochemical Society, 2008. **155**(2): p. K19-K22.

166. Zhang, H., G.P. Cao, and Y.S. Yang, *Using a cut-paste method to prepare a carbon nanotube fur electrode.* Nanotechnology, 2007. **18**(19).

167. Lee, S.W., D.K. Park, J.K. Lee, J.B. Ju, and T.W. Sohn, *Discharge capacitance of electric double layer capacitor with electrodes made of carbon nanotubes directly deposited on SUS304 plates.* Korean Journal of Chemical Engineering, 2001. **18**(3): p. 371-375.

168. Zhang, B., J. Liang, C.L. Xu, B.Q. Wei, D.B. Ruan, and D.H. Wu, *Electric double-layer capacitors using carbon nanotube electrodes and organic electrolyte.* Materials Letters, 2001. **51**(6): p. 539-542.

169. Zhang, H., G.P. Cao, and Y.S. Yang, *Electrochemical properties of ultra-long, aligned, carbon nanotube array electrode in organic electrolyte.* Journal of Power Sources, 2007. **172**(1): p. 476-480.

170. Honda, Y., T. Haramoto, M. Takeshige, H. Shiozaki, T. Kitamura, K. Yoshikawa, and M. Ishikawaa, *Performance of Electric Double-Layer Capacitor With Vertically Aligned MWCNT Sheet Electrodes Prepared by Transfer Methodology.* Journal of The Electrochemical Society, 2008. **155**(12): p. A930-A935.

171. Wang, D., P.C. Song, C.H. Liu, W. Wu, and S.S. Fan, *Highly oriented carbon nanotube papers made of aligned carbon nanotubes.* Nanotechnology, 2008. **19**(7).

172. Jung, M., H.G. Kim, J.K. Lee, O.S. Joo, and S. Mho, *EDLC characteristics of CNTs grown on nanoporous alumina templates.* Electrochimica Acta, 2004. **50**(2-3): p. 857-862.

173. Chen, Q.L., K.H. Xue, W. Shen, F.F. Tao, S.Y. Yin, and W. Xu, *Fabrication and electrochemical properties of carbon nanotube array electrode for supercapacitors.* Electrochimica Acta, 2004. **49**(24): p. 4157-4161.

174. Pushparaj, V.L., M.M. Shaijumon, A. Kumar, S. Murugesan, L. Ci, R. Vajtai, R.J. Linhardt, O. Nalamasu, and P.M. Ajayan, *Flexible energy storage devices based on nanocomposite paper.* Proceedings of the National Academy of Sciences of the United States of America, 2007. **104**(34): p. 13574-13577.

175. Honda, Y., T. Ono, M. Takeshige, N. Morihara, H. Shiozaki, T. Kitamura, K. Yoshikawa, M. Morita, M. Yamagata, and M. Ishikawa, *Effect of MWCNT Bundle Structure on Electric Double-Layer Capacitor Performance.* Electrochemical and Solid State Letters, 2009. **12**(3): p. A45-A49.

176. Lu, W., L.T. Qu, K. Henry, and L.M. Dai, *High performance electrochemical capacitors from aligned carbon nanotube electrodes and ionic liquid electrolytes.* Journal of Power Sources, 2009. **189**(2): p. 1270-1277.

177. Skunik, M., M. Chojak, L.A. Rutkowska, and P.J. Kulesza, *Improved capacitance characteristics during electrochemical charging of carbon nanotubes modified with polyoxometallate monolayers.* Electrochimica Acta, 2008. **53**(11): p. 3862-3869.

178. Pan, H., C.K. Poh, Y.P. Feng, and J.Y. Lin, *Supercapacitor electrodes from tubes-in-tube carbon nanostructures.* Chemistry of Materials, 2007. **19**(25): p. 6120-6125.

179. Pandey, G.P., S.A. Hashmi, and Y. Kumar, *Multiwalled Carbon Nanotube Electrodes for Electrical Double Layer Capacitors with Ionic Liquid Based Gel Polymer Electrolytes.* Journal of The Electrochemical Society, 2010. **157**(1): p. A105-A114.

180. Whitten, P.G., A.A. Gestos, G.M. Spinks, K.J. Gilmore, and G.G. Wallace, *Free standing carbon nanotube composite bio-electrodes.* Journal of Biomedical Materials Research Part B-Applied Biomaterials, 2007. **82B**(1): p. 37-43.

181. Pieta, P., E. Grodzka, K. Winkler, M. Warczak, A. Sadkowski, G.Z. Zukowska, G.M. Venukadasula, F. D'Souza, and W. Kutner, *Conductive, Capacitive, and Viscoelastic Properties of a New Composite of the $C_{(60)}$-Pd Conducting Polymer and Single-Wall Carbon Nanotubes.* Journal of Physical Chemistry B, 2009. **113**(19): p. 6682-6691.

182. Sherrell, P.C., J. Chen, J.M. Razal, I.P. Nevirkovets, C. Crean, G.G. Wallace, and A.I. Minett, *Advanced microwave-assisted production of hybrid*

electrodes for energy applications. Energy & Environmental Science, 2010. **3**(12): p. 1979-1984.

183. Liu, C.G., Y.S. Lee, Y.J. Kim, I.C. Song, and J.H. Kim, *Electrochemical characteristics of hydrothermally deposited nickel hydroxide on multi-walled carbon nanotube for supercapacitor electrode.* Synthetic Metals, 2009. **159**(19-20): p. 2009-2012.
184. Yuan, C.Z., L.R. Hou, L. Yang, D.K. Li, J. Tan, L.F. Shen, F. Zhang, and X.G. Zhang, *Synthesis of $Ru_{(0.58)}In_{(0.42)}O_{(y)}$center dot $nH_{(2)}O$ nanoparticles dispersed onto poly(sodium-4-styrene sulfonate)-functionalized multi-walled carbon nanotubes and their application for electrochemical capacitors.* Journal of Colloid and Interface Science, 2011. **354**(2): p. 804-809.
185. Hughes, M., G.Z. Chen, M.S.P. Shaffer, D.J. Fray, and A.H. Windle, *Electrochemical Capacitance of a Nanoporous Composite of Carbon Nanotubes and Polypyrrole.* Chem. Mater., 2002. **14**(4): p. 1610-1613.
186. Jurewicz, K., S. Delpeux, V. Bertagna, F. Beguin, and E. Frackowiak, *Supercapacitors from nanotubes/polypyrrole composites.* Chemical Physics Letters, 2001. **347**: p. 36-40.
187. Peigney, A., C. Laurent, E. Flahaut, R.R. Bacsa, and A. Rousset, *Specific surface area of carbon nanotubes and bundles of carbon nanotubes.* Carbon, 2001. **39**(4): p. 507-514.
188. Hummers, W.S. and R.E. Offeman, *Preperation of Graphitic Oxide.* Journal of the American Chemical Society, 1958. **80**(6): p. 1339-1339.
189. Liu, P.G. and K.C. Gong, *Synthesis of polyaniline-intercalated graphite oxide by an in situ oxidative polymerization reaction.* Carbon, 1999. **37**(4): p. 706-707.
190. Gilje, S., S. Han, M. Wang, K.L. Wang, and R.B. Kaner, *A chemical route to graphene for device applications.* Nano Letters, 2007. **7**(11): p. 3394-3398.
191. Peng, X.Y., X.X. Liu, D. Diamond, and K.T. Lau, *Synthesis of electrochemically-reduced graphene oxide film with controllable size and thickness and its use in supercapacitor.* Carbon, 2011. **49**(11): p. 3488-3496.
192. Lin, Z.Y., Y. Liu, Y.G. Yao, O.J. Hildreth, Z. Li, K. Moon, and C.P. Wong, *Superior Capacitance of Functionalized Graphene.* Journal of Physical Chemistry C, 2011. **115**(14): p. 7120-7125.

193. Qiu, Y.C., X.F. Zhang, and S.H. Yang, *High performance supercapacitors based on highly conductive nitrogen-doped graphene sheets.* Physical Chemistry Chemical Physics, 2011. **13**(27): p. 12554-12558.

194. Yan, X.B., J.T. Chen, J. Yang, Q.J. Xue, and P. Miele, *Fabrication of Free-Standing, Electrochemically Active, and Biocompatible Graphene Oxide-Polyaniline and Graphene-Polyaniline Hybrid Papers.* Acs Applied Materials & Interfaces, 2010. **2**(9): p. 2521-2529.

195. Lu, T., Y.P. Zhang, H.B. Li, L.K. Pan, Y.L. Li, and Z. Sun, *Electrochemical behaviors of graphene-ZnO and graphene-$SnO_{(2)}$ composite films for supercapacitors.* Electrochimica Acta, 2010. **55**(13): p. 4170-4173.

196. Wu, Q., Y.X. Xu, Z.Y. Yao, A.R. Liu, and G.Q. Shi, *Supercapacitors Based on Flexible Graphene/Polyaniline Nanofiber Composite Films.* ACS Nano, 2010. **4**(4): p. 1963-1970.

197. Wang, H.B., Z.H. Liu, X. Chen, P.X. Han, S.M. Dong, and G.L. Cui, *Exfoliated graphite nanosheets/carbon nanotubes hybrid materials for superior performance supercapacitors.* Journal of Solid State Electrochemistry, 2011. **15**(6): p. 1179-1184.

198. Yu, A.P., I. Roes, A. Davies, and Z.W. Chen, *Ultrathin, transparent, and flexible graphene films for supercapacitor application.* Applied Physics Letters, 2010. **96**(25).

199. Du, Q.L., M.B. Zheng, L.F. Zhang, Y.W. Wang, J.H. Chen, L.P. Xue, W.J. Dai, G.B. Ji, and J.M. Cao, *Preparation of functionalized graphene sheets by a low-temperature thermal exfoliation approach and their electrochemical supercapacitive behaviors.* Electrochimica Acta, 2010. **55**(12): p. 3897-3903.

200. Xu, Y.X., K.X. Sheng, C. Li, and G.Q. Shi, *Self-Assembled Graphene Hydrogel via a One-Step Hydrothermal Process.* ACS Nano, 2010. **4**(7): p. 4324-4330.

201. Le, L.T., M.H. Ervin, H.W. Qiu, B.E. Fuchs, and W.Y. Lee, *Graphene supercapacitor electrodes fabricated by inkjet printing and thermal reduction of graphene oxide.* Electrochemistry Communications, 2011. **13**(4): p. 355-358.

202. Lai, L.F., L.W. Chen, D. Zhan, L. Sun, J.P. Liu, S.H. Lim, C.K. Poh, Z.X. Shen, and J.Y. Lin, *One-step synthesis of $NH_{(2)}$-graphene from in situ*

graphene-oxide reduction and its improved electrochemical properties. Carbon, 2011. **49**(10): p. 3250-3257.

203. Shi, W.H., J.X. Zhu, D.H. Sim, Y.Y. Tay, Z.Y. Lu, X.J. Zhang, Y. Sharma, M. Srinivasan, H. Zhang, H.H. Hng, and Q.Y. Yan, *Achieving high specific charge capacitances in $Fe_{(3)}O_{(4)}$/reduced graphene oxide nanocomposites.* Journal of Materials Chemistry, 2011. **21**(10): p. 3422-3427.
204. Wang, H.W., Z.A. Hu, Y.Q. Chang, Y.L. Chen, Z.Q. Lei, Z.Y. Zhang, and Y.Y. Yang, *Facile solvothermal synthesis of a graphene nanosheet-bismuth oxide composite and its electrochemical characteristics.* Electrochimica Acta, 2010. **55**(28): p. 8974-8980.
205. Zhu, Y.W., S. Murali, M.D. Stoller, A. Velamakanni, R.D. Piner, and R.S. Ruoff, *Microwave assisted exfoliation and reduction of graphite oxide for ultracapacitors.* Carbon, 2010. **48**(7): p. 2118-2122.
206. Shao, Y.Y., J. Wang, M. Engelhard, C.M. Wang, and Y.H. Lin, *Facile and controllable electrochemical reduction of graphene oxide and its applications.* Journal of Materials Chemistry, 2010. **20**(4): p. 743-748.
207. Chen, Y., X.O. Zhang, D.C. Zhang, P. Yu, and Y.W. Ma, *High performance supercapacitors based on reduced graphene oxide in aqueous and ionic liquid electrolytes.* Carbon, 2011. **49**(2): p. 573-580.
208. Sun, Y.Q., Q.O. Wu, Y.X. Xu, H. Bai, C. Li, and G.Q. Shi, *Highly conductive and flexible mesoporous graphitic films prepared by graphitizing the composites of graphene oxide and nanodiamond.* Journal of Materials Chemistry, 2011. **21**(20): p. 7154-7160.
209. Li, Y.M., M. van Zijll, S. Chiang, and N. Pan, *KOH modified graphene nanosheets for supercapacitor electrodes.* Journal of Power Sources, 2011. **196**(14): p. 6003-6006.
210. Zhu, Y.W., S. Murali, M.D. Stoller, K.J. Ganesh, W.W. Cai, P.J. Ferreira, A. Pirkle, R.M. Wallace, K.A. Cychosz, M. Thommes, D. Su, E.A. Stach, and R.S. Ruoff, *Carbon-Based Supercapacitors Produced by Activation of Graphene.* Science, 2011. **332**(6037): p. 1537-1541.
211. Jeong, H.M., J.W. Lee, W.H. Shin, Y.J. Choi, H.J. Shin, J.K. Kang, and J.W. Choi, *Nitrogen-Doped Graphene for High-Performance Ultracapacitors and*

the Importance of Nitrogen-Doped Sites at Basal Planes. Nano Letters, 2011. **11**(6): p. 2472-2477.

212. Wu, Q., Y.Q. Sun, H. Bai, and G.Q. Shi, *High-performance supercapacitor electrodes based on graphene hydrogels modified with 2-aminoanthraquinone moieties.* Physical Chemistry Chemical Physics, 2011. **13**(23): p. 11193-11198.
213. Hao, Q.L.H.Q.L., H.L. Wang, X.J. Yang, L.D. Lu, and X. Wang, *Morphology-controlled fabrication of sulfonated graphene/polyaniline nanocomposites by liquid/liquid interfacial polymerization and investigation of their electrochemical properties.* Nano Research, 2011. **4**(4): p. 323-333.
214. Liu, C.G., Z.N. Yu, D. Neff, A. Zhamu, and B.Z. Jang, *Graphene-Based Supercapacitor with an Ultrahigh Energy Density.* Nano Letters, 2010. **10**(12): p. 4863-4868.
215. Yang, S.Y., K.H. Chang, H.W. Tien, Y.F. Lee, S.M. Li, Y.S. Wang, J.Y. Wang, C.C.M. Ma, and C.C. Hu, *Design and tailoring of a hierarchical graphene-carbon nanotube architecture for supercapacitors.* Journal of Materials Chemistry, 2011. **21**(7): p. 2374-2380.
216. Lu, X.J., H. Dou, B. Gao, C.Z. Yuan, S.D. Yang, L. Hao, L.F. Shen, and X.G. Zhang, *A flexible graphene/multiwalled carbon nanotube film as a high performance electrode material for supercapacitors.* Electrochimica Acta, 2011. **56**(14): p. 5115-5121.
217. Yu, D.S. and L.M. Dai, *Self-Assembled Graphene/Carbon Nanotube Hybrid Films for Supercapacitors.* Journal of Physical Chemistry Letters, 2010. **1**(2): p. 467-470.
218. Yang, X.W., J.W. Zhu, L. Qiu, and D. Li, *Bioinspired Effective Prevention of Restacking in Multilayered Graphene Films: Towards the Next Generation of High-Performance Supercapacitors.* Advanced Materials, 2011. **23**(25): p. 2833-+.
219. Yoo, J.J.Y.J.J., K. Balakrishnan, J.S. Huang, V. Meunier, B.G. Sumpter, A. Srivastava, M. Conway, A.L.M. Reddy, J. Yu, R. Vajtai, and P.M. Ajayan, *Ultrathin Planar Graphene Supercapacitors.* Nano Letters, 2011. **11**(4): p. 1423-1427.

220. Ning, G.Q., Z.J. Fan, G. Wang, J.S. Gao, W.Z. Qian, and F. Wei, *Gram-scale synthesis of nanomesh graphene with high surface area and its application in supercapacitor electrodes.* Chemical Communications, 2011. **47**(21): p. 5976-5978.

221. Zhang, K., L. Mao, L.L. Zhang, H.S.O. Chan, X.S. Zhao, and J.S. Wu, *Surfactant-intercalated, chemically reduced graphene oxide for high performance supercapacitor electrodes.* Journal of Materials Chemistry, 2011. **21**(20): p. 7302-7307.

222. Mishra, A.K. and S. Ramaprabhu, *Functionalized Graphene-Based Nanocomposites for Supercapacitor Application.* Journal of Physical Chemistry C, 2011. **115**(29): p. 14006-14013.

223. Xu, J.J., K. Wang, S.Z. Zu, B.H. Han, and Z.X. Wei, *Hierarchical Nanocomposites of Polyaniline Nanowire Arrays on Graphene Oxide Sheets with Synergistic Effect for Energy Storage.* ACS Nano, 2010. **4**(9): p. 5019-5026.

224. Wang, H.L., Q.L. Hao, X.J. Yang, L.D. Lu, and X. Wang, *Effect of Graphene Oxide on the Properties of Its Composite with Polyaniline.* Acs Applied Materials & Interfaces, 2010. **2**(3): p. 821-828.

225. Liu, S., X.H. Liu, Z.P. Li, S.R. Yang, and J.Q. Wang, *Fabrication of free-standing graphene/polyaniline nanofibers composite paper via electrostatic adsorption for electrochemical supercapacitors.* New Journal of Chemistry, 2011. **35**(2): p. 369-374.

226. Bose, S., N.H. Kim, T. Kuila, K.T. Lau, and J.H. Lee, *Electrochemical performance of a graphene-polypyrrole nanocomposite as a supercapacitor electrode.* Nanotechnology, 2011. **22**(29).

227. Xu, C.H., J. Sun, and L. Gao, *Synthesis of novel hierarchical graphene/polypyrrole nanosheet composites and their superior electrochemical performance.* Journal of Materials Chemistry, 2011. **21**(30): p. 11253-11258.

228. Zhang, D.C., X. Zhang, Y. Chen, P. Yu, C.H. Wang, and Y.W. Ma, *Enhanced capacitance and rate capability of graphene/polypyrrole composite as electrode material for supercapacitors.* Journal of Power Sources, 2011. **196**(14): p. 5990-5996.

229. Tien, C.P. and H.S. Teng, *Polymer/graphite oxide composites as high-performance materials for electric double layer capacitors.* Journal of Power Sources, 2010. **195**(8): p. 2414-2418.

230. Wu, Z.S., D.W. Wang, W. Ren, J. Zhao, G. Zhou, F. Li, and H.M. Cheng, *Anchoring Hydrous $RuO_{(2)}$ on Graphene Sheets for High-Performance Electrochemical Capacitors.* Advanced Functional Materials, 2010. **20**(20): p. 3595-3602.

231. Cheng, Q., J. Tang, J. Ma, H. Zhang, N. Shinya, and L.C. Qin, *Graphene and nanostructured $MnO_{(2)}$ composite electrodes for supercapacitors.* Carbon, 2011. **49**(9): p. 2917-2925.

232. Fan, Z.J., J. Yan, T. Wei, L.J. Zhi, G.Q. Ning, T.Y. Li, and F. Wei, *Asymmetric Supercapacitors Based on Graphene/$MnO_{(2)}$ and Activated Carbon Nanofiber Electrodes with High Power and Energy Density.* Advanced Functional Materials, 2011. **21**(12): p. 2366-2375.

233. Wu, Z.S., W.C. Ren, D.W. Wang, F. Li, B.L. Liu, and H.M. Cheng, *High-Energy $MnO_{(2)}$ Nanowire/Graphene and Graphene Asymmetric Electrochemical Capacitors.* ACS Nano, 2010. **4**(10): p. 5835-5842.

234. Chen, S., J.W. Zhu, X.D. Wu, Q.F. Han, and X. Wang, *Graphene Oxide-$MnO_{(2)}$ Nanocomposites for Supercapacitors.* ACS Nano, 2010. **4**(5): p. 2822-2830.

235. Wang, S.Y., S.P. Jiang, and X. Wang, *Microwave-assisted one-pot synthesis of metal/metal oxide nanoparticles on graphene and their electrochemical applications.* Electrochimica Acta, 2011. **56**(9): p. 3338-3344.

236. Wang, J., Z. Gao, Z.S. Li, B. Wang, Y.X. Yan, Q. Liu, T. Mann, M.L. Zhang, and Z.H. Jiang, *Green synthesis of graphene nanosheets/ZnO composites and electrochemical properties.* Journal of Solid State Chemistry, 2011. **184**(6): p. 1421-1427.

237. Lu, T., L.K. Pan, H.B. Li, G.A. Zhu, T.A. Lv, X.J. Liu, Z. Sun, T. Chen, and D.H.C. Chua, *Microwave-assisted synthesis of graphene-ZnO nanocomposite for electrochemical supercapacitors.* Journal of Alloys and Compounds, 2011. **509**(18): p. 5488-5492.

238. Yan, J., T. Wei, W.M. Qiao, B. Shao, Q.K. Zhao, L.J. Zhang, and Z.J. Fan, *Rapid microwave-assisted synthesis of graphene nanosheet/$Co_{(3)}O_{(4)}$*

composite for supercapacitors. Electrochimica Acta, 2010. **55**(23): p. 6973-6978.

239. Wang, Y., C.X. Guo, J.H. Liu, T. Chen, H.B. Yang, and C.M. Li, *$CeO_{(2)}$ nanoparticles/graphene nanocomposite-based high performance supercapacitor.* Dalton Transactions, 2011. **40**(24): p. 6388-6391.
240. Chen, Y., X. Zhang, P. Yu, and Y.W. Ma, *Electrophoretic deposition of graphene nanosheets on nickel foams for electrochemical capacitors.* Journal of Power Sources, 2010. **195**(9): p. 3031-3035.
241. Harima, Y., S. Setodoi, I. Imae, K. Komaguchi, Y. Ooyama, J. Ohshita, H. Mizota, and J. Yano, *Electrochemical reduction of graphene oxide in organic solvents.* Electrochimica Acta, 2011. **56**(15): p. 5363-5368.
242. Wang, D.G. and X.G. Wang, *Self-Assembled Graphene/Azo Polyelectrolyte Multilayer Film and Its Application in Electrochemical Energy Storage Device.* Langmuir, 2011. **27**(5): p. 2007-2013.
243. Kim, T.Y.K.T.Y., H.W. Lee, M. Stoller, D.R. Dreyer, C.W. Bielawski, R.S. Ruoff, and K.S. Suh, *High-Performance Supercapacitors Based on Poly(ionic liquid)-Modified Graphene Electrodes.* ACS Nano, 2011. **5**(1): p. 436-442.
244. Han, T.H., W.J. Lee, D.H. Lee, J.E. Kim, E.Y. Choi, and S.O. Kim, *Peptide/Graphene Hybrid Assembly into Core/Shell Nanowires.* Advanced Materials, 2010. **22**(18): p. 2060-+.
245. Gao, Z., J. Wang, Z.S. Li, W.L. Yang, B. Wang, M.J. Hou, Y. He, Q. Liu, T. Mann, P.P. Yang, M.L. Zhang, and L.H. Liu, *Graphene Nanosheet/$Ni^{(2+)}$/$Al^{(3+)}$ Layered Double-Hydroxide Composite as a Novel Electrode for a Supercapacitor.* Chemistry of Materials, 2011. **23**(15): p. 3509-3516.
246. Barrientos, H., I. Moggio, E. Arias-Marin, A. Ledezma, and J. Romero, *Layer-by-layer films of enzymatically synthesized poly(aniline)/bacterial poly(y-glutamic acid) for the construction of nanocapacitors.* European Polymer Journal, 2007. **43**: p. 1672-1680.
247. Guranathan, K., A.V. Murugan, R. Marimuthu, U.P. Mulik, and D.P. Amalnerkar, *Electrochemically synthesised conducting polymeric materials for applications towards technology in electronics, optoelectronics and energy storage devices.* Materials Chemistry and Physics, 1999. **61**: p. 173-191.

248. Mastragostino, M., C. Arbizzani, R. Paraventi, and A. Zanelli, *Polymer selection and Cell design for Electric-Vehicle Supercapacitors.* Journal of the Electrochemical Society, 2000. **147**(2): p. 407-412.

249. Mastragostino, M., R. Paraventi, and A. Zanelli, *Supercapacitors based on Composite Polymer Electrodes.* Journal of the Electrochemical Society, 2000. **147**(9): p. 3167-3170.

250. Fusalba, F., N. El Mehdi, L. Breau, and D. Belanger, *Physicochemical and Electrochemical Characterization of Polycyclopenta[2,1-b;3,4-b']dithiophen-4-one as an Active Electrode for Electrochemical Supercapacitors.* Chem. Mater., 1999. **11**(10): p. 2743-2753.

251. Fusalba, F. and D. Belanger, *Electropolymerization of Polypyrrole and Polyaniline-Polypyrrole from Organic Acidic Medium.* J. Phys. Chem. B, 1999. **103**(42): p. 9044-9054.

252. Downs, C., J. Nugent, P.M. Ajayan, D.J. Duquette, and K.S.V. Santhanam, *Efficient Polymerization of Aniline at Carbon Nanotube Electrodes.* Advanced Materials, 1999. **11**(12): p. 1028-1031.

253. Barsukov, V. and S. Chivikov, *The "Capacitor" concept of the current-producing process mechanism in polyaniline-type conducting polymers.* Electrochimica Acta, 1996. **41**(11/12): p. 1773-1779.

254. Ferraris, J.P., M.M. Eissa, I.D. Brotherston, D.C. Loveday, and A.A. Moxey, *Preparation and electrochemical evaluation of poly (3-phenylthiophene) derivatives: Potential materials for electrochemical capacitors.* Journal of Electroanalytical Chemistry, 1998. **459**: p. 57-69.

255. Ghosh, S. and O. Inganas, *Conducting Polymer Hydrogels as 3D Electrodes: Applications for Supercapacitors.* Advanced Materials, 1999. **11**(14): p. 1214-1218.

256. Ma, R.Z., J. Liang, B.Q. Wei, B. Zhang, C.L. Xu, and D.H. Wu, *Study of electrochemical capacitors utilizing carbon nanotube electrodes.* Journal of Power Sources, 1999. **84**: p. 126-129.

257. Diederich, L., E. Barborini, P. Piseri, A. Podesta, P. Milani, A. Schneuwly, and R. Gallay, *Supercapacitors based on nanostructured carbon electrodes grown by cluster-beam deposition.* Applied Physics Letters, 1999. **75**(17): p. 2662-2664.

258. Honda, K., T.N. Rao, D.A. Tryk, A. Fujishima, M. Watanabe, K. Yasui, and H. Masuda, *Electrochemical Characterization of the Nanoporous Honeycomb Diamond Electrode as an Electrical Double-Layer Capacitor.* Journal of the Electrochemical Society, 2000. **147**(2): p. 659-664.

259. Honda, K., T.N. Rao, D.A. Tryk, A. Fujishima, M. Watanabe, K. Yasui, and H. Masuda, *Impedance Characteristics of the Nanoporous Honeycomb Diamond Electrodes for Electrical Double-Layer Capacitor Applications.* Journal of the Electrochemical Society, 2001. **148**(7): p. A668-A679.

260. Templeton, A.C., W.P. Wuelfing, and R.W. Murray, *Monolayer-Protected Cluster Molecules.* Acc. Chem. Res., 2000. **33**(1): p. 27-36.

261. Leff, D.V., P.C. Ohara, J.R. Heath, and W.M. Gelbart, *Thermodynamic Control of Gold Nanocrystal Size - Experiment and Theory.* Journal of Physical Chemistry, 1995. **99**(18): p. 7036-7041.

262. *chain lengths below four do not provide a sufficient energy barrier to isolate the gold cores. alkanethiol chains longer than fourteen are solid at RT making unreacted thiols harder to remove from the nanoparticles via precipitation.*

263. Oldfield, G., T. Ung, and P. Mulvaney, *Au@SnO Core-Shell Nanocapacitors.* Advanced Materials, 2000. **12**(20): p. 1519-1522.

264. Brust, M., M. Walker, D. Bethell, D.J. Schiffrin, and R. Whyman, *Synthesis of Thiol-Derivatized Gold Nanoparticles in a 2-Phase Liquid-Liquid System.* Journal of the Chemical Society-Chemical Communications, 1994(7): p. 801-802.

265. Hicks, J.F., D.T. Miles, and R.W. Murray, *Quantized double-layer charging of highly monodisperse metal nanoparticles.* Journal of the American Chemical Society, 2002. **124**(44): p. 13322-13328.

266. Green, S.J., J.J. Stokes, M.J. Hostetler, J. Pietron, and R.W. Murray, *Three-Dimensional Monolayers: Nanometer-Sized Electrodes of Alkanethiolate-Stabilized Gold Cluster Molecules.* J. Phys. Chem. B, 1997. **101**(14): p. 2663-2668.

267. Hostetler, M.J., J.E. Wingate, C.J. Zhong, J.E. Harris, R.W. Vachet, M.R. Clark, J.D. Londono, S.J. Green, J.J. Stokes, G.D. Wignall, G.L. Glish, M.D. Porter, N.D. Evans, and R.W. Murray, *Alkanethiolate gold cluster molecules*

with core diameters from 1.5 to 5.2 nm: Core and monolayer properties as a function of core size. Langmuir, 1998. **14**(1): p. 17-30.

268. Green, S.J., J.J. Pietron, J.J. Stokes, M.J. Hostetler, H. Vu, W.P. Wuelfing, and R.W. Murray, *Three-Dimensional Monolayers: Voltammetry of Alkanethiolate-Stabilized Gold Cluster Molecules.* Langmuir, 1998. **14**(19): p. 5612-5619.
269. Fan, F.R.F. and A.J. Bard, *An electrochemical coulomb staircase: Detection of single electron-transfer events at nanometer electrodes.* Science, 1997. **277**(5333): p. 1791-1793.
270. Ingram, R.S., M.J. Hostetler, R.W. Murray, T.G. Schaff, J.T. Khoury, R.L. Whetten, T.P. Bigioni, D.K. Guthrie, and P.N. First, *28 kDa Alkanethiolate-Protected Au Clusters Give Analogous Electrochemistry and STM Coulomb Staircases.* Journal of the American Chemical Society, 1997. **119**: p. 9279-9280.
271. Ingram, R.S., M.J. Hostetler, R.W. Murray, T.G. Schaaff, J. Khoury, R.L. Whetten, T.P. Bigioni, D.K. Guthrie, and P.N. First, *28 kDa Alkanethiolate-Protected Au Clusters Give Analogous Solution Electrochemistry and STM Coulomb Staircases.* J. Am. Chem. Soc., 1997. **119**(39): p. 9279-9280.
272. Quinn, B.M., P. Liljeroth, V. Ruiz, T. Laaksonen, and K. Kontturi, *Electrochemical Resolution of 15 Oxidation States for Monolayer Protected Gold Nanoparticles.* J. Am. Chem. Soc., 2003. **125**(22): p. 6644-6645.
273. Jimenez, V.L., D.G. Georganopoulou, R.J. White, A.S. Harper, A.J. Mills, D. Lee, and R.W. Murray, *Hexanethiolate Monolayer Protected 38 Gold Atom Cluster.* Langmuir, 2004. **20**(16): p. 6864-6870.
274. Jadzinsky, P.D., G. Calero, C.J. Ackerson, D.A. Bushnell, and R.D. Kornberg, *Structure of a thiol monolayer-protected gold nanoparticle at 1.1 angstrom resolution.* Science, 2007. **318**(5849): p. 430-433.
275. Teo, B.K., X. Shi, and H. Zhang, *Pure gold cluster of 1:9:9:1:9:9:1 layered structure: a novel 39-metal-atom cluster [(Ph3P)$_{14}$Au$_{39}$Cl$_6$]Cl$_2$ with an interstitial gold atom in a hexagonal antiprismatic cage.* J. Am. Chem. Soc., 1992. **114**(7): p. 2743-2745.
276. Laibinis, P.E., G.M. Whitesides, D.L. Allara, Y.T. Tao, A.N. Parikh, and R.G. Nuzzo, *Comparison of the structures and wetting properties of self-assembled*

monolayers of n-alkanethiols on the coinage metal surfaces, copper, silver, and gold. J. Am. Chem. Soc., 1991. **113**(19): p. 7152-7167.

277. Akola, J., M. Walter, R.L. Whetten, H. Hakkinen, and H. Gronbeck, *On the Structure of Thiolate-Protected Au_{25}.* J. Am. Chem. Soc., 2008. **130**(12): p. 3756-3757.
278. Hakkinen, H., M. Walter, and H. Gronbeck, *Divide and Protect: Capping Gold Nanoclusters with Molecular Gold-Thiolate Rings.* J. Phys. Chem. B, 2006. **110**(20): p. 9927-9931.
279. Zhu, M., C.M. Aikens, F.J. Hollander, G.C. Schatz, and R. Jin, *Correlating the Crystal Structure of A Thiol-Protected Au_{25} Cluster and Optical Properties.* J. Am. Chem. Soc., 2008. **130**(18): p. 5883-5885.
280. Heaven, M.W., A. Dass, P.S. White, K.M. Holt, and R.W. Murray, *Crystal Structure of the Gold Nanoparticle $[N(C_8H_{17})_4][Au_{25}(SCH_2CH_2Ph)_{18}]$*. J. Am. Chem. Soc., 2008. **130**(12): p. 3754-3755.
281. Donkers, R.L., D. Lee, and R.W. Murray, *Synthesis and Isolation of the Molecule-like Cluster $Au_{38}(PhCH_2CH_2S)_{24}$.* Langmuir, 2004. **20**(5): p. 1945-1952.
282. Balasubramanian, R., R. Guo, A.J. Mills, and R.W. Murray, *Reaction of $Au_{55}(PPh_3)_{12}Cl_6$ with Thiols Yields Thiolate Monolayer Protected Au_{75} Clusters.* J. Am. Chem. Soc., 2005. **127**(22): p. 8126-8132.
283. Toikkanen, O., V. Ruiz, Ro, x, G. nnholm, N. Kalkkinen, P. Liljeroth, and B.M. Quinn, *Synthesis and Stability of Monolayer-Protected Au_{38} Clusters.* J. Am. Chem. Soc., 2008. **130**(33): p. 11049-11055.
284. Novak, J.P., C. Nickerson, S. Franzen, and D.L. Feldheim, *Purification of Molecularly Bridged Metal Nanoparticle Arrays by Centrifugation and Size Exclusion Chromatography.* Anal. Chem., 2001. **73**(23): p. 5758-5761.
285. Laaksonen, T., V. Ruiz, P. Liljeroth, and B.M. Quinn, *Ion Limited Charging of Nanoparticle Thin Films.* Journal of Physical Chemistry C, 2008. **112**(40): p. 15637-15642.
286. Tunc, I., U.K. Demirok, S. Suzer, M.A. Correa-Duatre, and L.M. Liz-Marzan, *Charging/Discharging of Au (Core)/Silica (Shell) Nanoparticles as Revealed by XPS.* Journal of Physical Chemistry B, 2005. **109**: p. 24182-24184.

287. Lee, J.S., S.I. Stoeva, and C.A. Mirkin, *DNA-Induced Size-Selective Separation of Mixtures of Gold Nanoparticles.* J. Am. Chem. Soc., 2006. **128**(27): p. 8899-8903.

288. Femoni, C., M. Carmela Iapalucci, G. Longoni, and P.H. Svensson, *New high-nuclearity Ni-Pt carbonyl clusters: synthesis and x-ray structure of the ordered $[HNi_{24}Pt_{17}(CO)_{46}]^{5-}$ and the substitutionally Ni/Pt disordered $[Ni_{32}Pt_{24}(CO)_{56}]^{6-}$ cluster anions.* Chem. Commun., 2004: p. 2274-2275.

289. Mond, L., D. Langer, and D. Quincke, *Action of carbon monoxide on nickel.* J. Chem. Soc. Trans., 1890. **57**: p. 749-753.

290. Femoni, C., M.C. Iapalucci, F. Kaswalder, G. Longoni, and S. Zacchini, *The possible role of metal carbonyl clusters in nanoscience and nanotechnologies.* Coordination Chemistry Reviews, 2006. **250**: p. 1580-1604.

291. Collini, D., C. Femoni, M. Carmela Iapalucci, G. Longoni, P.H. Svensson, and P. Zanello, *Tuning electronic behaviour of Carbonyl Metal Clusters by substitution of interstitial and capping atoms.* Angew. Chem. Int. Ed., 2002. **41**(19): p. 3685-3687.

292. Fabrizi de Biani, F., C. Femoni, M.C. Iapalucci, G. Longoni, P. Zanello, and A. Ceriotti, *Redox Behavior of $[H_6\text{-}nNi_{38}Pt_6(CO)_{48}]^{n-}$ (n = 4-6) Anions: A Series of Metal Carbonyl Clusters Displaying Electron-Sink Features.* Inorg. Chem., 1999. **38**(16): p. 3721-3724.

293. Collini, D., F.d. Biani, S. Fedi, C. Femoni, F. Kaswalder, M.C. Iapalucci, G. Longoni, C. Tiozzo, S. Zachini, and P. Zanello, *Synthesis and Electrochemistry of New Rh-Centered and Conjuncto Rhodium Carbonyl Clusters. X-ray Structure of $[NEt_4]_3[Rh_{15}(CO)_{27}]$, $[NEt_4]_3[Rh_{15}(CO)_{25}(MeCN)_2]â_2MeCN$, and $[NEt_4]_3[Rh_{17}(CO)_{37}]$.* Inorganic Chemistry, 2007. **46**: p. 7971-7981.

294. Kemal, L., X.C. Jiang, K. Wong, and A.B. Yu, *Experiment and Theoretical Study of Poly(vinyl pyrrolidone)-controlled Gold Nanoparticles.* Journal of Physical Chemistry C, 2008. **112**(40): p. 15656-15664.

295. Wasa, K. and S. Hayakawa, *Handbook of sputter deposition technology : principles, technology and applications*. Materials science and process technology series. Electronic materials and process technology. 1992, Park Ridge, N.J: Noyes. xii, 304 p.

296. Buffat, P. and J.P. Borel, *Size Effect on Melting Temperature of Gold Particles.* Physical Review A, 1976. **13**(6): p. 2287-2298.

297. Ke, T.S., *High Temperature Anelastic Effects in Polycrystalline Aluminum.* Physical Review, 1946. **70**(1-2): p. 105-105.

298. Kay, E., *Magnetic Field Effects On An Abnormal Truncated Glow Discharge and Their Relation To Sputtered Thin-Film Growth.* Journal of Applied Physics, 1963. **34**(4): p. 760-&.

299. Gill, W.D. and E. Kay, *Efficient Low Pressure Sputtering In A Large Inverted Magnetron Suitable For Film Synthesis.* Review of Scientific Instruments, 1965. **36**(3): p. 277-&.

300. Everhart, T.E. and R.F.M. Thornley, *Wide-Band Detector for Micro-Microampere Low-Energy Electron Currents.* Journal of Scientific Instruments, 1960. **37**(7): p. 246-248.

301. Hell, S.W., *Far-field optical nanoscopy.* Science, 2007. **316**(5828): p. 1153-1158.

302. Chang, C.C., *Auger Electron Spectroscopy.* Surface Science, 1971. **25**(1): p. 53-&.

303. Fadley, C.S., *Angle-Resolved X-ray Photoelectron-Spectroscopy.* Progress in Surface Science, 1984. **16**(3): p. 275-388.

304. Binnig, G., C.F. Quate, and C. Gerber, *Atomic Force Microscope.* Physical Review Letters, 1986. **56**(9): p. 930.

305. Rugar, D. and P. Hansma, *Atomic Force Microscopy.* Physics Today, 1990. **43**(10): p. 23-30.

306. Martin, Y., C.C. Williams, and H.K. Wickramasinghe, *Atomic Force Microscope Force Mapping and Profiling on a Sub 100-A Scale.* Journal of Applied Physics, 1987. **61**(10): p. 4723-4729.

307. Meyer, G. and N.M. Amer, *Novel Optical Approach to Atomic Force Microscopy.* Applied Physics Letters, 1988. **53**(12): p. 1045-1047.

308. Deckman, H.W. and J.H. Dunsmuir, *Applications of Surface Textures Produced with Natural Lithography.* Journal of Vacuum Science & Technology B, 1983. **1**(4): p. 1109-1112.

309. Fredriksson, H., Y. Alaverdyan, A. Dmitriev, C. Langhammer, D.S. Sutherland, M. Zaech, and B. Kasemo, *Hole-mask colloidal lithography.* Advanced Materials, 2007. **19**(23): p. 4297-+.

310. Haynes, C.L. and R.P. Van Duyne, *Nanosphere lithography: A versatile nanofabrication tool for studies of size-dependent nanoparticle optics.* Journal of Physical Chemistry B, 2001. **105**(24): p. 5599-5611.

311. Hulteen, J.C. and R.P. Van Duyne, *Nanosphere lithography: A materials general fabrication process for periodic particle array surfaces.* J. Vac. Sci. Technol. A, 1995. **13**(3): p. 1553-1558.

312. Li, C., G.S. Hong, P.W. Wang, D.P. Yu, and L.M. Qi, *Wet Chemical Approaches to Patterned Arrays of Well-Aligned ZnO Nanopillars Assisted by Monolayer Colloidal Crystals.* Chemistry of Materials, 2009. **21**(5): p. 891-897.

313. Pakizeh, T., M.S. Abrishamian, N. Granpayeh, A. Dmitriev, and M. Kall, *Magnetic-field enhancement in gold nanosandwiches.* Optics Express, 2006. **14**(18): p. 8240-8246.

314. Sauerbrey, G., *Verwendung Von Schwingquarzen Zur Wagung Dunner Schichten Und Zur Mikrowagung.* Zeitschrift Fur Physik, 1959. **155**(2): p. 206-222.

315. Lu, C.S. and O. Lewis, *Investigation of Film-Thickness Determination by Oscillating Quartz Resonators With Large Mass Load.* Journal of Applied Physics, 1972. **43**(11): p. 4385-&.

316. Yurov, V.Y. and A.N. Klimov, *Scanning Tunneling Microscope Calibration and Reconstruction of Real Image - Drift and Slope Elimination.* Review of Scientific Instruments, 1994. **65**(5): p. 1551-1557.

317. Yang, S.M., S.G. Jang, D.G. Choi, S. Kim, and H.K. Yu, *Nanomachining by colloidal lithography.* Small, 2006. **2**(4): p. 458-475.

318. Ozin, G.A. and S.M. Yang, *The race for the photonic chip: Colloidal crystal assembly in silicon wafers.* Advanced Functional Materials, 2001. **11**(2): p. 95-104.

319. Stein, A., *Sphere templating methods for periodic porous solids.* Microporous and Mesoporous Materials, 2001. **44**: p. 227-239.

320. Zhang, J.H., Y.F. Li, X.M. Zhang, and B. Yang, *Colloidal Self-Assembly Meets Nanofabrication: From Two-Dimensional Colloidal Crystals to Nanostructure Arrays.* Advanced Materials, 2010. **22**(38): p. 4249-4269.

321. Haynes, C.L., A.D. McFarland, M.T. Smith, J.C. Hulteen, and R.P. Van Duyne, *Angle-resolved nanosphere lithography: Manipulation of nanoparticle size, shape, and interparticle spacing.* Journal of Physical Chemistry B, 2002. **106**(8): p. 1898-1902.

322. Ye, X.Z. and L.M. Qi, *Two-dimensionally patterned nanostructures based on monolayer colloidal crystals: Controllable fabrication, assembly, and applications.* Nano Today, 2011. **6**(6): p. 608-631.

323. Deckman, H.W. and J.H. Dunsmuir, *Natural Lithography.* Applied Physics Letters, 1982. **41**(4): p. 377-379.

324. Hikosaka, K., T. Mimura, and K. Joshin, *Selective Dry Etching of AlGaAs-GaAs Hetrojunction.* Japanese Journal of Applied Physics, 1981. **20**(11): p. L847-L850.

325. Smith, T.P., B.B. Goldberg, P.J. Stiles, and M. Heiblum, *Direct Measurement of the Density Of States of a Two-Dimensional Electron-Gas.* Physical Review B, 1985. **32**(4): p. 2696-2699.

326. Smith, T.P., K.Y. Lee, C.M. Knoedler, J.M. Hong, and D.P. Kern, *Electronic Spectroscopy of Zero-Dimensional Systems.* Physical Review B, 1988. **38**(3): p. 2172-2175.

327. Bornside, D.E., C.W. Macosko, and L.E. Scriven, *On the Modeling of Spin Coating.* Journal of Imaging Technology, 1987. **13**(4): p. 122-130.

328. Dozier, W.D., K.P. Daly, R. Hu, C.E. Platt, and M.S. Wire, *Fabrication of High-Tc Josephson Effect Devices by Natural Lithography.* Ieee Transactions on Magnetics, 1991. **27**(2): p. 3223-3226.

329. Fang, H., R. Zeller, and P.J. Stiles, *Fabrication of Quasi-Zero-Dimensional Sub-Micron Dot Array and Capacitance Spectroscopy in a GaAs/AlGaAs Hetrostructure.* Applied Physics Letters, 1989. **55**(14): p. 1433-1435.

330. Kim, B.J., H. Jung, H.Y. Kim, J. Bang, and J. Kim, *Fabrication of GaN nanorods by inductively coupled plasma etching via $SiO_{(2)}$ nanosphere lithography.* Thin Solid Films, 2009. **517**(14): p. 3859-3861.

331. Wong, S., V. Kitaev, and G.A. Ozin, *Colloidal crystal films: Advances in universality and perfection.* Journal of the American Chemical Society, 2003. **125**(50): p. 15589-15598.

332. Haes, A.J. and R.P. Van Duyne, *A nanoscale optical blosensor: Sensitivity and selectivity of an approach based on the localized surface plasmon resonance spectroscopy of triangular silver nanoparticles.* Journal of the American Chemical Society, 2002. **124**(35): p. 10596-10604.

333. Jensen, T.R., M.D. Malinsky, C.L. Haynes, and R.P. Van Duyne, *Nanosphere lithography: Tunable localized surface plasmon resonance spectra of silver nanoparticles.* Journal of Physical Chemistry B, 2000. **104**(45): p. 10549-10556.

334. Jensen, T.R., M.L. Duval, K.L. Kelly, A.A. Lazarides, G.C. Schatz, and R.P. Van Duyne, *Nanosphere lithography: Effect of the external dielectric medium on the surface plasmon resonance spectrum of a periodic array of sliver nanoparticles.* Journal of Physical Chemistry B, 1999. **103**(45): p. 9846-9853.

335. Marquez, M. and B.P. Grady, *The use of surface tension to predict the formation of 2D arrays of latex spheres formed via the Langmuir-Blodgett-like technique.* Langmuir, 2004. **20**(25): p. 10998-11004.

336. Du, H., Y.B. Bai, Z. Hui, L.S. Li, Y.M. Chen, X.Y. Tang, and T.J. Li, *Two-dimensional arrays from polymer spheres in nanoscale prepared by the Langmuir-Blodgett method.* Langmuir, 1997. **13**(9): p. 2538-2540.

337. Fulda, K.U. and B. Tieke, *Monolayers of mono- and bidisperse spherical polymer particles at the air/water interface and Langmuir-Blodgett layers on solid substrates.* Supramolecular Science, 1997. **4**(3-4): p. 265-273.

338. Pan, F., J.Y. Zhang, C. Cai, and T.M. Wang, *Rapid fabrication of large-area colloidal crystal monolayers by a vortical surface method.* Langmuir, 2006. **22**(17): p. 7101-7104.

339. Rybczynski, J., U. Ebels, and M. Giersig, *Large-scale, 2D arrays of magnetic nanoparticles.* Colloids and Surfaces a-Physicochemical and Engineering Aspects, 2003. **219**(1-3): p. 1-6.

340. Bohmer, M., *In situ observation of 2-dimensional clustering during electrophoretic deposition.* Langmuir, 1996. **12**(24): p. 5747-5750.

341. Lu, Z.C. and M. Zhou, *Fabrication of large scale two-dimensional colloidal crystal of polystyrene particles by an interfacial self-ordering process.* Journal of Colloid and Interface Science, 2011. **361**(2): p. 429-435.

342. Denkov, N.D., O.D. Velev, P.A. Kralchevsky, I.B. Ivanov, H. Yoshimura, and K. Nagayama, *Mechanism of Formation of 2-Dimensional Crystals From Latex-Particles on Substrates.* Langmuir, 1992. **8**(12): p. 3183-3190.

343. Denkov, N.D., O.D. Velev, P.A. Kralchevsky, I.B. Ivanov, H. Yoshimura, and K. Nagayama, *2-Dimensional Crystallization.* Nature, 1993. **361**(6407): p. 26-26.

344. Shimmin, R.G., A.J. DiMauro, and P.V. Braun, *Slow vertical deposition of colloidal crystals: A Langmuir-Blodgett process?* Langmuir, 2006. **22**(15): p. 6507-6513.

345. *Manual of Symbols and Terminology for Physicochemical Quantities and Units.* Appendix II: Definitions, Terminology and Symbols in Colloid and Surface Chemistry, 1972. **31**(577): p. 606.

346. Hulteen, J.C., D.A. Treichel, M.T. Smith, M.L. Duval, T.R. Jensen, and R.P. Van Duyne, *Nanosphere lithography: Size-tunable silver nanoparticle and surface cluster arrays.* Journal of Physical Chemistry B, 1999. **103**(19): p. 3854-3863.

347. Deegan, R.D., O. Bakajin, T.F. Dupont, G. Huber, S.R. Nagel, and T.A. Witten, *Capillary flow as the cause of ring stains from dried liquid drops.* Nature, 1997. **389**(6653): p. 827-829.

348. Jan, B., *Method of treating bodies of semiconductive material by chemically etching with an acid etching liquid*. 1965, Google Patents.

349. Trigueiro, J., N. Bundaleski, A.G. Silva, and O. Teodoro, *Influence of the patch field on work function study using the onset method.* Vacuum, 2013. **98**: p. 41-44.

350. Cazaux, J., *Material contrast in SEM: Fermi energy and work function effects.* Ultramicroscopy, 2010. **110**(3): p. 242-253.

351. Brown, R., *XXVII. A brief account of microscopical observations made in the months of June, July and August 1827, on the particles contained in the pollen of plants; and on the general existence of active molecules in organic and inorganic bodies.* The Philosophical Magazine, or Annals of Chemistry,

Mathematics, Astronomy, Natural History and General Science, 1828. **4**(21): p. 161-173.

352. Einstein, A., *The theory of the brownian movement.* Ann. der Physik, 1905. **17**: p. 549.
353. Klein, R. and P. Meakin, *Universality in colloid aggregation.* Nature, 1989. **339**(3).
354. Bullen, H.A. and S.J. Garrett, *TiO_2 nanoparticle arrays prepared using a nanosphere lithography technique.* Nano Letters, 2002. **2**(7): p. 739-745.
355. Burmeister, F., C. Schafle, T. Matthes, M. Bohmisch, J. Boneberg, and P. Leiderer, *Colloid monolayers as versatile lithographic masks.* Langmuir, 1997. **13**(11): p. 2983-2987.
356. Andreazza, P., C. Andreazza-Vignolle, J.P. Rozenbaum, A.L. Thomann, and P. Brault, *Nucleation and initial growth of platinum islands by plasma sputter deposition.* Surface & Coatings Technology, 2002. **151**: p. 122-127.
357. Venables, J.A., G.D.T. Spiller, and M. Hanbucken, *Nucleation and Growth of Thin-Films.* Reports on Progress in Physics, 1984. **47**(4): p. 399-459.
358. Grovenor, C.R.M., H.T.G. Hentzell, and D.A. Smith, *The Development of Grain-Structure During Growth of Metallic-Films.* Acta Metallurgica, 1984. **32**(5): p. 773-781.
359. Thornton, J.A., *Influence of apparatus geometry and deposition conditions on the structure and topography of thick sputtered coatings.* Journal of Vacuum Science & Technology, 1974. **11**(4): p. 666-670.
360. Abruna, H.D., Y. Kiya, and J.C. Henderson, *Batteries and electrochemical capacitors.* Physics Today, 2008. **61**(12): p. 43-47.
361. Jayalakshmi, M. and K. Balasubramanian, *Simple Capacitors to Supercapacitors - An Overview.* International Journal of Electrochemical Science, 2008. **3**(11): p. 1196-1217.
362. Winter, M. and R.J. Brodd, *What are batteries, fuel cells, and supercapacitors?* Chemical Reviews, 2004. **104**(10): p. 4245-4269.
363. Oldfield, G., T. Ung, and P. Mulvaney, *Au@SnO_2 core-shell nanocapacitors.* Advanced Materials, 2000. **12**(20): p. 1519-1522.

364. Cazaux, J., K.H. Kim, O. Jbara, and G. Salace, *Charging Effects of MgO Under Electron-Bombardment and Nonohmic Behaviour of the Induced Specimen Current.* Journal of Applied Physics, 1991. **70**(2): p. 960-965.

365. Leff, D.V., L. Brandt, and J.R. Heath, *Synthesis and characterization of hydrophobic, organically-soluble gold nanocrystals functionalized with primary amines.* Langmuir, 1996. **12**(20): p. 4723-4730.

366. Grffiths, D., *Introduction to Electrodynamics*. 3rd ed. 1999.

367. McHale, J.M., A. Auroux, A.J. Perrotta, and A. Navrotsky, *Surface energies and thermodynamic phase stability in nanocrystalline aluminas.* Science, 1997. **277**(5327): p. 788-791.

368. Serway, R.A., *Priciples of Physics*. 2nd ed. 1998.

369. Shchipalov, Y.K., *Surface energy of crystalline and vitreous silica.* Glass and Ceramics, 2000. **57**(11-12): p. 374-377.

370. Ashkenov, N., B.N. Mbenkum, C. Bundesmann, V. Riede, M. Lorenz, D. Spemann, E.M. Kaidashev, A. Kasic, M. Schubert, M. Grundmann, G. Wagner, H. Neumann, V. Darakchieva, H. Arwin, and B. Monemar, *Infrared dielectric functions and phonon modes of high-quality ZnO films.* J. Appl. Phys., 2003. **99**.

371. Singh, R., M. Kumar, and S. Chandra, *Growth and characterization of high resistivity c-axis oriented ZnO films on different substrates by RF magnetron sputtering for MEMS applications.* J. Mater. Sci., 2007 **42**: p. 4675-4683.

372. Xu, F., P. Zhang, A. Navrotsky, Z.Y. Yuan, T.Z. Ren, M. Halasa, and B.L. Su, *Hierarchically assembled porous ZnO nanoparticles: Synthesis, surface energy, and photocatalytic activity.* Chemistry of Materials, 2007. **19**(23): p. 5680-5686.

373. Gu, G.R., Z. He, Y.C. Tao, Y.A. Lia, J.J. Li, H. Yin, W.Q. Lia, and Y.N. Zhao, *Conductivity of nanometer TiO_2 thin films by magnetron sputtering.* Vacuum, 2003. **70**(1): p. 17-20.

374. Kuo, D.H. and K.H. Tzeng, *Characterization and properties of r.f.-sputtered thin films of the alumina-titania system.* Thin Solid Films, 2004. **460**(1-2): p. 327-334.

375. Akl, A.A., H. Kamal, and K. Abdel-Hady, *Fabrication and characterization of sputtered titanium dioxide films.* Applied Surface Science, 2006. **252**(24): p. 8651-8656.

376. Zhang, H.Z., B. Chen, and J.F. Banfield, *The size dependence of the surface free energy of titania nanocrystals.* Physical Chemistry Chemical Physics, 2009. **11**(14): p. 2553-2558.

377. Hsu, C.T., Y.K. Su, and M. Yokoyama, *High Dielectric-Constant of RF-Sputtered HFO_2 Thin-Films.* Japanese Journal of Applied Physics Part 1-Regular Papers Brief Communications & Review Papers, 1992. **31**(8): p. 2501-2504.

378. Hsu, C.T., J.W. Li, C.H. Liu, Y.K. Su, T.S. Wu, and M. Yokoyama, *High Luminous Efficiency Thin-Film Electroluminescent Devices With Low Resistivity Insulating Materials.* Journal of Applied Physics, 1992. **71**(3): p. 1509-1512.

379. Pereira, L., P. Barquinha, E. Fortunato, and R. Martins, *Influence of the oxygen/argon ratio on the properties of sputtered hafnium oxide.* Materials Science and Engineering B-Solid State Materials for Advanced Technology, 2005. **118**(1-3): p. 210-213.

380. Mukhopadhyay, A.B., J.F. Sanz, and C.B. Musgrave, *First-principles calculations of structural and electronic properties of monoclinic hafnia surfaces.* Physical Review B, 2006. **73**(11).

381. Black, R.D., S.D. Arthur, R.S. Gilmore, N. Lewis, E.L. Hall, and R.D. Lillquist, *Silicon and Silicon Dioxide Thermal Bonding for Silicon-on-Insulator Applications.* Journal of Applied Physics, 1988. **63**(8): p. 2773-2777.

382. Ton-That, C., L. Weston, and M.R. Phillips, *Characteristics of point defects in the green luminescence from Zn- and O-rich ZnO.* Physical Review B, 2012. **86**(11).

383. Phillips, M.R., O. Gelhausen, and E.M. Goldys, *Cathodoluminescence properties of zinc oxide nanoparticles.* Physica Status Solidi a-Applied Research, 2004. **201**(2): p. 229-234.

384. Ton-That, C., M. Foley, M.R. Phillips, T. Tsuzuki, and Z. Smith, *Correlation between the structural and optical properties of Mn-doped ZnO nanoparticles.* Journal of Alloys and Compounds, 2012. **522**: p. 114-117.

385. Choi, S., C. Ton-That, M.R. Phillips, and I. Aharonovich, *Observation of whispering gallery modes from hexagonal ZnO microdisks using cathodoluminescence spectroscopy.* Applied Physics Letters, 2013. **103**(17).

386. McBean, K.E., M.R. Phillips, and E.M. Goldys, *Synthesis and characterization of doped and undoped ZnO nanostructures.* Microscopy and Microanalysis, 2006. **12**(4): p. 327-330.

387. Ton-That, C., M. Foley, and M.R. Phillips, *Luminescent properties of ZnO nanowires and as-grown ensembles.* Nanotechnology, 2008. **19**(41).

388. Harris, H., K. Choi, N. Mehta, A. Chandolu, N. Biswas, G. Kipshidze, S. Nikishin, S. Gangopadhyay, and H. Temkin, *HfO_2 gate dielectric with 0.5 nm equivalent oxide thickness.* Applied Physics Letters, 2002. **81**(6): p. 1065-1067.

389. Wilk, G.D., R.M. Wallace, and J.M. Anthony, *Hafnium and zirconium silicates for advanced gate dielectrics.* Journal of Applied Physics, 2000. **87**(1): p. 484-492.

390. Forst, C.J., C.R. Ashman, K. Schwarz, and P.E. Blochl, *The interface between silicon and a high-k oxide.* Nature, 2004. **427**(6969): p. 53-56.

391. R, L.D., *CRC Handbook of Chemistry and Physics*. 85th edition ed. 2005.

392. Wasa. Kiyotaka., H.S., *Handbook of Sputter Deposition Technology*. 1992: NOYES PUBLICATIONS.

393. Seiler, H., *Secondary electron emission in the scanning electron microscope. J. Appl. Phys.*, 1983. **54**: p. R1-R17.

394. Cazaux, J., *Calculated influence of work function on SE escape probability and Secondary Electron Emission yield.* Applied Surface Science, 2010. **257**(3): p. 1002-1009.

395. Egerton, R.F., P. Li, and M. Malac, *Radiation damage in the TEM and SEM.* Micron, 2004. **35**(6): p. 399-409.

396. P., C.N., *Industrial Solvents Handbook*. 2nd edition ed. 2003: Marcel Dekker Inc.

397. Na, S.H. and C.H. Park, *First-Principles Study of the Surface Energy and the Atom Cohesion of Wurtzite ZnO and ZnS - Implications for Nanostructure Formation.* Journal of the Korean Physical Society, 2010. **56**(1): p. 498-502.

398. Lee, H.Y., P.S. Chen, C.C. Wang, S. Maikap, P.J. Tzeng, C.H. Lin, L.S. Lee, and M.J. Tsai, *Low-power switching of nonvolatile resistive memory using hafnium oxide.* Japanese Journal of Applied Physics Part 1-Regular Papers Brief Communications & Review Papers, 2007. **46**(4B): p. 2175-2179.

399. Li, F.M., B.C. Bayer, S. Hofmann, J.D. Dutson, S.J. Wakeham, M.J. Thwaites, W.I. Milne, and A.J. Flewitt, *High-k (k=30) amorphous hafnium oxide films from high rate room temperature deposition.* Applied Physics Letters, 2011. **98**(25).

400. R., W.J., *Polystyrene: Synthesis, Production and Applications*, ed. R. Dolbey. 2000: Rapra Technology Ltd.

401. Patnode, W. and W.J. Scheiber, *The Density, Thermal Expansion, Vapor Pressure, and Refractive Index of Styrene, and the Density and Thermal Expansion of Polystyrene.* Journal of the American Chemical Society, 1939. **61**(12): p. 3449-3451.

402. Golan, Y., L. Margulis, and I. Rubinstein, *Vacuum-Deposited Gold-Films .1. Factors Affecting the Film Morphology.* Surface Science, 1992. **264**(3): p. 312-326.

403. Uosaki, K., Y. Shen, and T. Kondo, *Preparation of a Highly Ordered Au(111) Phase on a Polycrystalline Gold Substrate by Vacuum Deposition and its Characterization by XRD, GISXRD, STM/AFM, and Electrochemical Measurements.* Journal of Physical Chemistry, 1995. **99**(38): p. 14117-14122.

404. Pashley, D.W. and M.J. Stowell, *Nucleation and Growth of Thin Films as Observed in Electron Microscope.* Journal of Vacuum Science & Technology, 1966. **3**(3): p. 156-&.

405. Needs, R.J. and M. Mansfield, *Calculations of the Surface Stress Tensor and Surface-Energy of the (111) Surfaces of Iridium, Platinum and Gold.* Journal of Physics-Condensed Matter, 1989. **1**(41): p. 7555-7563.

406. Jaccodine, R.J., *Surface Energy of Germanium and Silicon.* Journal of the Electrochemical Society, 1963. **110**(6): p. 524-527.

407. Saito, N., H. Haneda, T. Sekiguchi, N. Ohashi, I. Sakaguchi, and K. Koumoto, *Low-Temperature Fabrication of Light-Emitting Zinc Oxide Micropatterns Using Self-Assembled Monolayers.* Advanced Materials, 2002. **14**(6): p. 418-421.

408. Lee, J.Y., Y.S. Choi, J.H. Kim, M.O. Park, and S. Im, *Optimizing n-ZnO/p-Si heterojunctions for photodiode applications.* Thin Solid Films, 2002. **403-404**: p. 553-557.

409. Liang, S., H. Sheng, Y. Liu, Z. Huo, Y. Lu, and H. Shen, *ZnO Schottky ultraviolet photodetectors.* Journal of Crystal Growth, 2001. **225**(2-4): p. 110-113.

410. Emanetoglu, N.W., C. Gorla, Y. Liu, S. Liang, and Y. Lu, *Epitaxial ZnO piezoelectric thin films for saw filters.* Materials Science in Semiconductor Processing, 1999. **2**(3): p. 247-252.

411. Rousset, J., E. Saucedo, and D. Lincot, *Extrinsic Doping of Electrodeposited Zinc Oxide Films by Chlorine for Transparent Conductive Oxide Applications.* Chemistry of Materials, 2009. **21**(3): p. 534-540.

412. Chen, Y., D. Bagnall, and T. Yao, *ZnO as a novel photonic material for the UV region.* Materials Science and Engineering B, 2000. **75**(2-3): p. 190-198.

413. Elias, J., R. Tena-Zaera, G.-Y. Wang, and C. LeÌ• vy-CleÌ• ment, *Conversion of ZnO Nanowires into Nanotubes with Tailored Dimensions.* Chemistry of Materials, 2008. **20**(21): p. 6633-6637.

414. Wang, X., G. Li, T. Chen, M. Yang, Z. Zhang, T. Wu, and H. Chen, *Polymer-Encapsulated Gold-Nanoparticle Dimers: Facile Preparation and Catalytical Application in Guided Growth of Dimeric ZnO-Nanowires.* Nano Lett., 2008. **8**(9): p. 2643-2647.

415. Hwang, W., J.-H. Choi, T.H. Kim, J. Sung, J.-M. Myoung, D.-G. Choi, B.-H. Sohn, S.S. Lee, D.H. Kim, and C. Park, *Control of the Area Density of Vertically Grown ZnO Nanowires by Blending PS-b-P4VP and PS-b-PAA Copolymer Micelles.* Chemistry of Materials, 2008. **20**(19): p. 6041-6047.

416. Liu, D.F., Y.J. Xiang, X.C. Wu, Z.X. Zhang, L.F. Liu, L. Song, X.W. Zhao, S.D. Luo, W.J. Ma, J. Shen, W.Y. Zhou, G. Wang, C.Y. Wang, and S.S. Xie, *Periodic ZnO nanorod arrays defined by polystyrene microsphere self-assembled monolayers.* Nano Letters, 2006. **6**(10): p. 2375-2378.

417. Kim, Y.J., C.H. Lee, Y.J. Hong, G.C. Yi, S.S. Kim, and H. Cheong, *Controlled selective growth of ZnO nanorod and microrod arrays on Si substrates by a wet chemical method.* Applied Physics Letters, 2006. **89**(16).

418. Weintraub, B., Y.L. Deng, and Z.L. Wang, *Position-controlled seedless growth of ZnO nanorod arrays on a polymer substrate via wet chemical synthesis.* Journal of Physical Chemistry C, 2007. **111**(28): p. 10162-10165.

419. Vayssieres, L., *Growth of Arrayed Nanorods and Nanowires of ZnO from Aqueous Solutions.* Advanced Materials, 2003. **15**(5): p. 464-466.

420. Zhao, F., X. Li, J.-G. Zheng, X. Yang, F. Zhao, K.S. Wong, J. Wang, W. Lin, M. Wu, and Q. Su, *ZnO Pine-Nanotree Arrays Grown from Facile Metal Chemical Corrosion and Oxidation.* Chemistry of Materials, 2008. **20**(4): p. 1197-1199.

421. Maissel, L.I. and P.M. Schaible, *Thin Films Deposited by Bias Sputteribg.* Journal of Applied Physics, 1965. **36**(1): p. 237-&.

422. Song, Q.M., B.J. Wu, B. Xie, F. Huang, M. Li, H.Q. Wang, Y.S. Jiang, and Y.Z. Song, *Resputtering of zinc oxide films prepared by radical assisted sputtering.* Journal of Applied Physics, 2009. **105**(4).

423. Jones, R.E., C.L. Standley, and L.I. Maissel, *Self-Sticking Coefficients of SiO_2 Films Deposited Through RF Sputtering.* Journal of Vacuum Science & Technology, 1966. **3**(5): p. 304-&.

424. Jones, R.E., C.L. Standley, and L.I. Maissel, *Self-Sticking Coefficients of SiO_2 Films Deposited Through RF Sputtering.* Vacuum, 1967. **17**(3): p. 165-&.

425. Pliskin, W.A., P.D. Davidse, H.S. Lehman, and L.I. Maissel, *Properties of Insulating Thin Films Deposited by RF Sputtering.* Ibm Journal of Research and Development, 1967. **11**(4): p. 461-&.

426. Jones, R.E., C.L. Standley, and L.I. Maissel, *Re-Emission Coefficients of Si and SiO_2 Films Deposited Through RF and DC Sputtering.* Journal of Applied Physics, 1967. **38**(12): p. 4656-&.

427. Jones, R.E., H.F. Winters, and L.I. Maissel, *Effect of Oxygen on RF-Sputtering Rate of SiO_2.* Journal of Vacuum Science & Technology, 1968. **5**(3): p. 84-&.

428. Maissel, L.I., R.E. Jones, and C.L. Standley, *Re-Emission of Sputtered SiO_2 During Growth and its Relation to Film Quality.* Ibm Journal of Research and Development, 1970. **14**(2): p. 176-&.

429. Koenig, H.R. and L.I. Maissel, *Application of RF Discharges to Sputtering.* Ibm Journal of Research and Development, 1970. **14**(2): p. 168-&.

430. Schottky, W., *Zur halbleitertheorie der sperrschicht-und spitzengleichrichter.* Zeitschrift für Physik, 1939. **113**(5-6): p. 367-414.

431. Dhananjay, J. Nagaraju, and S.B. Krupanidhi, *Investigations on magnetron sputtered ZnO thin films and Au/ZnO Schottky diodes.* Physica B 2007. **391**: p. 344-349.

432. Newton, M.C., S. Firth, and P.A. Warburton, *ZnO tetrapod Schottky photodiodes.* Applied Physics Letters, 2006. **89**(7).

433. Coburn, J.W., E. Taglauer, and E. Kay, *Glow-Discharge Mass-Spectometry - Technique for Determining Elemental Composition Profiles In Solids.* Journal of Applied Physics, 1974. **45**(4): p. 1779-1786.

434. Coburn, J.W., E.W. Eckstein, and E. Kay, *Elemental Composition Profiling In Thin-Films By Glow-Discharge Mass-Spectometry - Depth Resolution.* Journal of Applied Physics, 1975. **46**(7): p. 2828-2830.

435. Citrin, P.H., G.K. Wertheim, and Y. Baer, *Core-Level Binding-Enegy and Density of States from Surface Atoms of Gold.* Physical Review Letters, 1978. **41**(20): p. 1425-1428.

436. Sigmund, P., *Theory of Sputtering .I. Sputtering Yield of Amorphous and Polycrystalline Targets.* Physical Review, 1969. **184**(2): p. 383-+.

437. Tuyen, L.T.T., D.X. Vinh, P.H. Khoi, and G. Gerlach, *Highly sensitive NOx gas sensor based on a Au/n-Si Schottky diode.* Sensors and Actuators B-Chemical, 2002. **84**(2-3): p. 226-230.

438. Monakhov, E.V., A.Y. Kuznetsov, and B.G. Svensson, *Zinc oxide: bulk growth, role of hydrogen and Schottky diodes.* Journal of Physics D-Applied Physics, 2009. **42**(15).

439. Chapman, S.J., D.P. Hewett, and L.N. Trefethen, *Mathematics of the Faraday Cage.* Siam Review, 2015. **57**(3): p. 398-417.

440. Umar, A., S.H. Kim, Y.S. Lee, K.S. Nahm, and Y.B. Hahn, *Catalyst-free large-quantity synthesis of ZnO nanorods by a vapor-solid growth mechanism: Structural and optical properties.* Journal of Crystal Growth, 2005. **282**(1-2): p. 131-136.

441. Lu, F., W.P. Cai, and Y.G. Zhang, *ZnO hierarchical micro/nanoarchitectures: Solvothermal synthesis and structurally enhanced photocatalytic performance.* Advanced Functional Materials, 2008. **18**(7): p. 1047-1056.

442. Meng, G., X.D. Fang, W.W. Dong, R.H. Tao, Y.P. Zhao, Z.H. Deng, S. Zhou, J.Z. Shao, and L. Li, *One step synthesis of vertically aligned ZnO nanowire arrays with tunable length.* Applied Surface Science, 2010. **256**(22): p. 6543-6549.

443. Wang, M., C.H. Ye, Y. Zhang, G.M. Hua, H.X. Wang, M.G. Kong, and L.D. Zhang, *Synthesis of well-aligned ZnO nanorod arrays with high optical property via a low-temperature solution method.* Journal of Crystal Growth, 2006. **291**(2): p. 334-339.

444. Park, S.K., J.H. Park, K.Y. Ko, S. Yoon, K.S. Chu, W. Kim, and Y.R. Do, *Hydrothermal-Electrochemical Synthesis of ZnO Nanorods.* Crystal Growth & Design, 2009. **9**(8): p. 3615-3620.

445. Moezzi, A., A. McDonagh, A. Dowd, and M. Cortie, *Zinc Hydroxyacetate and Its Transformation to Nanocrystalline Zinc Oxide.* Inorganic Chemistry, 2013. **52**(1): p. 95-102.

446. Moezzi, A., M. Cortie, A. Dowd, and A. McDonagh, *On the formation of nanocrystalline active zinc oxide from zinc hydroxide carbonate.* Journal of Nanoparticle Research, 2014. **16**(4).

447. Moezzi, A., A.M. McDonagh, and M.B. Cortie, *Zinc oxide particles: Synthesis, properties and applications.* Chemical Engineering Journal, 2012. **185**: p. 1-22.

448. Barth, S., F. Hernandez-Ramirez, J.D. Holmes, and A. Romano-Rodriguez, *Synthesis and applications of one-dimensional semiconductors.* Progress in Materials Science, 2010. **55**(6): p. 563-627.

449. Liu, Y., Z.H. Kang, Z.H. Chen, I. Shafiq, J.A. Zapien, I. Bello, W.J. Zhang, and S.T. Lee, *Synthesis, Characterization, and Photocatalytic Application of Different ZnO Nanostructures in Array Configurations.* Crystal Growth & Design, 2009. **9**(7): p. 3222-3227.

450. Baviskar, P.K., P.R. Nikam, S.S. Gargote, A. Ennaoui, and B.R. Sankapal, *Controlled synthesis of ZnO nanostructures with assorted morphologies via simple solution chemistry.* Journal of Alloys and Compounds, 2013. **551**: p. 233-242.

451. Ahsanulhaq, Q., A. Umar, and Y.B. Hahn, *Growth of aligned ZnO nanorods and nanopencils on ZnO/Si in aqueous solution: growth mechanism and structural and optical properties.* Nanotechnology, 2007. **18**(11).

452. Chen, K., D.D. Thang, S. Ishii, R.P. Sugavaneshwa, and T. Nagao, *Selective patterned growth of ZnO nanowires/nanosheets and their photoluminescence properties.* Optical Materials Express, 2015. **5**(2): p. 353-360.

453. Huang, M.H., Y.Y. Wu, H. Feick, N. Tran, E. Weber, and P.D. Yang, *Catalytic growth of zinc oxide nanowires by vapor transport.* Advanced Materials, 2001. **13**(2): p. 113-116.

454. Xu, S., N. Adiga, S. Ba, T. Dasgupta, C.F.J. Wu, and Z.L. Wang, *Optimizing and Improving the Growth Quality of ZnO Nanowire Arrays Guided by Statistical Design of Experiments.* ACS Nano. **0**(0).

455. Ahsanulhaq, Q., J.H. Kim, and Y.B. Hahn, *Controlled selective growth of ZnO nanorod arrays and their field emission properties.* Nanotechnology, 2007. **18**(48).

456. Sepulveda-Guzman, S., B. Reeja-Jayan, E. de la Rosa, A. Torres-Castro, V. Gonzalez-Gonzalez, and M. Jose-Yacaman, *Synthesis of assembled ZnO structures by precipitation method in aqueous media.* Materials Chemistry and Physics, 2009. **115**(1): p. 172-178.

457. She, G., X. Zhang, W. Shi, X. Fan, and J.C. Chang, *Electrochemical/chemical synthesis of highly-oriented single-crystal ZnO nanotube arrays on transparent conductive substrates.* Electrochemistry Communications, 2007. **9**(12): p. 2784-2788.

458. Tong, Y., Y. Liu, L. Dong, D. Zhao, J. Zhang, Y. Lu, D. Shen, and X. Fan, *Growth of ZnO nanostructures with different morphologies by using hydrothermal technique.* Journal of Physical Chemistry B, 2006. **110**(41): p. 20263-20267.

459. Ashfold, M.N.R., R.P. Doherty, N.G. Ndifor-Angwafor, D.J. Riley, and Y. Sun, *The kinetics of the hydrothermal growth of ZnO nanostructures.* Thin Solid Films, 2007. **515**(24): p. 8679-8683.

460. Cao, B.Q., W.P. Cai, F.Q. Sun, Y. Li, Y. Lei, and L.D. Zhang, *Fabrication of large-scale zinc oxide ordered pore arrays with controllable morphology.* Chemical Communications, 2004(14): p. 1604-1605.

461. Cui, M.L., X.M. Wu, L.J. Zhuge, and Y.D. Meng, *Effects of annealing temperature on the structure and photoluminescence properties of ZnO films.* Vacuum, 2007. **81**(7): p. 899-903.

462. Li, Q.H., Q. Wan, Y.X. Liang, and T.H. Wang, *Electronic transport through individual ZnO nanowires.* Applied Physics Letters, 2004. **84**(22): p. 4556-4558.

463. Ton-That, C., M.R. Phillips, M. Foley, S.J. Moody, and A.P.J. Stampfl, *Surface electronic properties of ZnO nanoparticles.* Applied Physics Letters, 2008. **92**(26).

464. Wang, X.J., L.S. Vlasenko, S.J. Pearton, W.M. Chen, and I.A. Buyanova, *Oxygen and zinc vacancies in as-grown ZnO single crystals.* Journal of Physics D-Applied Physics, 2009. **42**(17).

465. Eustis, S. and M.A. El-Sayed, *Why gold nanoparticles are more precious than pretty gold: Noble metal surface plasmon resonance and its enhancement of the radiative and nonradiative properties of nanocrystals of different shapes.* Chemical Society Reviews, 2006. **35**(3): p. 209-217.

466. Haruta, M. and M. Date, *Advances in the catalysis of Au nanoparticles.* Applied Catalysis a-General, 2001. **222**(1-2): p. 427-437.

467. Huang, M.H., S. Mao, H. Feick, H.Q. Yan, Y.Y. Wu, H. Kind, E. Weber, R. Russo, and P.D. Yang, *Room-temperature ultraviolet nanowire nanolasers.* Science, 2001. **292**(5523): p. 1897-1899.

468. Alvarez, M.M., J.T. Khoury, T.G. Schaaff, M.N. Shafigullin, I. Vezmar, and R.L. Whetten, *Optical absorption spectra of nanocrystal gold molecules.* Journal of Physical Chemistry B, 1997. **101**(19): p. 3706-3712.

469. Sonnichsen, C., T. Franzl, T. Wilk, G. von Plessen, J. Feldmann, O. Wilson, and P. Mulvaney, *Drastic reduction of plasmon damping in gold nanorods.* Physical Review Letters, 2002. **88**(7).

470. Zhao, L.L., K.L. Kelly, and G.C. Schatz, *The extinction spectra of silver nanoparticle arrays: Influence of array structure on plasmon resonance wavelength and width.* Journal of Physical Chemistry B, 2003. **107**(30): p. 7343-7350.

471. Hovel, H., S. Fritz, A. Hilger, U. Kreibig, and M. Vollmer, *Width of Cluster Plasmon Resonances - Bulk Dielectric Functions and Chemical Interface Damping.* Physical Review B, 1993. **48**(24): p. 18178-18188.

472. Maier, S.A., M.L. Brongersma, P.G. Kik, S. Meltzer, A.A.G. Requicha, and H.A. Atwater, *Plasmonics - A route to nanoscale optical devices.* Advanced Materials, 2001. **13**(19): p. 1501-+.

473. Kelly, K.L., E. Coronado, L.L. Zhao, and G.C. Schatz, *The optical properties of metal nanoparticles: The influence of size, shape, and dielectric environment.* Journal of Physical Chemistry B, 2003. **107**(3): p. 668-677.

474. Schubert, G., F. Huster, and P. Fath, *Physical understanding of printed thick-film front contacts of crystalline Si solar cells- Review of existing models and recent developments.* Solar Energy Materials and Solar Cells, 2006. **90**(18-19): p. 3399-3406.

475. Brabec, C.J., N.S. Sariciftci, and J.C. Hummelen, *Plastic solar cells.* Advanced Functional Materials, 2001. **11**(1): p. 15-26.

476. Springer, J., A. Poruba, L. Mullerova, M. Vanecek, O. Kluth, and B. Rech, *Absorption loss at nanorough silver back reflector of thin-film silicon solar cells.* Journal of Applied Physics, 2004. **95**(3): p. 1427-1429.

477. Coutts, M.J., M.B. Cortie, M.J. Ford, and A.M. McDonagh, *Rapid and Controllable Sintering of Gold Nanoparticle Inks at Room Temperature Using a Chemical Agent.* The Journal of Physical Chemistry C, 2009. **113**(4): p. 1325-1328.

478. Bishop, P.T., L.J. Ashfield, A. Berzins, A. Boardman, V. Buche, J. Cookson, R.J. Gordon, C. Salcianu, and P.A. Sutton, *Printed gold for electronic applications.* Gold Bull., 2010. **43**(3): p. 181-188.

479. Wu, Y., Y. Li, P. Liu, S. Gardner, and B.S. Ong, *Studies of gold nanoparticles as precursors to printed conductive features for thin-film transistors.* Chem. Mater., 2006. **18**(19): p. 4627-4632.

480. Ko, S.H., H. Pan, C.P. Grigoropoulos, C.K. Luscombe, J.M.J. Fréchet, and D. Poulikakos, *Air stable high resolution organic transistors by selective laser sintering of ink-jet printed metal nanoparticles.* Appl. Phys. Lett., 2007. **90**: p. 141103.

481. Bakhishev, T. and V. Subramanian, *Investigation of gold nanoparticle inks for low-temperature lead-free packaging technology.* J. Electronic Mater., 2009. **38**(12): p. 2720-2725.

482. Ingham, B., T.H. Lim, C.J. Dotzler, A. Henning, M.F. Toney, and R.D. Tilley, *How nanoparticles coalesce: an in situ study of Au nanoparticle aggregation and grain growth.* Chem. Mater, 2011. **23** p. 3312–3317.

483. Ristau, R., R. Tiruvalam, P.L. Clasen, E.P. Gorskowski, M.P. Harmer, C.J. Kiely, I. Hussain, and M. Brust, *Electron microscopy studies of the thermal stability of gold nanoparticle arrays.* Gold Bull., 2009. **42**(2): p. 133-143.

484. Yamauchi, H., T. Dobashi, and S. Sato, *Gold-nanoparticle Inks for Room-temperature Formation of Conductive Films.* Chemistry Letters, 2012. **41**(10): p. 1154-1156.

485. Tobjork, D., H. Aarnio, P. Pulkkinen, R. Bollstrom, A. Maattanen, P. Ihalainen, T. Makela, J. Peltonen, M. Toivakka, H. Tenhu, and R. Osterbacka, *IR-sintering of ink-jet printed metal-nanoparticles on paper.* Thin Solid Films, 2012. **520**(7): p. 2949-2955.

486. Coutts, M., M.B. Cortie, M.J. Ford, and A.M. McDonagh, *On the mechanism of sintering of thiol-stabilized gold nanoparticles: Formation of conductive gold films at room temperature.* J. Phys. Chem. C, 2009. **113**(4): p. 1325-1328.

487. Breitinger, D. and W. Herrmann, *Synthetic Methods of Organometallic and Inorganic Chemistry*. Vol. 5. 1999, Stuttgart: George Thieme Verlag.

488. Brust, M., M. Walker, D. Bethell, D.J. Schiffrin, and R. Whyman, Chem. Commun., 1994: p. 801-802.

489. Huang, D., F. Liao, S. Molesa, D. Redinger, and V. Subramanian, *Plastic-compatible low resistance printable gold nanoparticle conductors for flexible electronics.* J. Electrochem. Soc., 2003. **150**(7): p. G412-G417.